Characterizing the aLIGO Interferometers

Primary thesis supervisor: Professor David Ottaway
Secondary thesis supervisor: Professor Peter Veitch

Eleanor Jean King

A thesis presented for the degree of
Doctor of Philosophy

School: School of Physical Sciences
Discipline: Physics University Name: University of Adelaide
Country: Australia
January 2020

CONTENTS

ABSTRACT

This thesis describes a variety of characterization measurements made on the Advanced LIGO (aLIGO) interferometers, which are important for understanding the as-built interferometer and enhancing sensitivity. The aLIGO detectors began detecting Gravitational Waves in 2015 after many decades of research and development, beginning a new age of gravitational wave astronomy. Moving into the future, continued improvements in detector sensitivity will increase the range and detecting capability of the instruments. Improvements to detector sensitivity will be achieved through a variety of efforts, including improving lock stability, improving mode matching, and decreasing power losses in the interferometer.

Characterizing the aLIGO interferometers is particularly challenging because the interferometers are enclosed within a large-scale vacuum system, which limits access to the equipment. The techniques described in this thesis illustrate ways that the properties of the cavities and optics may be probed when the components of the cavities are not easily accessible for individual measurement.

Chapter 1 presents an introduction to gravitational wave detection. Chapter 2 introduces the theoretical background for cavity characterization measurements which underpin many of the measurements presented in later chapters. Chapter 3 describes measurements performed on the interferometer cavities using locked cavity techniques. These measurements yielded accurate results for arm cavity g-factor, power recycling cavity length and Gouy phase, Schnupp asymmetry length, and signal recycling cavity length. The SRC Gouy phase was not accurately measured using this technique due to the low Finesse of this cavity. Chapter 4 discusses a method for measuring

the Gouy phase of an unlocked cavity, which may be used to measure the Gouy phase of a low finesse cavity, and describes how this method was used in the signal recycling cavity. Chapter 5 presents in-situ scattering and absorption measurements of the input- and end-test masses and input mode cleaner optics, using cameras and Hartmann wavefront sensors. Chapter 5 also discusses the impact of these properties on power build-up and thermal lensing. Chapter 6 presents a technique which can be used for faster modelling of thermal deformation in optics, which may be used to improve time-dependent interferometer models.

The measured properties of the cavities and optics presented in this thesis allow for improved understanding of mode matching and power build-up in the aLIGO interferometers. This information will be used in future commissioning efforts to improve detector sensitivity.

THESIS DECLARATION

I certify that this work contains no material which has been accepted for the award of any other degree or diploma in my name, in any university or other tertiary institution and, to the best of my knowledge and belief, contains no material previously published or written by another person, except where due reference has been made in the text. In addition, I certify that no part of this work will, in the future, be used in a submission in my name, for any other degree or diploma in any university or other tertiary institution without the prior approval of the University of Adelaide and where applicable, any partner institution responsible for the joint-award of this degree.

I acknowledge that copyright of published works contained within this thesis resides with the copyright holder(s) of those works.

I also give permission for the digital version of my thesis to be made available on the web, via the Universitys digital research repository, the Library Search and also through web search engines, unless permission has been granted by the University to restrict access for a period of time.

I acknowledge the support I have received for my research through the provision of an Australian Government Research Training Program Scholarship.

ACKNOWLEDGMENTS

Undertaking the work presented in this thesis has been a huge project that never would have reached completion without the guidance and collaboration of many people. This is no doubt true of all PhD projects, but has been particularly apparent working on such a large-scale scientific collaboration as the LIGO project. Many people across the word have helped to make this research possible, and I extend my heart-felt thanks to all of them.

In particular I wish to thank my thesis supervisors David and Peter, my family, especially Mum, Dad, Dan and Anne-Marie, and collaborators Yuri, and Andreas, for their continued support. Thank you to all of my fantastic colleagues and friends that I worked with at the the University of Adelaide and the LIGO observatories. A special thanks has to go Daniel for feeding us each Thursday, and to Keita, John, Dick, Nutsinee and Ed from the LIGO bluegrass band.

This thesis is dedicated to Tom, Max, and Michael.

LIST OF FIGURES

1. INTRODUCTION

This thesis covers detector characterization work performed on the aLIGO interferometers. The chapter begins with an introduction to gravitational waves and gravitational wave detectors. This is followed by an overview of the aLIGO detectors, including a discussion of noise sources and other factors which influence detector sensitivity. A particular focus is given to mode matching and power build-up, and how such issues will be addressed in future upgrades. The chapter concludes with introduction to the work in this thesis, and the impact that detector characterization efforts has upon future detector upgrades.

1.1 The Dawn of Gravitational Wave Astronomy

Over a billion years ago, two black holes orbiting each other in a binary system spiraled together to coalesce into a single black hole. The event created a distortion in space-time that rippled outwards at the speed of light, carrying three solar masses worth of matter converted into energy. On 14 September 2015, these gravitational waves passed through Earth. The two aLIGO gravitational wave detectors, which had begun recording data only days beforehand, measured a strain in space-time[1]. Gravitational waves had been detected for the first time in history. The 2015 detection marked the beginning of a new era in the field of gravitational wave (GW) science.

The event detected by the aLIGO detectors is illustrated in Figure 1.1. The bottom illustration shows the gravitational wave signal that was detected and the top illustration shows the corresponding phases of the binary system coalescence: the

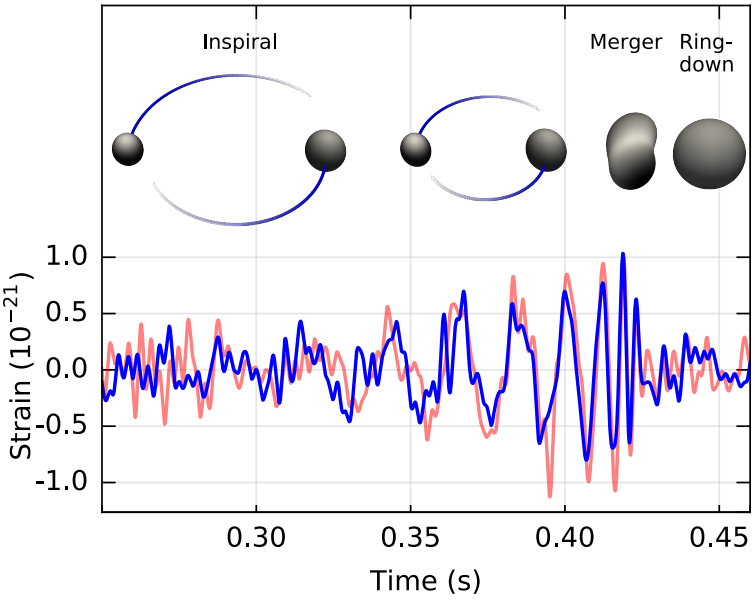

Fig. 1.1: Plot of the gravitational wave signal from the both of the LIGO observatories (The LIGO Livingston signal is in blue while the LIGO Hanford signal, time-shifted (as the signal arrived at Hanford 6.9ms later) and inverted, is in red) overlaid with images from a simulation of the evolution of the black hole structure as the GW signal develops.[1]

separation of the black holes decreases during the inspiral phase until the black holes collide and merge, followed by a ring down phase. The signal increases in frequency and amplitude during the inspiral phase (sometimes called a "chirp" signal), reaching a maximum in frequency and amplitude at the merger.

In the wake of this discovery, astrophysical observations are being made from the detected signal[2]. This detection established the existence of intermediate mass black holes and their occurrence in binary systems[1]. Analysis of the gravitational waves showed that the initial black holes had masses of 36^{+5}_{-4} and 29^{+4}_{-4} solar masses, and the final blackhole was 62^{+4}_{-4} solar masses[1]. Three solar masses of matter had been converted into gravitational wave energy, making this the most energetic event ever to be observed.

Since the first detection, other binary black hole inspirals have been detected [3, 4]. On August 17 2017, binary neutron star inspiral GW170817 was detected by three detectors; the two LIGO detectors and the European Virgo detector, as well

as by many other observatories across the electromagnetic spectrum[5]. GW170817 was significant because it was the first multi-messenger detection. These detections herald a new era in gravitational-wave astronomy; the field has moved from bounding astrophysics by setting upper limits for an astrophysical system to direct observations of gravitational waves emitted from astronomical bodies. GW astronomy allows us to learn about the universe in ways that were previously impossible, just as observing the sky in electromagnetic frequencies beyond visible light revealed new insights into the universe.

For the scientists building the detectors, the goal has shifted from building an instrument that could detect gravitational waves to improving the observatory to uncover as much as possible. This will be achieved by increasing detector sensitivity to achieve the best signal to noise ratio (SNR) possible. Improvements to the LIGO detectors that increase astrophysical reach are being continuously implemented. The work in this thesis is part of the effort being made towards understanding current detectors and planning for improvements for future generations of gravitational wave detectors.

1.2 What are Gravitational Waves?

Gravitational waves are distortions in the fabric of spacetime caused by accelerating masses. The effect was first suggested by Einstein as a consequence of his theory of General Relativity, in which the linearized weak-field equations have wave solutions [6]. Gravitational waves will be emitted by any source whose mass quadrupole moment changes with time[1], for example when two masses orbit each other or when a single rotating mass has a non-axially symmetric mass distribution, as illustrated in Figure 1.2. The amplitude of a gravitational wave drops as $\frac{1}{R}$ as it travels a distance R from its source.

A gravitational wave stretches and compresses local spacetime as it passes through

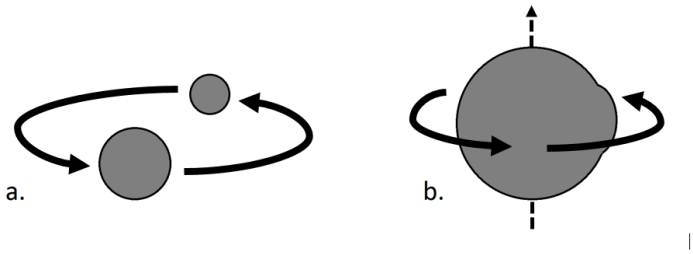

Fig. 1.2: Two examples of rotating bodies that are not axially-symmetric.
a. Two objects in a binary system.
b. An approximately spherical object, with a deformed portion which breaks axial symmetry around if it rotates about the y axis. Note that if it rotates around the x axis, axial symmetry is conserved and no gravitational waves would be emitted.

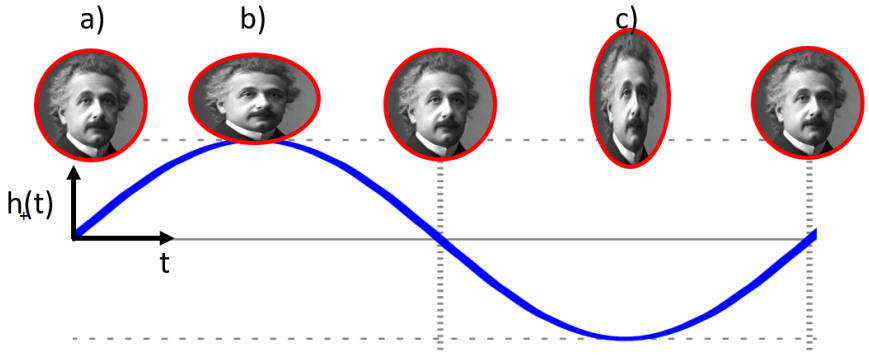

Fig. 1.3: The effect of gravitational waves on a distant object, illustrated here by Einstein's head. The gravitational wave is moving into the page and is polarized in the horizontal and vertical directions. As the local strain ($h(t)$) caused by the gravitational wave varies over time (t), the unperturbed object a. is first stretched along one axis b., and then along the other axis c.

at the speed of light, as illustrated in Figure 1.3 [7]. This stretching and compressing effect is a quadrapole strain, which is characterized by two polarizations, + and x, which are the same strain patterns rotated by 45°. The local strain $h(t)$ can be described mathematically by Equation 1.1, where $\Delta L(t)$ is the length change over distance L, characterized as a combination of + and x polarizations which change over time as functions of $F_{+}(t)$ and $F_{\mathrm{x}}(t)$[8], which are determined by the gravitational wave source and the distance from its observer. The sensitivity of a detector to $F_{+}(t)$ and $F_{\mathrm{x}}(t)$ depends on the orientation of the detector relative to the sources.

$$h(t) \equiv \frac{\Delta L(t)}{L} = F_{+}(t) + F_{\mathrm{x}}(t) \tag{1.1}$$

While the energy in the gravitational wave can be enormous, the strain amplitude is very small. As an example, a binary inspiral merger of two 1 solar mass objects at a distance 10 Mpc, ie about the distance of the Virgo cluster, would produce a strain amplitude on earth of roughly 10^{-21}[9, 10]. This would cause two objects on Earth separated by 1km to change their separation by only 10^{-18}m. A high sensitivity detector is therefore required in order to observe a large volume of space. The rate at which events are detected will allow us to better understand the populations of binary black holes and neutron stars, and other novel astrophysical objects in the universe.

Sources that might be detected by ground-based observatories include binary star inspirals, pulsars with non-axially symmetric mass distributions and Big Bang background GW radiation[11]. Each event will create a unique GW signal in a specific characteristic frequency regime, as illustrated in Figure 1.4. We can predict how many GW events a detector of a particular sensitivity might see using astrophysical models of the source to calculate expected GW signals, and estimating the event frequency by estimating source populations. An understanding of GW sources and their expected GW signals is necessary for setting sensitivity requirements for GW detectors, which informs both detector design and the prioritization of detector upgrades.

Binary Black Hole Inspirals

The first gravitational wave signals detected were produced by the inspiral of binary black holes (BBH)[1, 3]. This came somewhat as a surprise, as this population of binary black holes was not accurately known, and many scientists believed the first detection of GWs would come from binary neutron star (BNS) systems, because the BNS population can be more easily estimated.

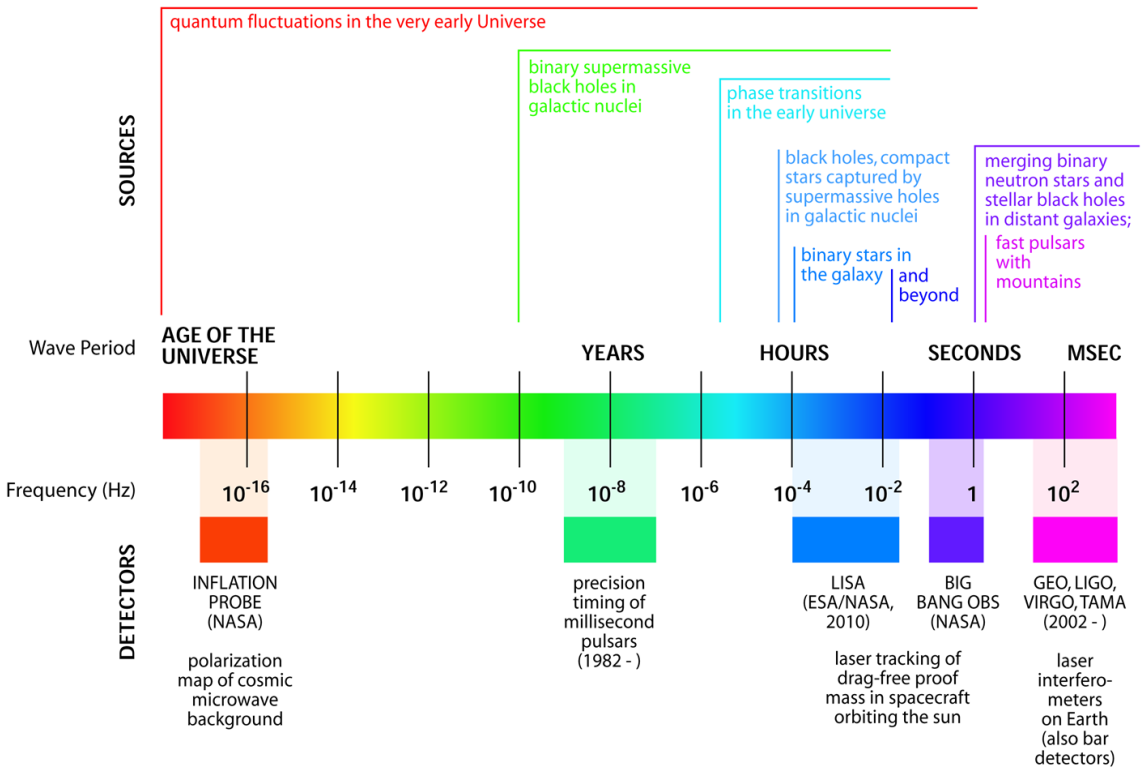

Fig. 1.4: The gravitational wave spectrum, showing the expected frequencies at which various sources will create gravitational waves. The LIGO observatory is sensitive to audio frequency GWs from binary system mergers and potentially to continuous pulsar sources.[12]

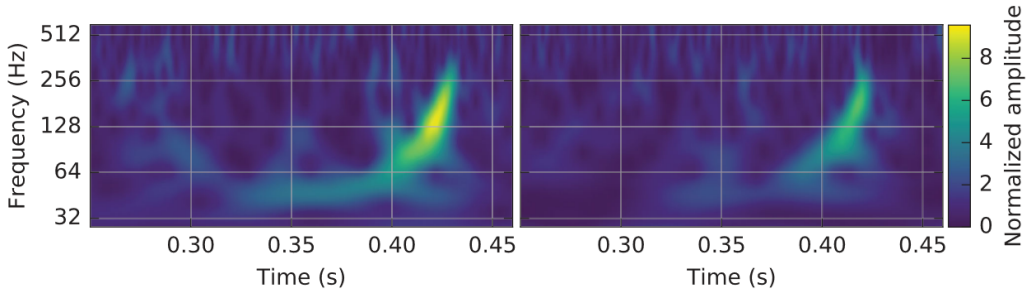

Fig. 1.5: A time-frequency plot of the gravitational strain detected at LHO (left) and LLO (right) during the detection of GW150914[1]. The signal frequency and strength increases over time.

Binary black hole systems have a large quadripole mass distribution and as a result radiate gravitational waves. Their orbit decays as a result of the energy emitted as gravitational waves, eventually causing them to inspiral and merge. This high-mass high-acceleration event produces a strong gravitational wave signature, and hence was the type of event that lead to the first detection of GWs on Earth, as illustrated in Figure 1.1. The masses of the two objects can be determined from the GW signal characteristics, with more massive objects having a lower frequency, shorter duration signal. The "omega scans" of the event at the LIGO Hanford and LIGO Livingston Observatories (LHO and LLO), which show the development on the signal strength versus frequency and time are plotted in Figure 1.5. This event produced a strong signal at frequencies of 100's of Hz [13]. The inspiral, coalescence and merger phases occurred over the order of seconds.

The BBH signals observed by the LIGO detectors have yielded new insights into GW astronomy. By studying the precise shape of the GW signal, properties such as the mass and spin of the black holes can be calculated[2]. The signals can also be used to test general relativity[14].

Binary Neutron Star Inspirals

Gravitational waves from a binary neutron star (BNS) merger were observed on 17 August 2017[5]. This detection was significant for a number of reasons, aside from being the first detection of a BNS merger. The detection occurred while both the LIGO and Virgo detectors were in observing mode, which allowed for good sky localization. The Fermi Gamma-ray Burst Monitor simultaneously measured a short-duration gamma ray burst, and observations in other regions of the electro-magnetic (EM) spectrum were made over the following days[15].

In general, neutron star chirp could be observed in the 10Hz to 7kHz frequency range, however current detectors lack the sensitivity to detect high frequency BNS signals. There is potential to determine the equations of state of neutron stars from the signal of the merger and ring-down of a binary neutron star system[16].

Continuous sources

Continuous wave (CW) GWs are expected to come from sources such as pulsars with a non axially-symmetric mass distribution[17]. Pulsars have rotational periods of milliseconds to hundreds of milliseconds, and thus would produce GWs with frequencies in the tens to thousands of hertz[18]. CW signals are expected to be weaker than burst signals, and detection is anticipated to require long integration times. CW signals may be seen in the next few years as the sensitivity of the detectors is improved and more data is recorded[17].

Other sources

It may one day be possible to detect residual GW background radiation from the Big Bang. In contrast to microwave background radiation, which can tell us information back to 10^5 years after the big bang (at which point the universe became transparent to microwave radiation), GW background radiation could tell us about as little as

10^{-22} seconds after the Big Bang[19].

There is also a project to detect very long timescale gravitational waves by looking at changes in pulsar timing amongst an array of pulsars[20]. Potential sources could be from super-massive blackhole mergers and primordial gravitational waves[21]. In this case, gravitational waves detected would have very low frequencies, in the region of nano-hertz $\big(< 100\text{nHz} \big)$[22].

1.3 Gravitational Wave Detectors

This section describes the types of detectors that have been developed and may one day be used to search for gravitational waves. Different detector configurations will be sensitive to different frequency bands, so the different detector types described in this section would search for GW from different sources.

1.3.1 Indirect Observations of Gravitational Waves

Prior to the 2015 detection of GWs, only indirect observations of gravitational waves were made. Hulse and Taylor discovered the first binary pulsar system in 1975, which provided the first evidence of gravitational wave emission[23]. The orbit of the two neutron stars in the binary system was slowly decaying, and thus their orbital frequency increased as the stars slowly spiraled inwards. The energy loss rate of the stars orbits matched the expected energy emission of gravitational wave radiation (Figure 1.6). The significance of this discovery was recognized when Hulse and Taylor were awarded the 1993 Nobel Prize in Physics for this observation.

1.3.2 Bar Detectors

Bar detectors measure changes in the amplitude of a mechanical resonance of large metal bars. Joseph Weber claimed to have detected gravitational waves using bar detectors in the 1970s[25] (pictured in Figure 1.7), but this result was called into

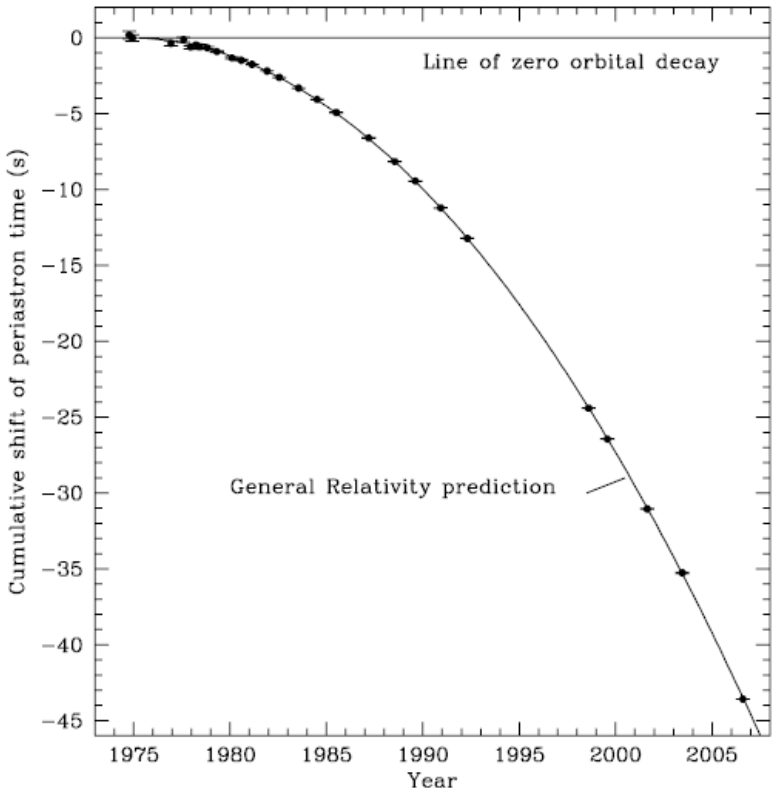

Fig. 1.6: Plot of the orbital decay of the binary pulsar system PSR 1913 + 16 used by Hulse and Taylor to demonstrate evidence for the existence of gravitational waves, including data up until 2012[24]. A system with a constant orbital period would have points that lie on a horizontal line, instead, the system is loosing energy, as indicated by the parabolic shape of the points. The energy lost from the system fits that expected to lost due to gravitational wave radiation.

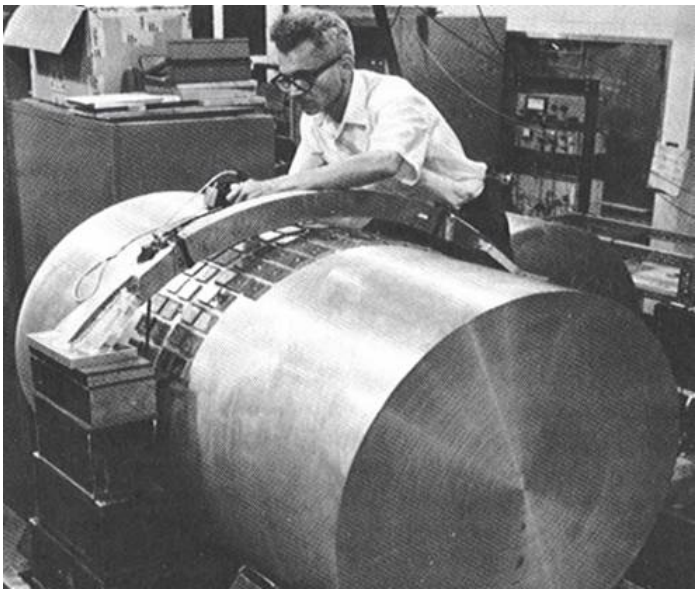

Fig. 1.7: Photograph of Weber with his bar detector (c.1965).[29]

question when it was not reproduced by other scientists [26]. Although the bar detectors achieved ground-breaking low strain sensitivities, they did not reach the sensitivities needed to detect GWs at the rates claimed by Weber. Even so, he was one of the founding figures in the search for gravitational waves, and he left a legacy of a network of cryogenic bar detectors, some of which still operate today.

AURIGA, EXPLORER and NAUTILUS are bar detectors that currently operate at cryogenic temperatures [27]. These detectors achieve strain sensitivities of around 10^{-21} $\mathrm{Hz}^{-1/2}$ in a narrow frequency band[28][26]. In more recent decades the focus of GW detector science has mainly shifted from resonant bar detectors to interferometric GW detectors, which operate over a much wider frequency band than the narrow frequency band of resonant bar detectors.

1.3.3 Space-based detectors

A space-based interferometer called LISA (Laser Interferometer Space Antenna) is predicted to launch in the 2030s[30]. LISA would search for lower frequency GW sources than ground-based detectors, such as those produced by supermassive black

hole binary coalescences[31].

1.3.4 Pulsar Timing Arrays

Pulsar timing arrays can be used to monitor very small glitches in the frequency of pulsar signals, which could be caused by the passage of low frequency (nanohertz) gravitational waves through the line of sight[22]. Candidate sources include super massive blackhole mergers and primordial gravitational waves[21] [20].

1.3.5 Ground-Based Interferometers

Ground-based gravitational wave interferometers are essentially Michelson interferometers. (The detector layout is discussed in Section 1.4.) They are designed to detect gravitational waves in the $10 - 10^4$ Hz frequency range[9]. Ground-based interferometers include LIGO based in the USA [32],Virgo[33] in PISA, Italy, GEO near Hannover, Germany [34], KAGRA in Japan[35].

The LIGO project has two detectors in the USA, the LIGO Hanford and the LIGO Livingston Observatories (LHO and LLO). Multiple upgrades have been made to these detectors since construction started in 1997. The incremental upgrades improved the strain sensitivity from 10^{-21} in initial LIGO (iLIGO) to a current 10^{-23}[8] in Advanced LIGO (aLIGO).The aLIGO detectors made the first direct detection of gravitational waves on September 14 2015 [1].

GW detection requires a network of ground based detectors. Multiple detectors allow for verification of coincident signals between two sites, increasing the combined signal-to-noise ratio. Having more detectors also increases the total duty cycle when the network is in an observing state[37]. Finally, having spatially separated detectors allows for better sky localization[37], achieved by comparing the signal arrival time at each detector. Two detectors can localize a source location to an arc in the sky, three detectors can locate it to a small region in the sky.

1.4 The LIGO Interferometers

While there are some differences between the LIGO detectors and other ground-based interferometers, they have similar designs and operate using the same fundamental principles.

1.4.1 Interferometer layout

A schematic of aLIGO is shown in Figure 1.8. Briefly, it consists of a power and signal-recycled Michelson interferometer that has Fabry-Perot cavities within each arm. This configuration of compound cavities is chosen to maximize the signal created by a differential strain in the arms and to minimize the effect of competing noise sources.

The laser shown in Figure 1.8 is a high power single frequency Nd:YAG laser that is intensity and frequency stabilized and produces a close-to-diffraction-limited output. The output mode shape and beam pointing is stabilized using the triangular Input Mode Cleaner (IMC). The mirrors of the IMC are suspended by multi-stage vibration isolation systems.

The output of the IMC is then incident on the Power Recycling Mirror (PRM) and mode-matched to the arm-cavity eigenmode using the PR2/PR3 off-axis reflective telescope. The Beam-Splitter (BS) divides the beam into two parts, one for each arm, which are incident on the Input Test Masses (ITM) and resonate in the Fabry-Perot arm cavities. The arm cavities begin at the ITMs and end at the End Test Masses (ETMs). The length differences between the BS and the ITMs are adjusted to ensure that the interference between the light fields reflected from each ITM results in the recombined beam traveling back to the PRM. Equivalently, the antisymmetric (AS) port of the BS is a "dark fringe". The non-common-mode-field fields at the BS due to the GW signal and non-common-mode aberrations are out-coupled into the AS port.

The PRM and the Michelson arms form a power-recycling cavity (PRC) that provides a build-up of the power stored in the arm cavities, thereby reducing shot noise.

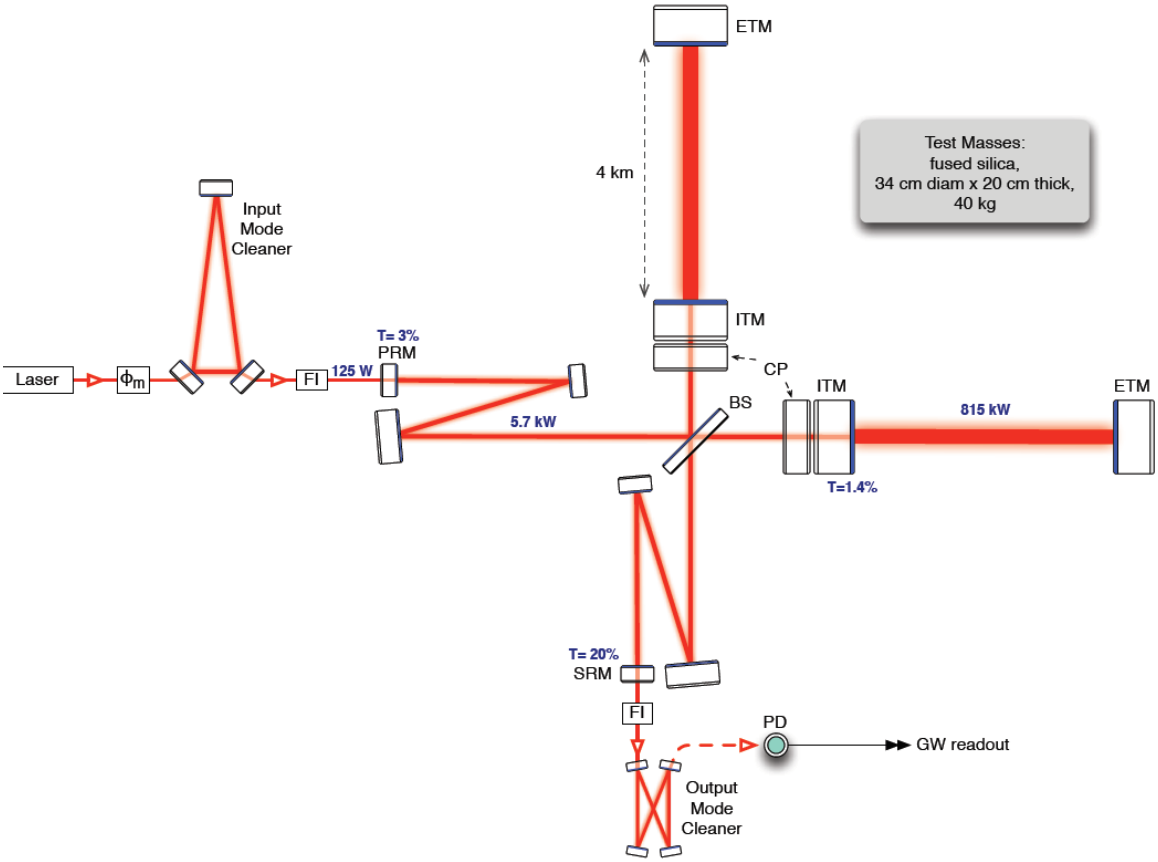

Fig. 1.8: Layout of the aLIGO interferometer.[38] The laser beam passes through the Input Mode Cleaner (IMC), through a Faraday Isolator (FI) and through the Power Recycling Mirror (PRM) into the power recycling cavity. The beam is split at the Beam-Splitter (BS), and enters the two arm cavities through the Input Test Masses (ITMs) which are backed by a Compensation Plate (CP). The End Test Masses (ETM's) mark the end of each arm. The beam exits the interferometer through the signal recycling cavity, through the Signal Recycling Mirror and another Faraday isolator. Finally, the beam passes through the Output Mode Cleaner to be read out on a Photo-Diode (PD).

The GW fields emerging from the BS are resonantly enhanced by the signal recycling cavity (SRC)[39]. This cavity and the Output Mode cCeaner (OMC) also filter out aberrated fields produced by wavefront distortion, thereby improving the detector sensitivity. A mathematical description of the cavities is presented in Chapter 2.

The independent suspension of the mirrors in the interferometer necessitates the use of mirror alignment and cavity length control systems. Pound-Drever-Hall RF-reflection locking [40] is used to control the interferometer degrees of freedom. This is achieved by phase modulating the carrier field at two frequencies: 9MHz and 45MHz, as shown in Figure 1.9. The 9MHz sidebands resonate mostly in the PRC and thus provide an error signal for control of this cavity. A Schnupp asymmetry between the lengths of the Michelson arms results in the 45MHz sidebands resonating in the low-finesse SRC.

A robust length and alignment system is necessary to lock the interferometer and to keep it locked over long timescales, before drifts like changes in environmental temperature can cause the instrument to move off its operating point. Bad alignment results in a loss in power which reduces the shot-noise-limited sensitivity of the interferometer and introduces other noise couplings[41]. The cavity length and alignment are controlled by the suspension actuators, which have low noise properties, but are also weak actuators. The weakness of the suspension actuators adds to the challenge of the locking process. Thermal drifts over long timescales introduce low-frequency motion to the suspensions.

These optics must be isolated from ground vibrations to achieve the required sensitivity. The ITMs and ETMs, for example, are suspended from a four-stage suspension[43], as shown in Figure 1.10. The other optics are suspended from three-stage suspension systems.

All of the optics shown in Figure 1.8, with the exception of the laser, are enclosed within a high-vacuum (10^{-9} torr[32]) to minimize the effect of acoustic noise and

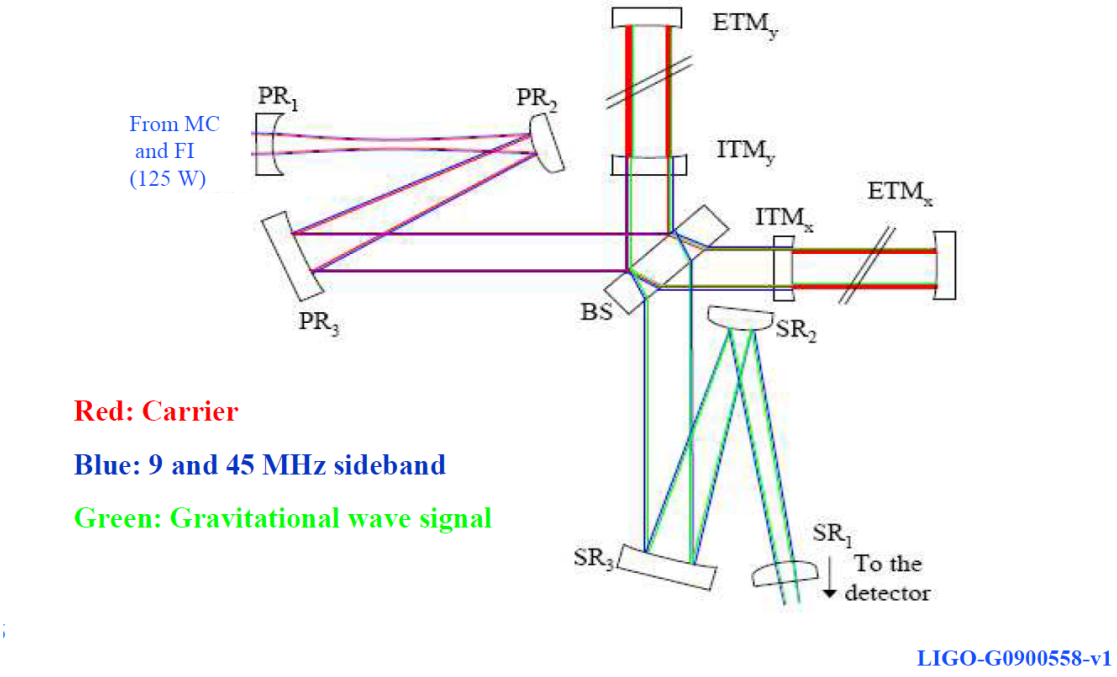

Fig. 1.9: The resonant sidebands within the interferometer[42].

random fluctuations in the optical length of the cavities. The optics themselves must have very low losses (which will be discussed further in Chapter 5.)

Unfortunately, residual optical absorption in the mirror coatings and substrates causes heating of the mirrors, which causes differential distortion of the carrier and the sidebands, and changes to the optical path traveled by the beam. This disrupts mode matching between the cavities, reducing power in the 1064nm TEM_{00} mode.

The Thermal Compensation System (TCS) consists of components used to measure and compensate for the effects of absorption-induced heating in the optics[45]. It includes the Hartmann wavefront sensors[45], which measure the wavefront distortion at each test mass, and ring heaters and CO_2-laser actuators, used to compensate for various distortions.

The ring heater actuators encircle each of the four test masses, and compensate for central heating due to absorption of the circulating 1064nm power. The CO_2-laser actuators image an annular CO_2 beam onto compensation plates located beside

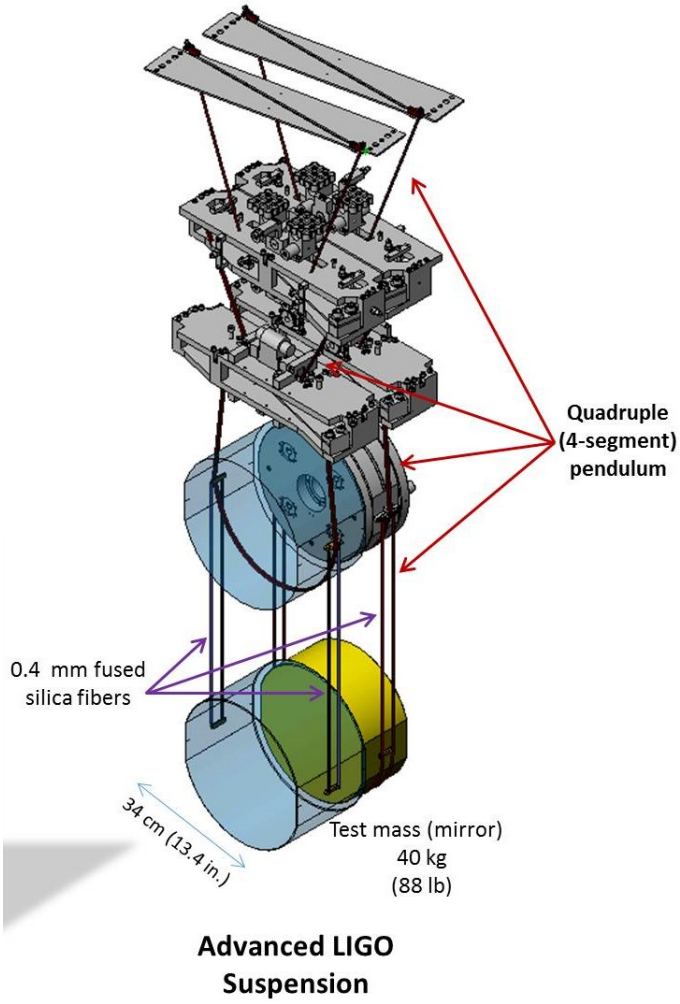

Fig. 1.10: The four-stage suspensions used in aLIGO to suspend the test masses[44]. The test mass sits on the fourth, lowest stage. A second suspension of reaction masses sits behind the test mass. The bottom-most optic on the suspension of reaction masses is called the compensation plate.

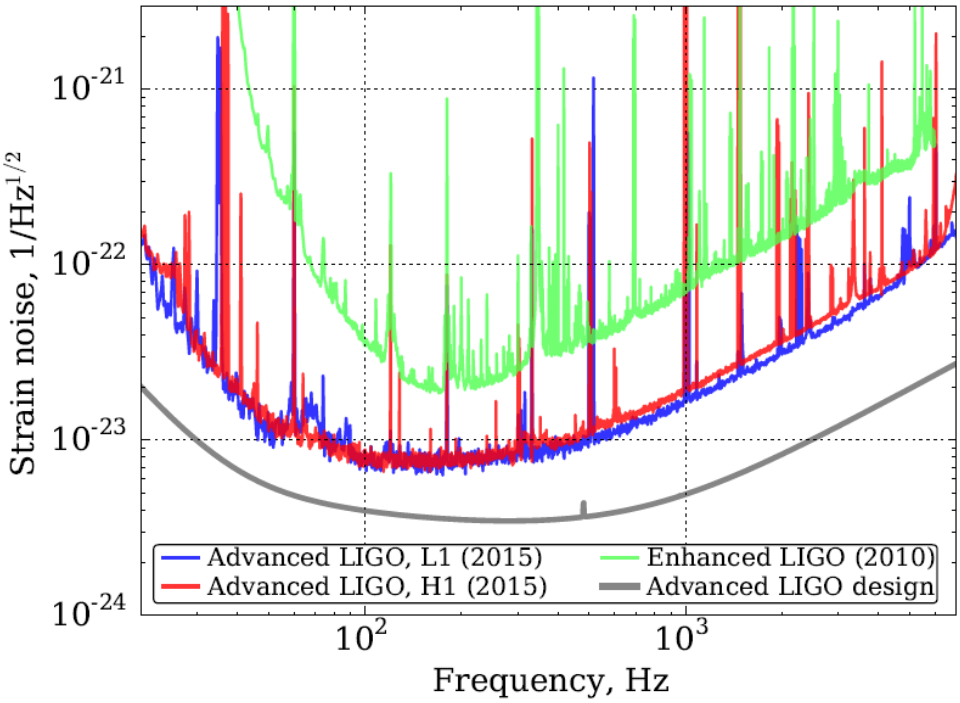

Fig. 1.11: Strain sensitivities for eLIGO, aLIGO in 2016, and anticipated aLIGO detectors [46].

the ITMs, to further improve the mode matching between the arms and the corner cavities.

1.5 Detector Sensitivity and Detection Rate

The rate at which GWs can be detected is determined by the sensitivity of the detector. An example of the detector sensitivity curve for the various generations of LIGO interferometers is shown in Figure 1.11. A higher sensitivity will enable the detection of waves from further away and nearby souces that have a smaller amplitude. The rate at which these events should occur can be estimated using astrophysical models.

There are two ways to increase the number of potential detections made during science runs. Increase the sensitivity of the detector by reducing the noise floor, and

increase the duty cycle so that the detectors are searching in coincidence for a greater amount of time. Adding more detectors to the network would also increase network sensitivity and improve sky localization.

The sensitivity of the detector can be improved by reducing noise sources that couple into the interferometer output signal. There are many factors that influence the detector noise sensitivity, and we will not cover them all here. At low frequencies seismic noise is significant. Noise due to quantum mechanical effects is a significant noise source across the entire aLIGO band. At lower frequencies, the main contributor to this is quantum radiation pressure noise due to fluctuating radiation pressure perturbing the positions of the test masses. Quantum noise in the form of photon shot noise becomes significant above approximately 50Hz. Photon shot noise is related to circulating power: any reduction in power increases the effect of shot noise and reduces the high frequency sensitivity. (Shot noise reduces with factor of $\sqrt{N}$ where N is the number of circulating photons[7].) Factors which reduce interferometer circulating power include losses due to scattering and poor mode matching due to both static or as-built mismatch and absorption-induced mismatch.

1.6 Motivation for Characterizing the aLIGO Cavities and Optics

There are many ongoing projects aimed at improving the detector sensitivity. This section lists some of the improvements that will be made in the near term, with a particular focus on factors that influence power build-up and mode matching. Precise knowledge of the as-built properties of the detector facilitates improvements to the detectors, and examples of this will be given in this section.

1.6.1 Improving the duty cycle

The detector duty cycle can be increased by improving the stability of the control systems and the speed of lock acquisition. An accurate model of the interferometer is

essential to understanding the complicated coupled optical cavities and optimize the length and alignment control loops. Precise cavity length and round trip Gouy phase measurements are necessary to produce accurate models for control system design. For example, mode-hopping in the SRC has been observed at the LIGO Hanford detector, which causes loss of control and reduced duty cycle[47, 48]. It has been suggested that this may be due to an SRC higher-order mode spacing that is different to the design specification, which raises questions about the accuracy of the models. It would be desirable to measure the Gouy phase of the SRC, which is one of the subjects of this thesis.

1.6.2 Operating at Higher Power and Optimizing the TCS

The aLIGO design assumes an input power >100W. While the first detection (GW150914) was made using only 20W of input power, higher powers are required to improve the signal-to-noise and event rate for BBH and BNS coalescences. Increasing the laser power, however, increases the heating of the test masses which increases the wavefront distortion, further degrading the mode matching and the interference at the BS. It would also change the shape of the mode in the SRC, exacerbating the mode-matching in that cavity.

The TCS thus becomes even more important but currently that system runs open-loop and is not optimized, as it must cope with optics that have varying optical absorption. Potential improvements to TCS include designing active control loops that keep the test mass lensing constant when the instrument loses lock, maintaining effective mirror curvatures over thermal relaxation times of a few hours. One of the potential challenges of this is avoiding cross talk with the alignment control loops, which use higher order modes to control cavity alignment. Changing the alignment changes the interferometer power, which may feed back into a TCS control system. The long time constants make this harder to measure, and therefore it is an interesting

candidate for modeling. TCS may also be used for adjustments to the contrast defect of the arms and damping of parametric instabilities[49]. Parametric instabilities are exponential increasess in the magnitude of the mechanical mode vibrations of the optical test masses caused by runaway optical pressure effects.

It would also be useful to know the absorptive properties of the optics in order to design appropriate set-points and control schemes for the TCS. This is particularly true for the absorption of the test masses, which are subjected to the full power stored in the Fabry-Perot arms. Structures which scatter light are also generally absorbers, so measurements of both scatter and absorption are useful for TCS optimization.

1.6.3 Squeezing

The use of squeezed light is a key technique for aLIGO [50], as it can improve the detector sensitivity without increasing the circulating power[51]. Squeezed light is injected into the interferometer behind the SRC cavity, and allows the in-phase quadrature signal at the antisymmetric port to be reduced below the shot-noise quantum limit.

The full benefit of squeezing can only be achieved however, if the optical losses between the squeezed light source and the arm cavities is sufficiently low. The goal is to have no more than 10-15% power losses total in order to achieve 6dB or better of squeezing in A+ LIGO[52]. Static and absorption-induced mode mismatch leads to significant optical loss. Thus, once again, it is essential that these effects are minimized through the used of improved TCS. Additionally, it is apparent that wavefront actuators need to be introduced into the SRC to compensate for as-built mismatch[53]. The design of these systems, however, rely on improved measurements of the SRC Gouy phase and the mode structure.

1.7 In This Thesis

In this thesis I present characterization measurements of the aLIGO detectors. The aim of these measurements is to improve the understanding of the as-built detector in preparation for further detector upgrades. The work in this thesis includes:

1. Characterizing aLIGO cavities by measurements of cavity length, Gouy phase, and mode matching.
2. Measuring scattering and absorption properties of the test masses in situ.
3. Developing techniques for faster modeling of thermal deformations of optics.

Chapter 2 introduces the mathematical framework for describing resonant power within the optical cavities in the aLIGO interferometers. The theory covered in Chapter 2 is used for the cavity characterization measurements in Chapters 3 and 4. Chapter 3 details length and Gouy phase measurements of the "corner station" cavities using locked-cavity techniques, while Chapter 4 discusses a method for measuring the Gouy phase of an unlocked cavity, and a discussion of how this was used in the signal recycling cavity.

In-situ measurement of scatter and absorption of the test masses, and the effects this has on power build-up and thermal lensing are discussed in Chapter 5.

Chapter 6 discusses improvements made to predicting time-dependent interferometer models, by developing a faster technique for modeling the thermal deformation of optics.

2. CAVITY THEORY

This chapter describes the theory of optical cavities. It begins with a description of a simple two-mirror Fabry-Perot cavity, and extends to a treatment of the fields in the compound cavities of the aLIGO interferometers. Finally, we introduce a technique for measuring the cavity length and its focusing properties through the measurement of the resonant frequencies of light within the cavity. This forms the background for the in-situ cavity characterization measurements of the aLIGO interferometer cavities described in Chapters 3 and 4.

2.1 The Fabry-Perot Cavity

Optical cavities are a fundamental component of Gravitational Wave (GW) interferometers, around which the entire instrument is built. Cavities of various types are used in GW detectors: linear cavities, ring cavities, and compound cavities; however much of their behavior can be understood by considering a simple linear cavity. In this section we consider the example of a simple two-mirror Fabry-Perot cavity. (A more in-depth discussion can be found in numerous textbooks, including Siegman's "Lasers"[54].)

A Fabry-Perot cavity is illustrated in Figure 2.1. Two partially transmissive mirrors are perpendicular to the optical axis. The mirrors are separated by length L and each mirror has a reflectivity R, transmissivity T and losses A. Small letters represent the reflection coefficient r, transmission coefficient t and loss coefficient a. R is defined as the fraction of the incident power reflected by the mirror and T is

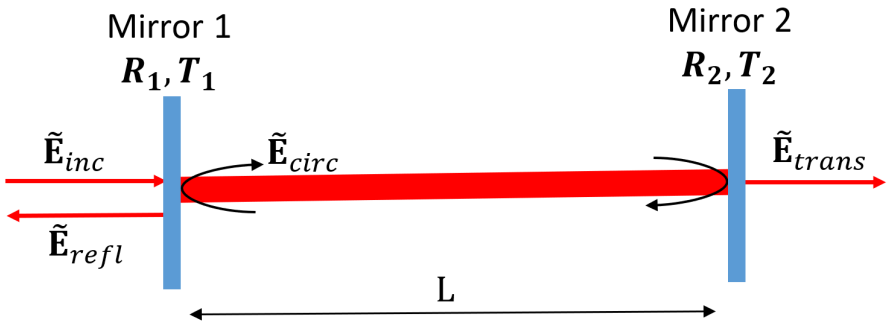

Fig. 2.1: A Fabry-Perot cavity. The circulating cavity field ($\tilde{\mathbf{E}}_{\mathbf{circ}}$), the reflected field ($\tilde{\mathbf{E}}_{\mathbf{refl}}$) and the transmitted fields ($\tilde{\mathbf{E}}_{\mathbf{trans}}$) are illustrated.

defined as the fraction of incident power transmitted through the mirror, $r^2 \equiv R$, $t^2 \equiv T$, and $a^2 \equiv A$ and $R + T + A = 1$.

The incident beam $\tilde{\mathbf{E}}_{\mathbf{inc}}$ is injected into the cavity along the optical axis. Constructive interference of the circulating field and the incident field within the cavity allows the circulating field to build up. Some of the circulating cavity field $\tilde{\mathbf{E}}_{circ}$ exits the cavity as either part of the reflected field $\tilde{\mathbf{E}}_{refl}$ or the transmitted field $\tilde{\mathbf{E}}_{trans}$.

2.1.1 The Cavity Fields

Consider a Fabry-Perot cavity with no losses (i.e. $A = 0$ and $R + T = 1$) in the plane wave approximation. A monochromatic electric field $\tilde{\mathbf{E}}$ is expressed as a function of position along the optical axis and time in Equation 2.1; where t is time, z is the distance along the optical axis, k is the wavenumber as defined in Equation 2.2, ω is the angular frequency of and E_0 is the field amplitude at $t = 0$, $z = 0$.

$$\tilde{\mathbf{E}}_{\mathbf{inc}} = E_0 e^{-i(kz+\omega t)} \tag{2.1}$$

$$k \equiv \frac{2\pi}{\lambda} = \frac{2\pi f}{c} \tag{2.2}$$

We use the convention that when an electric field $\tilde{\mathbf{E}}$ interacts with a mirror, the fields transmitted and reflected from that mirror become $it\tilde{\mathbf{E}}$ and $r\tilde{\mathbf{E}}$ respectively. Thus,

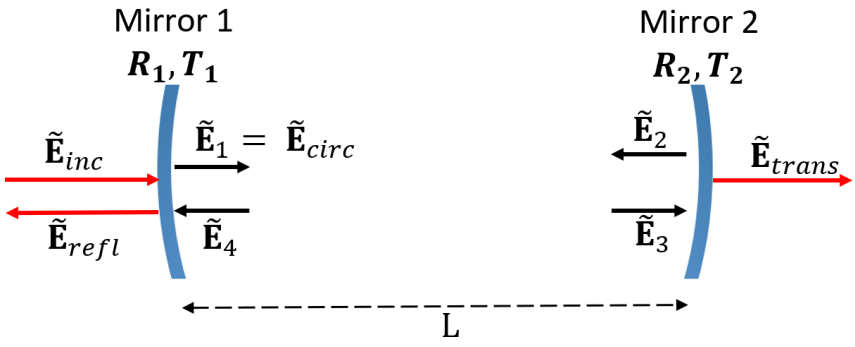

Fig. 2.2: A Fabry-Perot cavity including a break-down the circulating cavity fields.

the cavity fields shown in Figure 2.2 must satisfy:

$$\tilde{\mathbf{E}}_{\mathbf{1}} = it_1\tilde{\mathbf{E}}_{\mathbf{inc}} + r_1\tilde{\mathbf{E}}_{\mathbf{4}} \tag{2.3}$$

$$\tilde{\mathbf{E}}_2 = e^{-ikL}\tilde{\mathbf{E}}_1 \tag{2.4}$$

$$\tilde{\mathbf{E}}_3 = r_2 e^{-ikL}\tilde{\mathbf{E}}_1 \tag{2.5}$$

$$\tilde{\mathbf{E}}_4 = r_2 e^{-2ikL}\tilde{\mathbf{E}}_1 \tag{2.6}$$

$$\tilde{\mathbf{E}}_{refl} = r_1\tilde{\mathbf{E}}_{inc} + it_1 r_2 e^{-2ikL}\tilde{\mathbf{E}}_1 \tag{2.7}$$

$$\tilde{\mathbf{E}}_{trans} = it_2 e^{-ikL}\tilde{\mathbf{E}}_1 \tag{2.8}$$

In the plane-wave approximation, the round-trip phase change ϕ_{rt} can be expressed in terms of cavity length L as in Equation 2.9.

$$\phi_{rt} = 2kL = \frac{4\pi}{\lambda}L \tag{2.9}$$

Solving Equations 2.3 to 2.9 and using $r^2+t^2=1$, the reflected field $\tilde{\mathbf{E}}_{\mathbf{refl}}$, transmitted field $\tilde{\mathbf{E}}_{\mathbf{trans}}$ and circulating field $\tilde{\mathbf{E}}_{\mathbf{circ}}$ can expressed in terms of $\tilde{\mathbf{E}}_{\mathbf{inc}}$ as in Equations 2.10, 2.11 and 2.12. These transfer functions describe the fraction of transmitted and reflected power relative to input power as a function of phase gained during one round trip of the cavity.

$$\frac{\tilde{\mathbf{E}}_{\mathbf{circ}}}{\tilde{\mathbf{E}}_{\mathbf{inc}}} = \frac{it_1}{1 - r_1 r_2 e^{-i\phi_{rt}}} \tag{2.10}$$

$$\frac{\tilde{\mathbf{E}}_{\mathbf{refl}}}{\tilde{\mathbf{E}}_{\mathbf{inc}}} = \frac{r_1 - r_2 e^{-i\phi_{rt}}}{1 - r_1 r_2 e^{-i\phi_{rt}}} \tag{2.11}$$

$$\frac{\tilde{\mathbf{E}}_{\mathbf{trans}}}{\tilde{\mathbf{E}}_{\mathbf{inc}}} = \frac{-t_1 t_2 e^{-\frac{i\phi_{rt}}{2}}}{1 - r_1 r_2 e^{-i\phi_{rt}}} \tag{2.12}$$

The transmission transfer function is plotted in Figure 2.3. The transmitted and circulating powers are maximized when the cavity is operating on a resonant condition; this occurs when $\phi_{rt} = l2\pi$, where l is an integer.

2.1.2 Properties of the Fabry-Perot Cavity

Three important properties that describe the Fabry-Perot Cavity are the Free Spectral Range, the Cavity Bandwidth and the finesse:

- The free spectral range ν_{fsr} is the frequency spacing between the resonance peaks in Figure 2.3, which is given by

$$\nu_{fsr} = \frac{c}{2L} \tag{2.13}$$

- The cavity bandwidth ν_{fwhm} (sometimes called the line-width in some texts) is defined as the full-width at half-maximum of the resonance peak.
- The finesse ($\mathcal{F}$) is defined as the ratio of the peak separation (ν_{fsr}) to the band-

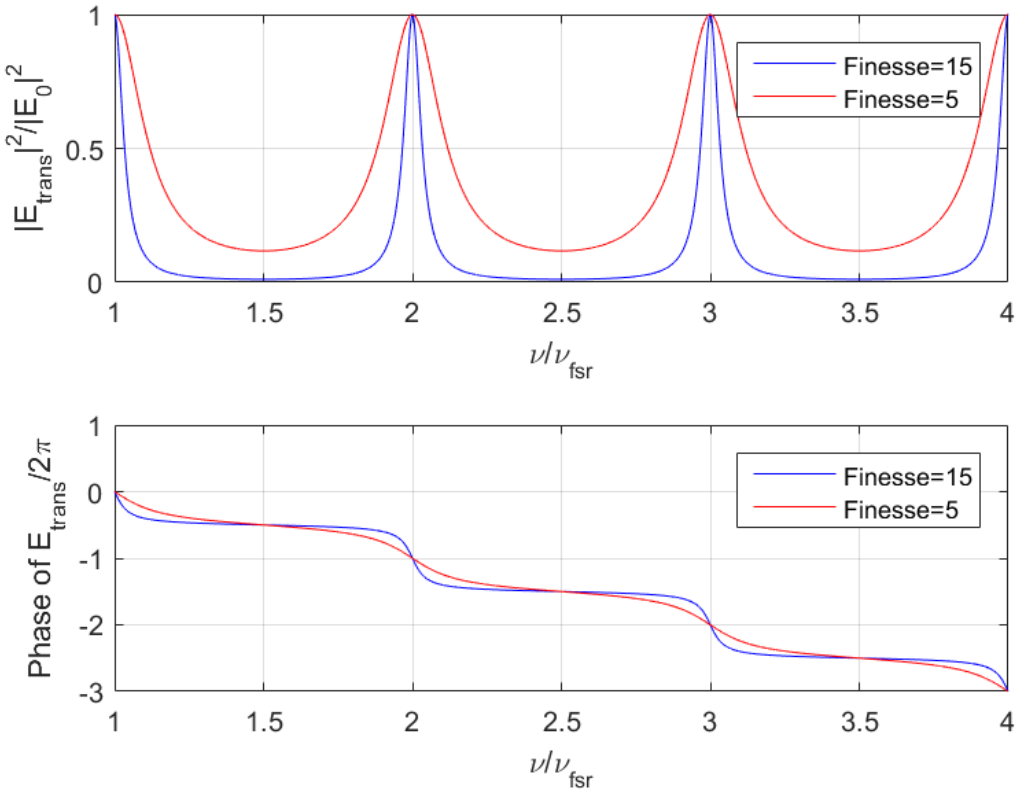

Fig. 2.3: The transmission transfer function of a Fabry-Perot cavity, as a function of the free spectral range. The cavity resonance frequencies occur at integer multiples of the ν_{fsr}.

width (ν_{fwhm}), as shown in Equation 2.14[7]. It can also be determined using the amplitude reflection coefficients of the two cavity mirrors as shown in Equation 2.15. A cavity with high reflectivity mirrors will have a high finesse, narrow resonance peaks, higher circulating power and minimal transmitted power off resonance.

$$\mathcal{F} \equiv \frac{\nu_{fsr}}{\nu_{fwhm}} \tag{2.14}$$

$$\mathcal{F} = \frac{\pi\sqrt{r_i r_o}}{1 - r_i r_o} \tag{2.15}$$

2.1.3 Cavity Losses

So far we have discussed the fields inside a lossless cavity. Sources of loss include light scattered due to imperfections on optics, aperture losses due to finite mirror apertures, and mode mismatch between the incident beam and the cavity mode. Losses reduce power build-up but do not change the resonant frequencies of the cavity[55, 56] .

2.1.4 Cavity Stability

LIGO cavities are designed to be stable[57]. A cavity is stable if it reproduces itself every round trip[58]. The stability of a cavity is determined by its geometry; it will be stable if its g factor is between -1 and 1:

$$-1 \leq g \leq 1 \tag{2.16}$$

where g is related to the end-mirror curvatures by:

$$g^2 = g_1 g_2 \tag{2.17}$$

$$g_1 = (1 - \frac{L}{R_1}) \tag{2.18}$$

$$g_2 = (1 - \frac{L}{R_2}) \tag{2.19}$$

where $R_i > 0$ for concave mirrors.

2.1.5 Fabry-Perot Cavities and Gaussian Beams

So far we have considered a Fabry-Perot cavity in the plane wave approximation, which implies flat wavefronts of infinite extent. Considering the more realistic gaussian beam propagation allows a deeper analysis of the cavity, as it introduces resonances from higher order eigenmodes (see section 2.1.6) and allows analysis of cavity stability for more complicated geometries[59, 58].

Gaussian beams are paraxial solutions of the scalar wave equation[60]:

$$\nabla^2 E(\vec{r}) + k^2 E(\vec{r}) = 0 \tag{2.20}$$

for which:

$$E(x, y, z) = U(x, y, z)e^{-ikz} \tag{2.21}$$

and assuming $\delta^2 U/\delta z^2 = 0$, giving:

$$\nabla^2 U - 2ik\frac{\delta U}{\delta z} = 0 \tag{2.22}$$

The lowest order solution, the TEM_{00} can be described by[61]

$$\tilde{\mathbf{E}}(\mathbf{r}, z) = E_0 \frac{w_0}{w(z)} \exp\left[- \frac{\mathbf{r}^2}{w(z)^2} \right] \exp\left[i \left[kz - \phi_{gouy} + \frac{k\mathbf{r}^2}{2R(z)} \right] \right] \tag{2.23}$$

and

$$I(r,z) = \frac{cn\epsilon_0}{2}|\tilde{\mathbf{E}}(\mathbf{r},z)|^2 = \frac{I_0}{\pi w(z)^2}\exp\left[-\frac{2r^2}{w(z)^2}\right] \tag{2.24}$$

where

- $w(z)$ is the beam diameter at distance z along the optical axis

$$w^2(z) = w_0^2[1 + \frac{z}{z_R}^2] \tag{2.25}$$

- z is the distance from the waist
- w_0 is the waist
- z_R is the Rayleigh range, which is distance z from the waist where the beam diameter $w(z) = \sqrt{2}\omega_0$
- $R(z)$ is the radius of curvature of the wavefront
- ϕ_{gouy} is the accumulated Gouy phase for the TEM_{00} Gaussian mode

$$\phi_{gouy} = \tan^{-1}\left(\frac{z}{z_R}\right) \tag{2.26}$$

- $k = 2\pi/\lambda$ is the wavenumber
- $r^2 = x^2 + y^2$ is the distance from the optical axis in the transverse plane

The complex beam parameter $q(z)$ describes the properties of a Gaussian beam at a distance z along the propagation axis. The relationship between $q(z)$, the radius of curvature of the wavefront $R(z)$ and the beam waist $w(z)$ for a beam with a vacuum wavelength λ_0 in a medium with refractive index n is determined by:

$$\frac{1}{q} = \frac{1}{R} - \frac{i\lambda_0}{\pi n w^2} \tag{2.27}$$

Within a Fabry-Perot cavity, the radius of curvature $R(z)$ of the Gaussian eigenmodes match the curvature of the mirrors. An example of a Gaussian eigenmode in a FP cavity is shown in Figure 2.4.

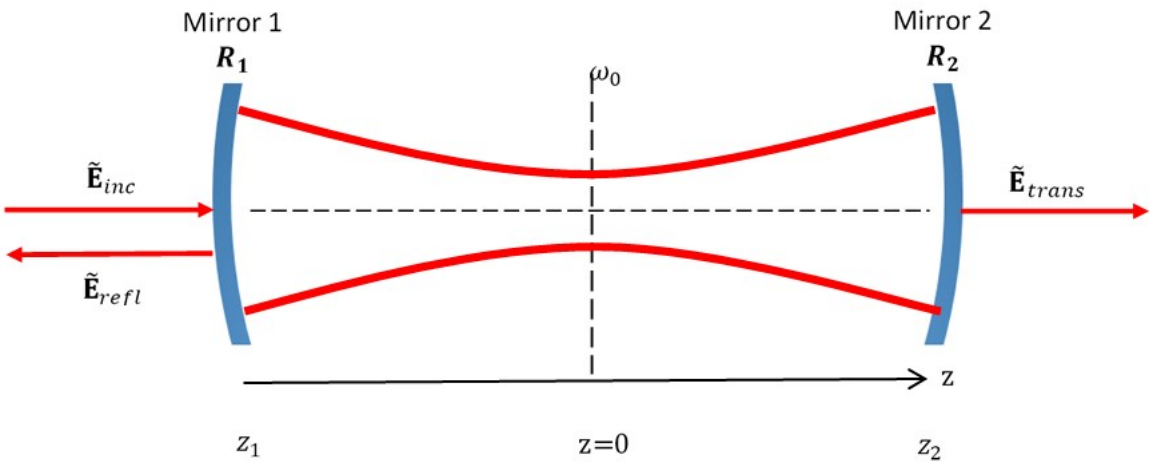

Fig. 2.4: The Gaussian beam shape in a cavity which has curved mirrors with radii of curvature R_1 and R_2. The beam size is largest at the mirrors and deceases to the beam waist ω_0 located at $z = 0$.

The round trip Gouy phase $\phi_{gouy,rt}$ is the Gouy phase accumulated by a beam during one round trip of a cavity[54]:

$$\phi_{gouy,rt} = 2\cos^{-1}\sqrt{g_1 g_2} \tag{2.28}$$

where g_1 and g_2 are the cavity g-factors defined in Section 2.1.4.

2.1.6 Higher-Order modes

Higher order modes (HOMs) can be either Hermite-Gauss (HG) modes, which use a Cartesian coordinate system, or Laguerre-Gauss (LG) modes, which use a cylindrical polar coordinate system. HG modes can be described by[61]:

$$E_{nm}(x,y,z) = E_0 \frac{w_0}{w(z)} H_m\Big(\frac{x}{\sqrt{2}w(z)}\Big) H_n\Big(\frac{y}{\sqrt{2}w(z)}\Big) exp\Big[-\frac{x^2+y^2}{w(z)^2}\Big] \\ exp\Big[-ikz - i\phi_{gouy} - \frac{ik(x^2+y^2)}{2R(z)}\Big] \tag{2.29}$$

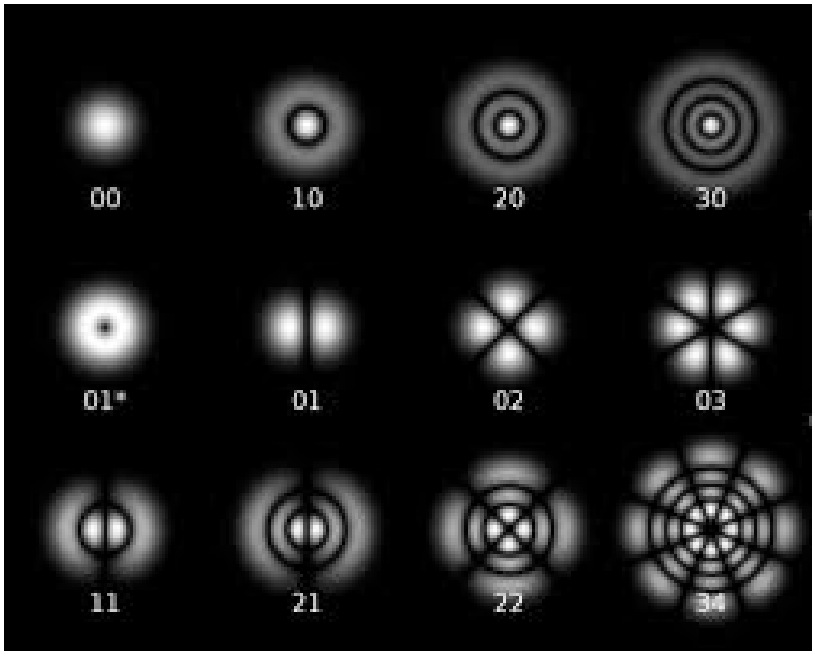

Fig. 2.5: Cross-sectional beam shape of the lowest order Lauguerre-Gauss modes.[62]

where H_l is a Hermite function of order l, and ϕ_{gouy} is the accumulated Gouy phase:

$$\phi_{gouy,accumulated} = (m + n + 1) \tan^{-1}(z/z_R) \tag{2.30}$$

The LG mode shapes are plotted in Figure 2.5 and the HG mode shapes are illustrated in Figure 2.6.

2.1.7 Resonance of Gaussian Beams in FP Cavities and Gouy Phase

While all Gaussian beams with a given w_0 have the same $R_(z)$ and thus can match the mirror curvature, they will have different resonance frequencies. For resonance, the single-pass phase shift $\phi_{single-pass}$ of the *mn-th* mode must satisfy[54]:

$$\phi_{single-pass} = kL - (m + n + 1)\left[\tan^{-1}(z_2/z_R) - \tan^{-1}(z_1/z_R)\right] \tag{2.31}$$

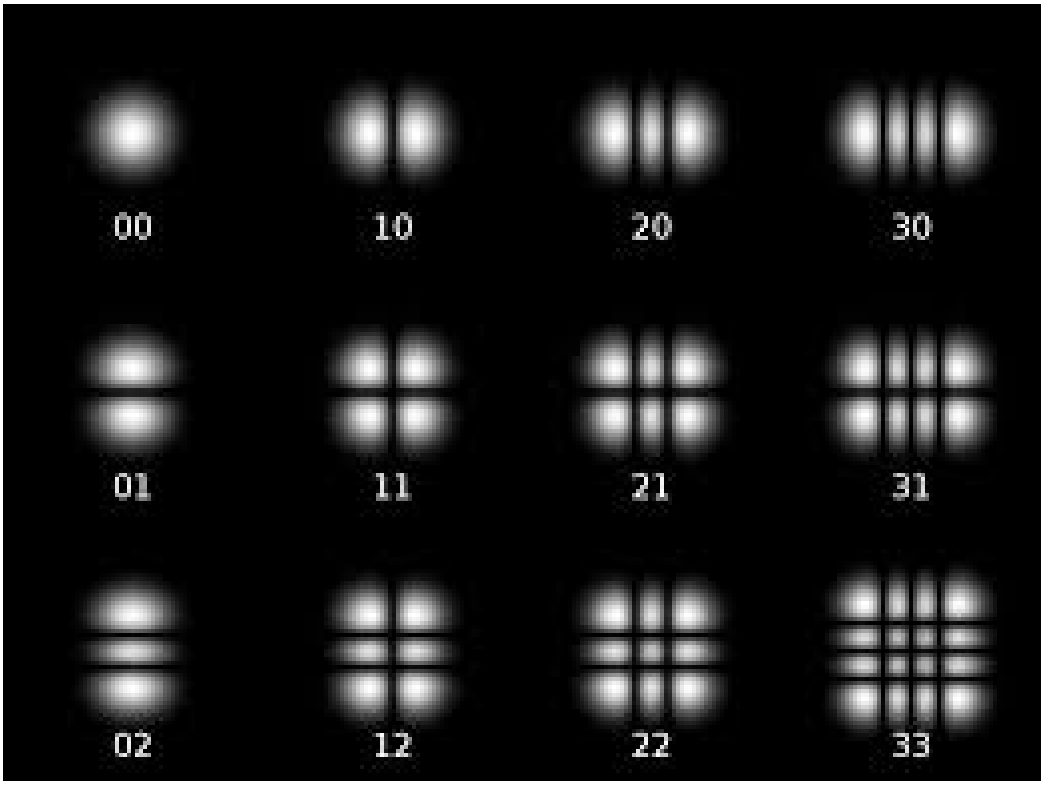

Fig. 2.6: Cross-sectional beam shape of the lowest order Hermite-Gauss modes[61]. Subscripts m,n in HG_{mn} refer to the mode numbers. m+n is the order of the mode.

where z_1 and z_2 are the locations of the mirrors, and $L = z_2 - z_1$ is the physical length of the cavity.

Equation 2.31 can be written in terms of the cavity g factors[54]:

$$\phi_{single-pass} = kL - (m + n + 1)\cos^{-1} \pm \sqrt{g_1 g_2} \tag{2.32}$$

Thus the resonant frequencies are given by:

$$\omega_{qmn} = \left[q + (m + n + 1)\frac{\cos^{-1} \pm \sqrt{g_1 g_2}}{\pi} \frac{2\pi c}{p} \right] \tag{2.33}$$

where $p = 2L$ for a linear cavity.

The cavity transfer function including the 0th, 1st and 2nd order modes is plotted in Figure 2.7. The heights in this plot are arbitrarily chosen, as they depend on the cavity mode matching, which will be discussed in Section 2.1.8. Note that the mode structure is not apparent in a low-finesse cavity.

2.1.8 Mode-matching

As described in Section 2.1.7, the curvature and spacing of the end mirrors defines the "cavity mode" or the Gaussian beam that will be resonant in that cavity. If the incoming beam shape does not match the cavity mode, some power will be lost out of the (useful) $TEM_{0,0}$ mode and may be coupled into higher order modes. The overlap integral of incident mode with the cavity mode determines the amount of light injected into different modes:

$$\eta = \frac{|\int \tilde{\mathbf{E}}_\mathbf{1} \tilde{\mathbf{E}}_\mathbf{2} dA|^2}{\int |\tilde{\mathbf{E}}_\mathbf{1}|^2 dA \int |\tilde{\mathbf{E}}_\mathbf{2}|^2 dA} \tag{2.34}$$

As a general rule of thumb, the TEM_{00} is scattered into Laguerre-Gauss HOMs if the curvature of the wavefront does not match the curvature of the mirrors. Light can be

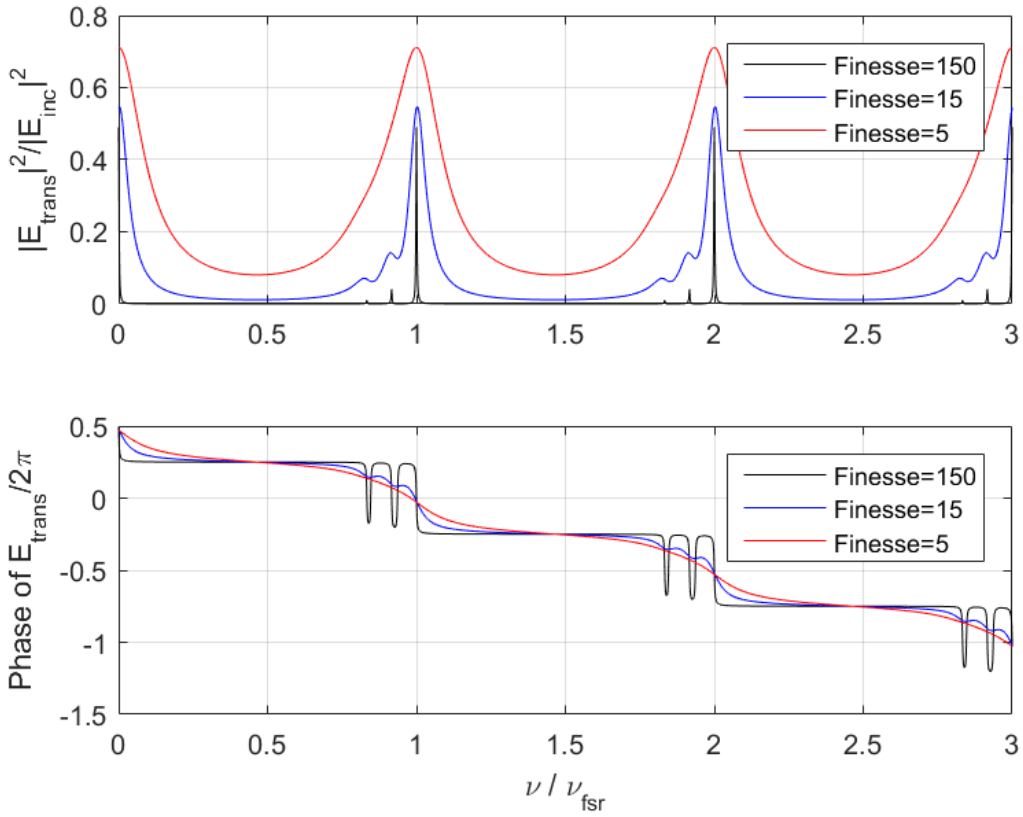

Fig. 2.7: Transmission transfer functions of three cavities with finesses of 150, 15, and 5. The transmission peaks for the 0^{th}, 1^{st} and 2^{nd} order modes are shown for cavity with a 30° Gouy phase. Note that the lower the cavity's finesse, the greater the overlap between the transmission peaks.

scattered into Hermite-Gauss HOMs if the mirrors are misaligned in angle or if there is a non-radially symmetric distortion of the mirrors.

Loss of carrier power due to poor mode-matching is detrimental to interferometer performance as it causes a drop in circulating power, increasing the impact of shot noise. Mode mismatches also decrease the efficiency with which GW signals are coupled from the arms to the output. If the mode mismatch is big enough, $TEM_{0,1}$ mode will register on alignment sensors even though the mode is not resonant in the cavity[63], which is another reason HOMs are undesirable.

A high finesse cavity which is locked to the $TEM_{0,0}$ mode frequency will suppress HOM resonances as they resonate at a different frequency as determined by their Gouy phase shift. There are some cases where higher order modes may be excited within the cavity, however:

1. HOMs with a round trip Gouy phase shift of 2π will also be resonant in the cavity. The LIGO cavities are designed so that this does not occur for low mode numbers, and the HOM components are generally very small, so this should not be a consideration in practice.
2. If the linewidth of the resonance peaks is wide enough that neighboring modes overlap, then a HOM can also resonate within the cavity. It is suspected that this may be occurring in the signal recycling cavity (SRC) of the LIGO Hanford Observatory, which is explored further in Chapter 4.

Higher-order modes (HOMs) have larger lateral extents, and so the size of the mirrors limits the maximum order of the mode that can resonate in a cavity.

2.2 Paraxial Ray Tracing in Misaligned Optical Systems

The ABCD ray transfer matrix method is often used to describe the propagation of light through an optical system. This is described in many well-known textbooks, such as Siegman's classic text "Lasers"[54]. In this section, we review paraxial ray-

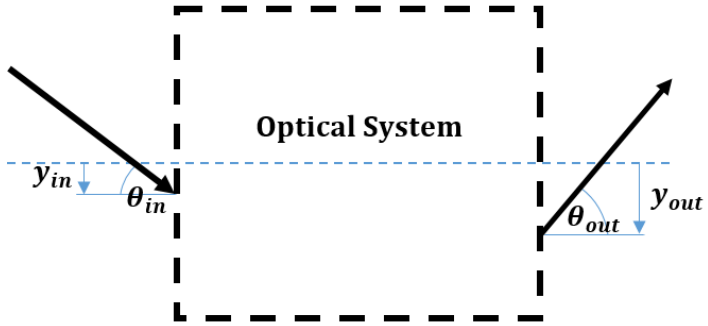

Fig. 2.8: An optical system described by ray transfer matrix $\mathbf{M}$ and the input and output beams $\tilde{y}_{in}$ and $\tilde{y}_{out}$. The transformation from the input beam to the output beam is the ray transfer matrix of this optical system.

tracing in misaligned systems, which will provide background material for Chapter 4.

2.2.1 Ray Transfer Matrix Method for Well-Aligned Systems

In a well-aligned optical system, the propagation of light can be modeled using ray transfer matrices[54], assuming that the beam deviation from the optical axis is small enough that the paraxial approximation $\sin\theta \approx \theta$ is valid. Figure 2.8 illustrates an optical system which has input beam $\tilde{y}_{in}$ and output beam $\tilde{y}_{out}$. The ray transfer matrix $\mathbf{M}$, which has elements A, B, C and D, relates $\tilde{y}_{in}$ to $\tilde{y}_{out}$ by:

$$\tilde{y}_{out} = \begin{bmatrix} y_{out} \\ \theta_{out} \end{bmatrix} = \begin{bmatrix} A & B \\ C & D \end{bmatrix} \begin{bmatrix} y_{in} \\ \theta_{in} \end{bmatrix} = \mathbf{M}\ \tilde{y}_{in} \tag{2.35}$$

The ray transfer matrix of a systems which comprises multiple optical elements is determined by multiplying the ray transfer matrices of the individual elements: $\mathbf{M} = \mathbf{M_i}...\mathbf{M_2}\mathbf{M_1}$, where $\mathbf{M_i}$ is the ray transfer matrix for the ith element, and element 1 is the first element in the optical system. For example the ray transfer matrix $\boldsymbol{M}$ of a beam that propagates a distance L and is then a reflected by a flat mirror is:

$$\boldsymbol{M} = \begin{bmatrix} 1 & 0 \\ 0 & 1 \end{bmatrix} \begin{bmatrix} 1 & L \\ 0 & 1 \end{bmatrix} \tag{2.36}$$

The Gouy phase accumulated by a beam which travels through an optical system can be calculated from the ray transfer matrix of that system:[64]

$$\phi_{gouy,accumulated} = sgn(B).\cos^{-1}\left(\frac{A+D}{2}\right) \tag{2.37}$$

2.2.2 Misalignment matrices

An optical system may contain misaligned elements. The beam path is then calculated using misalignment or ABCDEF) matrices[54]:

$$\begin{bmatrix} y_{out} \\ \theta_{out} \\ 1 \end{bmatrix} = \begin{bmatrix} A & B & E \\ C & D & F \\ 0 & 0 & 1 \end{bmatrix} \begin{bmatrix} y_{in} \\ \theta_{in} \\ 1 \end{bmatrix} \tag{2.38}$$

where the values A, B, C and D describe the aligned element and E and F describe the displacement and angular misalignment of the element axis with respect to the optical axis.

It is convenient to represent the misalignment matrix as a partitioned matrix:

$$\begin{bmatrix} \tilde{\mathbf{y}}_{\mathbf{out}} \\ \hline 1 \end{bmatrix} = \left[\begin{array}{c|c} \boldsymbol{M} & \boldsymbol{E} \\ \hline 0 & 1 \end{array}\right] \begin{bmatrix} \tilde{\mathbf{y}}_{\mathbf{in}} \\ \hline 1 \end{bmatrix} \tag{2.39}$$

where

$$\boldsymbol{M} = \begin{bmatrix} A & B \\ C & D \end{bmatrix}, \ \boldsymbol{E} = \begin{bmatrix} E \\ F \end{bmatrix} \tag{2.40}$$

as it simplifies calculation of the total misalignment matrix.

To visualize this, consider a system with three optical elements. The overall input and output beam positions are defined by:

$$\begin{bmatrix} \tilde{\mathbf{y}}_{\mathbf{out}} \\ \hline 1 \end{bmatrix} = \left[\begin{array}{c|c} \boldsymbol{M_{tot}} & \boldsymbol{E_{tot}} \\ \hline 0 & 1 \end{array}\right] \begin{bmatrix} \tilde{\mathbf{y}}_{\mathbf{in}} \\ \hline 1 \end{bmatrix} \tag{2.41}$$

where

$$\left[\begin{array}{c|c} \boldsymbol{M_{tot}} & \boldsymbol{E_{tot}} \\ \hline 0 & 1 \end{array}\right] = \left[\begin{array}{c|c} \boldsymbol{M_3} & \boldsymbol{E_3} \\ \hline 0 & 1 \end{array}\right] \left[\begin{array}{c|c} \boldsymbol{M_2} & \boldsymbol{E_2} \\ \hline 0 & 1 \end{array}\right] \left[\begin{array}{c|c} \boldsymbol{M_1} & \boldsymbol{E_1} \\ \hline 0 & 1 \end{array}\right] \tag{2.42}$$

$$= \left[\begin{array}{c|c} \boldsymbol{M_3 M_2 M_1} & \boldsymbol{M_3 M_2 E_1 + M_3 E_2 + E_3} \\ \hline 0 & 1 \end{array}\right] \tag{2.43}$$

Thus, the trajectory of the output beam relative to the optical axis is given by:

$$\tilde{\mathbf{y}}_{\mathbf{out}} = \boldsymbol{M_3 M_2 M_1} \tilde{\mathbf{y}}_{\mathbf{in}} + \boldsymbol{M_3 M_2 E_1} + \boldsymbol{M_3 E_2} + \boldsymbol{E_3} \tag{2.44}$$

and thus the **change** in location and angle of the beam due to the misalignment is given by:

$$\delta\tilde{\mathbf{y}}_{\mathbf{out}} = \boldsymbol{M_3 M_2 E_1} + \boldsymbol{M_3 E_2} + \boldsymbol{E_3} \tag{2.45}$$

For example, if the system is an optic that is misaligned in angle $\theta_{misalign}$, then[54]:

$$\boldsymbol{E} = \begin{bmatrix} 0 \\ 2\theta_{misalign} \end{bmatrix} \tag{2.46}$$

$$\begin{bmatrix} y_{out} \\ \theta_{out} \\ 1 \end{bmatrix} = \begin{bmatrix} A & B & 0 \\ C & D & 2\theta_{misalign} \\ 0 & 0 & 1 \end{bmatrix} \begin{bmatrix} y_{in} \\ \theta_{in} \\ 1 \end{bmatrix} \tag{2.47}$$

and thus the change in the output of the beam due to the misalignment $\delta\tilde{\mathbf{y}}_{out}$ is:

$$\delta\tilde{\mathbf{y}}_{out} = \begin{bmatrix} A & B \\ C & D \end{bmatrix} \begin{bmatrix} 0 \\ 2\theta_{misalign} \end{bmatrix} \tag{2.48}$$

$$\delta\tilde{\mathbf{y}}_{out} = \begin{bmatrix} 2B\theta_{misalign} \\ 2D\theta_{misalign} \end{bmatrix} \tag{2.49}$$

For a three element optical system in which element $\boldsymbol{M_2}$ is a misaligned mirror, and all other elements remain aligned such that $\boldsymbol{E_1} = \boldsymbol{E_2} = 0$, then:

$$\tilde{\mathbf{y}}_{\mathbf{out}} = \boldsymbol{M_3 M_2 M_1} \tilde{\mathbf{y}}_{\mathbf{in}} + \boldsymbol{M_3 E_2} \tag{2.50}$$

and

$$\delta\tilde{\mathbf{y}}_{\mathbf{out}} = \boldsymbol{M_3 E_2} \tag{2.51}$$

The change in the output beam position and angle therefore depends only on the misalignment angle of the mirror and the ray transfer matrix after the mirror. Thus, if a controlled misalignment E_2 could be produced then the change in the output could be used to determine M_3. This approach will be employed in Chapter 4 to determine the round-trip Gouy phase of the SRC.

2.3 Compound Cavities in the aLIGO Interferometer

The aLIGO interferometer is a compound cavity comprised of the corner station cavities and the arm cavities, as shown in 2.9. In this section, we will consider the behavior of the corner station consisting of the Michelson interferometer (MICH), the Power Recycled Michelson Interferometer (PRMI), the Signal Recycled Michelson Interferometer (SRMI), and the Dual Recycled Michelson Interferometer (DRMI).

The Michelson interferometer (MICH) is made up of the two Input Test Masses

(ITMx and ITMy) and the Beam-Splitter (BS). The reflective surface of the BS is the input to MICH. There are two other optics within the MICH: the Compensation Plates (CPx and CPy), which are located between the BS and the ITM. These CPs are used to compensate for differential absorption-induced wavefront distortion in the MICH.

The Power Recycling Cavity starts at the Power Recycling Mirror (PRM) and ends at the Michelson output. The "PRC length" is generally defined as the distance between the PRM and the BS (so not including the ITMs). Similarly, the "PRC" Gouy phase is defined as the accumulated Gouy phase of a beam that travels from PRM to BS, as there is negligible Gouy phase shift in the MICH. To lock the PRC, the MICH may be locked and then the position of the PRM is controlled to bring the PRC into resonance. This configuration is called the Power-Recycled Michelson Interferometer (PRMI).

The Signal Recycling Cavity starts at the Michelson input and ends at the Signal Recycling Mirror (SRM). As for the PRC, the "SRC length" is generally defined as the distance between the BS and the SRM and the "SRC" Gouy phase is considered the accumulated Gouy phase of a beam that travels from BS to SRM. To lock the SRC, the Michelson may be locked and then the position of the SRM optics optic is controlled to bring the SRC into resonance. This configuration is called the Signal-Recycled Michelson Interferometer (SRMI).

Thus, the paths through the cavities illustrated in Figure 2.9 are defined as follows:

- The Michelson (MICH) path starts at the BS HR surface, and travels towards the two ITMs. It passes through the compensation plates, through the AR-coated back face of the ITMs, to be reflected by the HR-coated front face of the ITM back to the BS 50:50 coating.
- The PRMI path starts at the HR surface of PRM, travels through the Power Recyling Cavity (PRC) to the BS where it is split into two. The two beams

travel through the MICH path to end up back at the BS 50:50 coating which marks the end of this cavity.

- The SRMI path starts at the BS, travels through the MICH path, and then through the BS substrate again, through the Signal Recycling Cavity (SRC) to the Signal Recycling Mirror (SRM) HR surface.
- The Dual Recyled Michelson Interferometer (DRMI) starts at the PRM, travels through the PRMI path, and then through the SRC to the SRM.

In the following sections we will derive expressions that describe the cavity fields within some of the compound cavities in the LIGO interferometers. The transfer function of a compound cavity can be determined by tracing the fields through each cavity in the same way as for the simple Fabry-Perot cavity introduced in Section 2.1.1, although this method becomes increasingly mathematically laborious with each additional cavity. An alternative approach is to treat a compound cavity as a single cavity with mirrors that have a frequency-dependent amplitude transmission coefficient that is the transfer function of the neighboring cavity. We use this approach in this Chapter. The field expressions derived in this section will be used for the cavity characterization measurements in Chapter 3.

2.3.1 The Michelson Interferometer and the Schnupp Asymmetry

In the LIGO interferometer, the corner-station Michelson interferometer (often referred to as MICH) lies between the Beam-Splitter (BS) and the two Input Test Masses (ITMs), as illustrated in the schematic in Figure 2.10. We will assume a lossless 50:50 beam-splitter and that the reflectivity of each ITM is the same. We use the convention for a beam-splitter with 50:50 coating on the input side, such that a beam transmitted through the BS gains a real complex transmission coefficient of $t = \frac{1}{\sqrt{2}}$, and a reflected beam gains a complex reflection coefficient $r = \pm\frac{1}{\sqrt{2}}$ which is real and negative when reflected from the air side of the coating and real and positive

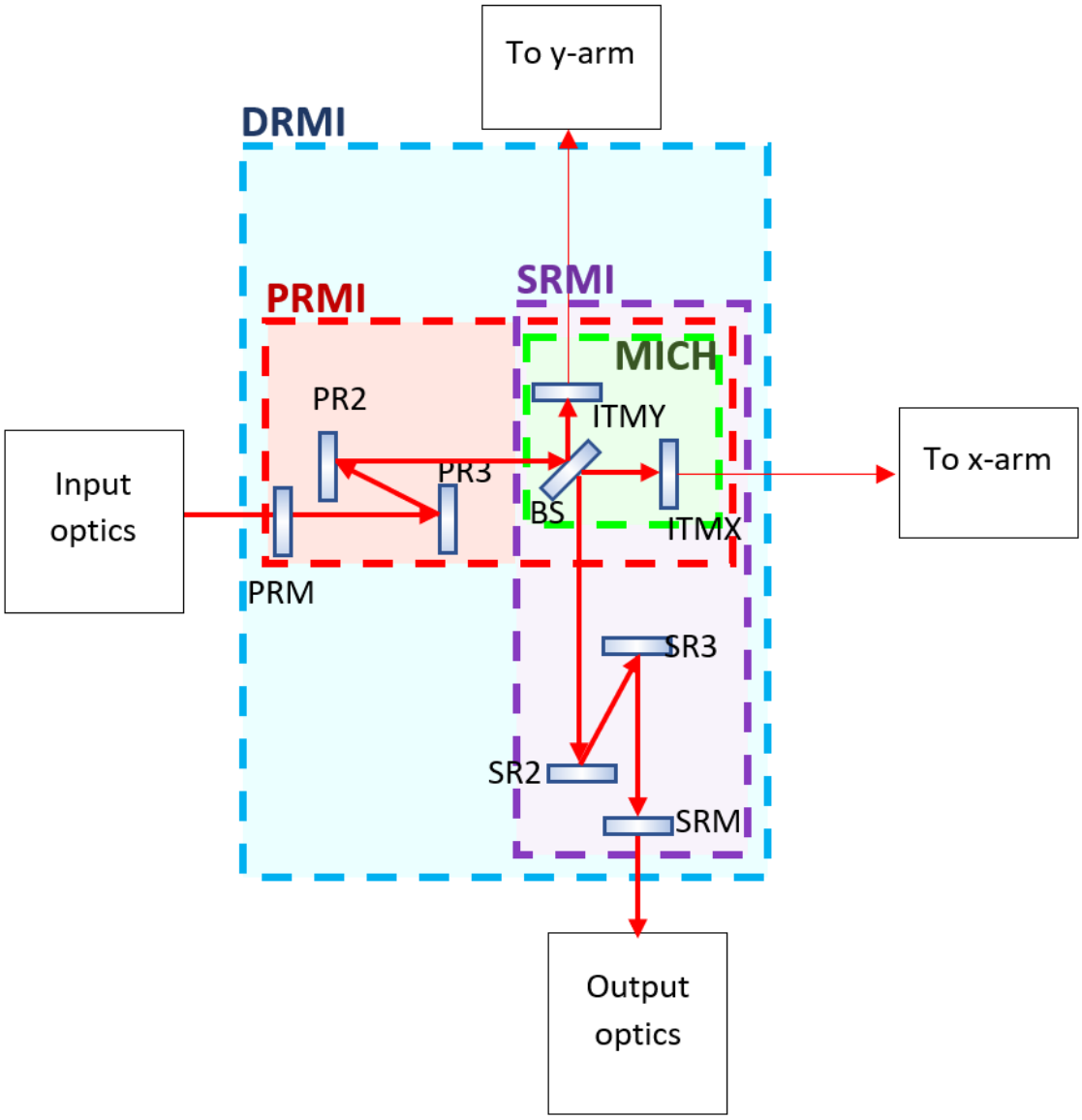

Fig. 2.9: The interferometer corner station which includes the Michelson interferometer MICH and cavities DRMI, PRMI, MICH, and SRMI. The Power Recycling Mirror (PRM), Beam Splitter (BS), Signal Recycling Mirror (SRM) and the two Input Test Mass (ITMx and ITMy) optics are marked.

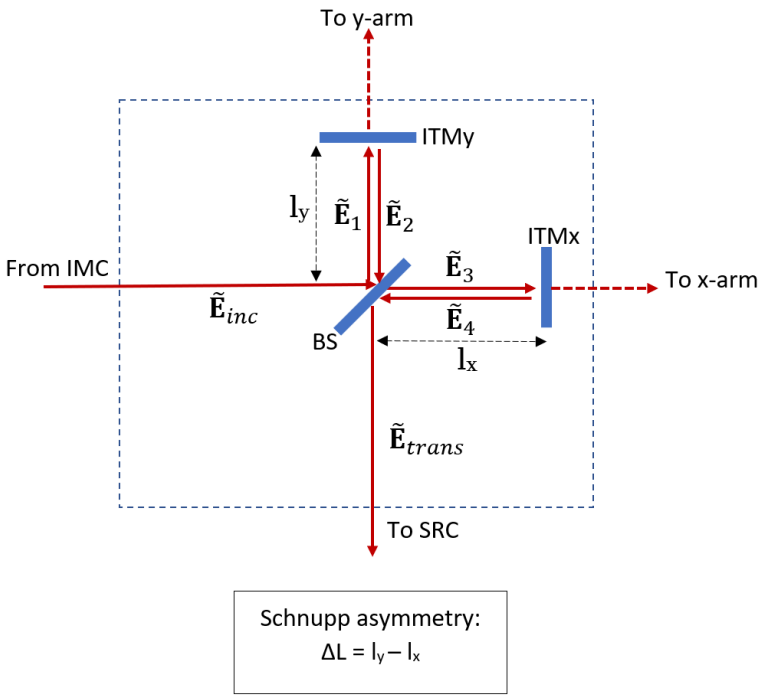

Fig. 2.10: The optical layout and cavity fields in the Michelson. When the Michelson is locked, the length difference between the two arms is equal to the Schnupp asymmetry.

when reflected from the substrate side of the coating. The choice of this convention is somewhat arbitrary but it is commonly used for the LIGO BS, and it is conceptually convenient because the light exiting the MICH will be anti-resonant when the two arms of the Michelson have equal length. The transfer function can be derived from the expressions for the cavity fields in Equations 2.52 to 2.56:

$$\tilde{\mathbf{E}}_{\mathbf{1}} = -r_{BS}\tilde{\mathbf{E}}_{\mathbf{inc}} \tag{2.52}$$

$$\tilde{\mathbf{E}}_{\mathbf{2}} = -r_{BS}r_{ITM}e^{-2ikl_y}\tilde{\mathbf{E}}_{\mathbf{inc}} \tag{2.53}$$

$$\tilde{\mathbf{E}}_{\mathbf{3}} = t_{BS}\tilde{\mathbf{E}}_{\mathbf{inc}} \tag{2.54}$$

$$\tilde{\mathbf{E}}_{\mathbf{4}} = t_{BS}r_{ITM}e^{-2ikl_x}\tilde{\mathbf{E}}_{\mathbf{inc}} \tag{2.55}$$

$$\tilde{\mathbf{E}}_{\mathbf{refl}} = -r_{BS}\tilde{\mathbf{E}}_{\mathbf{2}} + t_{BS}\tilde{\mathbf{E}}_{\mathbf{4}} \tag{2.56}$$

$$\tilde{\mathbf{E}}_{\mathbf{trans}} = t_{BS}\tilde{\mathbf{E}}_{\mathbf{2}} + r_{BS}\tilde{\mathbf{E}}_{\mathbf{4}} \tag{2.57}$$

Solving the above cavity equations simultaneously gives the transmitted and reflected field transfer functions:

$$\tilde{\mathbf{E}}_{\mathbf{refl}} = \frac{1}{2} r_{ITM}\tilde{\mathbf{E}}_{\mathbf{inc}}\Big(\exp(-2ikl_x) + \exp(-2ikl_y)\Big) \tag{2.58}$$

$$\tilde{\mathbf{E}}_{\mathbf{trans}} = -\frac{1}{2i} r_{ITM}\tilde{\mathbf{E}}_{\mathbf{inc}}\Big(\exp(-2ikl_x) - \exp(-2ikl_y)\Big) \tag{2.59}$$

We define the common arm length $L_{MICH} = \frac{l_x + l_y}{2}$, and the length difference between the two arms $\Delta L = \frac{l_x - l_y}{2}$. Thus, the amplitude reflection and transmission coefficients of the Michelson interferometer, r_{MICH} and t_{MICH}, are:

$$r_{MICH} = \frac{\tilde{\mathbf{E}}_{\mathbf{refl}}}{\tilde{\mathbf{E}}_{\mathbf{inc}}} = r_{ITM}\exp\Big(-i2kL_{MICH}\Big)\cos(k\Delta L) \tag{2.60}$$

$$t_{MICH} = \frac{\tilde{\mathbf{E}}_{\mathbf{trans}}}{\tilde{\mathbf{E}}_{\mathbf{inc}}} = -r_{ITM}\exp\Big(-i2kL_{MICH}\Big)\sin(k\Delta L) \tag{2.61}$$

The reflected and transmitted field amplitudes can also be used to write the transfer function for power and the phase change in reflection and transmission:

$$\frac{|\tilde{\mathbf{E}}_{\mathbf{refl}}|^2}{|\tilde{\mathbf{E}}_{\mathbf{inc}}|^2}\alpha\cos\Big(k\Delta L\Big)^2 \tag{2.62}$$

$$angle(\tilde{\mathbf{E}}_{\mathbf{refl}}) = -2kL_{MICH} \tag{2.63}$$

$$\frac{|\tilde{\mathbf{E}}_{\mathbf{trans}}|^2}{|\tilde{\mathbf{E}}_{\mathbf{inc}}|^2}\alpha\sin\Big(k\Delta L\Big)^2 \tag{2.64}$$

$$textangle(\tilde{\mathbf{E}}_{\mathbf{refl}}) = -2kL_{MICH} + 1 \tag{2.65}$$

The transfer function and phase gain is plotted for transmission in Figure 2.11. The power changes with a period of 1.6GHz, as determined by the ΔL term in Equation

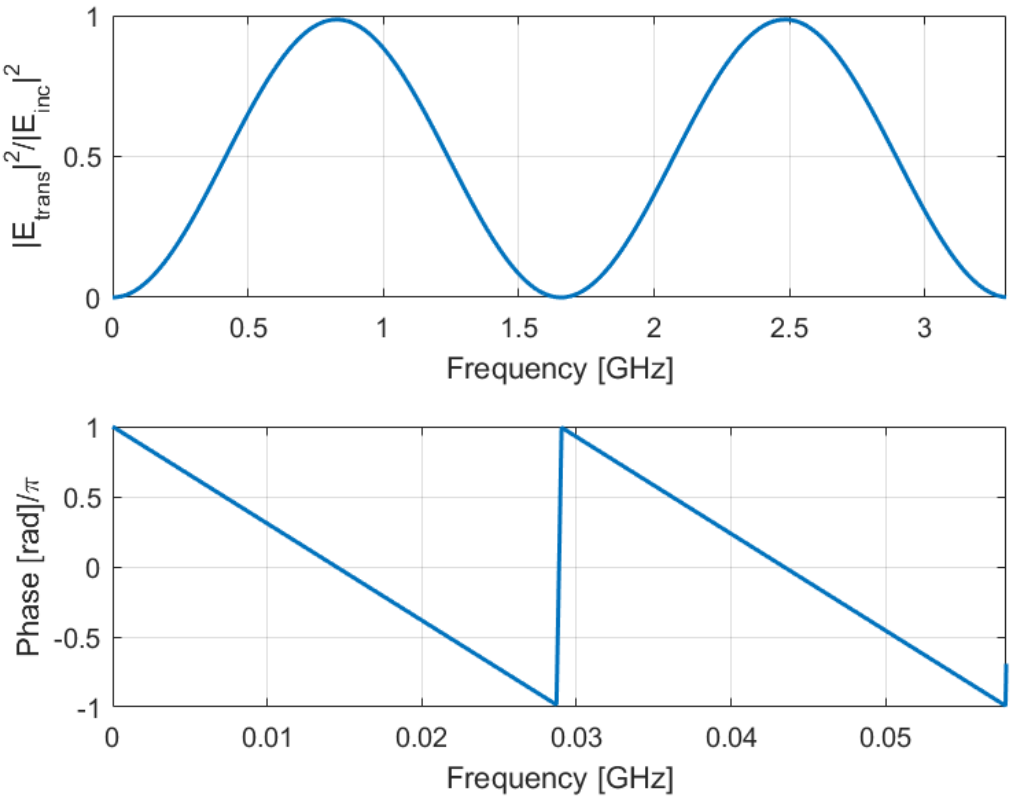

Fig. 2.11: The transmitted power transfer function and phase change for a swept sideband when the LHO Michelson where the carrier is locked to the dark fringe. The transmitted power changes with a cosine relationship over 1.6GHz due to the Schnupp asymmetry.

2.64, and the phase changes by 2π over 28.9MHz as determined by the L_{MICH} term in Equation 2.65.

The length difference ΔL can be further divided into $\Delta L = L_{schnupp} + \delta L$ where $L_{schnupp}$ is the Schnupp asymmetry, which is a constant macroscopic length difference of about 9cm in the LIGO interferometers and δL is a smaller differential length change which may be caused by motions of swinging optics in an unlocked interferometer or a passing gravitational wave in a locked interferometer. If $\Delta L = \frac{n\lambda_c}{2}$ where λ_c is the wavelength of the carrier then no carrier power will be transmitted through the Michelson into the antisymmetric (AS) output of the Beam-Splitter. When δl is controlled such that this condition is met, MICH is said to be operating on the "dark"

condition. When microscopic length of MICH is controlled to maximum carrier transmission, the MICH is said to be locked to the "bright" condition. The presence of the 9cm Schupp asymmetry allows the 45MHz sidebands to leak through the Michelson when it is locked to the carrier dark condition.

2.3.2 The Power Recycled Michelson Interferometer

The reflected and circulating fields for the PRMI can be determined using Equations 2.10 and 2.11, $r_2 = r_{MICH}$, $t_2 = t_{MICH}$ and length l_{PRM} is the distance between the Power Recycling Mirror (PRM) and the Beam-Splitter. The transmitted field can be determined by propagating the circulating field term from the PRM to the Beam-splitter and then through MICH. This gives the equations:

$$\tilde{\mathbf{E}}_{\mathbf{refl}} = \frac{r_{PRM} - r_{MICH}\exp\Big(-2ikl_{prm}\Big)}{1 - r_{PRM}r_{MICH}\exp\Big(-2ikl_{prm}\Big)}\tilde{\mathbf{E}}_{\mathbf{inc}} \tag{2.66}$$

$$\tilde{\mathbf{E}}_{\mathbf{circ}} = \frac{it_{PRM}}{1 - r_{PRM}r_{MICH}\exp\Big(-2ikl_{prm}\Big)}\tilde{\mathbf{E}}_{\mathbf{inc}} \tag{2.67}$$

$$\tilde{\mathbf{E}}_{\mathbf{trans}} = t_{MICH}\tilde{\mathbf{E}}_{\mathbf{circ}}\exp\Big(-ikl_{prm}\Big) \tag{2.68}$$

In aLIGO, $R_1 = R_{PRM} = 97\%$, and $R_{ITM} = 98.5\%$ and the distance between the PRM and the BS is 57.6m, which corresponds to a ν_{FSR} of the power recycling cavity (PRC) of 2.6MHz[65]. For an interferometer in which the PRMI is locked to the carrier at 1064nm, the transfer function of PRMI as a function of sideband frequency f_{sb} is plotted in Figure 2.12. As expected, the sideband is maximally transmitted into the AS output when $k\Delta L = (2n+1)\pi/2$ for which $f_{sb} = \frac{2n+1}{2}$8.3x10^{8}Hz and $f_{sb} = m$2.6x10^{8}Hz.

The reflectance as a function of f_{sb} is plotted across a much larger frequency

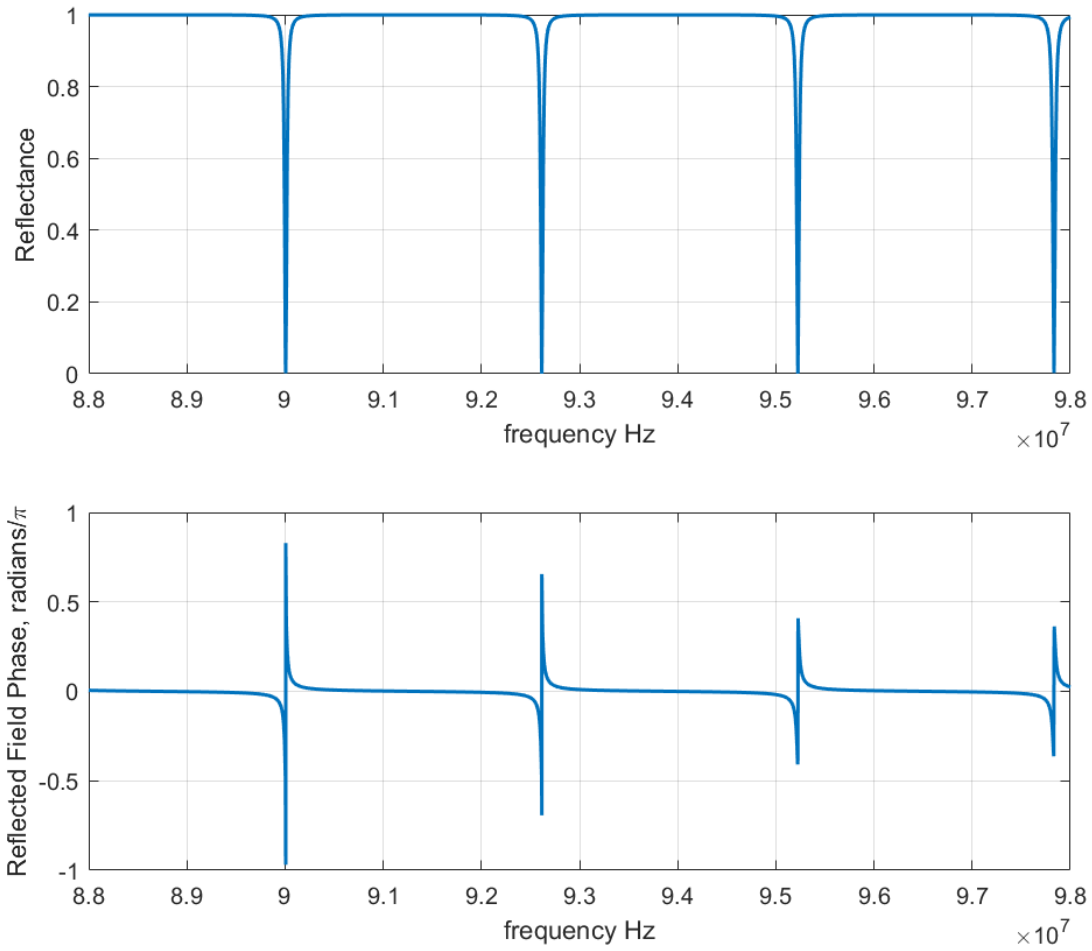

Fig. 2.12: The reflected transfer function of the PRMI, at a frequency range where the MICH reflectivity is equal to the PRM reflectivity and the transmission through the PRC contrast is maximum.

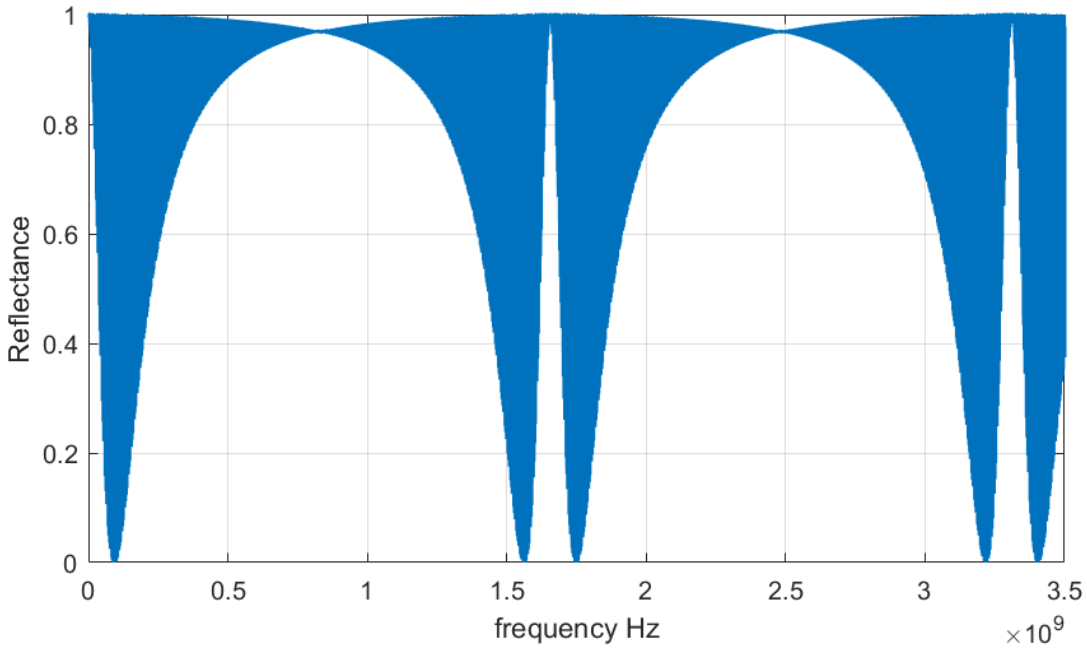

Fig. 2.13: The reflected transfer function of PRMI, over the 1.8Gz period over which MICH reflectivity changes. Note over this range, the PRMI does not behave like a simple cavity. The Reflectance moves up and down between a maximum and a minimum value with a period of $\nu_{fsr,PRMI}$. This maximum and minimum value for reflectance is indicated for a given frequency by the edges of the solid blue shape in this graph.

range in Figure 2.13. It is clear the frequency-varying behavior of the PRMI is more complex than for a FP cavity. The transmission through the PRMI is maximum when $R_{PRM} = R_{MICH}$. The PRMI finesse is maximum when R_{MICH} is 100% reflective, decreases to zero when R_{MICH} is 100% transmissive, as illustrated in Figure 2.14. The ν_{FSR} of the PRMI, $\nu_{fsr,PRMI}$, is independent of R_{MICH} and is constant.

2.3.3 The Signal Recycled Michelson Interferometer

The fields for the Signal Recycled Michelson Interferometer (SRMI) can also be calculated using Equations 2.10 to 2.12, and $r_1 = r_{MICH}$. The LIGO SRC length is 56m and the Signal Recycling Mirror (SRM) reflectivity is $R = 37\%$, which means that the

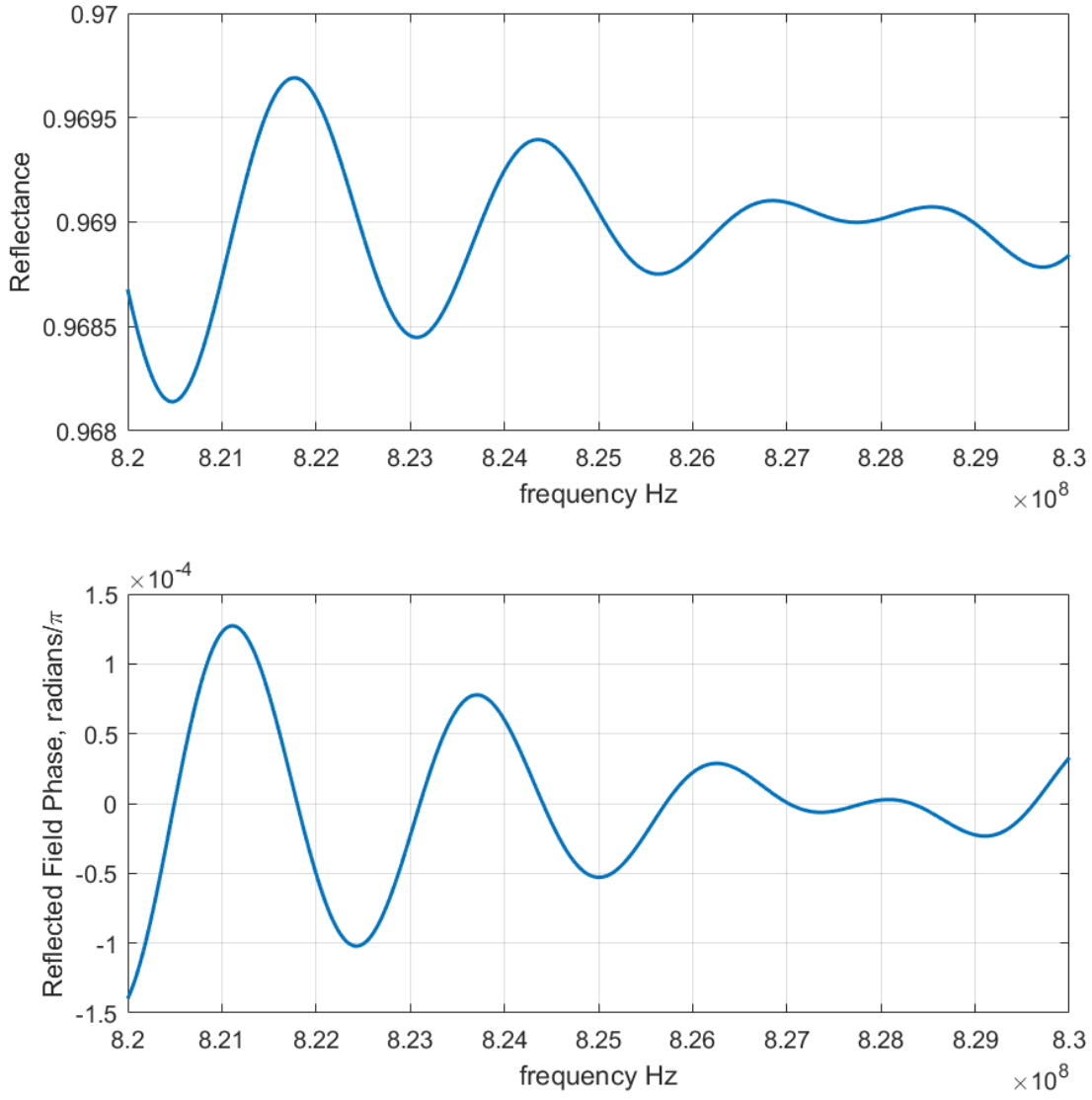

Fig. 2.14: The reflected transfer function of PRMI,at a frequency range where the MICH has almost 100% transmission. On this plot, which has a finer resolution than the previous plot in Figure 2.13, it is clear the Reflectance changes over $\nu_{fsr,PRMI}$

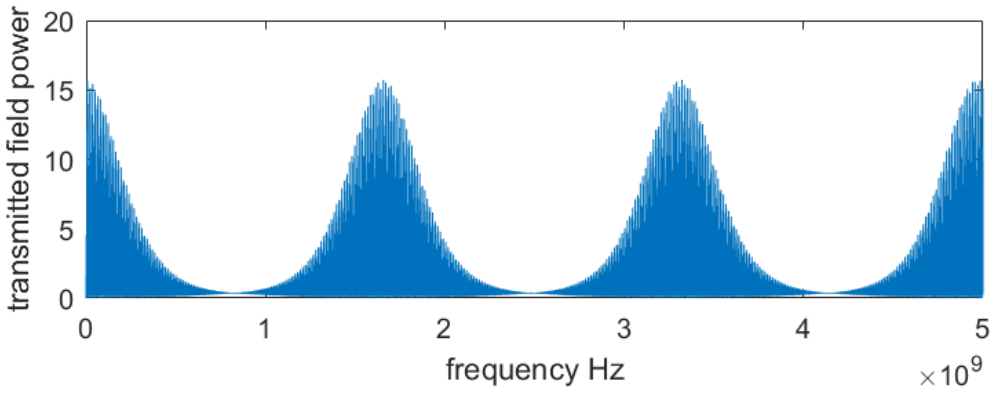

Fig. 2.15: The transmitted light transfer function of the SRC.

SRMI has a finesse of only 13.5. The transfer function of the SRMI in transmission is plotted in Figure 2.15. As expected, the SRMI power build-up and thus the transmittance is maximum when MICH is maximally transmissive of the sideband frequency, when $f_{sb} = (2n + 1)8.3\text{x}10^8$Hz. Just like the PRMI, the finesse of the SRMI does not remain constant for all sideband frequencies, as the complex reflection coefficient r_{MICH} and hence the phase gained within the MICH section of the SRMI varies with frequency. This is important to note because in later Chapters we will measure the transfer function of the SRMI to measure the resonance condition and the length of the SRC.

2.3.4 Higher-order Modes in the PRMI and SRMI

Higher order modes should be anti-resonant in the cavities in order to prevent mode hopping[57]. To achieve this, the PRMI and SRMI are designed so that the accumulated Gouy phase and thus the resonant frequency of the first order HOMs are at least one cavity line-width away from the fundamental frequency.

The PRC and SRC are folded cavities, as shown in Figure 2.9 in which the fold mirrors form telescopes (using mirrors PR2 and PR3 in the PRC and SR2 and SR3 in the SRC) that match the recycling cavity eigenmode to that of the arm cavities and match the arm cavity mode to the eigenmode of the output mode cleaner[57].

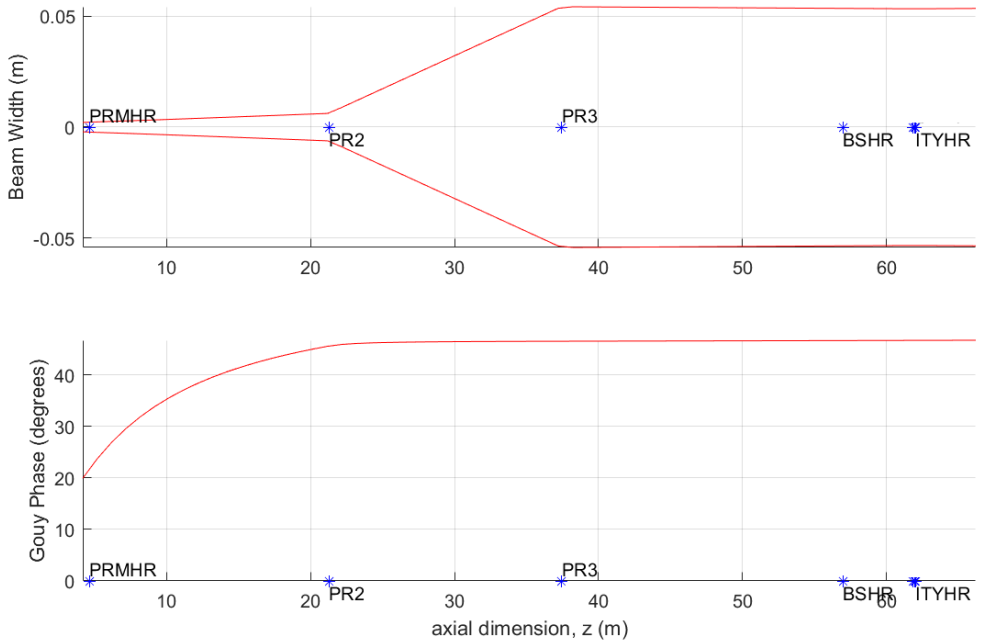

Fig. 2.16: The beam size and accumulated Gouy phase of the beam in the PRMI. The beam travels from the PRM (labeled PRMHR), is reflected from the PR2, PR3 and Beam-Splitter (labeled as BSHR) optics, and travels through the ITMy compensation plate (not labeled) to the ITMY (labeled ITMYHR). z=0 is set at optic SM1, 5m before the PRM.

Plots of the mode size within the PRMI and SRMI are shown in Figures 2.16 and 2.17 respectively. The distances between the mirrors and the radii of curvature of the mirrors within each cavity are the critical parameters that determine the Gouy phase shift of the cavities (and hence these parameters determine the mode matching into these cavities).[57]

2.4 Conclusion

In this chapter I have described the fields in a simple Fabry-Perot cavity, considering both longitudinal and transverse modes. I have described how the properties of the cavity are related to the resonant frequencies in the cavity. (Section 2.1)

I have used the field analysis of a cavity to describe the compound cavities of the aLIGO interferometer. This chapter is the background for the measurements of

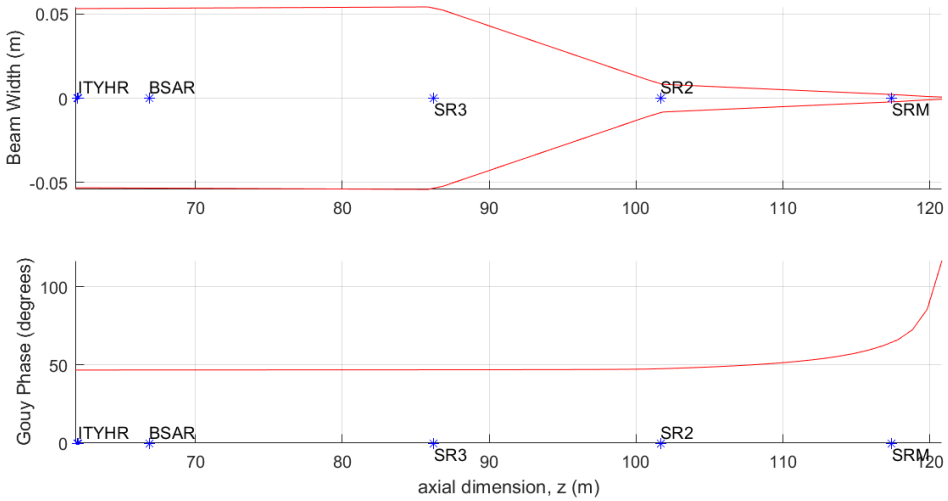

Fig. 2.17: The beam size and accumulated Gouy phase of the beam in the SRMI. The beam travels from the ITMY (labeled ITYHR), through the compensation plate (not labeled) through the Beam-Splitter (labeled BSAR), through the SRC optics to the SRM. z=0 is set at optic SM1, 5m before the PRM.

aLIGO cavity properties described in Chapters 3 and 4.

3. CHARACTERIZATION OF THE CORNER CAVITIES: SWEPT-FREQUENCY TECHNIQUES

Swept-frequency scanning techniques, described in Section 3.1, have been used to characterize LIGO cavities, yielding accurate results for high-finesse cavities. For example, they have been used to characterize the LHO arm cavities, the LLO IMC, and the LHO power recycling cavity [66, 45, 67, 68, 69]. This chapter reports additional measurements used to characterize other cavities of the aLIGO interferometers.

In Sections 3.2-3.4, I present the results of measurements in which I participated but was not the lead investigator, including:

- Section 3.2: Characterization of a test mass ring heater, performed in order to compare the in-situ performance of the ring heater with the predicted performance.
- Section 3.3: Investigation of optical absorption in the Input Mode Cleaner (IMC), performed to detect any changes to the optical absorption after commissioning work was performed inside the IMC vacuum chambers.
- Section 3.4: Measurement of the power recycling cavity (PRC) length and Gouy phase, to determine how well the as-built parameters agree with the design values.

Investigations I led are discussed in the measurement of the Schnupp asymmetry at LHO in Section 3.5, and an investigation of the Signal Recycling Cavity at LHO in Section 3.6.

Finally, there is a discussion of the impact of these results on future cavity design

and commissioning. This includes a discussion of the limitations of these measurements, highlighting a need for alternative cavity characterization techniques in the case of low finesse cavities (which will be the subject of Chapter 4).

3.1 Swept-Frequency Techniques for Cavity Characterization

A schematic of the measurement system is shown in Figure 3.1. The cavity length is locked to the main laser using RF-reflection or PDH locking[40]. Lock is achieved by controlling the length of the cavity by adjusting the suspensions on which the mirrors are mounted. A tunable measurement frequency is generated by frequency-offset-locking an auxiliary NPRO laser using photodiode PDA and a phase-locked loop[70]. The power incident on the reflection and transmission photodiodes, PDB and PDC, then consists of components at the resonance frequency and the tunable frequency, yielding a heterodyne beat at the offset frequency. The transfer functions are determined by using a spectrum analyzer to measure the beat signal. The rate at which the offset frequency is swept must be sufficiently slow that the transmission and reflections are not affected by the storage time of the cavity. In practice however, the cavity storage times of the corner cavities are so short that this is not difficult.

The frequency spacing of the TEM_{00} modes reveals the length of the cavity as per Equation 2.13 while the spacing of the higher order modes is used to determine the Gouy phase shift of the cavity. The measurement sensitivity is dependent on the finesse of the cavity. It can be improved by measuring over multiple free spectral ranges. If the finesse is higher, the peak width is smaller, and the uncertainty in fitting the peak frequency will be lower. Thus, swept frequency measurements work best in cavities with a high finesse where the resonance peaks are well resolved. If the finesse is low, such as in the signal recycling cavity, other techniques can be used to characterize the cavity, as discussed in Chapter 4.

The Gouy phase of the cavity can be determined using the frequency offset of

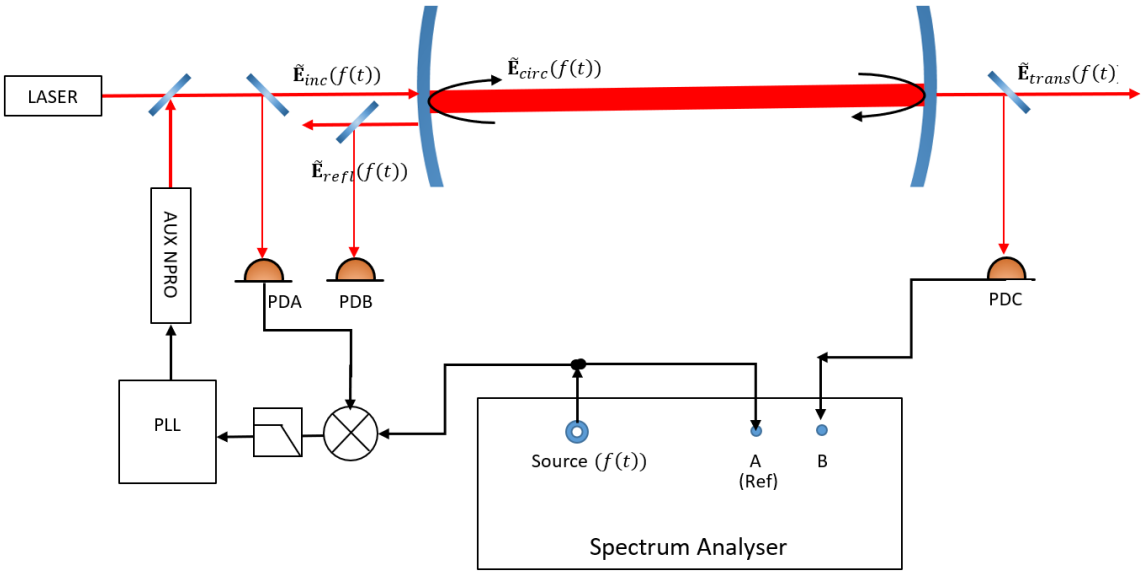

Fig. 3.1: Equipment schematic for a measurement of the transfer function in transmission in a LIGO-style suspended cavity. The light reflected from the input mirror is shown spatially offset from the incident light for clarity.

the HOMs. The symmetry of the swept beam relative to the cavity mode is broken to enable excitation of the HOMs, typically by obscuring part of the beam using a toothpick. The spatial symmetry of the beam incident on the detector photodiodes must also be broken to enable detection of the anti-symmetric HOMs. In practice the power in the HOMs injected into the cavity is low, so it is important that the symmetry breaking at the input is achieved without blocking a significant portion of the beam, or the power HOMs will be so low that the output signal will not be detected above the noise floor.

3.2 Characterization of an End-Test-Mass Ring Heater

The test-mass ring heaters are used in the Thermal Compensation System (TCS)[45] to tune the interferometer and compensate for absorption-induced wavefront distortion. In particular, they change the radius of curvature of the ITM and the ETM. The effect of the ring heater on the change in the radius of curvature of the ETMy at

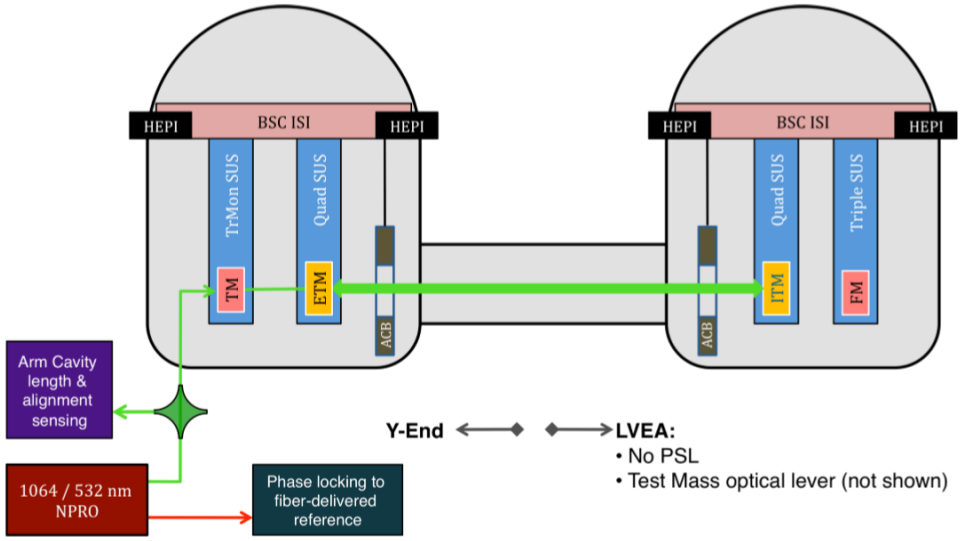

Fig. 3.2: Equipment layout for the One Arm Test, Figure 1 from T1100080.[73]

LHO was investigated by measuring the change in the offset frequencies of the HG_{10}, LG_{10} and LG_{20} HOMs[67, 71] as part of the LHO One Arm Test (OAT)[72].

Schematics of the layout for the OAT are shown in Figures 3.2 and 3.3. During the OAT, the length of the y-arm was locked using the end-station ALS laser which was injected into the y-arm cavity through the ETMy. This laser was a 532nm TEM_{00} laser system, produced by SHG of a 1064nm NPRO that could be phase-locked to a 1064nm laser resonant in a reference cavity. The reference cavity was used to simulate the LIGO pre-stabilized laser (PSL).

Acoustic frequency sidebands that could be swept 30-80kHz were added to the laser beam incident on the arm cavity using the system shown in Figure 3.4 and the phase of the reflection was analyzed to determine the offset frequencies of the HG_{10}, LG_{10} and LG_{20} HOMs[67, 71].

The offset frequencies ν_{offset} of HG_{mn} and LG_{pl} modes are given by[58]

$$\nu_{offset} = \frac{(m+n+1)}{\pi}\cos^{-1}\left(\sqrt{g_1 g_2}\right)\nu_{FSR} \tag{3.1}$$

and

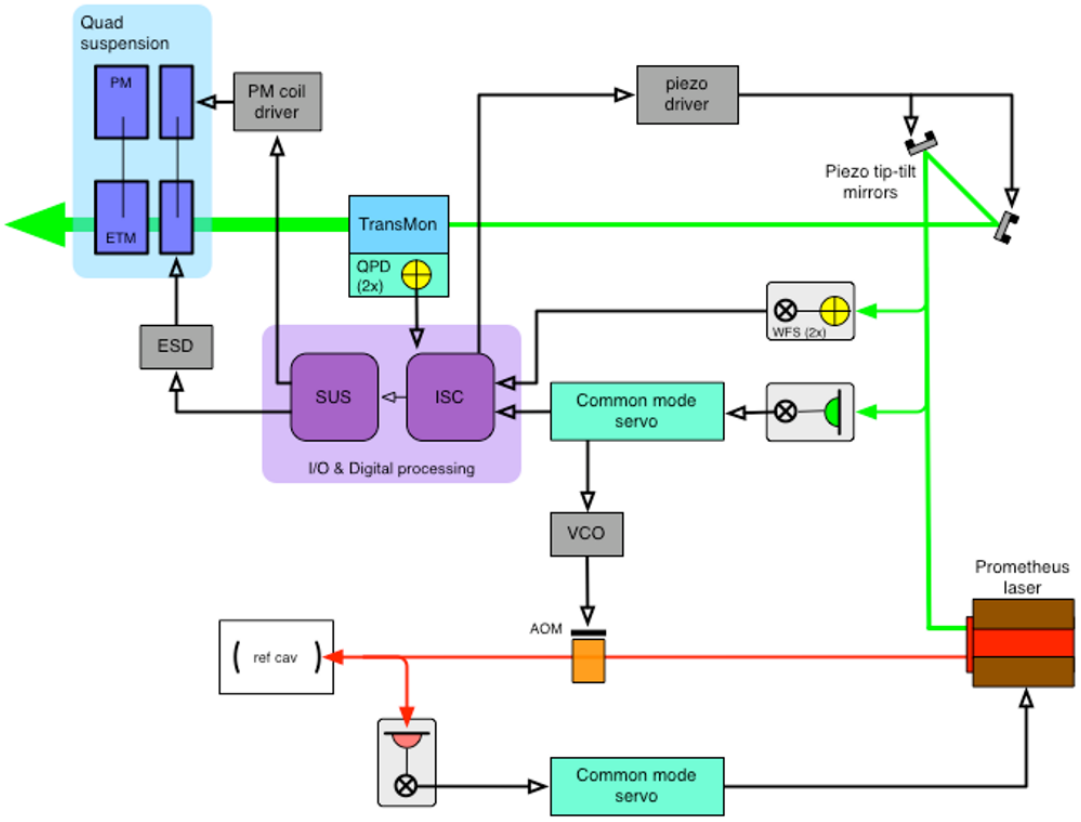

Fig. 3.3: Servo block diagram for the LHO One Arm Test, Figure 2 from T1100080.[73]

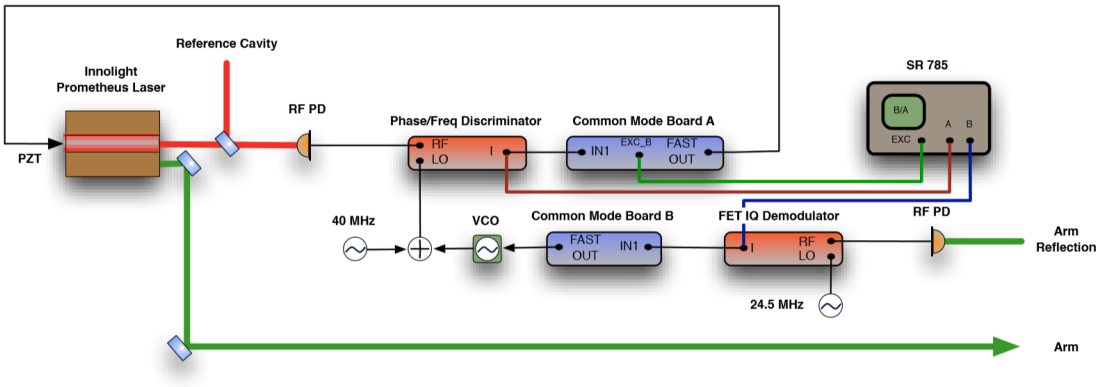

Fig. 3.4: Equipment schematic for a swept-frequency measurement of the arm cavity, reproduced from LHO alog entry 403.[71]

LHO y-arm parameters	
L	3996m
R_{ITM}	2307m
R_{ETM}	2312m
ν_{FSR}	37.5kHz

Tab. 3.1: Parameters of the LHO y-arm cavity.

$$\nu_{offset} = \frac{(2p+l+1)}{\pi}\cos^{-1}\left(\sqrt{g_1 g_2}\right)\nu_{FSR} \tag{3.2}$$

where ν_{FSR} is the y-arm cavity free spectral range defined in Section 2.1.2, g-factors $g_1 = 1 - \frac{L}{R_1}$, $g_2 = 1 - \frac{L}{R_2}$ defined in Section 2.1.4, L is the cavity length, and R_1 and R_2 are the curvatures of the cavity mirrors. These values are specified for the LHO y-arm in Table 3.1. Heating the ETM via the ring heater reduces its radius of curvature and thus reduces ν_{offset}.

The result of a single cavity scan is shown in Figure 3.5. The locations of the HG_{10}, LG_{10} and LG_{20} resonances are marked. These resonances were tracked as the ETMy was heated by the ring heater, and were used to calculate the change in ETMy curvature over time, as plotted in Figure 3.6. This measurement verified that the ring heater changed the radius of curvature of the ETMy by 0.79 micro-diopters per watt. It showed a slight disagreement with the COMSOL[74] model, assumed to be due to invalid assumptions in the model. (This discrepancy is revisited in Chapter 6.)

3.3 Investigation of optical absorption in the IMC

The IMC is used in aLIGO to filter the TEM_{00} mode from the pre-stabilized laser (PSL) prior to injection into the interferometer (IFO). The length of the IMC is phase-locked to the frequency of the PSL. Changes in the optical absorption of the IMC mirrors would change their curvature, thereby changing the mode matching, which would degrade the throughput of the IMC and could affect the locking process. The

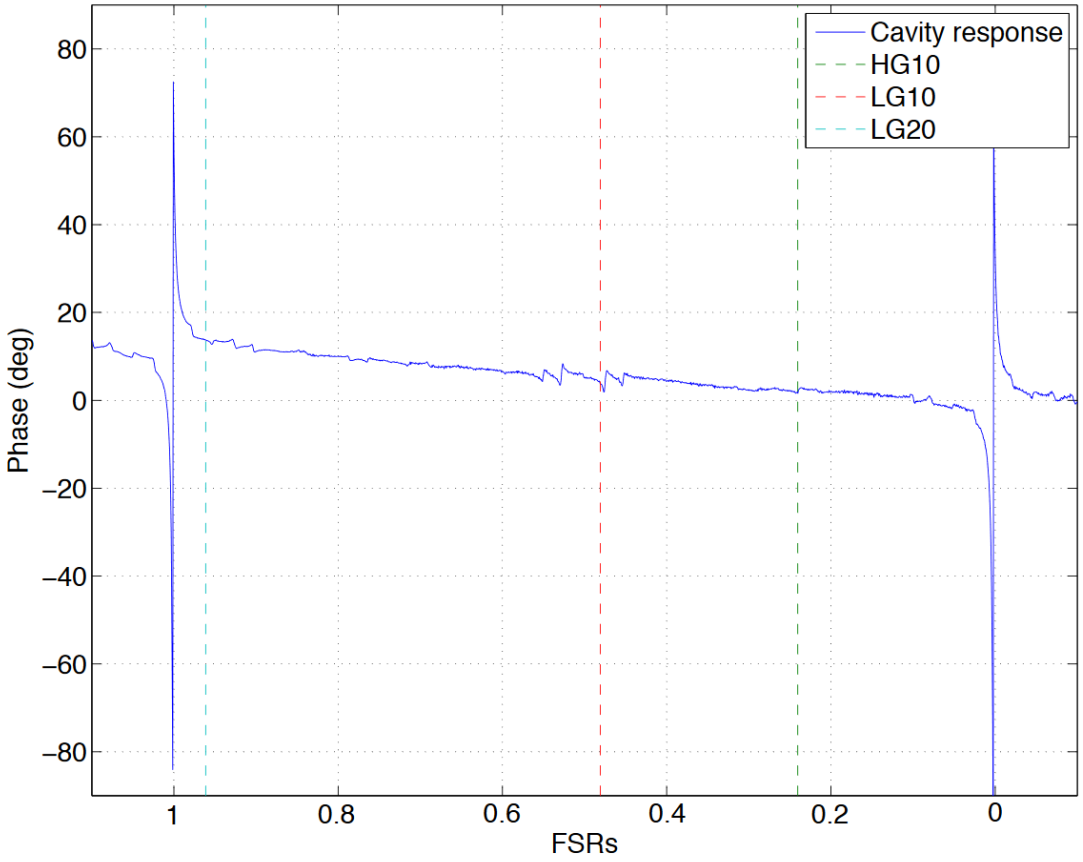

Fig. 3.5: Plot of the phase response from a single cavity scan of the arm cavity[67]. The HG_{10}, LG_{10} and LG_{20} higher order modes are marked with dashed lines. The peaks at 0 and 1 FSRs are the 0^{th} and 1^{th} carrier harmonics.

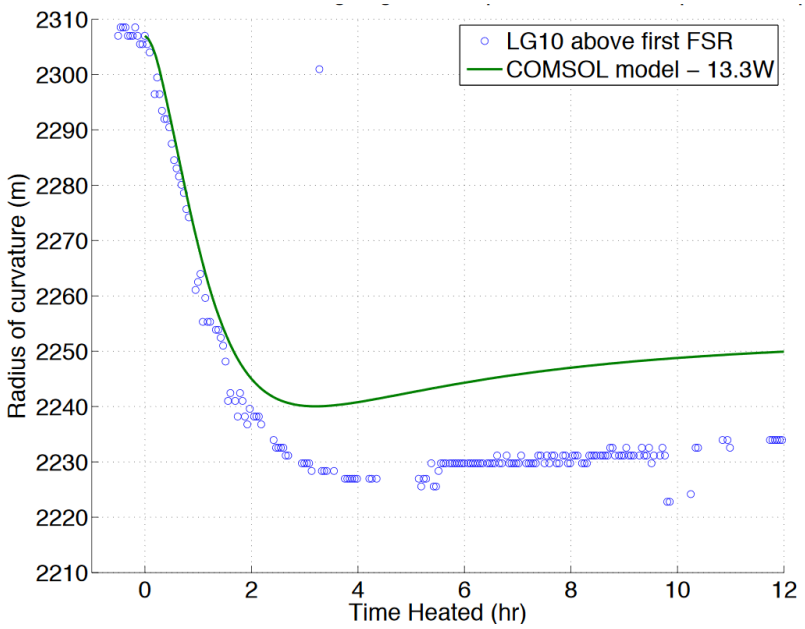

(a) Plot of change of ETM ROC over time due to ring heater actuation, as measured by LG_{01} cavity resonance, and as predicted by Comsol model.[67]. The ring heater was turned on to output 13.3W at time t=0. The measured radius of curvature disagrees with the prediction, which is unexpected.

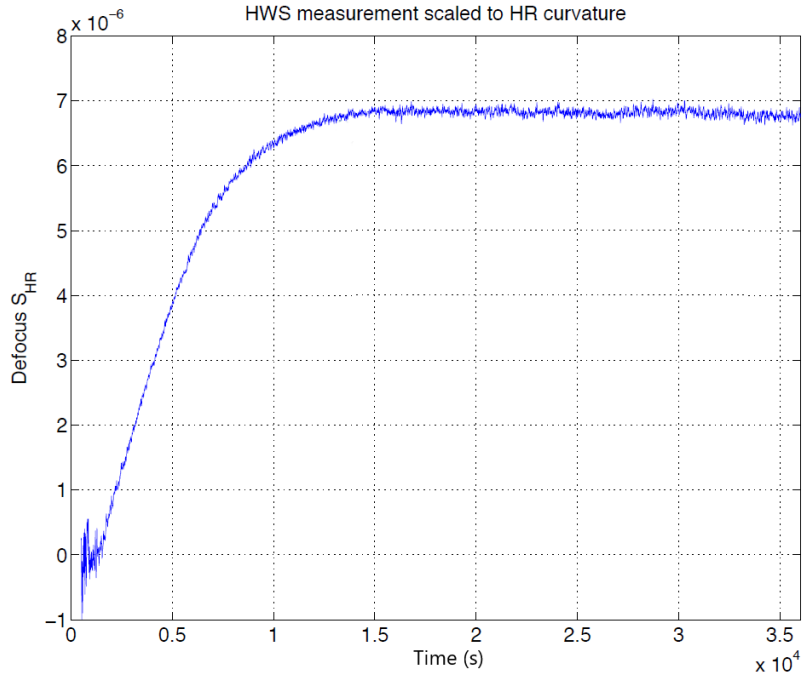

(b) Plot of thermal lensing in the ETMy substrate over time as the ring heater is switched on and run at constant current, as measured by the HWS.[75]

Fig. 3.6: The time-dependent behaviour of the arm cavity due to ring-heater actuation, measured during the One Arm Test

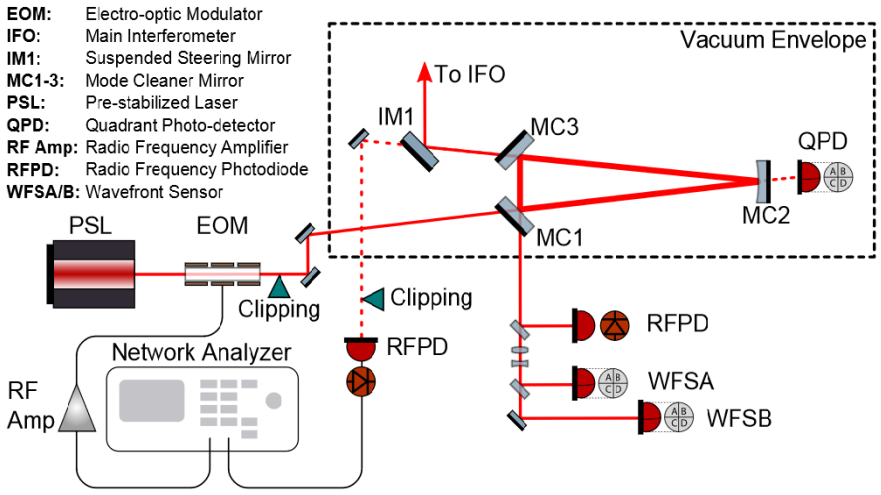

Fig. 3.7: Equipment schematic for the IMC HOM resonance measurement[68]. The IMC is locked to the PSL and the probe beam is generated by adding swept sidebands to the resonant carrier beam using the electro-optic modulator. The signal is generated by demodulating in transmission.

optical absorption of the IMC mirrors could potentially change due to contamination after maintenance work is performed inside the IMC vacuum chambers.

The optical absorption was investigated by measuring the power dependence of the HOM offset frequencies. The measurement system is shown in Figure 3.7. Swept sideband frequencies were added to the beam using an Electro-Optic Modulator (EOM). HOMs are excited by clipping the beam before it entered the IMC. The resonant frequency of the HG_{01} mode was measured with the IMC locked at different powers.

The change in the local sagitta δs of an optic over the beam radius ω due to absorption of the beam is given by Equation 3.3[76]:

$$\delta s = \frac{\alpha}{4\pi\kappa} P_a \tag{3.3}$$

where κ is the thermal conductivity and P_a is the absorbed power, and α is the coefficient of thermal expansion.

A typical scan of the IMC is plotted in Figure 3.8; The TEM_{00} modes are denoted [0]; the HG_{01} are denoted [1].

Changes in the offset frequency of the HG_{01} mode were analyzed by:

1. Calculating the change in curvature of each mirror in the IMC assuming they absorb the same power from the incident HG_{00} beam, using a COMSOL model[76].
2. Calculating the resulting change in the offset frequency of the HG_{01} mode by modelling[77] the IMC resonant frequencies as they depend on mirror curvature.
3. Comparing the measured change in offset frequency with the result of step 2 to determine the power absorbed by each mirror.

The results are shown in Figure 3.9. They indicate that the absorption of the optics decreased slightly over time during which multiple vacuum incursions occurred. This result was somewhat unexpected, as there was a concern that each time the vacuum chambers were opened the optics might become more contaminated, yet the errors calculated for these measurements due to uncertainties of the fit are small. Possibly the decrease in absorption is due to an improvement in the cleanliness of the optics as more is learned regarding the best cleaning and contamination control procedures for these large in-vacuum optics. In any case, the result confirms that the current contamination control procedures are effective at maintaining the cleanliness of the optics during vacuum incursions.

These IMC absorption measurements were compared with complimentary measurements made by tracking changes in scattered light from IMC optics, which were taken over the same time period, as will be discussed in Chapter 5.

3.4 Measurement of the Power Recycling Cavity Length and Gouy Phase

The Power Recycling Cavity (PRC) length and round-trip Gouy phase were determined by measuring the resonant frequencies of Hermite-Gauss modes in the PRC. The mode spacing was used to calculate PRC length and Gouy phase as per Equations

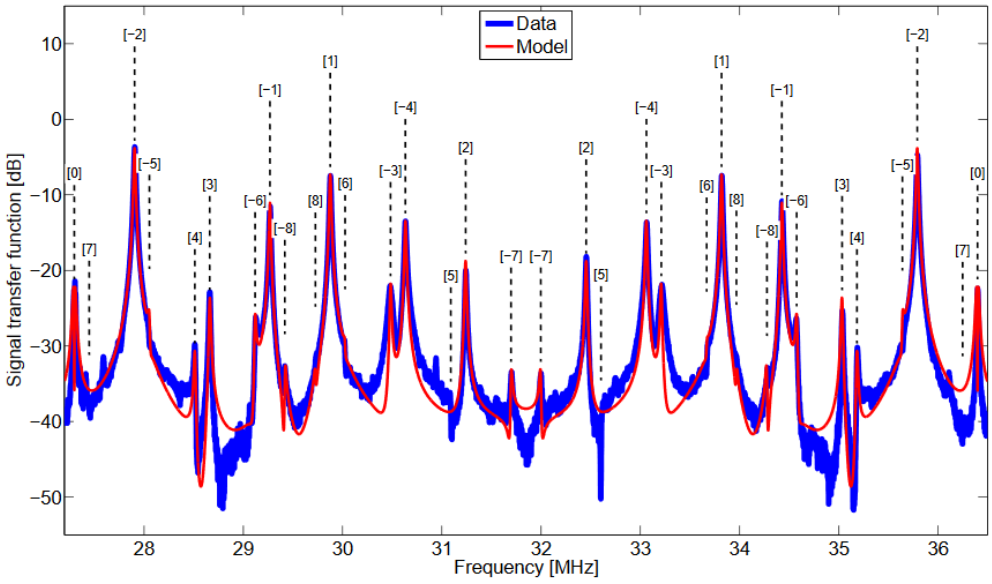

Fig. 3.8: An example HOM resonance measurement of the IMC, where the probe beam is swept across a full free spectral range of the input mode cleaner (IMC), together with a FINESSE model[68]. The peaks are labeled with their spatial mode orders (n+m) with a minus sign indicating the split peaks of the odd orders (n). Since the IMC eigenspectra are probed with phase modulation, each peak appears twice from being excited independently by the upper and lower sideband.

Date	Power (W)	f_{10} (Hz)	Δf_{10} (Hz)	Abs. (ppm/mir.)
1/17/2013	3.11	$29,266,891 \pm 60$	$6,230 \pm 69$	2.39 ± 0.02
	30.5	$29,273,121 \pm 35$		
7/23/2013	0.517	$29,268,352 \pm 65$	245 ± 85	1.50 ± 0.46
	1.03	$29,268,597 \pm 56$		
8/6/2013	0.203	$29,267,831 \pm 14$	358 ± 15	1.42 ± 0.06
	1.01	$29,268,189 \pm 6$		
9/30/2013	1.07	$29,266,056 \pm 39$	$1,175 \pm 54$	1.53 ± 0.06
	3.08	$29,267,230 \pm 37$		
6/17/2014	1.79	$29,269,212 \pm 23$	$1,585 \pm 42$	0.50 ± 0.01
	10.2	$29,270,797 \pm 36$		

Fig. 3.9: The inferred absorption from numerous repetitions of the Gouy Phase measurements in the LLO IMC. The power and $f_{1,0}$ and Abs. columns show the shift in this peak between power levels and inferred absorption.[68]

3.4 and 3.5 (where L is the distance from the PRM to the BS).

$$L = \frac{c}{2\nu_{fsr}} \tag{3.4}$$

$$\phi_{gouy} = \frac{\nu_{modespacing}}{\nu_{fsr}} 180^{\circ} \tag{3.5}$$

Schematics of the electronics and the optics used for the PRMI measurements are shown in Figures 3.10 and 3.11 respectively. The auxiliary laser beam is injected through IM4, which has 0.22% transmission. The prompt reflection of the auxiliary beam and a small portion of the incident PSL beam transmitted through IM4 are incident on photodiode NF1811, located on in-air table IOT2R. The resulting beat-note is mixed with the LO output of the HP4395A Spectrum Analyzer, and used to offset-lock the auxiliary laser to the PSL.

The beat-note due to the reflection of the auxiliary laser at the PRM and PRMI transmission through the PRM is measured by the NF1611 photodiode, located on the in-air table ISCT1 on the "REFL_AIR_B" photodiode path. This beat-note is combined with the LO signal of the Spectrum Analyzer to measure the reflection transfer function of the PRMI.

The measurement procedure is as follows:

1. Misalign SRM and ETMs to prevent flashes from unlocked cavities
2. Lock the PRMI
3. Lock the auxiliary laser frequency to the PSL frequency (with a variable offset)
4. Scan the auxiliary laser frequency
5. Read out the PRC transfer function in reflection using a Network Analyzer
6. Repeat measurement over multiple free spectral ranges

A typical PRMI transfer function is plotted in Figure 3.12. Fitting the frequency of each peak and taking the slope of dip location vs frequency gives an ν_{fsr} = 2,600,073±9 Hz. A 400 Hz uncertainty on the residual for a measurement span-

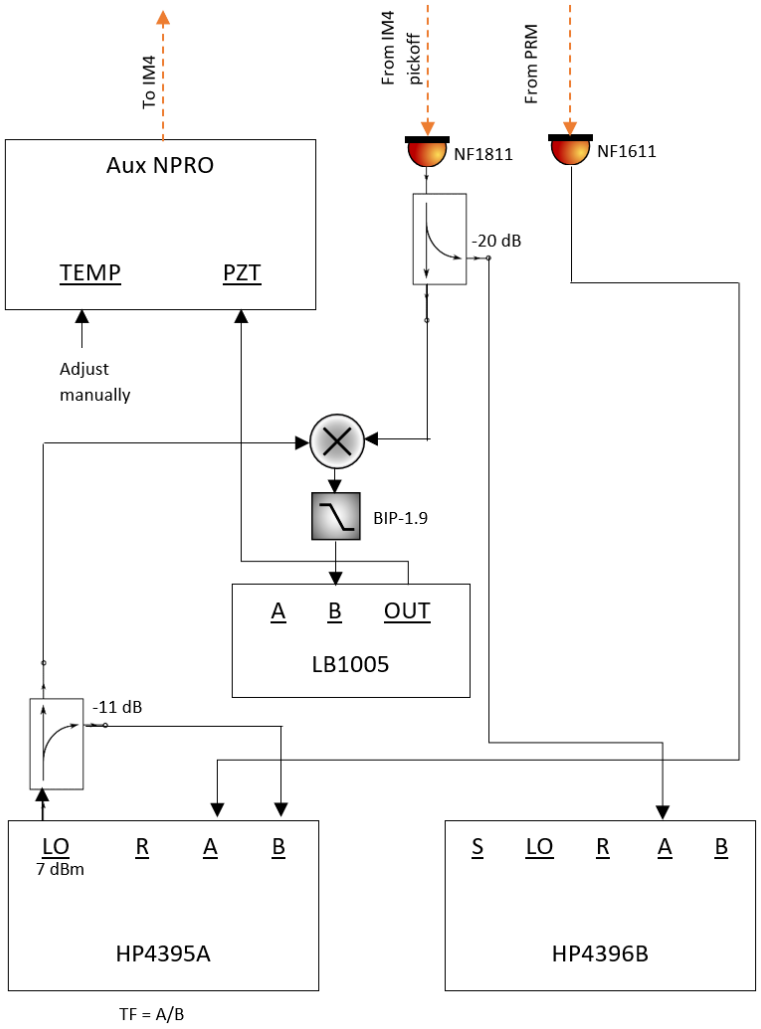

Fig. 3.10: Electronic layout for the measurement of the transfer functions of the PRMI, SRMI and DRMI cavities. The HP4396B spectrum analyzer is used to watch the beat-note location of the Auxiliary laser and the carrier. The LB1005 servo controller is used to set up the Phase Locked Loop (PLL) to lock the auxiliary laser to the PSL. The HP4395A is used to introduce a frequency offset to the PLL, and is also used to measure the transfer function of the reflected beam.

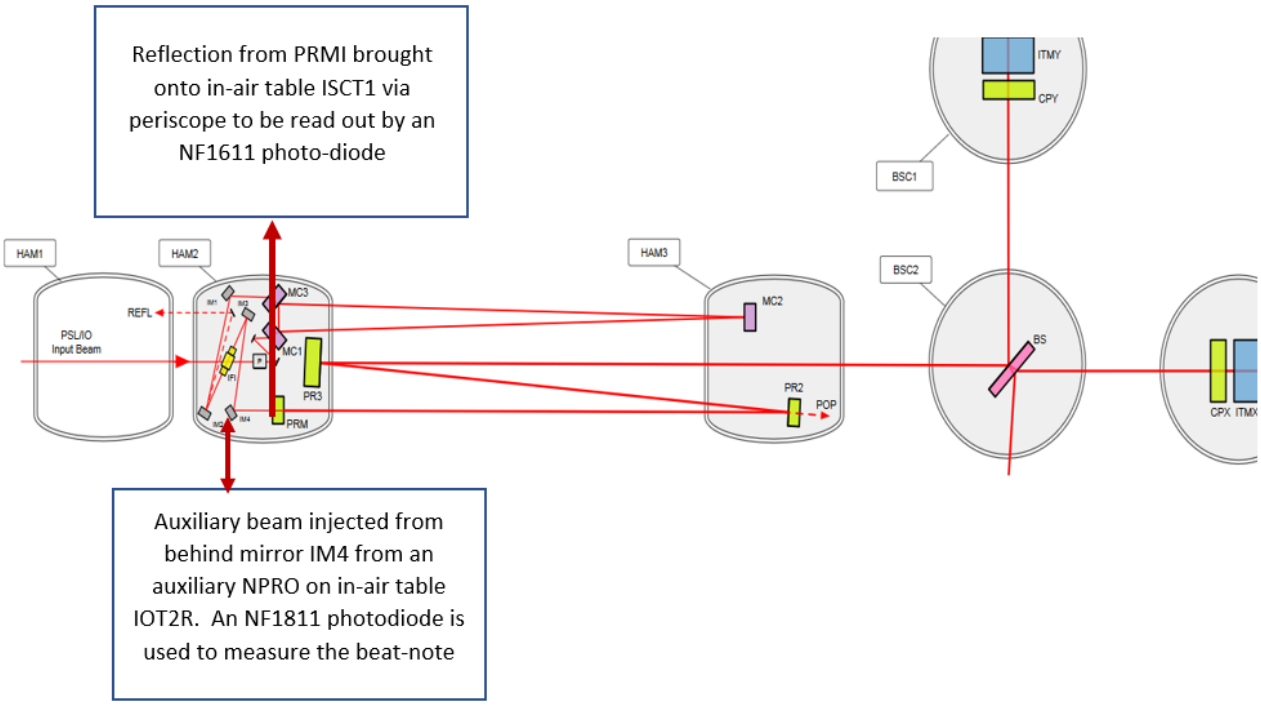

Fig. 3.11: Optical layout used for the measurement of the transfer functions of the PRMI, SRMI and DRMI cavities. The auxiliary laser is injected from in-air table IOT2R and the PRMI reflection is read out on a photo diode on in-air table ISCT1.

ning the 12.5 ν_{fsr}'s gives an uncertainty of 32 Hz in ν_{fsr}. Thus, L=57.6508±0.0007 m [78].

Scans looking for higher order modes, performed by Paul Fulda and myself, are plotted in Figure 3.13. The spacing between the HG_{00} and HG_{01} modes resonances was 0.29MHz. Thus, the one way Gouy phase is 20.8 degrees. Based on the design values of the PRC cavity, we expect a one-way Gouy phase of about 18 degrees if there is no ITM thermal lensing.

3.5 Measurement of the Schnupp asymmetry

This section describes a measurement of the Schnupp asymmetry at the LIGO Hanford Observatory. Recall that the Schnupp asymmetry is the length difference between the two Michelson arms, illustrated in Figure 3.14.

The design length of the Schnupp Asymmetry is 8cm[80]. If the Schnupp asymmetry is off by a few cm, it can lead to difficulties in lock acquisition and length control, as was observed in iLIGO. The Schnupp asymmetry was increased from 5cm to 8cm to address those issues[81]. Accurate knowledge of the Schnupp asymmetry is needed for precise modeling of the control design [82]. Thus, we wished to verify the Schnupp asymmetry length to sub-millimeter accuracy.

The optical layout and electronics, shown in Figure 3.15, for this measurement were similar to that used for the length measurement of the power recycling cavity except

- A wide-band NF1611 photodiode was used to detect the heterodyne beat between the auxiliary and PSL beams from IM4.
- The transfer function signal was high-pass filtered and amplified to improve the sensitivity.

The procedure to measure the Schnupp asymmetry is as follows:

1. Misalign the PRM, SRM, ETM optics to prevent added noise from flashes from

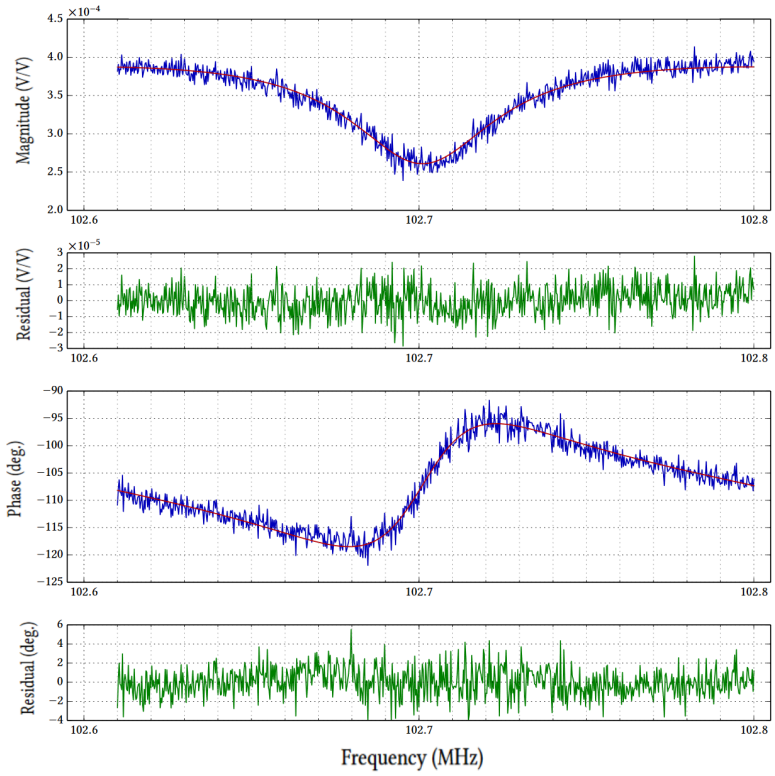

(a) An example of the reflection dip measured and fitted transfer function for the PRMI.

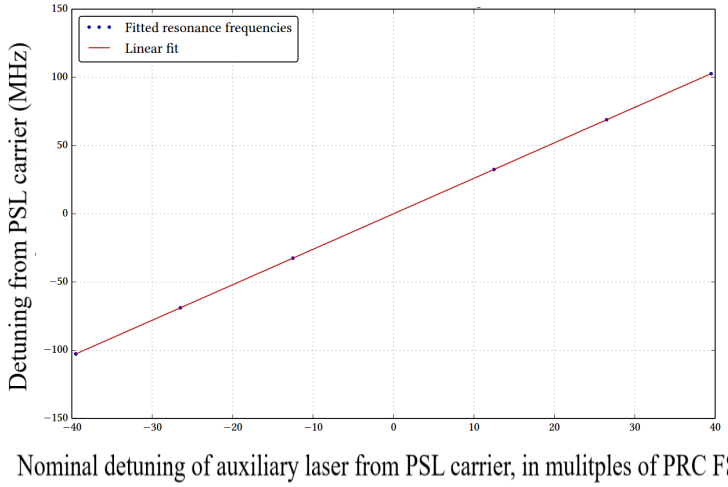

(b) Plot of transmission peak frequency vs frequency, with a linear fit.

Fig. 3.12: PRC length measurements.[78]

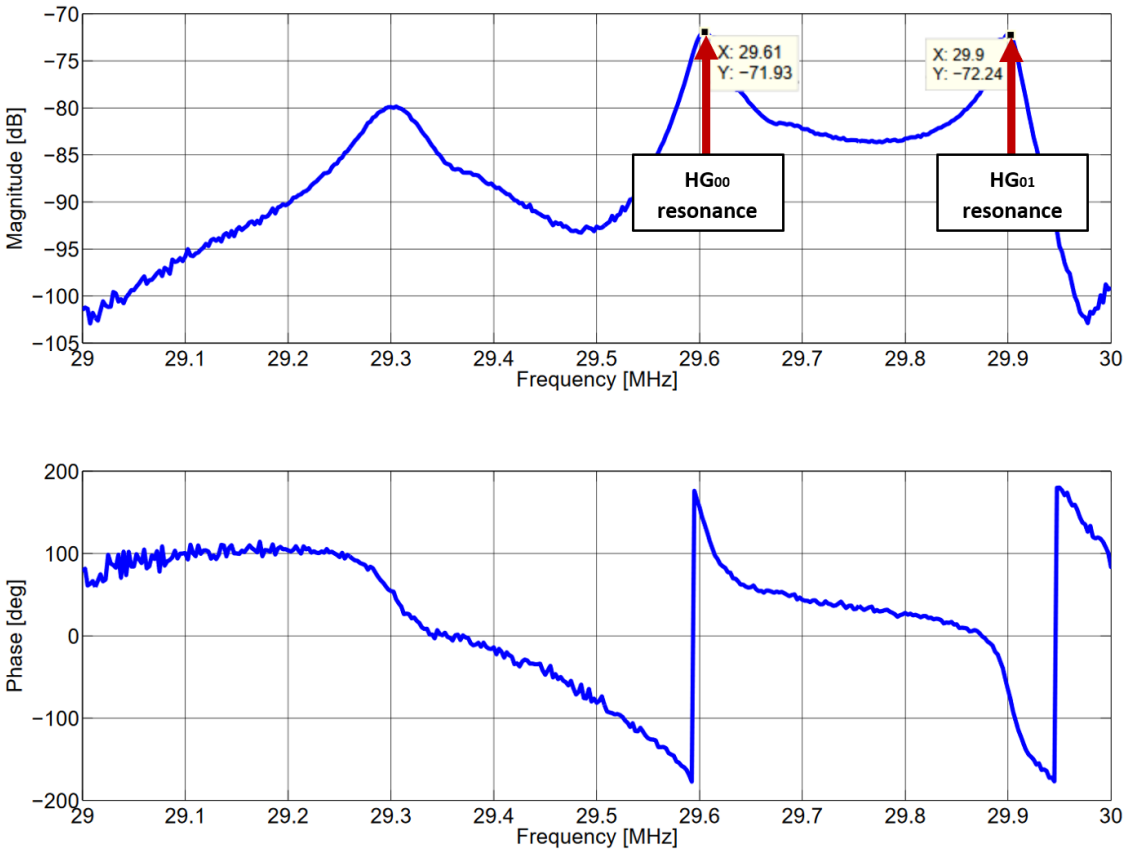

Fig. 3.13: Cavity scan of the PRC in reflection- looking for HOM resonances[79]. The HG_{00} and HG_{01} modes resonances are marked.

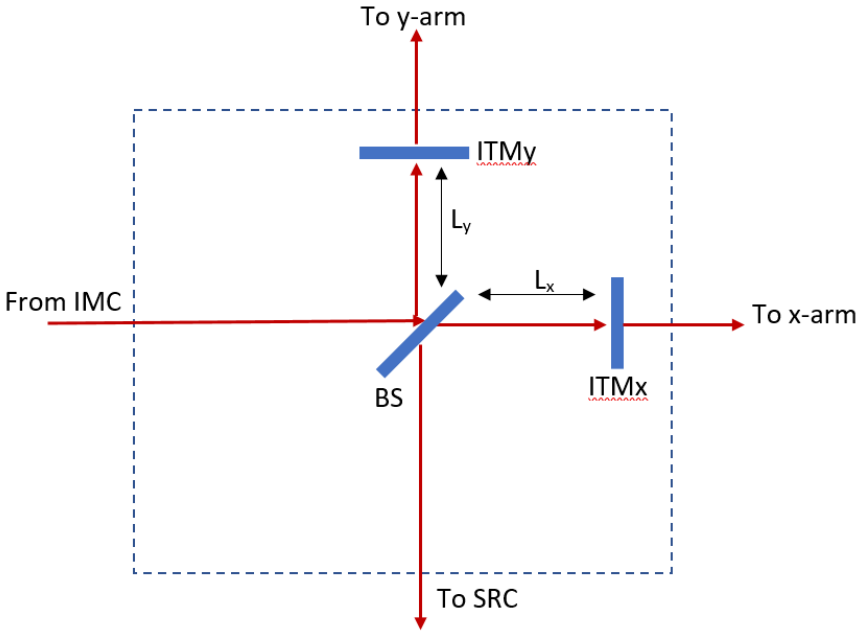

Fig. 3.14: Layout of the corner Michelson with the Schnupp asymmetry marked. The Schnupp asymmetry is the length difference between two Michelson arms: $L_{Schnupp} = (L_y - L_x)/2$.

other unlocked cavities.

2. Lock MICH to the bright fringe for the PSL.
3. Inject an auxiliary sideband which is locked at a frequency offset to the PSL carrier frequency
4. Offset the auxiliary NPRO by -0.9MHz so it is on a dark fringe, and manually scan around these frequencies to find offset frequency, f_1 of the transmission minimum
5. Offset the auxiliary NPRO by +0.9MHz so it is on the next fringe, and repeat step to to locate the frequency,f_2, of this transmission minimum.

The Schnupp asymmetry is then calculated using Equations 3.6 to 3.7:

$$P \, \alpha \, cos^2\left(\frac{L_{Schnupp}}{c} 2\pi f\right) \tag{3.6}$$

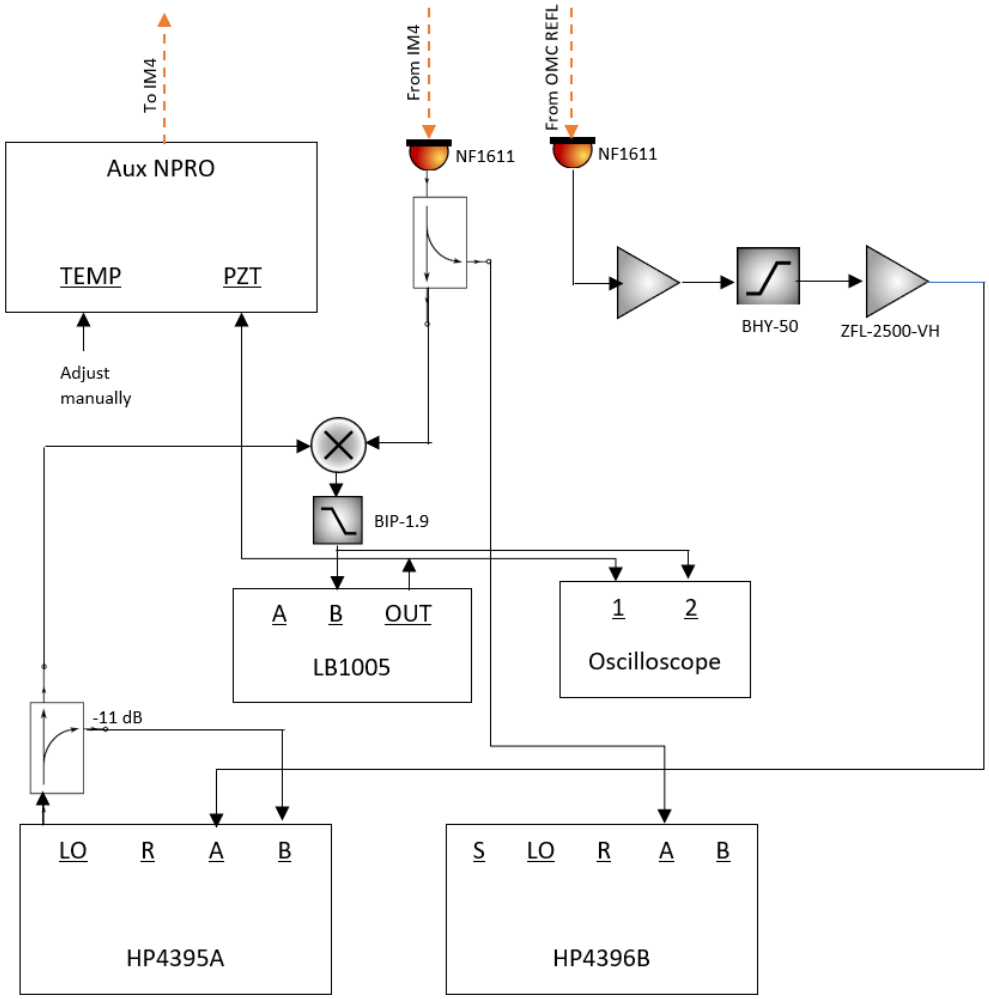

Fig. 3.15: The equipment setup for the Schupp asymmetry measurement. A beam from an Auxiliary NPRO is locked at a frequency offset from the PSL carrier frequency using an LB1005 servo controller. A HP339A Signal Analyzer provides the error signal. The transmitted beat-note of the carrier and the NPRO sideband is measured and demodulated against the error signal frequency using the Spectrum Analyzer. The amplitude of this transmitted power at the sideband frequency is recorded and used to calculate the Schnupp asymmetry.

$$L_{Schnupp} = \frac{c}{2(f_2 - f_1)} \tag{3.7}$$

The result of the two minima scans is shown in Figure 3.16. To find the location of the two minima, the cosine squared function in Equation 3.6 was fitted for each scan using least-squares fitting. Note that the frequency response of the 1611 photodiode was removed from the measurement before fitting.

The upper- and lower- minima are at +901±10MHz and -782±10MHz. The Schnupp asymmetry was then calculated using Equation 3.7, giving $L_{Schnupp}$ =8.9cm±0.1cm. This is different to the nominal value of 8cm. Future models of the interferometer frequency response and error signals can use this revised value for Schnupp asymmetry.

3.6 Characterizing the Signal Recycling Cavity

We attempted to measure the SRC length and Gouy phase using the technique used for the PRC, with the measurement systems shown in Figures 3.10 and 3.11. Both the SRMI and DRMI were probed in separate measurements. We first tried using the SRMI cavity but it has a low finesse and the results were unreliable. The DRMI cavity was then used with a frequency at which the Michelson was 100% transmissive, for which the cavity length is the sum of the PRC and SRC lengths.

The procedure to measure the SRC length with a locked DRMI went as follows:

1. Lock the corner cavity in a DRMI configuration
2. Engage Alignment Sensing and Control (ASC) System to improve long term stability of the suspension systems
3. Lock the auxiliary laser to the PSL frequency offset using a Phase Locked Loop.
4. At a 842.7 MHz offset from the PSL frequency, the Mich transmissivity is 100%, and the DRMI appears like a two mirror cavity with the length of the SRC and

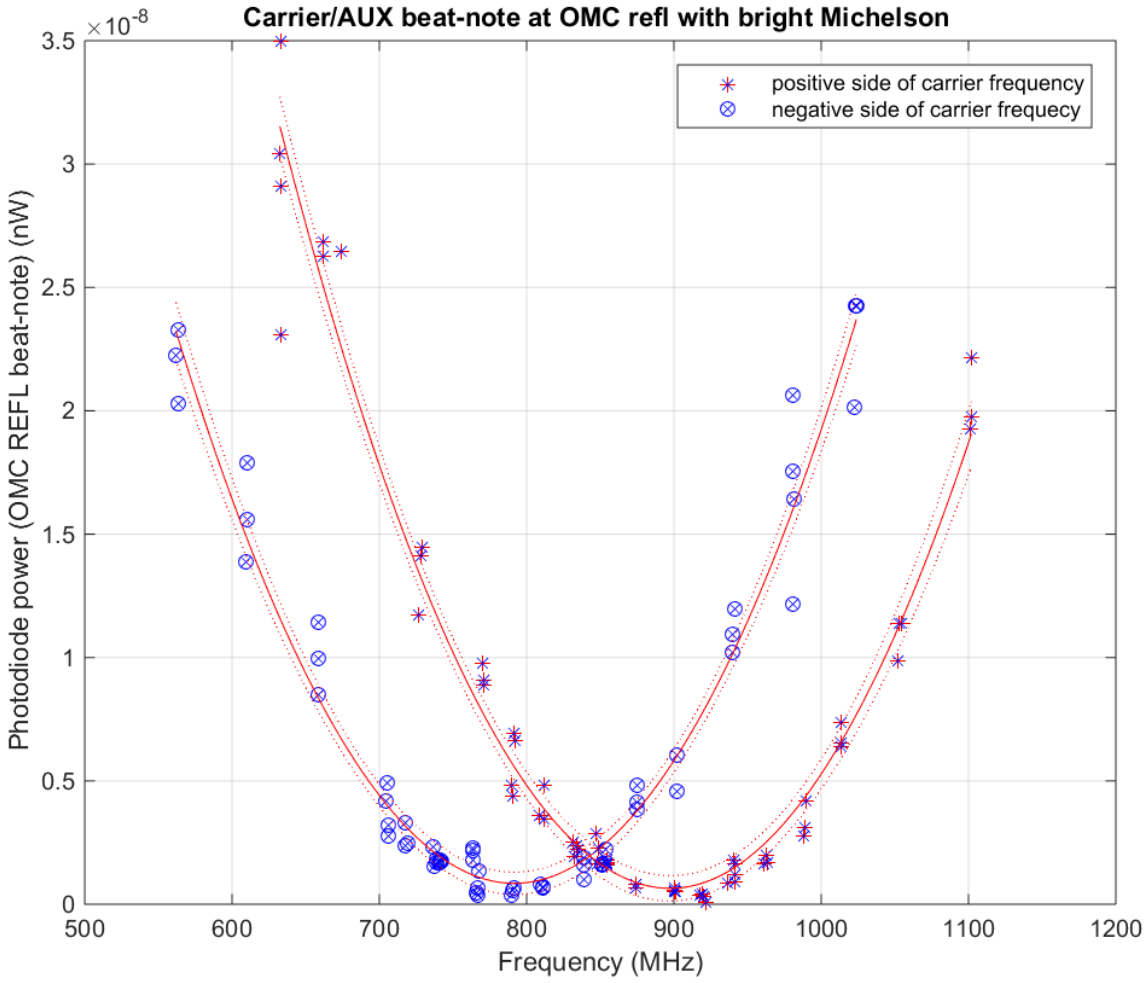

Fig. 3.16: Cavity scan results for the Schnupp asymmetry measurement. The plot shows the peak transmitted light vs frequency in the Michelson for a sideband offset to the carrier frequency. The Michelson is locked to the bright carrier fringe. The spacing between the two frequency minima is used to calculate the Schnupp asymmetry. Note that the first dark fringes for the sideband frequency on the positive and negative side of the carrier fringe are plotted. For ease of graphing, the absolute frequency values for the negative fringe are used as the x-variables.

the PRC combined.

5. The reflected beatnote of the PSL and the Aux laser is read out by the NF1611 photodiode on the REFLAIR port. The frequencies of the transmission dips closest to +/-842MHz were fitted using a Lorentzian function.

SRMI Cavity Measurement

The reflection transfer function for the SRMI, is plotted in Figure 3.17. The expected transfer function, as calculated from theory, is also drawn. As shown in the detail views, the frequency of the reflection peaks matches up but the absolute power measured doesn't agree with the theory curve. It is unknown why this behavior occurs, perhaps it is due to slow drifts in the mirror alignment. Fitting peaks around the region where the SRC becomes maximally transmissive, the SRC length was measured to be 56.015+/-.005m.

DRMI Cavity Measurement

The measured reflection DRMI transfer function is shown in Figure 3.18, along with fits for -842.14 ± 0.02MHz and +841.933 ± 0.02MHz. We estimate that the number of ν_{fsr} between these peak frequencies is 1277, as if the number of ν_{fsr} were off by ±1, the cavity length would differ by ±10cm and we have already established from the SRMI measurement that the SRC length was not off by this much. This corresponds to a combined PRC/SRC cavity ν_{fsr} of 1.319MHz, and a length of 113.664 ± 0.0027m. The PRC length was already measured to 57.6508 ± 0.0007m[78], so the SRC length is 56.013 ± 0.0035m. This is 4.8 ± 3.5mm longer than the design SRC length of 56.008m.

Graphs of the reflected beat-note power vs aux laser frequency offset are plotted across a larger frequency range in Figure 3.19. There is an 11MHz oscillation in the reflected power which is not yet explained. The phase has had a linear phase term

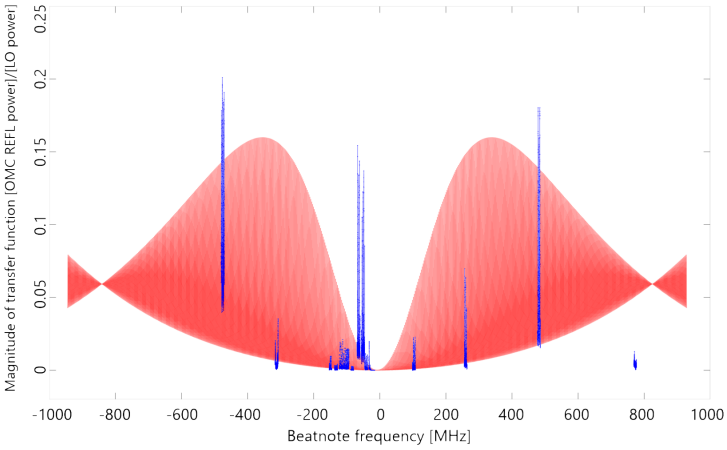

(a)

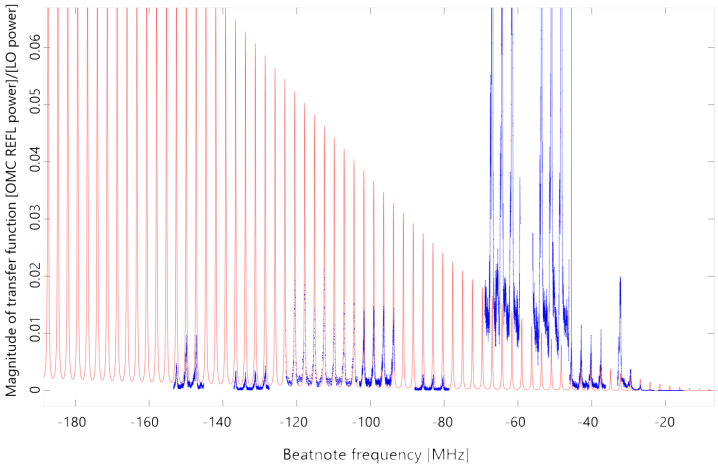

(b)

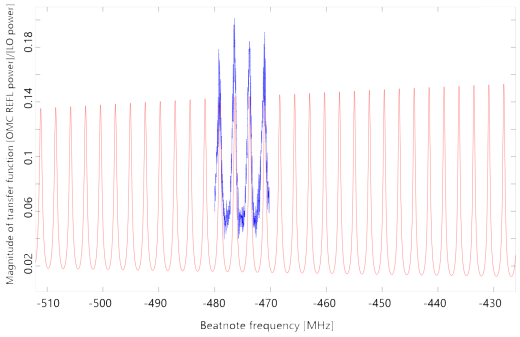

(c)

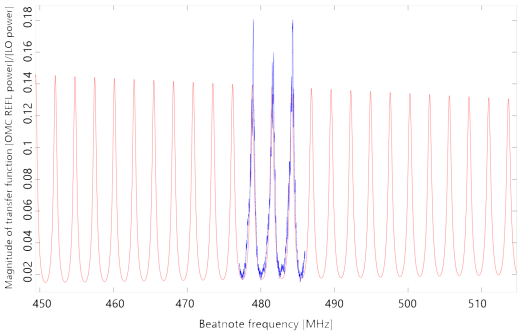

(d)

Fig. 3.17: The transmitted transfer function measured through the SRMI, in blue, and the expected transfer function calculated from theory, in red. Subplot (a) shows the full frequency range of the measurement, subplots (b) through (d) show zoomed-in regions of (a).

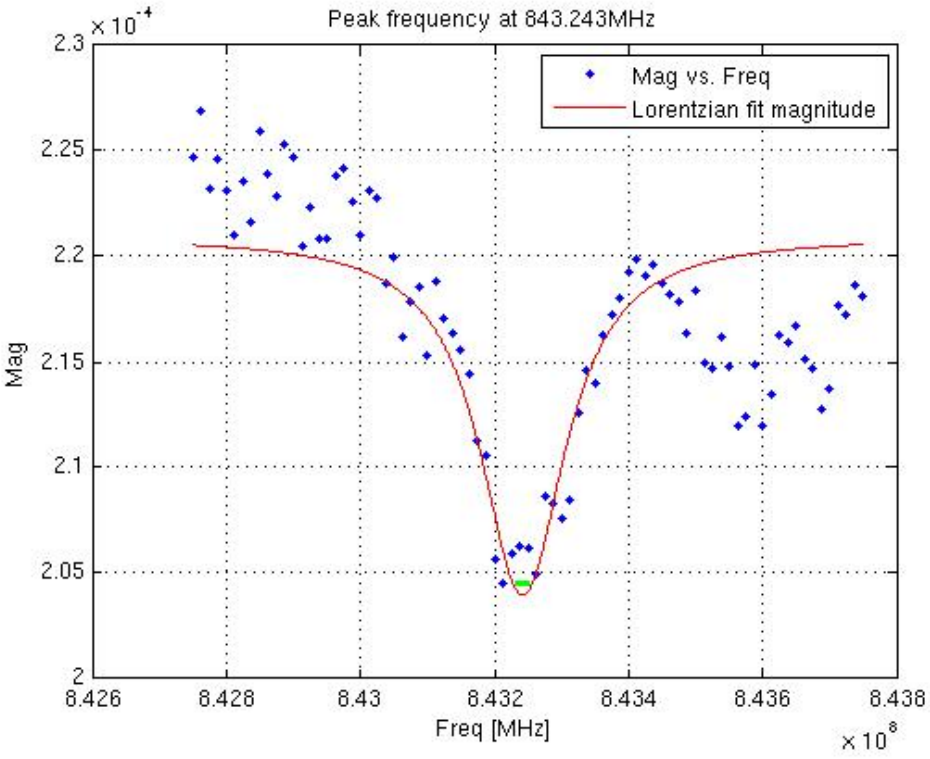

(a) Magnitude

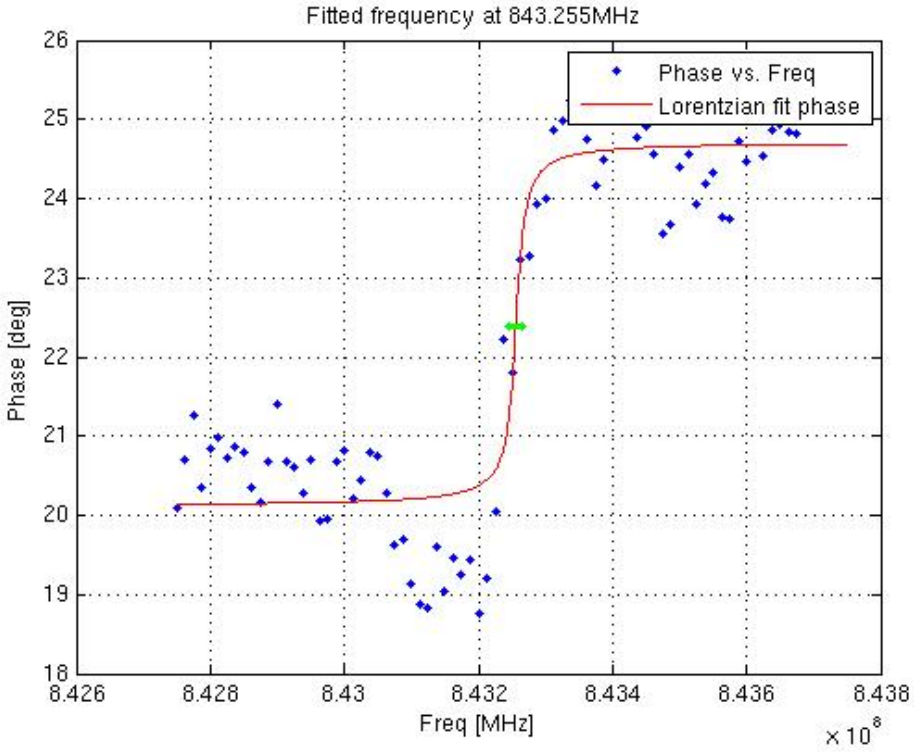

(b) Phase

Fig. 3.18: A single transmission minimum for a locked DRMI, measured using cavity scanning techniques.

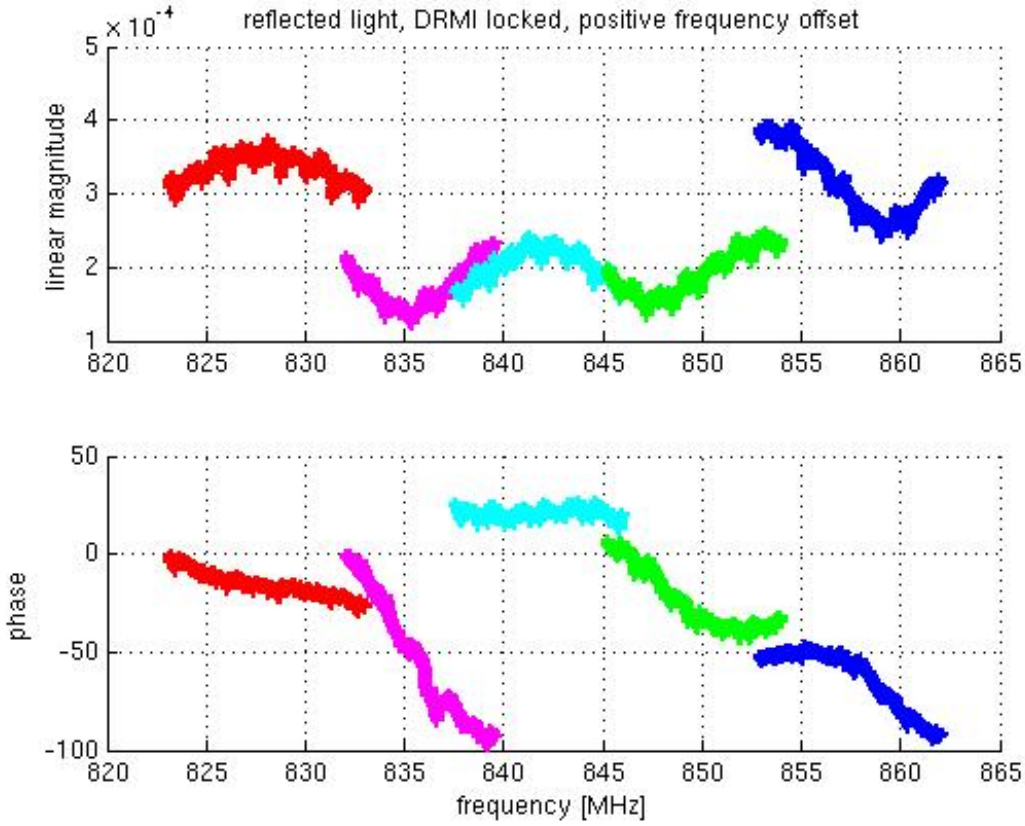

Fig. 3.19: A cavity scan of the locked DRMI. The different colored curves were measured one after another in separate frequency scans. The slow-timescale wander of the graphs is not well understood, but is believed to be due to slow drifts in the mirror alignment.

removed, but is not continuous from sweep to sweep, perhaps due to small changes in the alignment of the aux laser to the PSL over time.

The finesse of the SRC is low, which makes the sensitivity of theses measurements lower. It was difficult to get a clear picture of what was happening, due to slow drifts in the ASC, because so many mirrors are involved, as illustrated in Figure 3.19. While the length of the SRC was measured, we were not able to make sense of the HOM spacing to measure the Gouy phase. In chapter 4, we discuss a different method for measuring the Gouy phase which does not need a high Finesse cavity as a condition for a sensitive measurement.

3.7 Conclusion

This Chapter has discussed measurements aLIGO cavities using locked cavity techniques. This technique can be used to probe cavity length and mirror curvature. Measuring the resonant frequencies of the cavity is a powerful method for probing high-Finesse cavities with well-defined peaks.

Measurements of the LHO y-arm and the LLO IMC HOM shifts can be used to track the change in mirror ROCs over time, which can be used to infer the absorption characteristics of the optics. In these cases, this information was used to check the performance of the ETMy ring-heater, and to confirm that the current contamination control procedures are effective at protecting the optics during the opening of the vacuum chambers.

In the PRC measurements, the cavity parameters measured were as expected by the design. No further action was taken in these cases. For the Schnupp asymmetry measurement, the measured result was slightly different to the design, although not enough to impact the function of the interferometer.

The methods are limited by the sensitivity dependence on finesse, so they are more difficult to implement in low finesse cavities such as the SRC. The SRC length was measured to be 56.013 ± 0.0035m, which is 4.8 ± 3.5mm longer than the design SRC length of 56.008m. The results of the SRC length measurement were complicated by additional signal content that couldn't be easily explained by cavity models, casting the suspicion on the measurement that there may be systematic errors in the result. HOM peaks were not successfully resolved. A different technique to measure SRC Gouy phase is discussed in Chapter 4.

4. MEASURING THE RAY TRANSFER MATRIX OF THE SRC

This chapter explores an alternative method for measuring the round trip Gouy phase of the Signal Recycling Cavity. We apply the theory of ray-transfer matrices with the aim of directly measuring the round-trip ray transfer matrix of the cavity, which can then be used to calculate the Gouy phase. This technique was explored because the sensitivity of this measurement is not degraded by the low finesse of the SRC. Significant effort was deployed in developing this technique, and noise sources were suppressed. Unfortunately the measurement did not achieve the required sensitivity due to drifts in the multiple suspended components that could not be removed.

In this chapter, we first discuss the motivation for performing the SRC Gouy phase measurement at LHO (Section 4.1), which includes a simulation of possible values of the SRC Gouy phase. We present the theory underpinning this measurement in Section 4.2. Section 4.3 describes the experimental method. Section 4.4 presents the results, which did not achieve the required sensitivity for this measurement, so it is followed by Section 4.5, which covers sources of error, assumptions, and possible future measurements.

4.1 Motivation

The round-trip Gouy phase of a cavity is determined by the distance between the cavity optics and the radius of curvature of those optics. The round-trip Gouy phase of a cavity can be measured using the cavity scan technique described in Chapter 3, by measuring the frequency spacing of the HOM resonance peaks. This technique

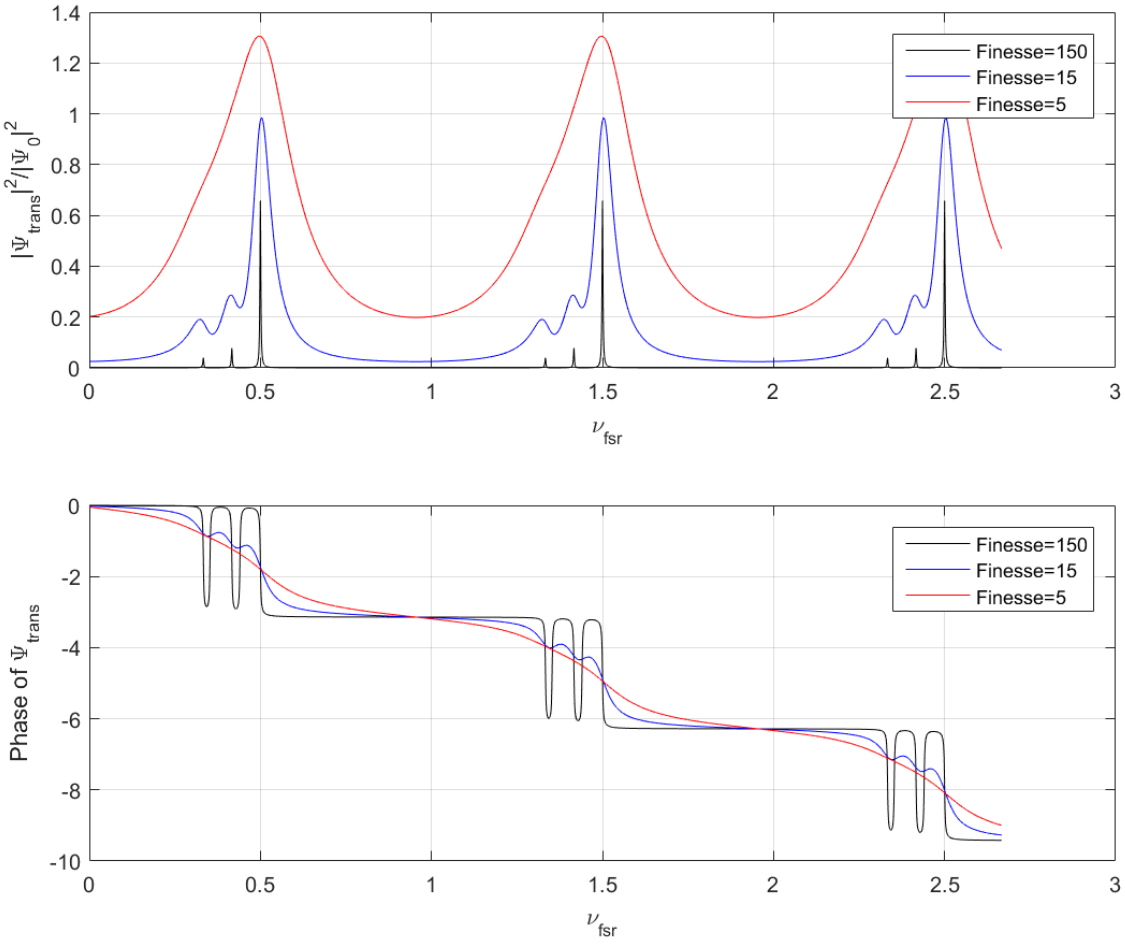

Fig. 4.1: Transmitted cavity transfer functions for three different cavities with Finesses of 150, 15, and 5. The transmission peaks for the 0^{th}, 1^{st} and 2^{nd} order modes are shown for cavity with a 30° Gouy phase. Note that the lower the cavity Finesse, the broader the peaks.

is commonly used to characterize cavities in gravitational wave interferometry, and yields a sensitive result for high-finesse cavities with sharp HOM peaks (see Figure 4.1). However, when the cavity finesse is low, the width of each resonance peak is broad which reduces sensitivity of the cavity scan technique(Figure 4.1). This technique ultimately fails when the width of each peak is broader than the spacing between the peaks, as illustrated in Figure 4.1. The LIGO SRC has a finesse of 13.5, so locked-cavity measurements of the SRC suffer from this issue. This chapter explores an alternative method for measuring the Gouy phase of a low-Finesse cavity.

The LHO SRC displays "mode-hopping" behavior, where it jumps from being

locked on the carrier 0^{th} order mode to the 1^{st} order mode[83]. Whenever a cavity does not behave as predicted, we consider the possibility that the as-built properties of the cavity may differ from the design values. In this case, the mode hopping problem that has been observed in the Hanford SRC has led to the question: *Could the SRC actually be unstable*? Although this scenario was assumed to be unlikely, we simulated what the cavity stability would be like at the extremes of the observed as-built tolerances in SRC optic positions and curvatures, in order to determine whether an unstable SRC was probable.

The stability criterion is expressed in terms of the half-trace of the SRC round trip ray transfer matrix and in terms of the half-trace of a cavity, as defined in Equations [54] and 4.1:

$$\text{Half-trace} \equiv \frac{A+D}{2} \tag{4.1}$$

$$\text{For a stable cavity:} \quad -1 \leq \frac{A+D}{2} \leq 1 \tag{4.2}$$

The round-trip Gouy phase can also be expressed in terms of the ray transfer matrix of the round-trip of the cavity:

$$\phi_{accumulated,roundtrip} = sgn(B).cos^{-1}(\frac{A+D}{2}) \tag{4.3}$$

Hence, if the measured the round-trip Gouy phase is different to the design value, this will show that the cavity stability will not be as expected.

4.1.1 Possible values for the SRC Gouy Phase

We performed a Monte Carlo simulation[84] of possible SRC cavity Gouy phases given the tolerances on the as-designed SRC optics. The Monte Carlo analysis was performed by modeling the path of the beam through the SRC using ray transfer matrices in the program aLaMode[85]. We started with a model of the as-designed

cavity, and adjusted the longitudinal position and the radius of curvature (ROC) of each mirror over the uncertainty in these parameters. We calculated the round-trip ray transfer matrix and the Gouy phase for the range possible SRC geometries. We used the round-trip ray transfer matrices to estimate the possible impact of variations in the cavity configuration on cavity stability.

The critical mirror parameters for determining the Gouy phase are the curvatures of the SR2 and SR3 mirrors, and the distance between these mirrors. For this simulation, the maximum ROC uncertainty was set to $\pm 1.5cm$ and length uncertainty between SR2 and SR3 was $\pm 1cm$. The uncertainty of $\pm 1.5cm$ on mirror curvature was chosen from correspondence with LIGO members Paul Fulda and Lisa Barsotti, although there is some speculation that the uncertainty may be even larger. The 1 cm uncertainty is the uncertainty we determined in the SRC length, as measured in Chapter 3.

The range of round-trip Gouy phase values calculated using this Monte-Carlo simulation is shown as a histogram in Figure 4.2. The model showed a large range of possible Gouy phase shifts; the mean Gouy phase was calculated to be 35.3°, the median 33.8°, and the standard deviation 8.3°.

This study showed it was possible, though somewhat unlikely, to have an unstable cavity given the uncertainties on the design cavity, as illustrated in Figure 4.3.

Given the observed mode hopping of the LHO SRC and the Monte-Carlo simulation of the SRC stability space, it seems plausible that the SRC is less stable that was intended in the design. The rest of this Chapter looks at measurements of the LHO SRC round-trip Gouy phase, which attempt to answer whether the Gouy phase is different to the design value of 37°.

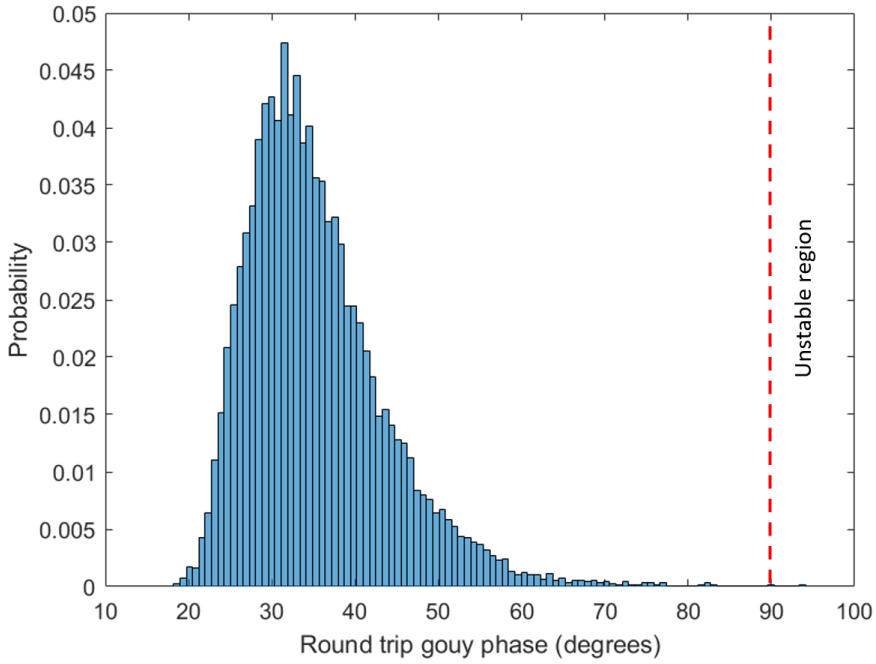

Fig. 4.2: Probability distribution of the SRC Gouy phase according to a Monte Carlo simulation of possible Gouy phases using the geometric uncertainties on the SRC optics. From this set of possible Gouy phase parameters, the mean Gouy phase was calculated to be 35.3°, the median 33.8°, and the standard deviation 8.3°.

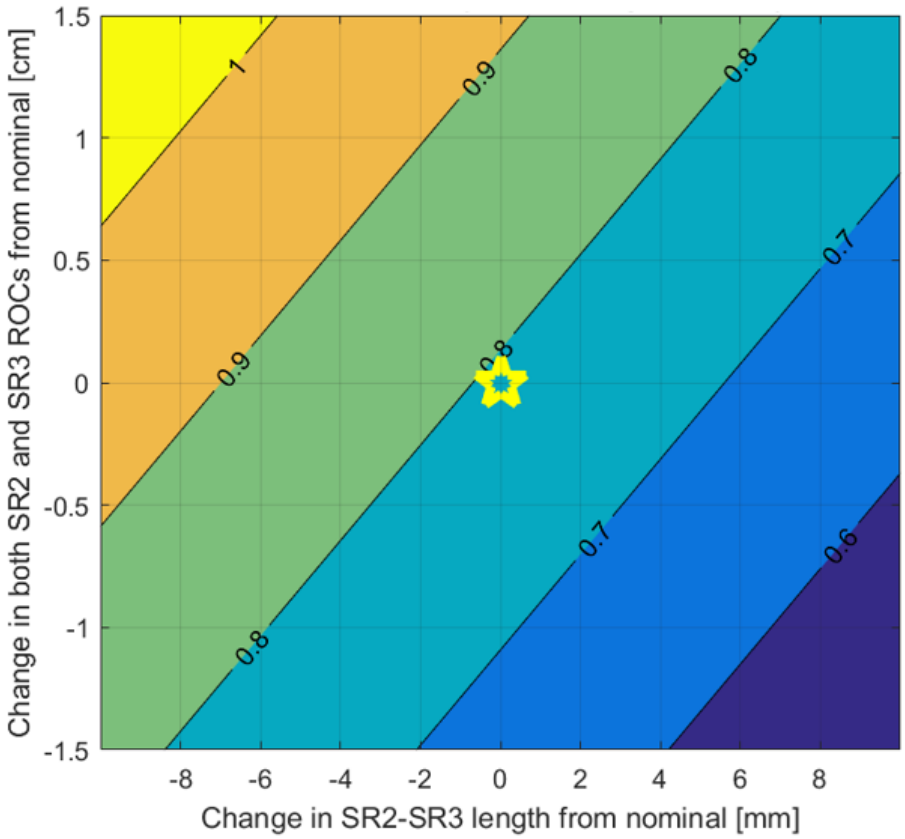

Fig. 4.3: Plot of possible half-traces of the SRC ray transfer matrix, across the parameter space of possible SRC length and SR2 and SR3 radii of curvature. A half-trace of above 1 means the cavity is unstable, and in the top left-hand corner of this map, the SRC could indeed potentially be in an unstable configuration. The star highlights the as-designed SRC geometry.

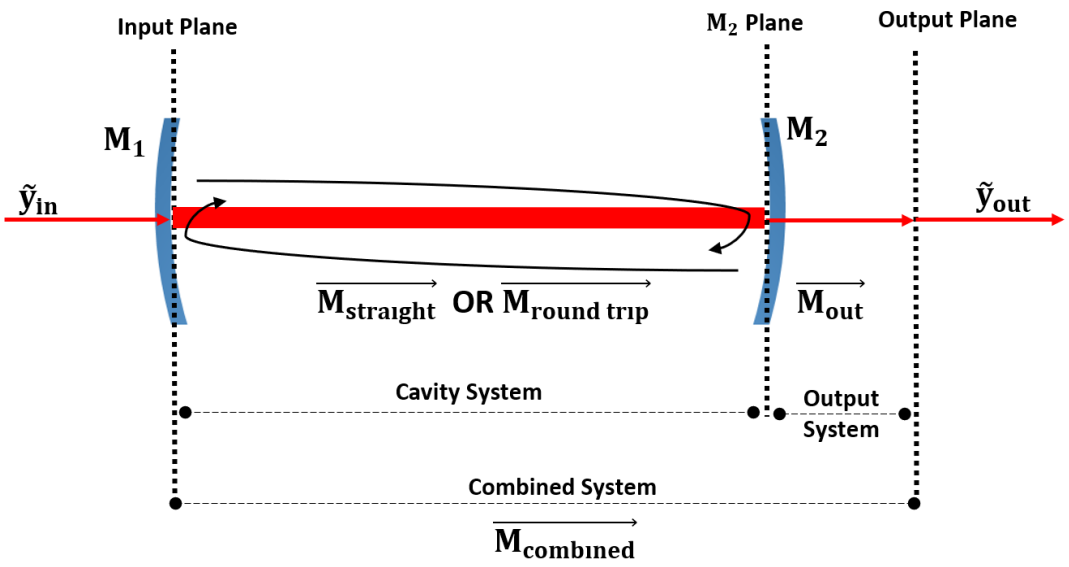

Fig. 4.4: The measurement layout for determining the round-trip ray transfer matrix of a cavity. The input plane lies on the M_1 mirror HR surface inside the cavity. The M_2 plane lies at the M_2 HR surface, just inside the cavity. Vectors $\tilde{y}_{in}$ and $\tilde{y}_{out}$ describe the beam geometry at the input and output planes, as defined in Section 2.2.1.

4.2 Theory: Measuring the Round-Trip Ray Transfer Matrix

Figure 4.4 shows the measurement layout. We define three optical planes, the "input" plane, the "M_2" plane, and the "output" plane, which form the boundaries of two optical systems. The "cavity" system consists of a cavity defined by end mirrors M_1 and M_2. The input plane lies just inside this cavity at the surface of M_1. The M_2 plane lies inside the cavity just at the surface of M_2. We define two optical paths a beam may take through the cavity system: the straight path $\mathbf{M}_{straight}$ which starts at the input plane and travels once through the cavity system to the M_2 plane, and the round-trip path $\mathbf{M}_{roundtrip}$ which starts at M_1 and travels through the cavity system to the M_2 plane, is reflected from M_2, travels back through the cavity system, and is reflected at M_1 to finish back at the input plane. The "output" system begins at the M_2 plane and ends at the output plane, and has ray transfer matrix $\mathbf{M}_{out}$.

In the case of the aLIGO SRC, there is no access to the beam coming directly

out of the cavity before it travels through the output system, and $\mathbf{M}_{out}$ is not well know. So only the transfer matrix of the combined system, $\mathbf{M}_{combined}$, can be directly measured. To determine $\mathbf{M}_{combined}$, we apply a known change to $\tilde{y}_{in}$ and measure the change to $\tilde{y}_{out}$, then recalling Section 2.2.1:

$$\Delta\tilde{y}_{out} = \begin{bmatrix} \Delta y_{out} \\ \Delta\theta_{out} \end{bmatrix} = \mathbf{M}_{combined}\Delta\tilde{y}_{in} = \mathbf{M}_{combined} \begin{bmatrix} \Delta y_{in} \\ \Delta\theta_{in} \end{bmatrix} \tag{4.4}$$

Ultimately we wish to determine $\mathbf{M}_{roundtrip}$. But in order to calculate $\mathbf{M}_{roundtrip}$ from $\mathbf{M}_{combined}$ when $\mathbf{M}_{output}$ is not well known, we must consider two paths a beam may take through the combined system: the "single passed" and the "double passed" paths: $\mathbf{M}_{combined,single}$ and $\mathbf{M}_{combined,double}$, where:

$$\mathbf{M}_{combined,single} = \mathbf{M}_{out}\mathbf{M}_{straight} \tag{4.5}$$

and

$$\mathbf{M}_{combined,double} = \mathbf{M}_{out}\mathbf{M}_{straight}\mathbf{M}_{roundtrip} \tag{4.6}$$

It is possible to measure $\mathbf{M}_{combined,single}$ and $\mathbf{M}_{combined,double}$ independently, by separating the single-passed and double-passed beams at the output plane and measuring $\tilde{y}_{out,single}$ and $\tilde{y}_{out,double}$. This is done by slightly misaligning one of the optics in the cavity system, as illustrated in Figure 4.5. Then:

$$\Delta\tilde{y}_{out,single} = \mathbf{M}_{combined,single}\Delta\tilde{y}_{in} = \mathbf{M}_{out}\mathbf{M}_{straight}\Delta\tilde{y}_{in} \tag{4.7}$$

$$\Delta\tilde{y}_{out,double} = \mathbf{M}_{combined,double}\Delta\tilde{y}_{in} = \mathbf{M}_{out}\mathbf{M}_{straight}\mathbf{M}_{roundtrip}\Delta\tilde{y}_{in} \tag{4.8}$$

and:

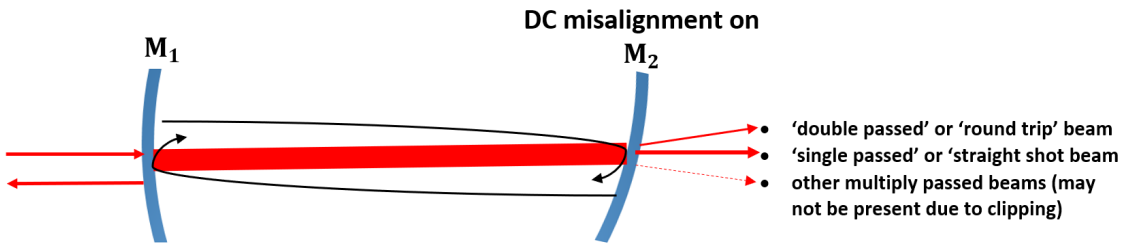

Fig. 4.5: An illustration of the splitting of the single trip and double-passed (or round-trip) beams which occurs when M_2 is misaligned. The split beams the pattern which can be viewed on a camera (assuming a large enough camera and mirrors that no clipping occurred.) The numbers refer to the number of round trips made by the beam before exiting the cavity. The beam becomes fainter after each round-trip through the cavity.

$$\mathbf{M}_{roundtrip} = (\mathbf{M}_{out}\mathbf{M}_{straight})^{-1}(\mathbf{M}_{out}\mathbf{M}_{straight})\mathbf{M}_{roundtrip} = \mathbf{M}^{-1}_{combined,single}\mathbf{M}_{combined,double} \tag{4.9}$$

Finally, $\mathbf{M}_{roundtrip}$ is used to calculated the round-trip Gouy phase using Equation 4.3.

4.2.1 Applying this Method to the SRC

Figure 4.6 shows the layout of the experiment in the SRC. M_1 is the Beam Splitter (BS) and M_2 is the Signal Recycling Mirror (SRM). The input plane sits at the HR surface of the BS and the output plane sits at the HR surface of the SRM. The PR2 optic, which we have named M_0), may be misaligned to introduce an angular misalignment of the beam at the BS. We introduce another ray transfer matrix, $\mathbf{M}_{in}$, which describes the beam path from the PR2 (M_0)) to the BS (M_1))

While the SRC includes both ITMs, we will only consider the "SRy" cavity here, which is formed when the ITMx is misaligned. The difference in accumulated Gouy phase change from the BS to the HR surface of ITMy (0.33°) is practically identical to the accumulated Gouy phase change from the BS HR surface through to the HR

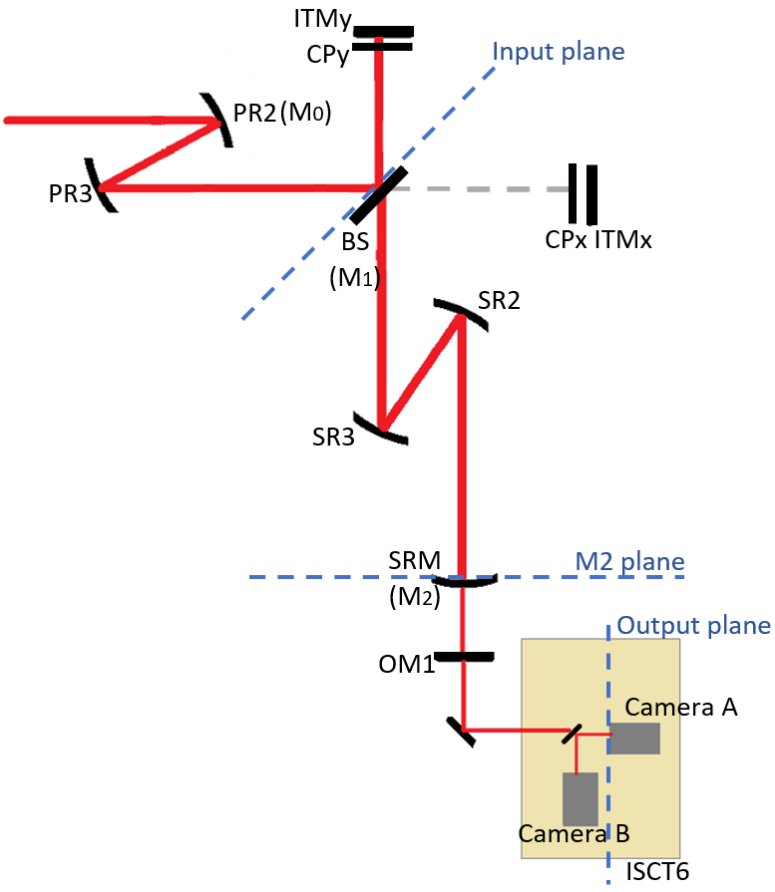

Fig. 4.6: Layout for determining the Gouy phase of the SRC.

surface of ITMx to within 1x10^{-6} degrees. The ETMs were totally misaligned during this experiment, to prevent any additional confusing back reflections.

A beam traveling the $\mathbf{M}_{straight}$ path begins at the reflection from the BS HR surface, travels through the compensation plate and the ITMy substrate to be reflected from the ITMy HR surface, travels back through the ITMy and compensation plate, through the BS, is reflected by the SR3 and SR2 optics, to the SRM HR surface. A beam following the $\mathbf{M}_{roundtrip}$ path follows this same path and is reflected from the SRM HR surface, is reflected by the SR2 and SR3 again, and travels through the BS to the BS HR surface. $\mathbf{M}_{out}$ starts at the front surface of the SRM, includes the transmission through the SRM, through the Output Mode cleaner optic OM1, and the propagation of the beam to the output plane. The output plane is located on

in-air table ISCT6.

The PSL was used as the probe beam. A probe beam might have been introduced into the SRC from the output side, except that at the time this measurement was performed, there was an output Faraday after the SRC which prevents light from being injected in the opposite direction. (This path is now available as modifications have been made to this path with the introduction of squeezing at LIGO Hanford.)

A change in the input beam position and angle $\Delta\tilde{y}_{in}$ can be applied by changing the angular alignment of an optic upstream of the cavity (recall Section 2.2.2). We misaligned the BS and the PR2 optics in separate measurements to introduce a change in $\tilde{y}_{in}$. If the PR2 is misaligned through angle θ_{PR2}, then:

$$\Delta\tilde{y}_{in,PR2} = M_{in} \begin{bmatrix} 0 \\ 2\theta_{PR2} \end{bmatrix} \tag{4.10}$$

Alternatively, the BS may be misaligned to find elements B and D of $M_{combined}$. This avoids introducing any uncertainty from M_{in} to these elements. In this case:

$$\Delta\tilde{y}_{in,BS} = \begin{bmatrix} 0 \\ 2\theta_{BS} \end{bmatrix} \tag{4.11}$$

The single-trip and round-trip beams were split within the SRC by misaligning a mirror inside the SRC. As the M_2 optic, the SRM, is only 68% reflective, the single-passed beam will appear brighter than the double-passed beam on the cameras. Note that other, even dimmer beams for the third-pass and higher passes would also be present, although these beams will be extremely dim and are not considered here.

$\Delta\tilde{y}_{out}$ was measured using two cameras located at the output plane on the in-air table ISCT6, as illustrated in 4.7. "Camera A" and "Camera B" were placed at distances l_a and l_b from a beam-splitter that separates the beam onto the two cameras, so that the effective camera separation is $L = l_a - l_b$. The change in beam

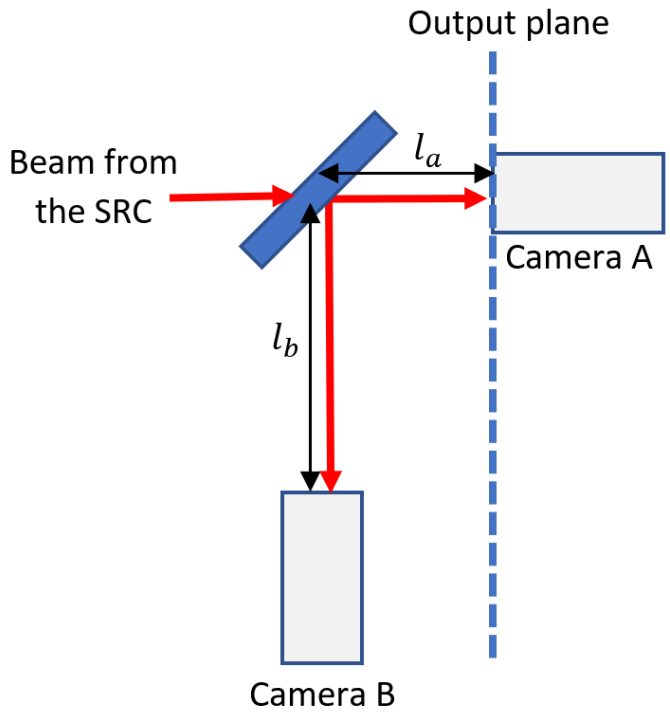

Fig. 4.7: The two cameras which measure the beam motion, and their locations relative to the output plane which defines the end of $\mathbf{M_{out}}$. The distance from the beam splitter to camera A is l_a and to camera B is l_b. The difference in camera locations is defined as $L = l_b - l_a$.

position Δy_{CAM_B} on camera B is related to the change in beam position on camera A Δy_{CAM_A} by:

$$\begin{bmatrix} \Delta y_{CAM\_B} \\ \Delta\theta_{CAM\_B} \end{bmatrix} = \begin{bmatrix} 1 & L \\ 0 & 1 \end{bmatrix} \begin{bmatrix} \Delta y_{CAM\_A} \\ \Delta\theta_{CAM\_A} \end{bmatrix} \tag{4.12}$$

So:

$$\Delta\tilde{y}_{out} = \begin{bmatrix} \Delta y_{CAM\_A} \\ \Delta\theta_{CAM\_A} \end{bmatrix} = \begin{bmatrix} \Delta y_A \\ \frac{\Delta y_{CAM\_B} - \Delta y_{CAM\_A}}{L} \end{bmatrix} \tag{4.13}$$

4.3 Experimental Method

The steps taken to perform this measurement were:

1. Separate the straight-shot and round-trip beams on the cameras by very slightly mis-aligning ITMy.
2. Introduce an angular misalignment θ_{PR2} or θ_{BS} at the input of the cavity. Both DC and an AC angular misalignments were tried.
3. Measure the output beam motion Δy_A and Δy_B on Cameras A and B.
4. Calculate $\mathbf{M}_{roundtrip}$ and the SRC Gouy phase.

These steps will be described in detail in this section.

4.3.1 Separating the Straight-Shot and Round-Trip Beams within the SRC

The single-trip and round-trip beams paths were separated slightly so that they could be resolved individually on the cameras at the SRC output by misaligning the ITMy slightly. The straight shot beam is much brighter than the round-trip beam due to the 68% reflective SRM. It was necessary to separate the beams on the cameras by at least a few beam widths in order to prevent severe interference fringes appearing between the two beams. Figures 4.8 and shows 4.9 examples of the fringes that appear when the beams are not and are adequately separated.

4.3.2 Introducing an Angular Misalignment to the Input Beam

In the LIGO corner station, the PR2 optic was used as the M_0 actuator to introduce angular misalignment $\Delta\theta_{M_0}$ and the BS optic was used as the M_1 actuator to produce $\Delta\theta_{M_1}$. The PR3 cannot be used as M_0 as it is not sufficiently separated in Gouy phase to produce much beam motion on the BS when it is misaligned. The optics were misaligned by tens of micro-radians for the measurements. The exact angles of misalignment were chosen so that clipping did not occur on any of the optics within the combined system. Both DC and AC misalignments of the input optics were

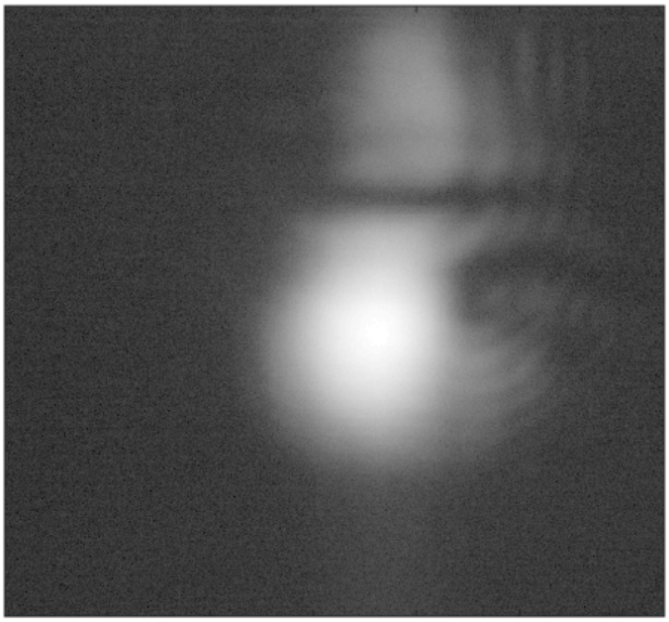

Fig. 4.8: An example image of beam interference when the beams are improperly separated. The beam-shapes are not round and there are large interference fringes between the two beams.

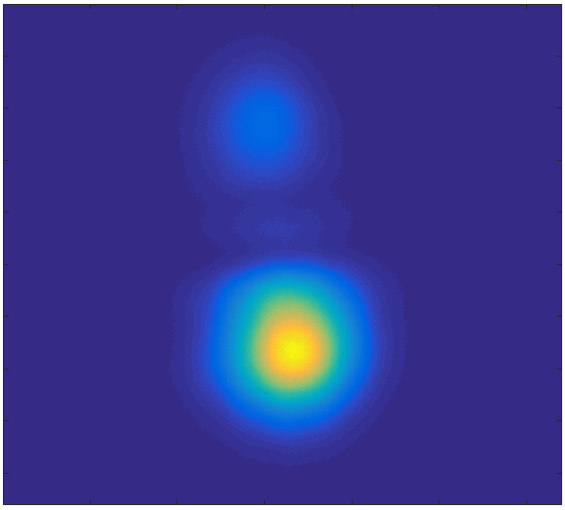

(a) Camera image

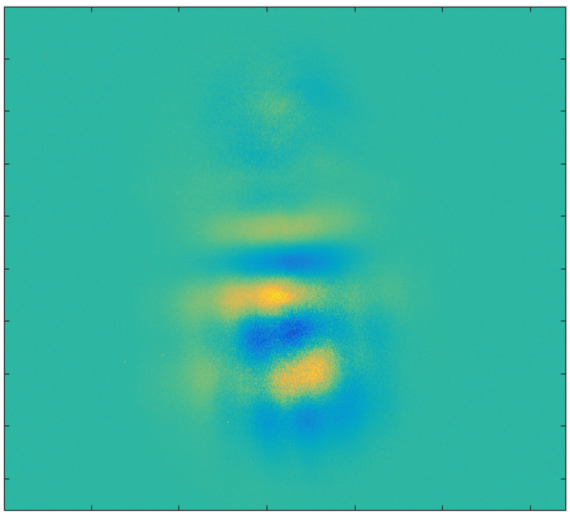

(b) Difference between the original image and two separately fitted gaussian beam profiles

Fig. 4.9: Two beams, and the residuals once the gaussian beam fit is subtracted from the original image which shows the interference between the two beams. In contrast to Figure 4.8, the beams are round and interference fringes are minimal.

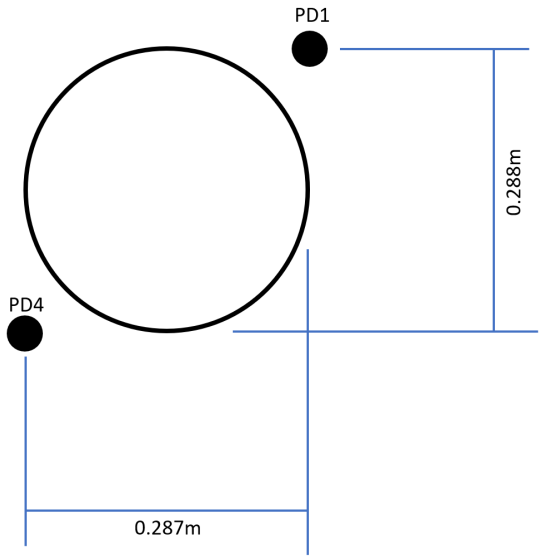

Fig. 4.10: Diagram of the ETMx baffle, showing the locations of the two baffle photodiodes which point look towards the ITM along the 4km arm.

explored.

4.3.3 Checking the Suspension Calibration

The PR2 and BS optics are suspended on pendulum suspensions and the angular position is controlled by electronic actuators. The PR2 and the BS suspensions must be calibrated to determine the angle the optic moves through for one voltage count on the suspension actuator. We checked the suspension calibrations by measuring the angular motion required to direct the PSL beam at the X-end station from it's usual location at the center of the ETMx to the baffle photodiodes. The two baffle photo diodes are located on the ETMx baffle, as illustrated on the baffle schematic in Figure 4.10. The baffle photodiode locations are separated by 0.288 m in the vertical direction, and by 0.287 m in the horizontal direction[86].

For this measurement, the PRM, SRM, ITMs, ETMs and TMS optics were misaligned to prevent flashes from other optics from corrupting the baffle PD signal. We moved the BS and PR2 optics one at a time to direct the PSL beam onto a baffle PD, then we moved the optic around and mapped out optic angle vs baffle PD intensity,

BS slider location	Pitch [counts]	Yaw [counts]
PD1	-329.4 ± 0.1	186.3 ± 0.1
PD2	-294.4 ± 0.2	150.7 ± 0.2
Difference	-35.00 ± 0.3	-35.6 ± 0.3

Tab. 4.1: The BS slider locations required to direct the PSL beam onto ETMy baffle PD1 and PD2, and the difference in slider locations.

PR2 slider location	Pitch [counts]	Yaw [counts]
PD1	4435 ± 1	1692 ± 1
PD2	4159 ± 2	1948 ± 2
Difference	294 ± 3	-256 ± 3

Tab. 4.2: The PR2 slider locations required to direct the PSL beam onto ETMy baffle PD1 and PD2, and the difference in slider locations.

as illustrated for the BS in Figures 4.11. A gaussian curve was fitted to this map to determine the actuator voltage required to center the PSL beam onto each baffle PD. Figure 4.12 illustrates an example of this fit for beam splitter angle vs intensity on PD1.

The alignment sliders showed the following deviation moving from one baffle PD to the other when fitted to the brightest position on the slider as listed in Tables 4.1 and 4.2. We assumed that the as-built curvatures of these optics and the lengths of the PRC, Michelson and arm cavities match the design values- which was previously verified through the PRC Gouy phase, length and arm length measurements, as summarized in Table 4.3.

The angular misalignment of the BS or PR2 required to direct the PSL beam onto the ETMy baffle photodiodes can be calculated using ray transfer matrices $\mathbf{M_{BS-to-ETMy}}$ and $\mathbf{M_{PR2-to-ETMy}}$, which describe the beam, path from the BS High-Reflectivity (HR) surface, through the ITMx compensation plate (CPx) and ITMx, to the ETM, and the path from the PR2 to PRM and then through the BS,

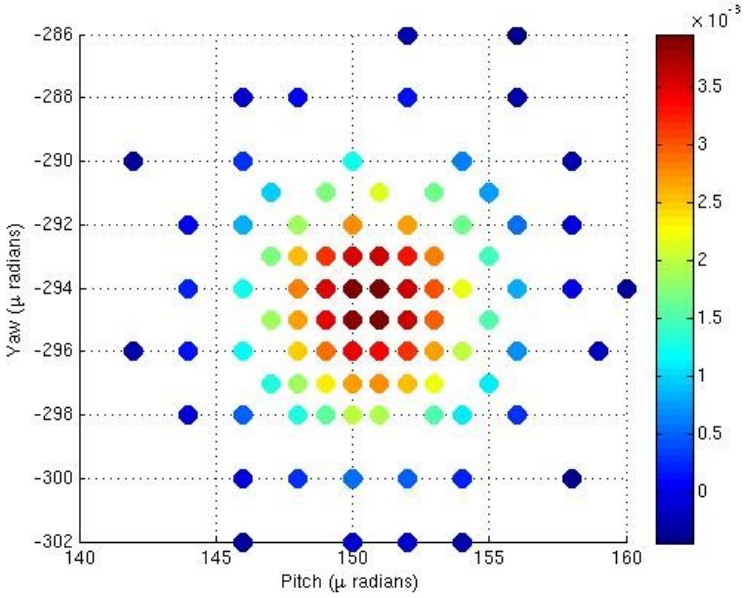

(a) Intensity (in arbitrary counts) vs BS angle (μrad) pitch and yaw on ETMx PD1

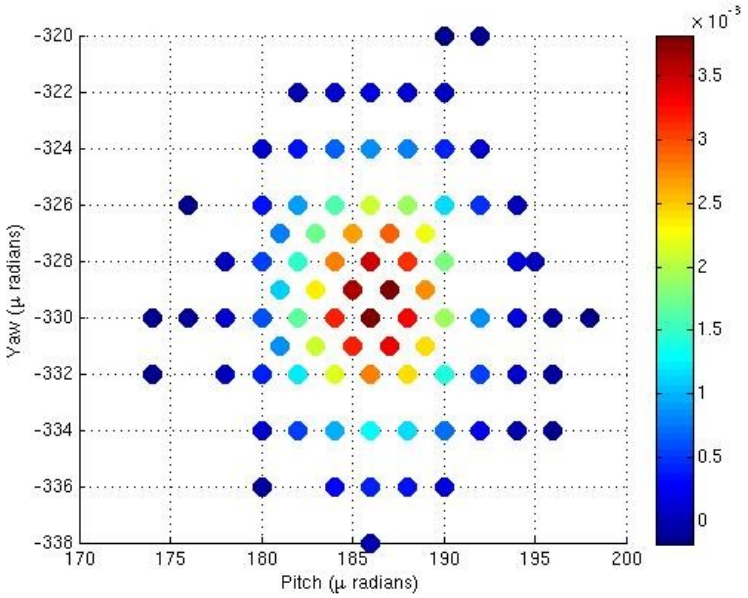

(b) Intensity (in arbitrary counts) vs BS angle pitch and yaw (μrad) on ETMx PD4

Fig. 4.11: Intensity of the beam scanned across baffle vs angular position of Beam-Splitter. The beam is centered on each photo diode at the angle where the intensity is maximized.

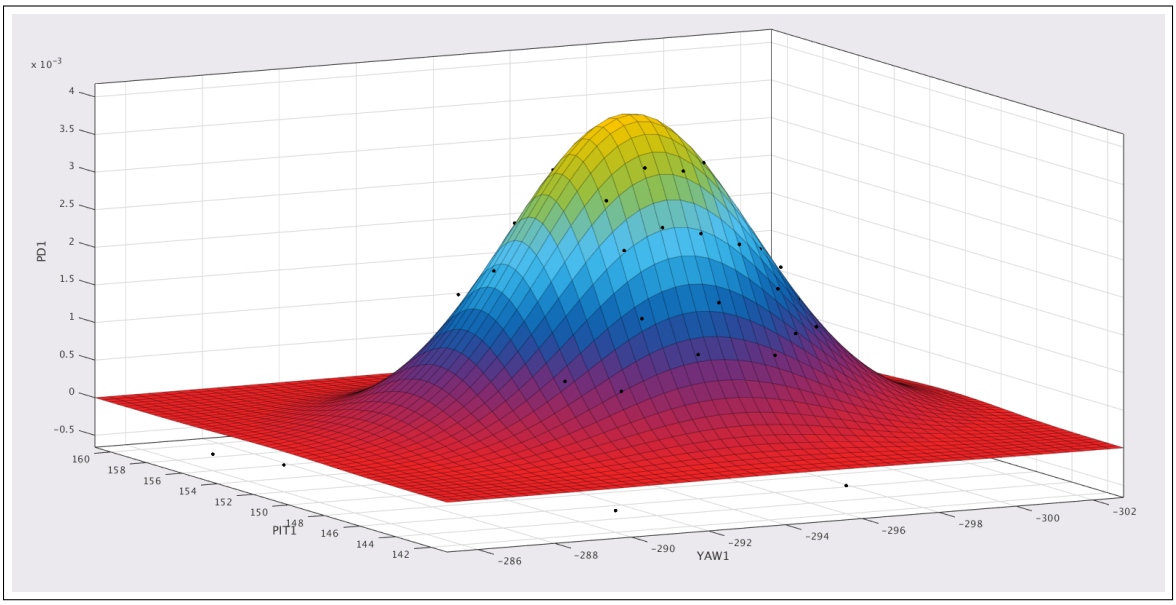

Fig. 4.12: PD intensity vs BS location for ETMx baffle PD1, with a fitted gaussian distribution. The gaussian fit is used to determine the optic angle where the light intensity is maximized on the baffle photodiode.

Optical Element	Distance from previous element [m]	Curvature [m]
PR2	0	-4.54
PR3	16.16	36.02
BS HR	19.54	inf
BS AR	68.5e-3	inf
CP side 1	4.83	inf
CP side 2	100e-3	inf
ITMy side 2	20e-3	inf
ITMy side 1	200e-3	1939.20
ETMy optic	3999.7	2238.90

Tab. 4.3: Parameters used to calculate the path from the PR2 and BS optics to the ETMy baffle

CPx and ITMx to the ETMx respectively .

$$\mathbf{M_{BS-to-ETMy}} = \begin{bmatrix} 0.07409 & 3999.8 \\ -0.0001653 & 4.572 \end{bmatrix} \tag{4.14}$$

$$\mathbf{M_{PR2-to-ETMy}} = \begin{bmatrix} -222.09 & 411.73 \\ -0.055430 & 0.09827 \end{bmatrix} \tag{4.15}$$

The BS must be misaligned in the horizontal by 35.921μradians and in the vertical by 35.971μradians to move the PSL beam at the ETMy from one baffle PD to the other, calculated using:

$$\delta\theta_{BS} = \frac{d}{2B_{BS-to-ETMy}} \tag{4.16}$$

where $d_x = 0.28735$m is the horizontal separation between the two baffles and $d_y = 0.28776$m is the vertical separation between the two baffles. This required BS movements of 35.0 counts and 35.6 counts on the horizontal and vertical BS alignment sliders.

Similarly, according to:

$$\delta\theta_{PR2} = \frac{d}{2B_{PR2-to-ETMy}} \tag{4.17}$$

the PR2 must be misaligned by $\delta\theta_{PR2}$ =348.95 μrad in the horizontal and 349.45 μrad in the vertical to move the PSL beam at the ETMy from one baffle PD to the other.

This required PR2 movements of 256 counts and 294 counts on the horizontal and vertical PR2 alignment sliders. The correction factors is for BS and PR2 alignment are summarised in Table 4.4.

Optic	Horizontal correction factor $\frac{\mu rad}{counts}$	Vertical correction factor $\frac{\mu rad}{counts}$
BS	1.026	1.010
PR2	1.36	1.189

Tab. 4.4: Correction factors measured for BS and PR2 sliders, used to convert from slider counts to μrad

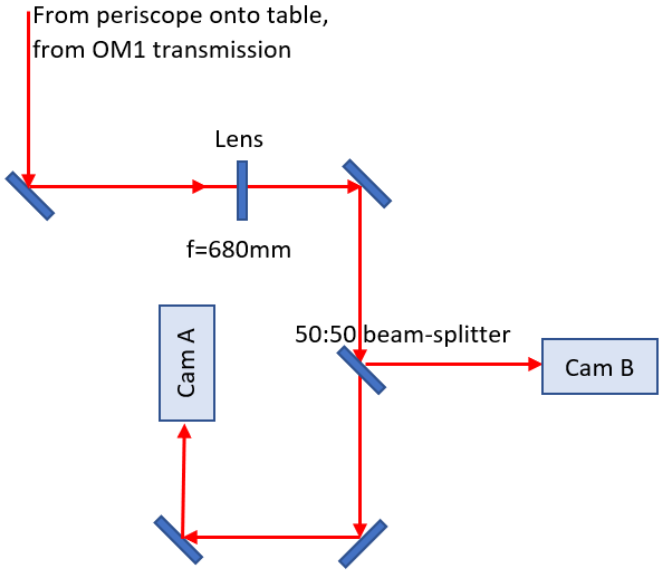

Fig. 4.13: The camera set-up on in-air Table "ISTC6". The beam is picked off from transmission through the Output mode Cleaner optic OM1 after leaving the SRC through the SRM.

4.3.4 Measuring $\tilde{y}_{out}$

The beam motion at the output plane was measured with two Basler Gige 100M cameras placed on the in-air table named "ISCT6" (Figure 4.13). This beam is picked off from the carrier beam after it leaves the SRC, as it is the transmitted beam through the OM1 optic in the Output Mode Cleaner (OMC).

The size and location of the beam waist on ISCT6 was measured using a nano-scan beam profiler to take images of the beam shape, and then then fitted to a gaussian beam profile (Figure 4.14). The two cameras were placed 0.33 ± 0.05cm apart on either side of the beam waist. The cameras needed to be positioned close enough to the beam waist on the table so that the beams were small enough that their motion

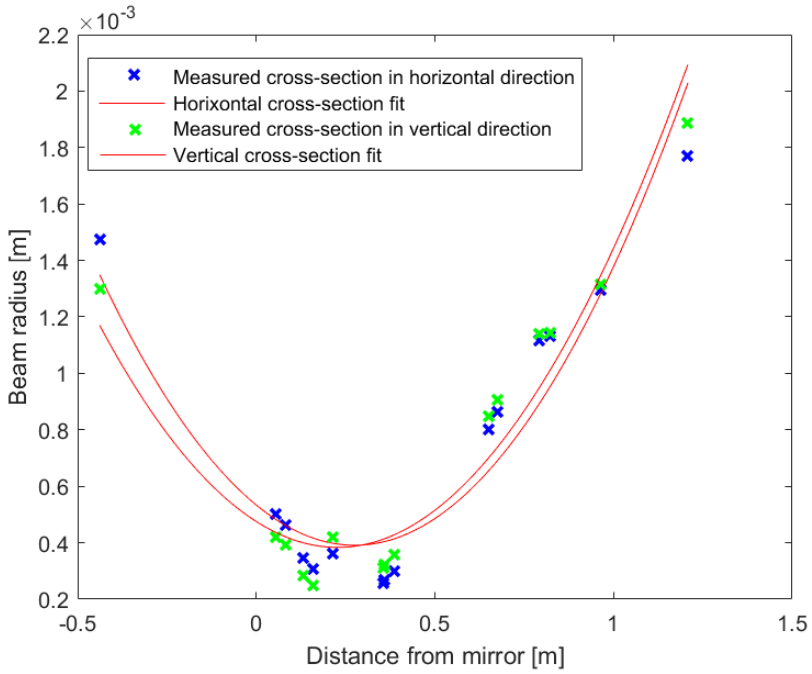

Fig. 4.14: Measurement of the beam size on in-air table ISCT6. The x axis shows the distance from the beam-splitter on ISCT6.The locations of cameras A and B were chosen to sit on either side of the beam waist.

is well captured on both cameras without clipping, while being separated as far apart in Gouy phase as possible.

Once images of the beam motion were captured by the cameras, the centroid of each beam was determined for each image by fitting a gaussian beam shape, including terms for ellipticity and tilt of the beam, to both beams. Figure 4.9 shows the appropriateness of the fit, illustrating the difference between the fit and the the fit from the original image.

4.3.5 Gouy Phase Calculation

The centroid location vs optic misalignment was plotted, and this was used to calculate the ray transfer matrices for the single-passed and double-passed beam paths. Examples of this are shown in Figure 4.15. The plot of centroid location vs optic misalignment showed a linear and a non-linear region. The non-linear region was

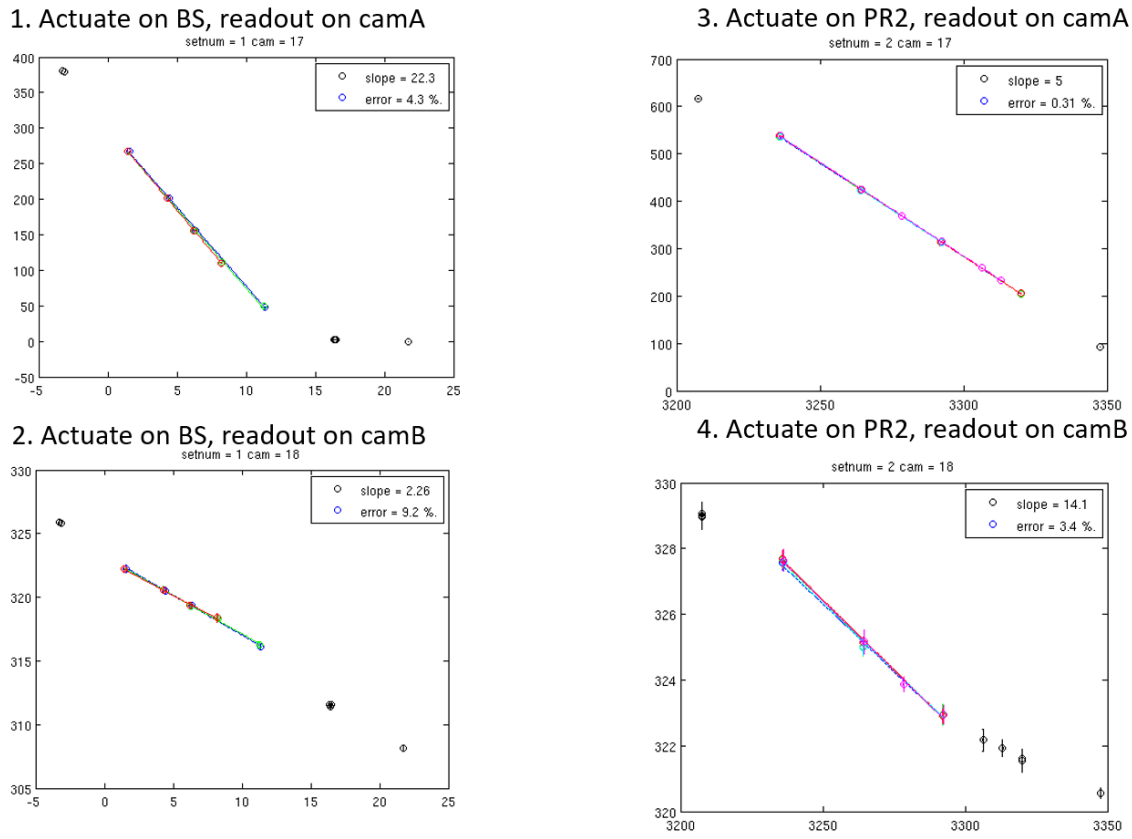

Fig. 4.15: Slopes for various single-bounce measurements

where clipping of the beam or non-linear behavior of the suspension actuator was occurring, these points were discounted.

The centroid location vs suspension alignment was plotted and a line was fit to the curve. Each measurement was performed multiple times allowing us to calculate the error in the slope. These values for beam motion vs optic location were used to calculate the ray transfer matrix and Gouy phase of the SRC.

4.4 Results

Two measurements were performed of the round-trip ray transfer matrix and Gouy phase of the SRC, one where DC motions of the BS and PR2 optics are used to produce the misalignments to the input beam, and one where AC motions are used. In both

measurements, the uncertainty on optic misalignment was too large to ultimately give a useful result, due to slow drifts on the unlocked suspensions. Nevertheless, the results and error analyses are summarized here.

4.4.1 DC measurement of the SRC ray transfer matrix

For this measurement, the BS was moved in increments of 0.5 to 5 μ radians and the PR2 was moved in increments of 5 to 20 μ radians, in order to move each beam across the face of each camera. We stepped the suspension alignment slider value using a script to control the suspension motion, resting at each step for 60s. The distance between the two cameras was $L = 0.16$m.

Images were taken on each camera and the centroid of both spot locations was calculated for each frame by fitting a gaussian beam to each frame, as in Figure 4.9. The camera centroids were calculated for each individual frame and then averaged over the 60s time frame of each suspension position. The entire measurement was performed multiple times in order to assess the repeatability of the measurement.

The average centroid location vs optic misalignment angle is plotted in Figure 4.16 for each beam actuated by each optic on each camera (a total of 8 plots). In the region where no clipping occurred, these plots are linear. The non-linear regions of the plots are due to beams clipping on the camera or SRC optics, and these regions were disregarded during further analysis. We fit a line to the linear region of each plot, to calculate the ratio of beam movement to optic misalignment in each of the eight cases, as are summarized in Table 4.5.

The measurement was performed multiple times, and in some cases the slope had changed, which we attribute to slow drifts in the suspension, as the cavities involved were aligned but not locked. Some of the slopes have much bigger errors than others, such as the double-passed beam motion when the BS is misaligned. This is a clipping issue either on the cameras or within the SRC, which meant that the suspensions

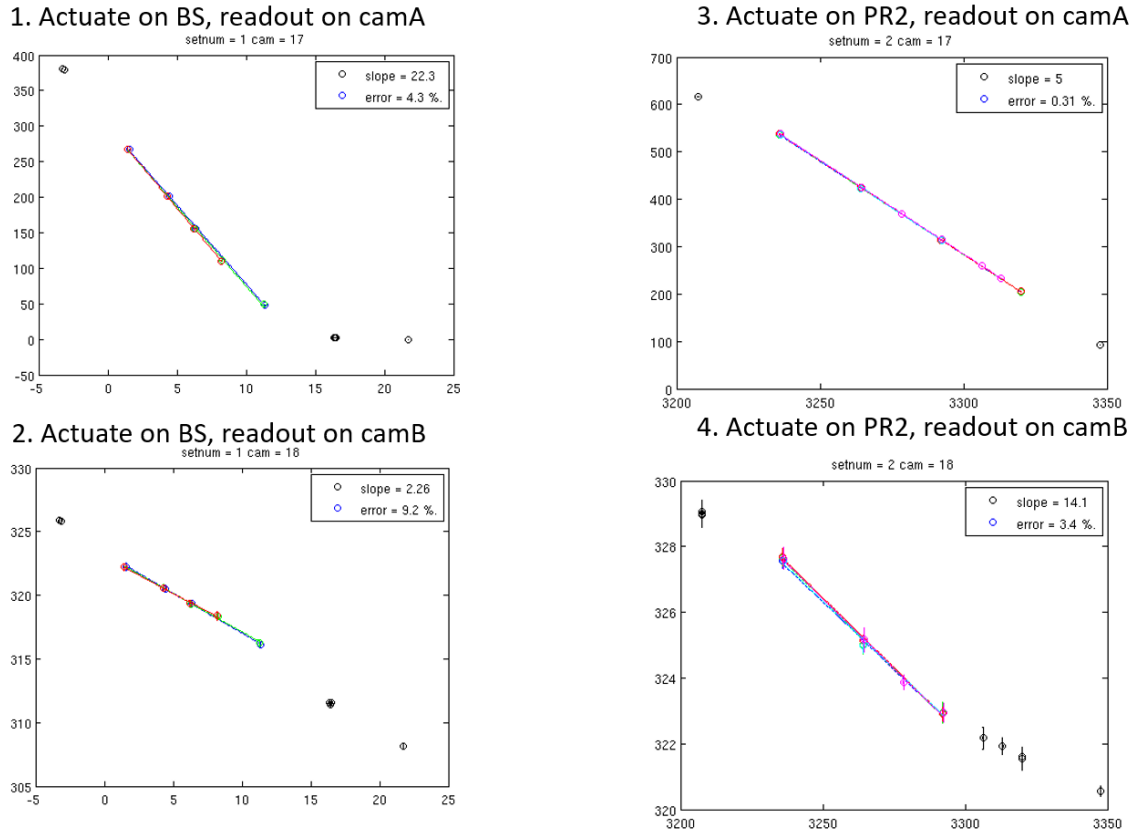

(a) Straight shot slopes and fits, for multiple measurements taken over different days

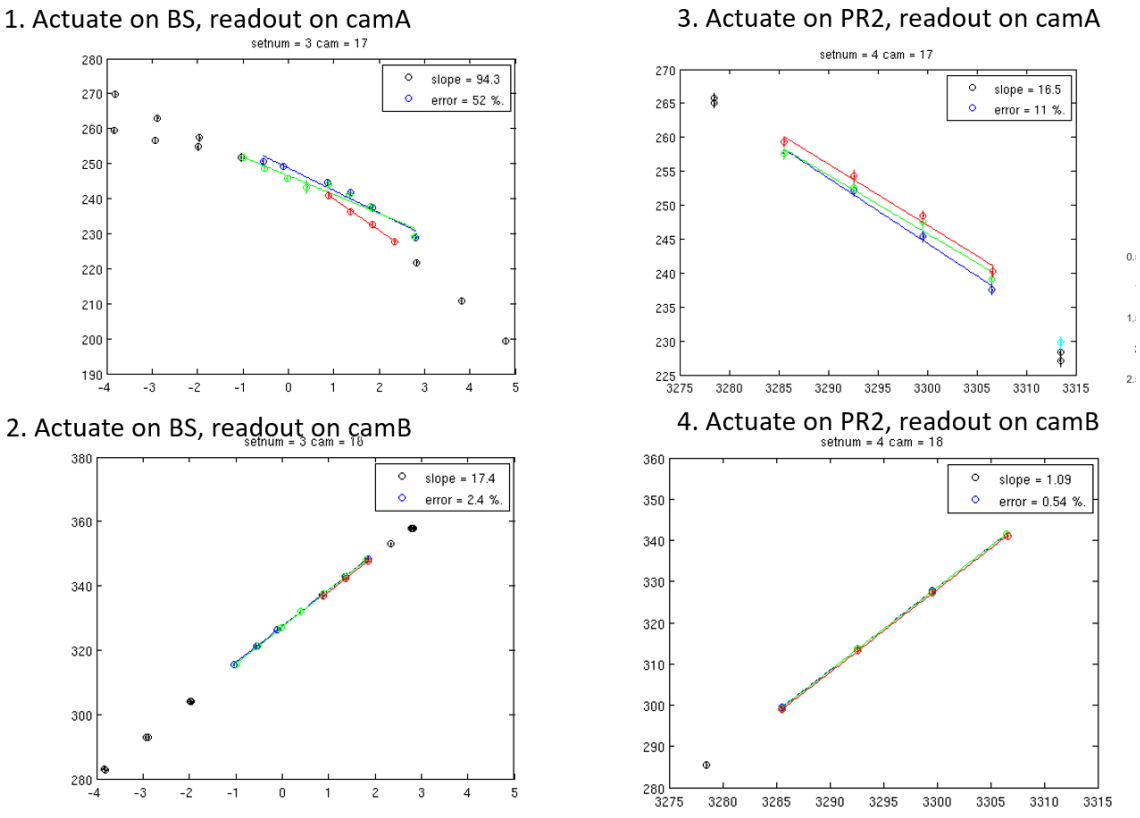

(b) Double-passed slopes and fits, for multiple measurements taken over different days

Fig. 4.16: Slopes for various measurements

Optic	Path	Movement of centroid on camera A [pixels] per μ rad suspension motion	Movement of centroid on camera B [pixels] per μ rad suspension motion
BS	single-pass	2.26 ± 9.2%	22.3 ±4.3%
PR2	single-pass	14.1 ± 3.4%	5 ± 0.31%
BS	double-pass	17.4 ± 2.4%	94.3 ± 52 %
PR2	double pass	16.5 ± 0.54%	16.5 ± 11%

Tab. 4.5: Summary of slopes and errors

could not move through such a large angle before clipping occurred. The beam is quite large in the SRC compared to the size of the optics, which limits the accuracy of this method.

$\mathbf{M_{in}}$ was calculated from the design values for the LHO PRC (which have agreed well with measured values, as shown in Chapter 3):

$$\mathbf{M_{in}} = \begin{bmatrix} -0.0848 & 18.17 \\ -0.0555 & 0.103 \end{bmatrix} \tag{4.18}$$

Using the equations derived in Section 4.2.1, $\mathbf{M_{round-trip}}$ was calculated as:

$$\mathbf{M_{round\_trip}} = \mathbf{M_{SRC}} = \begin{bmatrix} -144 & 3097 \\ 48 & 1047 \end{bmatrix} \tag{4.19}$$

and the Gouy phase was calculated as $\phi_{gouy,round-trip} = 0.0 - 520i^{\circ}$. Clearly this result is non-nonsensical. Looking at the error analysis, the errors on the beam locations are far too large which is the reason for the imaginary result. It is believed long term drifts in the suspensions hamper this method, especially because the cavity is unlocked, so the mirror suspensions are not under active alignment control. The error analysis in Section 4.4.2 shows that the uncertainty in the centroid locations, which is impacted by optic alignment, limits the precision of the Gouy phase measurement.

4.4.2 Error analysis

In order to reduce the uncertainty on the fitted slopes which reduces the uncertainty in the Gouy phase, we retook the measurement with an AC dither. Our Monte Carlo simulation indicates that if each slope had an uncertainty <0.2%, we would reduce the uncertainty in the Gouy phase measurement to <6%, which is less than the uncertainty on the SRC Gouy phase due to uncertainties in the optic locations and ROC of about 8%.

After the Gouy phase was calculated, the errors on the slopes and the distance between the two cameras were added using a Monte Carlo simulation to estimate the error on the Gouy phase result. The errors used for this calculation were the errors in the slopes summarized in Table 4.5 and 0.01m for the distance between the cameras. The results of this analysis are shown in Figure 4.17. We constructed the ray transfer matrix of the SRC system with a nominal Gouy phase and output path using the ray tracing program A La Mode[85]. This model is used to calculate the spot motion on the cameras as the mirrors in this system are misaligned. Errors on spot motion and suspension calibration were added to the model.

This showed that with slope errors of 0.5-50% for the DC measurement, the error on the measurement of the SRC gouy phase, shown in Figure 4.17, is significantly higher than the error on a Monte Carlo estimation from the as built parameters of the cavity, as shown in Figure 4.2. If all slope errors were reduced to 0.2%, the measurement uncertainty would be low enough to be useful. This was the motivation for applying an AC misalignment to the optics instead of a DC misalignment.

4.4.3 AC Measurements

To reduce the uncertainty on the suspension motions, the beam motion was re-measured using an AC misalignment of the PR2 and BS optics. An 0.2Hz excitation was applied to the BS and then in a second measurement, to the PR2. The motion

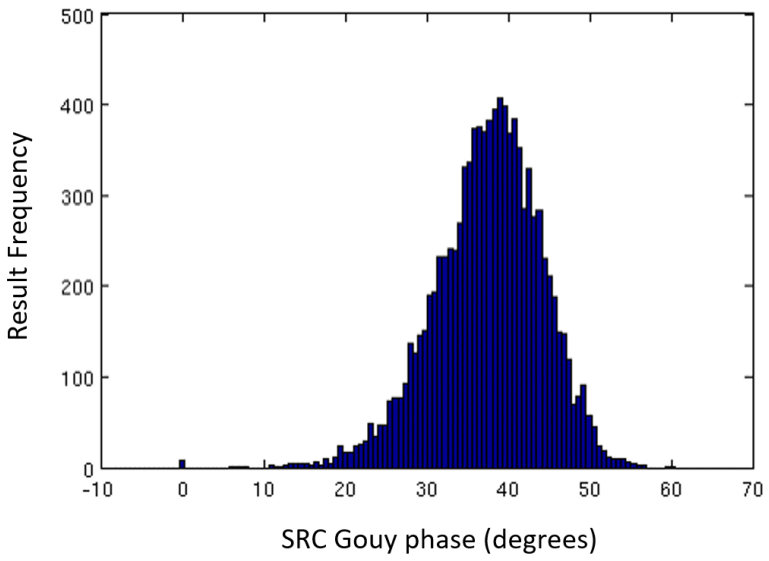

Fig. 4.17: A Monte Carlo simulation of the expected Gouy phase parameter given the measurement uncertainties- this indicates the uncertainty expected on this measurement. Measurement Gouy phase uncertainties: mean=37.5° median=38.0° standard deviation=6.6°

was captured by video on the two cameras. Figure 4.18 show example images of the beams on the cameras. This time the cameras were spaced 323mm ± 3mm apart. The beams were separated further so that only one beam was visible on the camera at once, to reduce interference between the two beams which might shift the location of each beam centroid.

The camera centroids were calculated frame by frame and the centroid location was plotted vs time. A sine function was fitted to get the change in beam location on each camera in x and in y. The total motion of the beam on the camera r was calculated by $r = \sqrt{x^2 + y^2}$. Figures 4.19 and 4.20 show examples of the centroid motion recorded on a camera, and the fitted sine function to the centroid motion. The amplitude of this sine function shows the relationship between suspension motion and centroid motion. The distance units used in this fit is pixels, which can be converted into meters given that the size of each pixel is 5.4x10^{-}6m^2. Some of the plots of suspension motion vs beam motion are quite clean, as in Figure 4.19, but some

(a) Camera A example 1 for AC measurement for the straight shot beam

(b) Camera A example 2 for AC measurement for the straight shot beam

Fig. 4.18: Two example images from a video taken of camera A while the PR2 optic had a 20μrad 0.2Hz excitation applied.

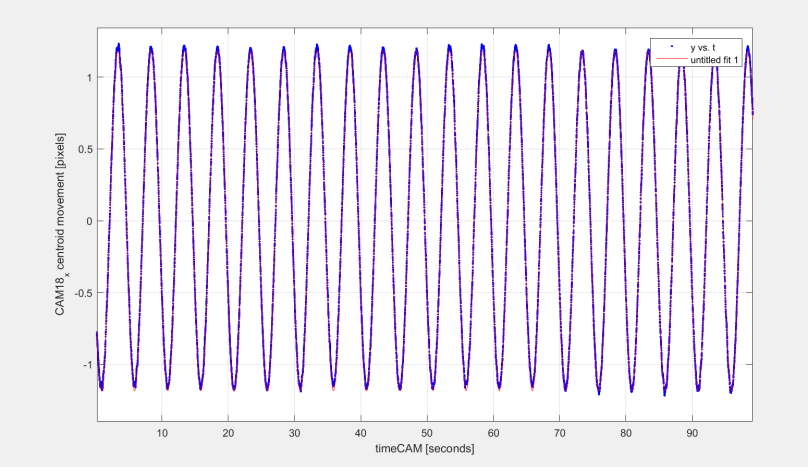

Fig. 4.19: Centroid motion with fitted sine curve on camera A due to a 3 μrad excitation on the BS yaw at 0.2Hz after a round trip through the SRC.

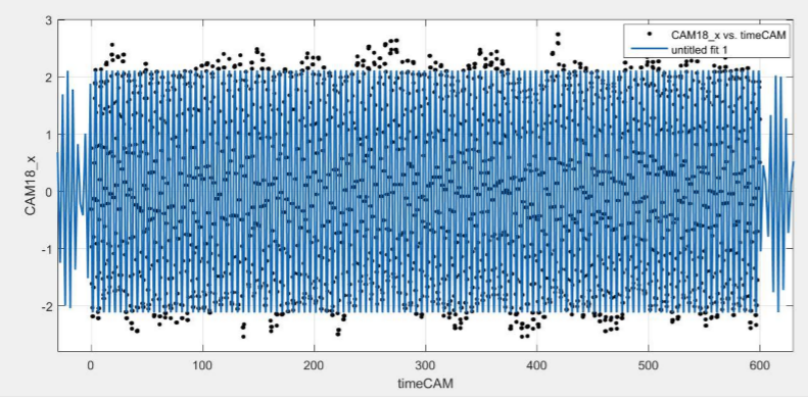

Fig. 4.20: Centroid motion with fitted sine curve on camera A due to a 10 μrad excitation on the PR2 yaw at 0.2Hz after a single-pass through the SRC.

are not, as in Figure 4.20. The uncertainty on this measurement was taken as the uncertainty on the amplitude.

It is evident that even using an AC measurement, the uncertainties on the centroid motion are too large (see for example Figure 4.20) to accurately calculate the Gouy phase of the SRC. Again, this is likely due to additional movements of the suspensions due to the unlocked cavity.

4.5 Discussion

There are further steps that could be taken to refine this technique.

One consideration is that the suspension actuator function is not the same for steady state vs a moving suspension, and the suspension position is calibrated in steady state. In this version of the experiment, the movement was done at a much lower frequency than the pendulum resonant frequency so that the actuator function is not much different from the steady state. To include the suspension actuator response, would be necessary to watch both slider value and optical lever value, make sure optical lever is well calibrated and use this as the suspension position. Fortunately the experiment is not overly sensitive to suspension calibration.

However, it appears that uncontrolled movement of the unlocked suspensions is a limiting factor of measuring relationship between suspension position and the beam locations on the cameras, as evidenced by the spread in the data points in Figure 4.20. Increasing the suspensions misalignment angle would reduce the effect of this error, but in practice this can't be done because baffles in the SRC cavity and the small size of the SRC optics start clipping the beam when the beam is misaligned through larger angles.

Since this measurement was performed, there have been other attempts to measure the SRC Gouy phase at LHO. The output Faraday path has now been re-configured so that a squeezing beam can be injected. This will allow a probe beam to be injected through this port which may make cavity scans feasible.

4.6 Conclusion

In this chapter we have described an alternative technique for measuring the Gouy phase of a cavity. We have presented the theory behind this technique, a practical application of this technique to measure the LHO SRC round-trip Gouy phase shift, and a discussion of errors and difficulties associated with this technique. It was discovered that this technique comes with its own difficulties, including fitting centroids with sufficient accuracy to the images of the beams captured by the cameras, and cop-

ing with slow drifts in the suspensions of the unlocked cavities, which make obtaining a meaningful result challenging in its own right.

We wished to measure the Gouy phase to better than $37^\circ \pm 8^\circ$ in order to make a meaningful measurement. This measurement was ultimately not accurate enough to reduce the uncertainty on the SRC Gouy phase, as it was limited by extraneous movements of the uncontrolled optical suspensions in the unlocked cavities.

5. OPTIC CHARACTERIZATION: SCATTERING AND ABSORPTION

This chapter describes absorption and scattering measurements performed on individual optics within the LIGO interferometer vacuum system:

1. Scatter measurements performed on the LHO test masses using digital cameras
2. Scatter measurements performed on the LLO Input Mode Cleaner (IMC) optics using digital cameras
3. Absorption measurements performed on the LHO test masses made using the Hartmann Wavefront Sensors

These measurements were used to assess whether these optics had become contaminated during maintenance tasks, to inform the loss budgets, and to understand the performance of the TCS system.

5.1 Motivation for performing In-Situ Scatter and Absorption Measurements

Optical scatter and absorption can impact detector sensitivity in two ways; by introducing noise into the system, and by increasing shot noise due to direct optical losses and absorption-induced mode-mismatch. Increased losses in circulating power also reduces the sensitivity gain that can be achieved by injecting squeezed light states into the interferometer, as discussed in Section 1.6.3.

Light scattered from the LIGO optics diverges from the main beam path in many directions, and it may be reintroduced to the system if it is reflected back into the

system. This light carries with it the spectral characteristics of the surface it scattered off and may introduce significant noise back into the system[87].

Absorption in an optical system causes a direct loss in power as a fraction of the light is converted into heat. However this effect is negligible in typical aLIGO applications. The real impact of absorption occurs because the optics heat up, causing a change in the light path due to changes in the optical path length and the refractive index of the optic. Changes to the shape of the optics effect the mode matching of a cavity. Poor mode matching between cavities in the LIGO interferometers leads to loss of power from the $TEM_{0,0}$ gaussian mode into higher order modes. There is a risk that if contaminants are accidentally deposited onto an optic's coating during handling, they might absorb enough laser power to become hot enough to cause coating damage

Thus, there are tight requirements on the allowable scatter and absorption on the alIGO optics. The four test masses must have surface scatter below 35 pmm, bulk scatter below 50ppm, and the coating absorption below 0.5ppm in order to achieve the design sensitivity of 10^{-23} for the aLIGO interferometers[88, 89]. The other core optics should have scatter below 20ppm and coating absorption below 0.5ppm[59].

There are strict contamination control procedures in place to minimize contaminant deposition onto the optics[90] and to maintain low-loss properties of the optics. If the optics are found to have excessive contamination,they may be able to be be cleaned. This requires air to be vented into the vacuum system, so that a technician may clean the optic by hand. However, every vacuum incursion reduces the lifetime of the vacuum equipment, so this is only performed if absolutely necessary.

When the vacuum chambers are opened, contamination control procedures are set in place to reduce potential contamination of the exposed optics[91]. The chamber is enclosed in a temporary positive-pressure clean tent. Personnel working inside the clean-tents wear ultra-clean "bunny-suits" and all tools and parts are cleaned and

baked before entering the clean-tent and the vacuum chamber. When the vacuum chambers are opened for commissioning or maintenance work,the optics may be coated in a removable polymer film called First Contact[92], which is designed to protect and clean precision optics.

The optics are characterized before being installed inside the vacuum chambers [93], but in-situ measurements are also useful because some properties of the optics may change over time. Both scatter and absorption measurements can be used to check for changes to the level of contaminants on the coating. The surface properties of the optic can change after installation or after vents, if for example contaminants such as dust are deposited onto the coating of the optic. It is important to monitor coating depositions and contaminants as these may burn onto the optics, permanently reducing the quality of the optic. It is particularly desirable to check for this type of contamination before running the interferometer at higher power.

Values for optical scatter and absorption are also used in various models and simulations of the interferometer, which are used to understand and predict interferometer behavior such as power budgets, noise budgets and locking schemes. Accurate in-situ measurements of the optical scatter and absorption are desirable as they improve the accuracy of these models.

5.2 Measuring Scatter

Scattering refers to processes that elastically scatter interferometer photons. Scattering occurs when imperfections in or on an optical medium cause the light to deviate from a single path, instead scattering the photons into many directions. Light can be scattered from contaminants on the coating of the optic, or from defects in the coating or within the bulk material of the optic itself. Features that cause scatter include micro roughness, and larger-scale deviations from the nominally spherical surface shape, including localized point scatterers[94]. Local point scatterers can be

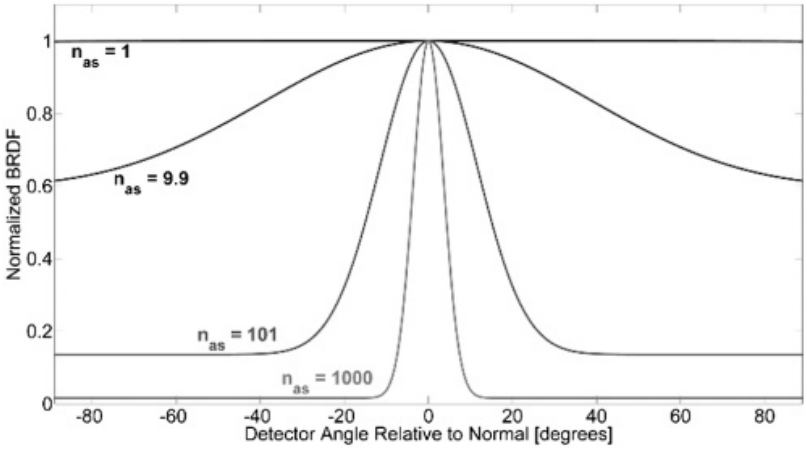

Fig. 5.1: The BRDF curve of various surfaces of various degrees of specular vs diffuse reflection[96]. The higher the fitting parameter n_{as}, the greater the proportion of specularly reflected light.

defects in the coating, or contaminants deposited on the surface of the coating.

The spatial distribution of surface scatter as a function of angle [95] can be described by the Bidirectional Reflectance Distribution Function (BRDF). Figure 5.1 shows a plot of the BRDF of various surfaces illuminated at normal incidence [96]. Optics with smaller surface features values have a higher proportion of light reflected back in a specular reflection, and less light reflected diffusely. At large angles, the BRDF can be approximated as a flat line. A general feature of scatter from a precision optic is that most of the light is reflected back in the specular reflection and at small angles, and less light is scattered into wider angles. LIGO-grade optics only scatter a small portion of the incident light diffusely, as they have very low scatter properties.

The BRDF at a given angle is defined in Equation 5.1:

$$BRDF = \frac{P_s}{P_i \Omega cos\theta_s} \tag{5.1}$$

where P_i is incident light power at normal incidence, P_s is scattered light over solid angle Ω, at angle θ_s off of normal to the optic surface.

The solid angle Ω of the camera or photo diode can be calculated using where A_{pd}

is the surface area of the photo-diode or detector measuring P_s and L is the distance from the optic to the detector:

$$\Omega = \frac{A_{pd}}{L^2} \tag{5.2}$$

When measuring the BRDF, the simplest approximation is to assume uniform scatter in all directions, and one specular reflection. More comprehensive measurements of BRDF involve measuring scattered light at multiple different angles to map out the BRDF shape in more detail.

The shape of the BRDF can indicate the types of scatterers present. Uniform, small-scale surface roughness scatters light diffusely (equally in all directions), and produce a constant BRDF over all angles. Larger features scatter light preferentially into smaller angles, resulting in a BRDF with a central peak. We expect the BRDF to contain a tall central peak dropping to a constant level at large angles since the surface features of the LIGO optics include both micro-roughness and some larger scale features.

5.2.1 Methods for performing In-Situ Scatter Measurements

A simple and very effective way to measure the scattered light power at a given angle P_s is to use a photo-diode. By performing the measurement at different angles, the BRDF may be estimated using Equation 5.1. A digital camera may be used instead of a photo-diode to measure scattered power, with the added advantage that a camera gives spatial information about the amount of scatter across the surface of the optic. If a digital camera is used, it must be calibrated first.

Camera calibration

A digital CCD (charge-coupled device) camera converts the light incident on each pixel into a voltage signal, which is digitized into some number of pixel counts p. The

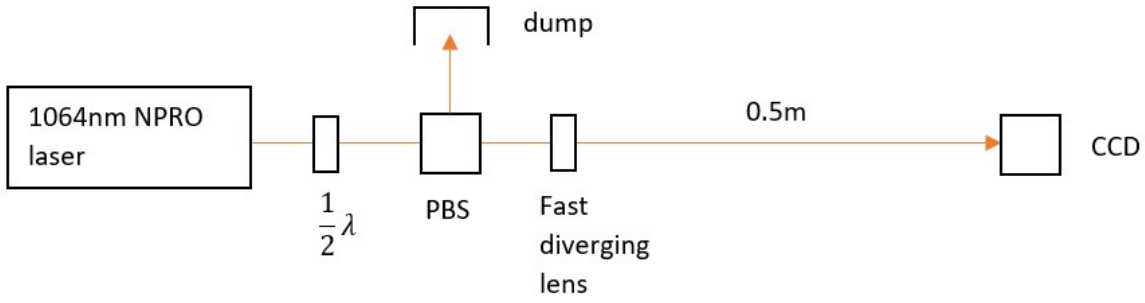

Fig. 5.2: Layout for GigE camera calibration.

relationship between p and the power incident on a single pixel P_{pixel} is:

$$P_{pixel} = \frac{pF_{cal}}{t} \tag{5.3}$$

where t is the exposure time, and F_{cal} is some calibration factor dependent on the conversion efficiency of light energy into an electrical voltage. Equation 5.3 describes a linear relationship between p and P_{pixel} which holds true until the camera saturates at a maximum p. In order to measure the power scattered from an optic using a camera, F_{cal} must first be measured for that camera. F_{cal} has units $\mu sW/counts$ and is wavelength specific.

We used Basler Ace 640-100um GigE cameras for the scatter measurements on the aLIGO interferometers. Figure 5.2 illustrates the setup used to determine F_{cal} for these cameras. 1064nm light was passed through a half wave plate and a Polarizing Beam Splitter (PBS), and then through a fast divergent lens. We placed the CCD camera 0.5m downstream from the divergent lens, as illustrated in Figure 5.2. The beam size at the CCD camera was 1 inch diameter and was uniform across the CCD (the active area of the CCD is 3x4mm). The camera could be swapped for a power meter to measure the absolute incident power at the location of the camera. The position of the CCD camera and the photodiode was marked on the table with clamps so that the camera and photodiode could be placed in the same position repeatably.

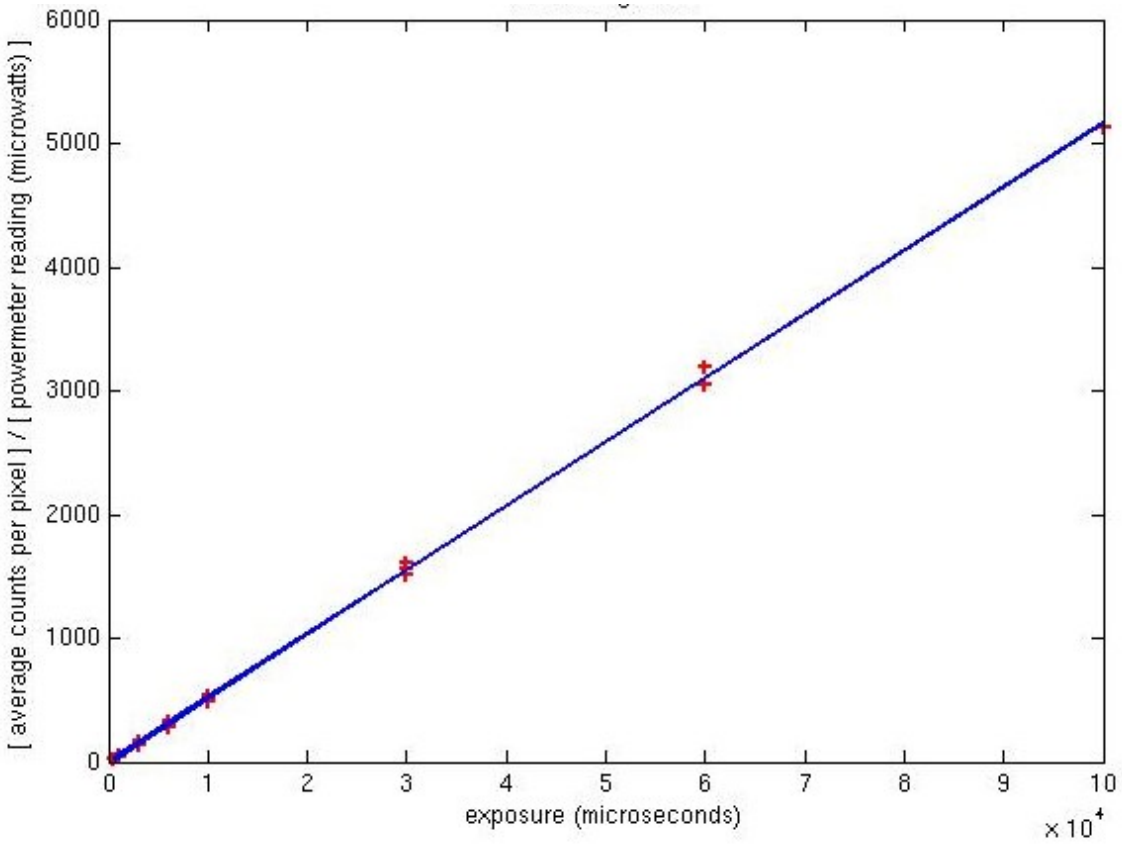

Fig. 5.3: Calibration curve for Basler GigE camera at 1064nm. The y-axis shows the ratio of the average pixel value p over the power measured by a power meter P, measured at the same location. Exposure time is plotted on the x-axis.

The measurement used to calculate F_{cal} is summarized in the plot in Figure 5.3. Each point represents a single image taken by the CCD camera. Between each image, we adjusted both the exposure time t and the incident power P_{inc}. It was necessary to adjust exposure time as well as incident laser power in order to keep the camera from becoming saturated. Each image also had the background image subtracted before analysis.

The calibration factor (F_{cal}) is calculated from this fitted slope as in Equation 5.4, where A_{pixel} is the surface area of a single pixel, and A_{pd} is the surface area of the photo diode.

$$F_{cal} = \frac{p}{P_{inc}} \frac{A_{pixel}}{A_{pd}} \tag{5.4}$$

The diameter of the power meter photo diode is 9.5mm, and the size of one pixel is $5.6\mu m^2$. This pixel size takes into account the dead area around the edge of that pixel. There are 659x494 pixels in the CCD array. The calibration factor was measured to be 8.6x10^{-12} $\frac{\mu sW}{counts}$, with camera set to 12-bit format, and 100 gain.

An uncertainty of $10^{-14}\mu sW/counts$ can be calculated from the residual error on the line of best fit in Figure 5.3. I believe that this uncertainty is smaller than the actual measurement uncertainty, as there are larger systematic errors that are not captured in the residual error, which include reflective surfaces of lenses which may be placed in front of the cameras, and a possible discrepancy in the place where the CCD is placed versus the plane where the photo-diode is placed.

This measurement has been repeated on other occasions by other parties, who produced similar calibration curves. There is a 20% difference in F_{cal} values measured by different parties at LLO. This is likely due to systematic errors in the measurements techniques, such as a difficulty in getting uniform light spread across the camera CCD. The large magnitude for these differences illustrates that it is difficult to perform an absolute calibration of power on a CCD camera which is free from systematic errors.

As a result, it is useful to check measurements made with the cameras using a photodiode, which doesn't have these uncertainties in the absolute calibration.

Image acquisition and processing

The GigE cameras are used to take images of both the illuminated and non-illuminated optics and a background subtraction is performed. This removes the effect of background light sources. The noise floor of the camera can be measured by taking a completely dark image. The best signal-to-noise ratio is achieved with the exposure set as high as possible, however it is critical that no pixels are saturated. If the pixels are saturated, it represents a major systematic error, as the brightest points can contain most of the total light power on the CCD. A noticeably higher signal-to-noise ratio is achieved when a 12-bit camera is used rather than an 8-bit camera image.

Smaller portions of the image can be analyzed to see the proportion of power that is being scattered from different parts of the optic, and whether the power is point scattered from a few point absorbers or more uniformly. Using camera images, the spatial distribution of scatterers can be tracked over time.

5.3 End Test Mass Scatter Measurements at LIGO Hanford

In early 2015, the LHO interferometer was configured to achieve full interferometer resonance of carrier light in both the DRMI and the arm-cavities. The LHO interferometer achieved full lock, but the power circulating in the arms was 3-6 times lower than expected[97]. It was determined that the lower power recycling gain was due to a loss in one of the arms, and that there was a 750ppm source of loss somewhere in the y-arm[98, 99] (compared to a 110ppm loss in the x-arm[98]). There were a number of possible causes for a power loss of this magnitude. An object could be clipping the beam, or something on the surface of an optic could be the source of the loss. The y-arm was probed in a number of ways, through measurements of cavity visibility,

cavity ring-down, imaging using various cameras, and scatter measurements, before it was determined that ETMy appeared to be the cause of the losses, and a end-station vent and clean was performed. This section describes the scatter measurements which formed part of this investigation. These scatter measurements were able to demonstrate that the source of the loss was on the ETMy optic, and that after cleaning, the scatter on this optic returned to a similar level to the ETMx optic.

5.3.1 Method

The ETMs can be photographed from one view-port, which views the ETM at 4° incidence to the HR surface normal. Since there is only one narrow viewing angle, it isn't useful to estimate a BRDF or a value for absolute scatter for this measurement. However, images of the ETMy and ETMx can be directly compared, and the relative brightness of the images correlates to the relative amount of scatter between the two mirrors.

While taking images of the ETMs, the ETMs were illuminated with the 1064nm beam and the photograph captured a portion of the scattered light from this source beam. The LHO ETMs were photographed in an illuminated state, and an un-illuminated state, so that the background light present in the chamber due to sources other than ETM scatter of laser light can be removed. This is illustrated in Figure 5.4. The optics were cropped and total scattered power from the optic was calculated.

Care was taken to ensure images were unsaturated, and the bit rate of the cameras was set as high as possible (which was found to significantly increase the signal-to-noise ratio). We found that when looking at the images, it could be helpful to plot them on a log intensity scale, as allowed the viewer to see the dimmer points that were otherwise poorly shown on the computer screen when plotted using a linear scale, as illustrated in Figure 5.5. Individual features of the images can be isolated and analyzed individually, to calculate the proportion of power scattered from these

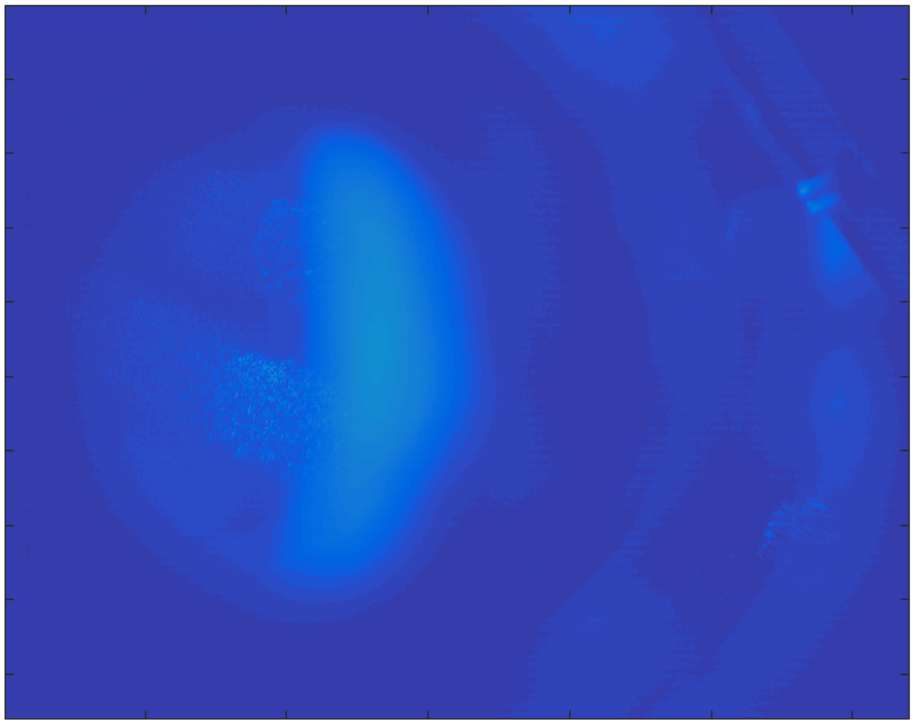

(a) Background image of ETMy, when no laser light is incident on the optic. Note there is still significant light inside the chamber from other light sources such as an unshuttered viewport.

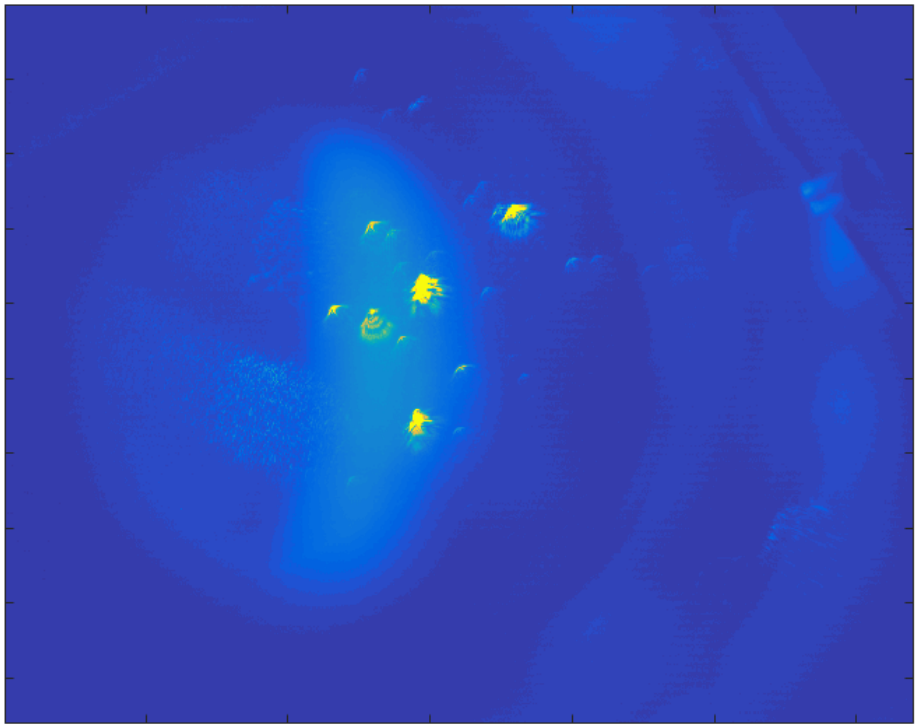

(b) Image of ETMy, illuminated by the 1064nm PSL beam with the y-arm locked. Note the image is somewhat out of focus, as this camera is used during green lock acquisition and the lens is focused for green light. Defocusing the image doesn't change the total light captured by the camera. The background light is also visible, but can be digitally subtracted from the image.

Fig. 5.4: Illuminated and background images of ETMy used to determine optical scatter.

OPTIC	Date taken	P_{inc} (W)	P_{PD} (W)
ETMy (before clean)	10 December 2014	18W	8.4e-7
ETMy (after clean)	5 January 2015	21W	1.16e-7
ETMx	11 December 2014	45W	8e-8

Tab. 5.1: Results of scattered light measurements of ETMy in December 2014, ETMy in January 2015 (after a vent and clean), and ETMx. P_{inc} is the incident power and P_{PD} is the scattered light power incident on the camera. Before cleaning, the power scattered from ETMy was 10x the ETMx scatter. After cleaning this was reduced to 1.5x the scatter from ETMx.

individual features.

5.3.2 Results

ETMy was both photographed using GigE cameras and the power scattered onto the camera was calculated in each case. Figure 5.6 shows the images of ETMy before and after cleaning.

The calculated powers are summarized in Table 5.1. Comparing the images of ETMx and ETMy, we saw 10x more scatter in ETMy. Before cleaning, the power scattered from ETMy was 10x the ETMx scatter. After cleaning this was reduced to 1.5x the scatter from ETMx. The scattering measurements taken with the camera were successfully able to detect the prescence of contaminants on the ETMy and confirm that the cleaning process had been successful.

By windowing the image, we calculated that 65% of the total power is in the three brightest points. When the optic was inspected, it was noticed that three pieces of first contact had been left after the last vent. These pieces of first contact could then be cleaned off the optic, reducing the ETMy scatter to a similar level to the ETMx scatter. This demonstrates the power of the camera to map out the spatial profile of scatterers on the optic's surface.

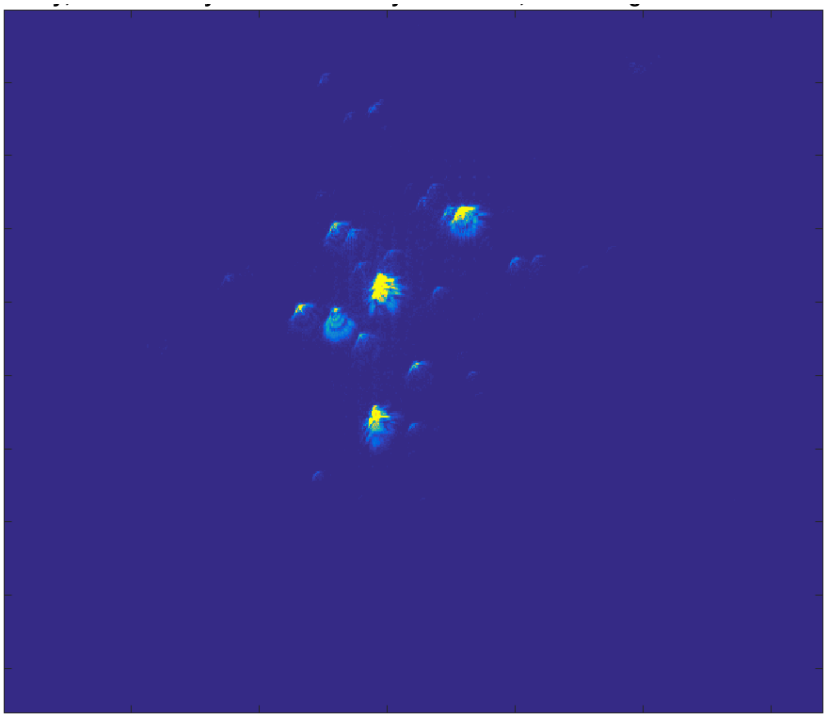

(a) Image plotted on a linear intensity scale. Only the brightest features are visible.

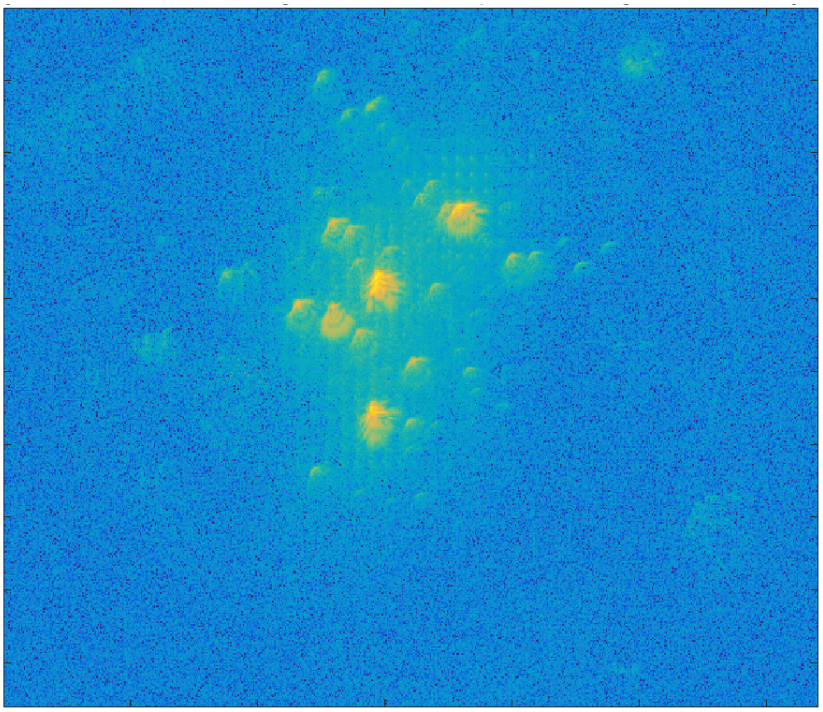

(b) Image plotted on a logarithmic intensity scale. Dimmer features are also visible, although it becomes harder to pick out the brightest features.

Fig. 5.5: Images of ETMy after background subtraction. The optic was illuminated by the resonant 1064nm PSL beam while the arm was locked.

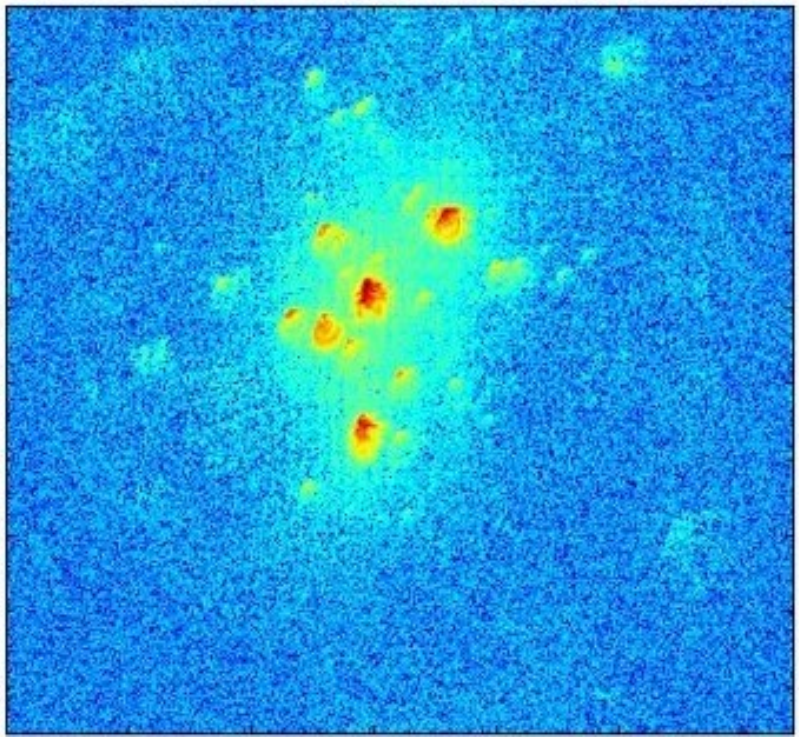

(a) ETMy front surface before cleaning.

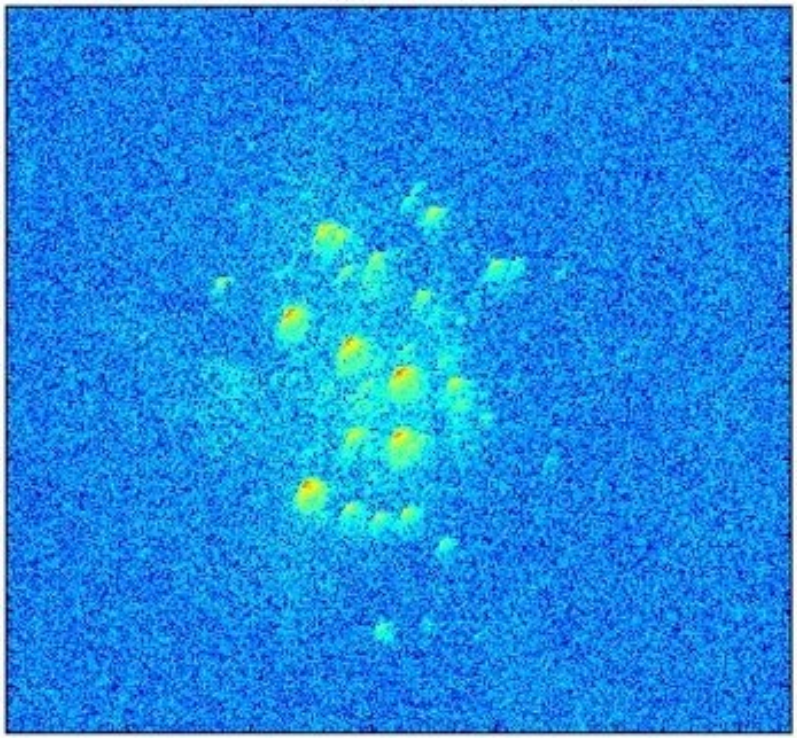

(b) ETMy front surface after cleaning

Fig. 5.6: GigE images of ETMy before and after cleaning, on a logarithmic intensity scale. Optics are illuminated with the PSL beam locked to the arm cavity, and background light has been digitally removed. In both images the optic is illuminated by 1064nm light, and the arm is locked to 1064nm, and the exposure time is the same.

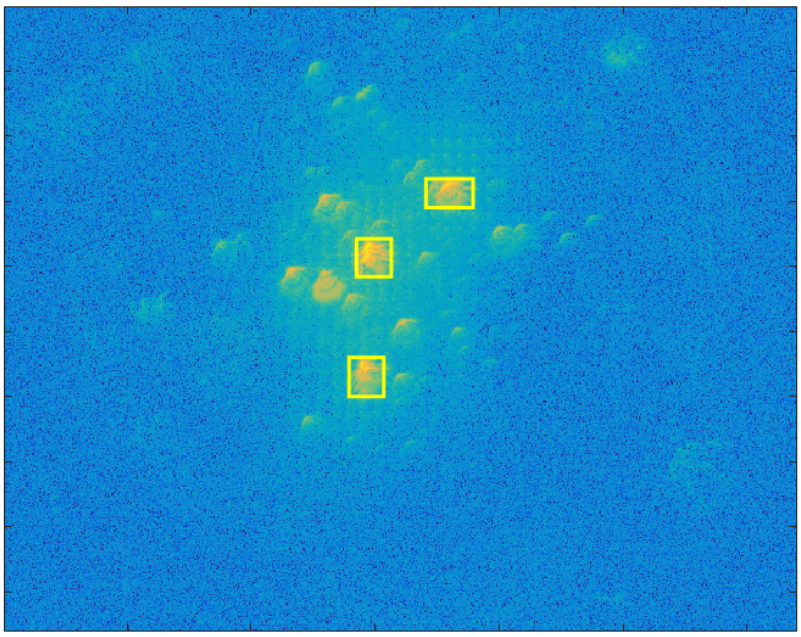

Fig. 5.7: Image of the ETMy with three brightest scatters highlighted.

Optic	Visibility	Cavity ringdown
Y-arm before Dec clean	750 ppm	1330±337 ppm
Y-arm after Dec clean	125±319ppm	Not measured
X-arm	108±378ppm	120±3360

Tab. 5.2: A summary of results from various loss measurements in the y-arm.

5.3.3 Discussion

During this period of activity, other methods were used concurrently to determine of loss in the arms. The results of these measurements are summarized in Table 5.2. The other loss measurements included cavity ring-down, arm-cavity visibility measurements and P-Cal camera images. The first two measurements determined that the additional loss was located in the y-arm cavity. Detailed measurements using the cameras were necessary to determine which optic was contaminated and guide the cleaning crew to its location.

Visibility measurements showed 108±19ppm for the X-arm and 750 ppm for Y-arm before cleaning and 125 ppm post clean), which agrees with the camera comparisons. Visibility is calculated using Equations 5.5, and 5.6. In Equation 5.5, A is the visibility

of the arm cavity which the square root of the ratio of the power at the end of the cavity between when the arm is locked (on resonance) and the the power when the arm is unlocked (off resonance). The loss in the arm is related to the visibility and the reflectivity of the input test mass to the arm r_I by through Equation 5.6.

$$A = \sqrt{\frac{P_{AS\_AIR}^{\text{on resonance}}}{P_{AS\_AIR}^{\text{off resonance}}}} \tag{5.5}$$

$$1 - L_E = \left[\frac{A - r_I}{Ar_I - 1}\right]^2 \tag{5.6}$$

The loss of the arm cavities were measured using cavity ring-down, method as described by [100]. Measured y-arm scatter was 1330±370ppm, x-arm scatter was 120±360ppm.

PCal cameras are used for calibration of the interferometers, can also be used to look at scattering from the optics. The PCal cameras are commercially bought cameras which look at each test mass. The advantage of these cameras is that they see multiple colors and produce higher resolution images than the GigE cameras. Figure 5.8 shows images of the ETMs taken with the PCal cameras before cleaning, as illuminated by the green 532nm ALS beam and the red 1064nm PSL beam. When illuminated in green, the ETMy optic shows a circle of residue, and when illuminated by the red beam, three very bright points are present. The three very bright points were three pieces of first contact. Interestingly, even after the ETMy was cleaned, a ring shape pattern can be seen scattered in green. This circle is the same region where the first contact was applied, and shows that there is some kind of residue left by the first contact on this optic.

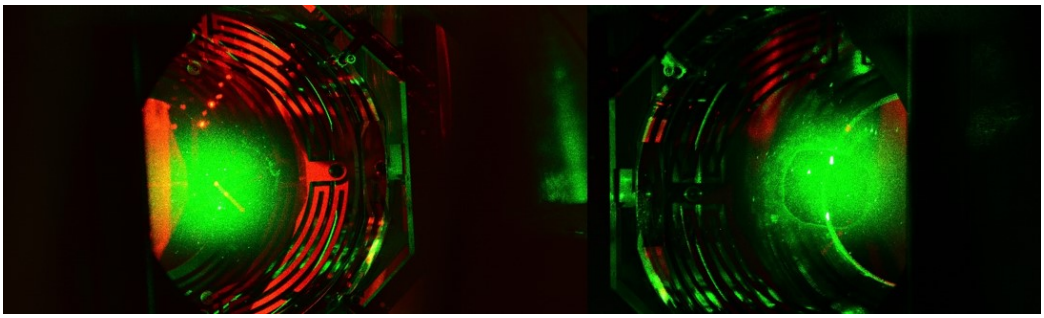

(a) Picture of ETMx and ETMy using the PCal camera, with the optic illuminated by the 532nm ALS beam.

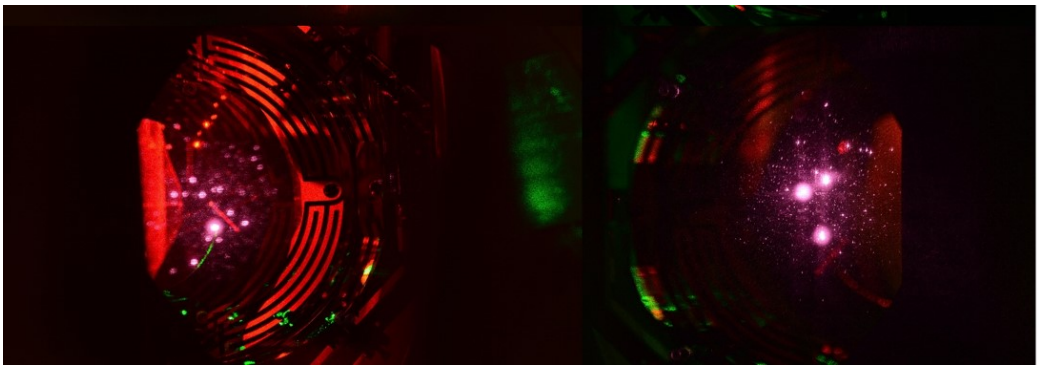

(b) Picture of ETMx and ETMy using the PCal camera, with the optic illuminated by the 1064nm PSL beam.

Fig. 5.8: Images of ETMx and ETMy taken with the PCal camera. Note ETMy has three very bright spots on it. These were pieces of first contact.

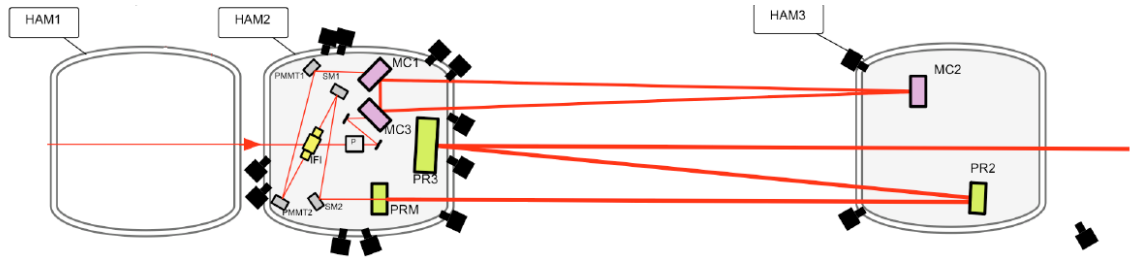

Fig. 5.9: Locations of view-ports with a view of the IMC optics.[101]

5.4 Input Mode Cleaner Scatter Measurements at LIGO Livingston

In mid-2013 at LIGO Livingston, the Input Mode Cleaner (IMC) vacuum chambers were opened in order to perform work on the IMC optics. Recall from Section 1.4.1 that the main IMC optics are the three optics that form the three-mirror IMC cavity: MC1, MC2 and MC3. In this series of measurements, the scatter of the IMC optics MC1 and MC2 was compared before and after vents. There was no good viewing angle from which to measure MC3 scatter. The aim of these measurements was to monitor whether venting air into the Input Mode cleaner (IMC) vacuum chambers during vacuum incursions introduces new dirt onto the optics. This verifies the effectiveness of the contamination control procedures for vents.

5.4.1 Method

There are multiple view-ports in the "HAM" vacuum chambers which hold the IMC optics, as illustrated in Figure 5.9. These view-ports provide multiple views of the MC1 and MC2 mirror front faces. There is no view-port which provides a clear view of the MC3 front face, which is why this IMC optic was not included in the measurement. Both GigE cameras and photo-diodes were used to measure the BRDF of these two optics. Two of the IMC optics, MC1 and MC2, could be imaged at large angles; MC1 at 22° in HAM23, and MC2 at 61° in HAM3. Ideally, the BRDF would be measured at more than one angle, however in the LIGO vacuum systems, the limited viewing angles through view-ports is a limitation of this method.

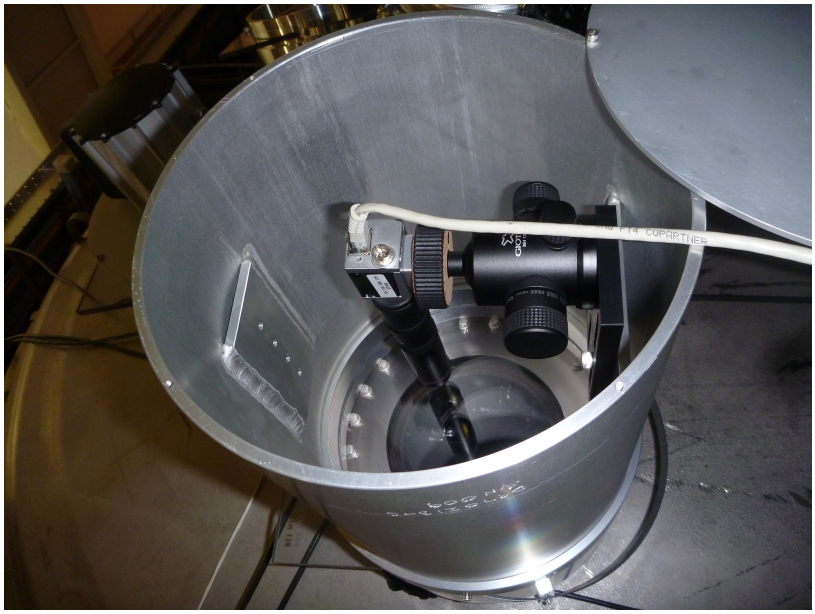

Fig. 5.10: A GigE camera installed into a HAM3 view-port, used to measure large-angle scatter from MC2.

The cameras and photo-diodes were set up in view-ports in the HAM 1 and HAM 2 vacuum chambers, as pictured in Figure 5.10. Basler ACE "GigE" cameras were used to measure scattered power to compare distributions of scatterers before and after the vents. The measurements were compared to a photo-diode reading made by a Thorlabs PMD100D photo-diode which was placed at the same location as the camera.

The unedited images from the two GigE cameras are shown in Figure 5.11. The measurement was performed with 1W input power incident on the IMC. The BRDF at a given scattering angle can be estimated using Equation 5.1.

5.4.2 Results

The light scattered from the MC1 and MC2 optics at large angles of 22° and 61° respectively was measured using a power-meter (Thorlabs PM100D). Power was measured a) with the beam shuttered, b) with the IMC misaligned, and c) with the IMC locked. The scatter results calculated using these images are summarized in Table

(a) Image of MC1 taken with a GigE camera at an angle of 22°, illuminated by 1W PSL beam.

(b) Image of MC2 taken with a GigE camera at an angle of 61°, illuminated by 1W PSL beam. In this image, there is an additional light source switched on in the vacuum chamber, which is why the edge of the optic is so brightly illuminated. This light source was switched off when the actual measurement was performed.

Fig. 5.11: Images of MC1 and MC2 taken from within the HAM1 and HAM2 viewports.

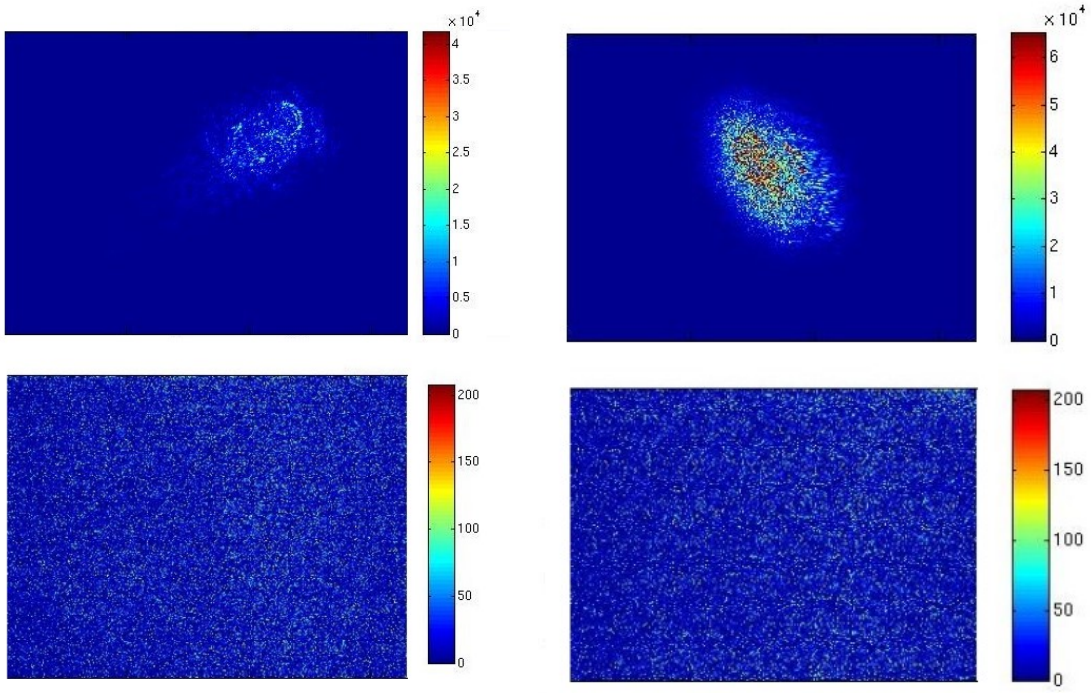

(a) MC1

(b) MC2

Fig. 5.12: Images of MC1 and MC2 taken with a digital GigE camera, with (top) and without (bottom) illumination by the PSL. The images without illumination are featureless, which means the background illumination is below the noise floor of the camera. The units in the colorbar indicate the relative brightness of the image in AU.

5.3. Examples of the images captured are shown in Figures 5.12 and 5.13.

This data was used to estimate BRDF using Equation 5.1, by assuming that the BRDF is constant over all scattering angles, as shown in Table 5.4. The background light was measured and subtracted from the image of the optic that was illuminated by the PSL beam. The distance from the camera to the view-port was 1.1m for MC1 and 1.2m for MC2.

This measurement was compared to other measurements of total scattered power performed at stages during the interferometer integration[102, 103]), summarized in Table 5.5.

A comparison of the measurements taken on different dates show that the scatter from MC1 dropped between October 2012 and January 2013. The scatter from MC2

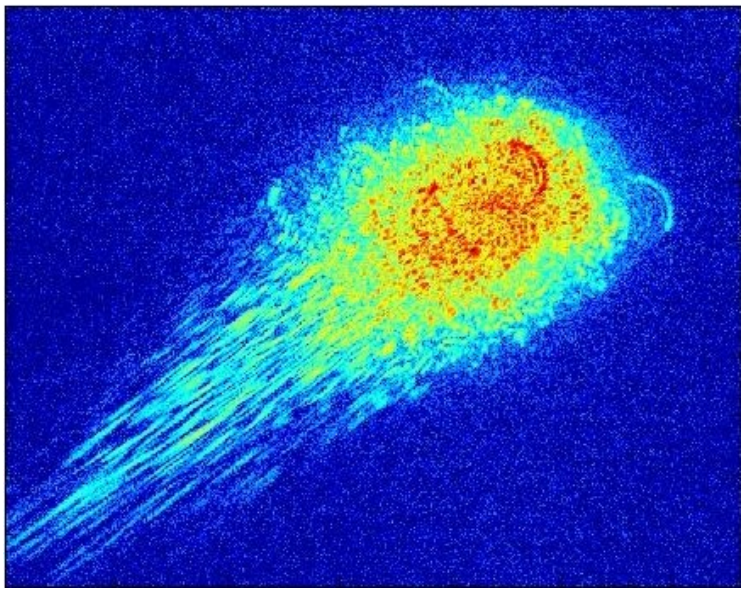

(a) MC1

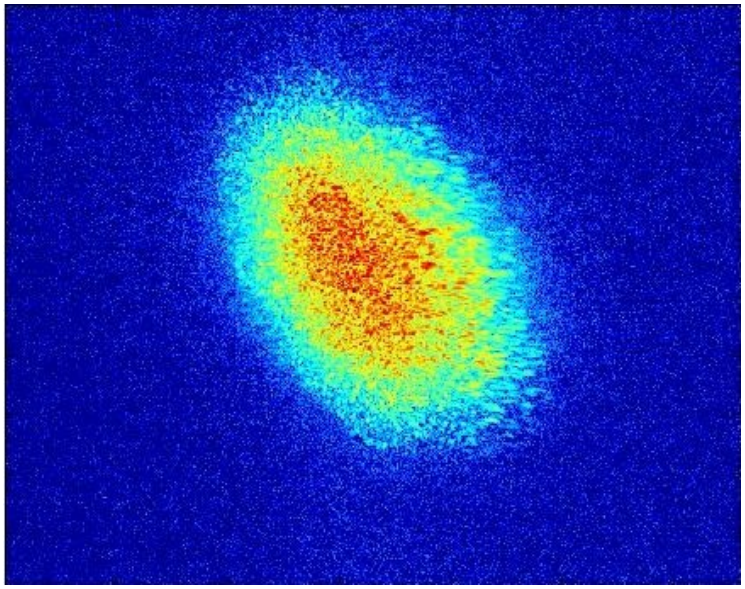

(b) MC2

Fig. 5.13: Images of MC1 and MC2 taken with a GigE camera, plotted on a logarithmic intensity scale to see more detail.

Power on camera	Dark image taken with the IMC misaligned (nW)	Illuminated optic taken with the IMC locked (nW)	Scattered power P_s (nW)
MC1 large angle	10	23	13 ± 0.65
MC2 large angle	22	32	10 ± 0.5

Tab. 5.3: Scattered powers from the MC1 and MC2 optics, as measured with the GigE cameras. An uncertainty of 5% on the total scattered power is attributed to the uncertainty on the reflectivity of the commercial camera lens used to focus the image on the camera.

Optic	Distance from optic to view-port (m)	θ_s	BRDF	Total scatter (ppm)
MC1	1.2 ± 0.05 22°	1.7x10^{-6}	5 ± 0.5	
MC2	1.1 ± 0.05	61°	2.1x10^{-6}	7 ± 0.7

Tab. 5.4: Parameters used to calculate the scatter from MC1 and MC2.

Measurement date	Total scattered power (ppm) MC1	Total scattered power (ppm) MC2
16 October 2012	32	24
09 January 2013	3	28
16 August 2013	5	7

Tab. 5.5: Scattered power from MC1 and MC2 over various dates, showing changes over time.

dropped between October 2012 and October 2013. There was a vent between each of these measurements. The fact that the scatter hasn't increased, and in fact has decreased, indicates that current contamination control procedures are adequate to maintain the cleanliness of the in-vacuum optics.

5.4.3 Discussion

The result indicates total scattered power has stayed the same or decreased. This result agrees with the measurements taken of the IMC HOM resonances discussed in Section 3.3, which also indicated the absorption of these optics decreased slightly over this time period.

The technique for the scatter measurement described in this section and the indirect absorption measurement inferred from the HOM resonances described in Section 3.3 have different advantages. Using cameras to measure scatter does not require much equipment and the result only concerns a single optic. The spatial distribution of contaminants over a single optic can be determined. The impact of the contaminants on the change of ROC and impact on mode matching cannot be directly measured using this technique. The accuracy of this technique is not impacted by the Finesse of the cavity or the reflectivity of the mirrors.

The frequency scanning technique looks at the impact of the contamination on the cavity performance as a whole. As seen in Section 3.2 where the change in ROC measured by the HWS was compared to change in HOM resonances, models of the ROC change due to absorption have their own limitations and errors associated with them.

The HWS sensor can directly measure the change in the ROC of the optic, which can then be used to comment of cavity performance or on absorption in that optic. This technique of optic characterization will be described in the next section.

5.5 Measuring Absorption

Absorption occurs when a small fraction of the incident light is absorbed at the optical coating or in the bulk of the optic and its energy is converted into heat. Absorption can be uniform throughout a homogeneous material, or it may occur at locally absorbing "hot-spots" where material inhomogeneities such as surface contaminants, coating defects or bulk defects are present. Material defects that cause local absorption will scatter light as well.

The total power absorbed by the LIGO optics is small, especially when compared to the total power scattered. However, absorbed light becomes heat which results in absorption-induced heating and wavefront distortion of the optics. For the test masses in the arms, this effect distorts the optic and results in power losses due to poor mode matching. This can be more detrimental than the larger scattering effects.

The absorption-induced heating will change the wavefront of the light in three ways:

1. Through change in the refractive index of the substrate ($\frac{dn}{dT}$)
2. Through thermal deformation ($\frac{dL}{dT}$)
3. Through change in refractive index with local strain ($\frac{dn}{d\varepsilon}$)

The first effect is the biggest, although this only effects the wavefront of light on transmission through the optic. The second effect changes the wavefront on reflection as well as for transmission. The third effect is almost always negligible[104].

The absorption of a test mass a can be calculated using Equation 5.7, where $P_{absorbed}$ is the absorbed power and P_{arm} is the incident power, which when the interferometer is locked is the power circulating in the arm.

$$a = \frac{P_{absorbed}}{P_{arm}} \tag{5.7}$$

P_{arm} can be calculated using Equation 5.8, where $P_{in,IMC} = 1.7W$ is the power

input to the IMC, where $e_F = 0.88$ is the IMC-Faraday throughput efficiency, G_R is the recycling gain, G_{arm} is the arm cavity gain, and T_{BS} is the transmission of the Beam Splitter.

$$P_{arm} = P_{inIMC} e_F e_R G_R T_{BS} G_{arm} \tag{5.8}$$

Arm cavity gain is calculated using Equation 5.9 , where $r_{ETM} = \sqrt{1 - T_{ETM} - L}$, T_{ETM} is the transmission of the ETM and L is the loss in the arm.

$$G_{arm} = \left[\frac{t_{ITM}}{(1 - r_{ITM} r_{ETM})} \right]^2 \tag{5.9}$$

$P_{absorbed}$ can be calculated from the change in the radius of curvature of the optic (assuming absorption is uniform), which can be measured using the HWS. This relation can be approximated using Winkler's relation[76] (Equation 3.3), or it can be calculated using Finite Element Analysis.

The Hartmann Wavefront Sensor

The Hartmann Wavefront Sensor senses a relative wavefront change in the light incident on the sensor, and can be used to monitor thermal deformations of the optics[105]. Figure 5.14 shows a schematic of the HWS. The HWS consists of a Charged-Coupled Device (CCD) camera array masked by a Hartmann plate, which is a thin metal plate with a uniform array of holes drilled into it. This produces an array of spots. The location of the spots is determined by the shape of the wavefront incident on the HWS. As the optic heats up and changes shape, the wavefront changes, and the locations on the spots on the CCD changes. This change in spot centroid locations is used to reconstruct the wavefront deformation.

The Corner-station layout of the HWS is shown in Figures 5.15. The corner station HWS use fiber coupled Super Luminescent Diodes.

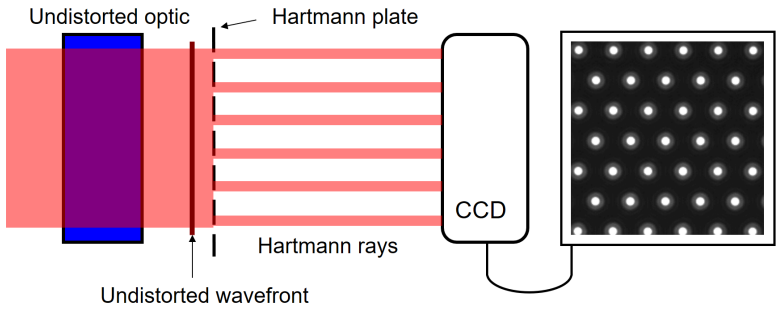

(a) Path of the beam through an optic with no thermal distortion.

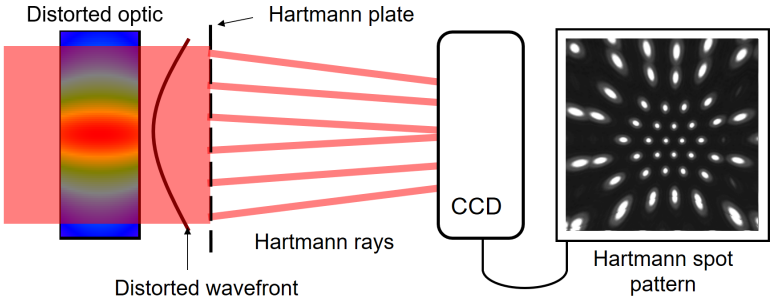

(b) Path of the beam through an optic with a thermal distortion present.

Fig. 5.14: Light rays traveling through an optic (left) and a Hartman plate onto the sensor before and after heating, and he change in the spot pattern seen on the HWS due to spherical wavefront change. The Temperature distribution of the optic is indicated by the colors (blue being cooler and red being hotter).[105]

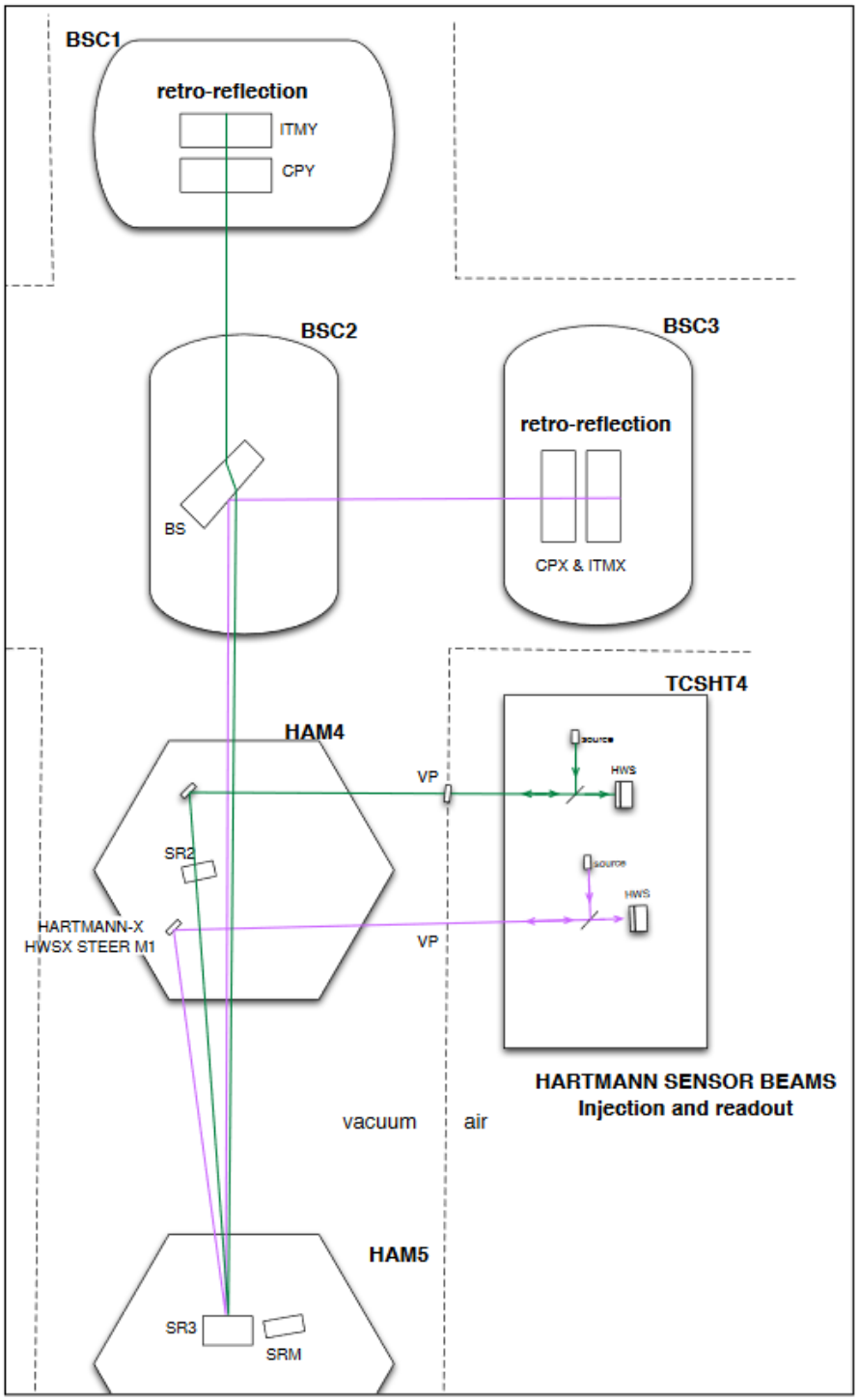

Fig. 5.15: The layout of the HWS system in the corner station. SLED probe beams are injected from the in-air table TCSHT4 into the vacuum chamber HAM4, to probe ITMx and ITMy[45].

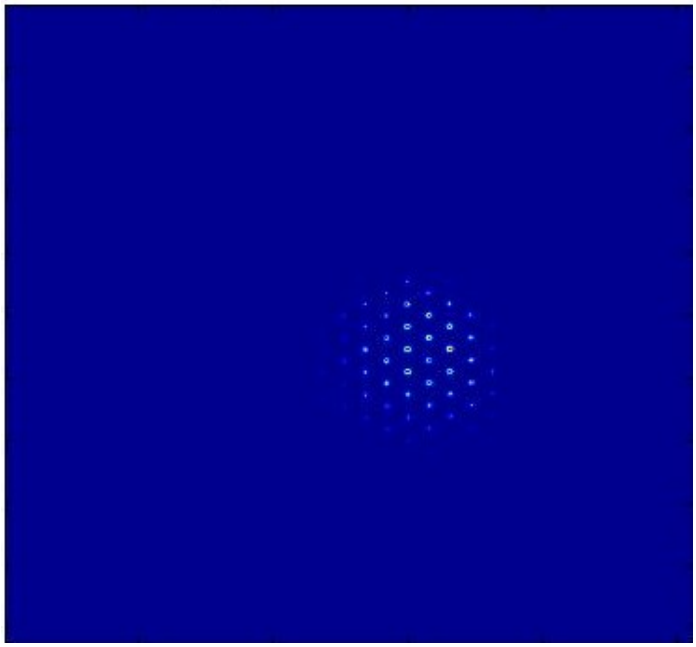

Fig. 5.16: The spot pattern captured by the ETMy HWS when it is illuminated by the green beam. The size of the beam is small compared to the HWS CCD.

The ETM HWS cameras use the green 532nm ALS beams to measure the curvature change of the ETMs. However the green beam is usually shuttered and not present in the interferometer once the interferometer is in its full-power, detecting state. To take a measurement with the HWS, we brought the interferometer to it's full-power, fully locked state, and then re-opened the ALS shutters and misalign the input angle of the ALS beam enough to only get a single reflection off of the ETM, with no return beam from the ITM. An example of the spot pattern on the ETM HWS illuminated with the ALS beam is illustrated in Figure 5.16.

5.6 Test Mass Absorption Measurements at LIGO Hanford

This Section presents measurements of optical absorption performed on the LHO Input and End Test Masses (ITMs and ETMs). These measurements were used to check the in-situ optical absorption of the test-masses, and to examine the time-dependent response of the optic's wavefront profile in response to actuation from the

TCS.

5.6.1 Absorption in the End Test Masses

Figures 5.17 and 5.18 show the change in ETMx and ETMy spherical power over time, over a period when the interferometer was locked for 30minutes at 25W. These measurements were taken using the ETM Hartmann Wavefront Sensors (HWS). The change in the spherical power of the ETMs was used to estimate the absorption of the ETMy. This measurement assumes the test masses have had enough time to reach thermal equilibrium, which actually takes longer than 30 minutes. This means that the absorption measurement is an underestimate. Ideally it would be desirable to get a measurement of a lock stretch of $> 1hr$, however this was not possible due to conflicts in the commissioning schedule at the time this measurement was made.

The absorption is calculated using Equations 5.8 and 5.9, $P_{in,IMC} = 1.7W$, $e_F = 0.88$, $G_R = 45$, $G_{arm} = 280$, $T_{BS} = 0.5$, and $L = 120ppm$. Values used in this calculation are presented in Table 5.6. The arm power calculation was verified against the four ASC_TR QPDs, which agree with the calculation using IMC input power, the variation between the four QPDs puts the uncertainty of the arm power at 15%. The spherical power of the thermal lens in ETMY was $30\mu D$ and the thermal lens in ETMX was $11\mu D$, measured after a 35 minute lock stretch at 25.3W input power. For a change in spherical power of $1\mu D$, 1.06mW of power is absorbed, according to an FEA COMSOL model of the test mass absorption[106]. The ETMx absorption was measured at 130ppb and the ETMy absorption was measured at 230ppb.

5.6.2 Absorption in the Input Test Masses

The change in curvature in the ITM was measured before and after the interferometer was locked (Figure 5.19). The change in curvature was $6\mu D$. According to FEA modeling of the test mass thermal response performed by Aidan Brooks[106], 1.06mW

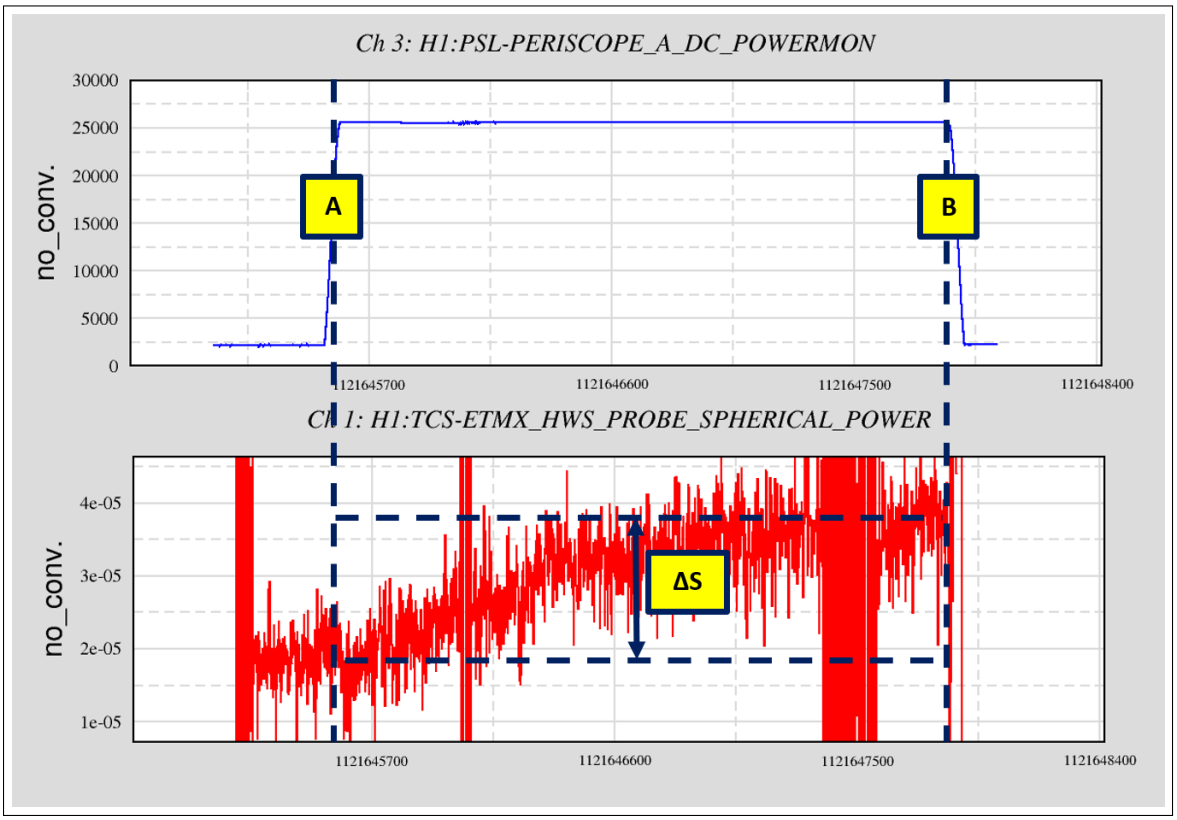

Fig. 5.17: Change in spherical power over time for the ETM. The top trace shows PSL power in arbitrary units, and indicates when the interferometer was in a high-power state. The bottom trace shows the spherical power in μD measured by the ETMx HWS.

Property	ETMX	ETMY
Spherical power at start of lock stretch	2.3e-5	4e-5
Spherical power at end of lock stretch	3.5e-5	7e-5
Change in spherical power (diopters)	1.1e-5	3.0e-5
Absorbed power in test mass	18mW	32mW
Power in arm	140.3kW	140.3kW
Test-mass absorption (ppb)	130ppb	230ppb

Tab. 5.6: Values used to calculate the ETM absorption.

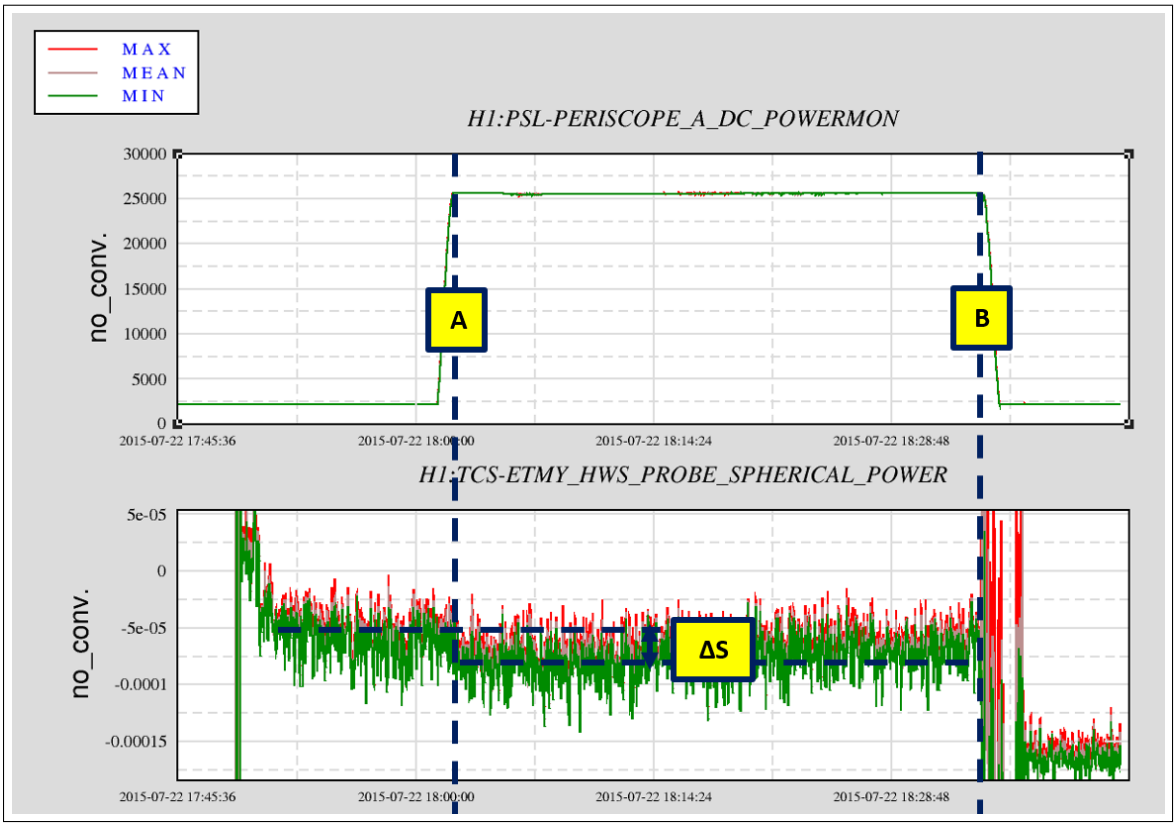

Fig. 5.18: Change in spherical power over time for the ETMy. The top trace shows PSL power in arbitrary units, and indicates when the interferometer was in a high-power state. The middle trace shows the spherical power in μD measured by the ETMy HWS. The bottom trace shows the spherical power in μD measured by the ETMy HWS.

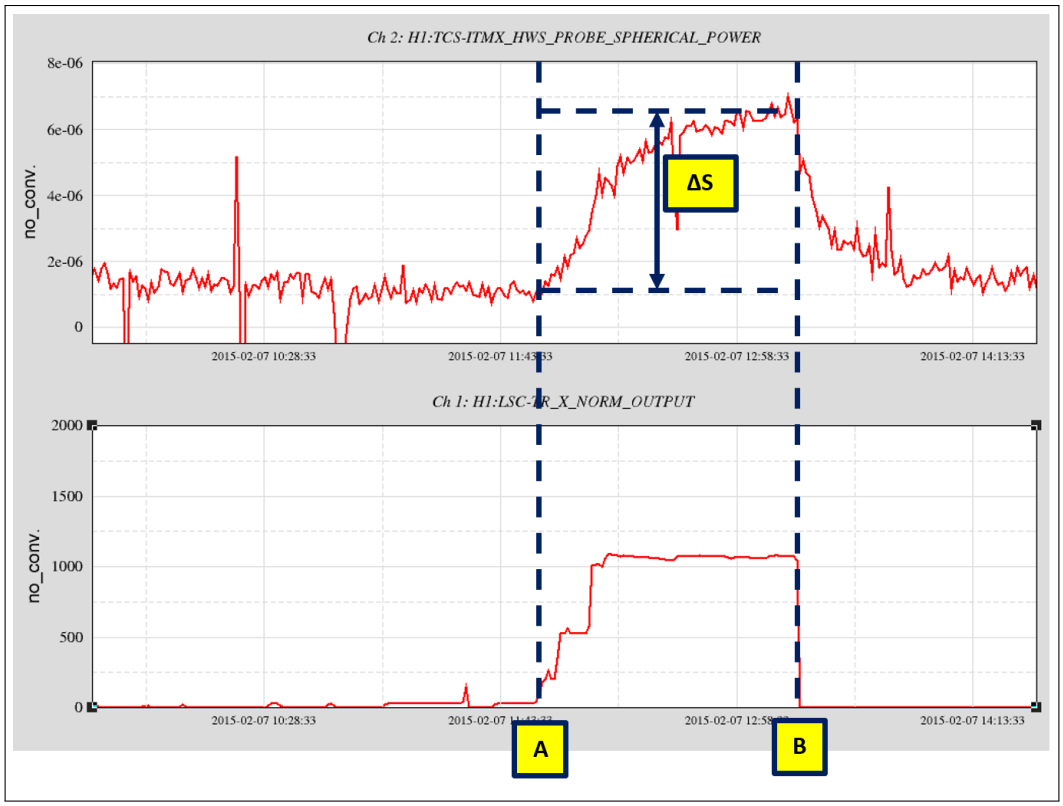

Fig. 5.19: ITMx HWS output showing the development of the thermal lens in the ITM as the optic heats up after the interferometer is locked. The top plot shows the change in spherical power (in μD) over a 30 min lock stretch, starting from the unlocked state. The bottom plot shows the power in the x-arm, in arbitrary units, which shows the power increase up to full power in the interferometer during the locking process.

of power is absorbed per 1mudiopter change in ITM curvature, which means that 6mW of power was absorbed during the measurement. The power in the arm can be calculated using Equations 5.8, and was 11.5kW, given an IMC input power of 2.81W, Recycling gain 36 W/W, X-arm cavity gain is 276 W/W.Thus, the ITMx absolution is calculated to be 520 ± 150ppb.

The absorption of the ITMy could not be measured during this round of measurements, as the ITMy HWS was not yet fully commissioned.

5.6.3 Discussion

The HWS measures changes in wavefront and can be used to infer heating distributions and absorption in the test masses. Using the HWS, we are able to measure absorption of individual optics, rather than average absorption of the cavity as with locked cavity techniques.

ITMx absorption was measured to be 520 ± 150ppb. For comparison, Livingston measured a somewhat lower absorption in the coating of 140-200 pppb in the ITMs[106]. This was re-measured and found to be consistent on multiple occasions over 2015. It is not unexpected that the individual ITM optics have different coating absorptions, and illustrates the value of in-situ measurements of optical properties, as variations can occur in optical absorption and scatter due to variations in the manufacturing and handling of individual optics.

These values were used to update various models[107].Areas for further work include improving models to agree with time-dependent absorption measurements, and adding time-dependent absorption behavior to FINESSE models. This last point will be further discussed in the next chapter.

5.7 Conclusion

Digital cameras can be used for in-situ, long-term monitoring of scattered light and surface properties of optics in systems such as the aLIGO interferometers. This method has advantages over other methods, that one can look at the spatial distribution of surface scatterers. This chapter has described a number of ways these cameras are used for calculating BRDF and total scatter, for looking at differences between optics, and looking at changes over time. In the case of IMC monitoring, we conclude that vents are not negatively impacting optic cleanliness. In the case of ETMy, the scatter measurements were part of the evidence that there was a major contaminant

on ETMy. The contaminant could be seen in the images. The decision was made to vent and clean the optic, and afterwards the scatter was reduced to an acceptable level. This was confirmed with images before and after the clean.

The optical absorption was measured for the LHO Input and End Test Masses. The absorptions measured were at or below the requirement of 0.5ppm. Knowledge of the absorption properties of individual optics is useful for a number of applications. It allows design of TCS actuation specific to individual optics, which is especially nice for time-dependent control schemes which are currently being defined. Changes in absorption properties can indicate changes after vents. Looking for larger localized scattering particles can point to for large deviations from a spherical lensing effect.Absorption measurements were used to track time-dependent heating behavior of optics.

6. MODELING THERMAL EFFECTS IN OPTICS USING ELASTO-DYNAMIC RECIPROCITY

In this chapter, I present a fast numerical method for modeling thermo-elastic distortions in optics. This method uses elasto-dynamic reciprocity relations as an alternative computational pathway to the conventional stress strain relations. This method may be used for modeling thermal effects on the interferometer control loops, by incorporating it into interferometer modeling programs such as FINESSE[77].

Section 6.1 covers the motivation for undertaking this work. Sections 6.2 and 6.3 cover the background and theory underpinning this work[104][108]. Section 6.4 presents the paper which describes this method. Section 6.5 discusses the scope for future work.

6.1 Motivation

Cavity optics in the aLIGO interferometers heat up due to absorption of the circulating laser light and due to actuation by the TCS ring heaters and CO_2 lasers. The absorption-induced heating of the optics causes thermal lensing, which impacts the path of the beam taken through the interferometer. This in turn impacts the response of the length, alignment, and thermal control systems, as well as potentially reducing detector sensitivity. Hence it is desirable to understand the impact of thermal changes in the individual optics on the interferometer as a whole.

The Thermal Compensation System (TCS) acts over time scales of hours to alter the temperature profile of the optics. TCS actuation interplays with the control

signals to the alignment control systems, which act over time scales of 10's of minutes to hours. These long time-scales make measuring the time-dependent interaction between these systems difficult, so detailed modeling of these effects is a useful tool for detector commissioning.

The time-dependent behavior of an individual optic due to a heat input can be modeled using Finite Element Analysis (FEA) techniques[109]. The circulating fields in the interferometer and the time-variant build-up of these fields and the interaction with the control loops can be modeled in a program such as FINESSE. FINESSE uses a modal model of the interferometer to calculate the spatial and frequency distribution of light in the interferometer, as well as the effects of control signals, TCS, scattering and surface defects. FINESSE calculates the resonant modes in each cavity by propagating light through the interferometer using scattering coefficients in a quasi-static condition. The effect on the wavefront at each mirror can be specified.

To model time-variant thermal effects in FINESSE, the absorption-induced wavefront deformation must be re-calculated using FEA for each time step, which can take a long time (order of tens of minutes to hours per iteration). So speeding up this process in any way is desirable to make these models a practical pathway to understanding the time-dependent iteration between the TCS and the length and alignment control systems. Reciprocity could be used as a faster alternative to traditional FEA methods to calculate the change in shape of each mirror due to various TCS inputs.

6.2 Background Theory

Temperature changes can occur in LIGO optics when they absorb the circulating laser light, and are heated by the TCS ring heaters and CO2 lasers. When optics change temperature, wavefront distortion occurs. This occurs through three mechanisms, listed here with the change they impose on a change in the optical path length $S$for a beam traveling through an optic:[108]

1. Thermo-optic change in refractive index n_T due to change in temperature T: $\Delta S - T = \int_S \Delta n_T dS = \frac{dn}{dT} \int_S \Delta T dS$
2. Elasto-optic change in refractive index n_E due to change in internal stresses: $\Delta S_E = \int_S \Delta n_E ds$
3. Thermo-elastic deformation u, the direct change in path length due to thermal expansion : $\Delta u \approx \alpha \int_s \Delta T ds$

where α is the coefficient of thermal expansion.

The phase distortion $\Phi(x, y)$ of a beam passing through the optic is related to the change in optical path length by:

$$\Phi(x, y) = \frac{2\pi}{\lambda} \Delta S(x, y) \tag{6.1}$$

All three effects alter the wavefront of a beam transmitted through the optic, but only the thermo-elastic distortion also affects a reflected wavefront. The thermo-optic effect is the largest effect, which impacts the wavefront 20x more than the thermo-elastic effect and 100x more than the elasto-optic effect, for a given change in temperature in a fused silica optic[104].

Light can be absorbed both at the surface of the optic or in the bulk with different absorption coefficients, and these effects must be considered separately. Point absorbers may absorb more light than the surrounding material.

6.2.1 The Hello-Vinet method

The Hello-Vinet approach calculates the wavefront distortion due to uniform optical absorption in a cylindrically symmetric system[110]. This analytical method is relatively quick and simple to implement and can be used to model both static and transient[111] heating effects.

6.2.2 Finite Element Analysis

For more complex heat inputs, such as the effect of the ring heater, Finite Element Analysis (FEA) is commonly used. A wide variety of problems can be solved numerically using FEA. The equations for calculating temperature T) and internal stress distribution (σ) for an unconstrained object in free fall, from a given heat distribution are:[112][104]

$$\rho C_p \frac{\delta T}{\delta t} + \nabla q = g(T, t, \mathbf{x}) \tag{6.2}$$

$$\sigma = -\frac{E\alpha\Delta T}{1-2\nu} \tag{6.3}$$

where ρ is the density, C_p is the heat capacity, t is time, $\mathbf{q}$ is the heat flux vector and g is a function that describes the heat input, and E is Young's modulus, α is the coefficient of thermal expansion, and ν is Poisson's ratio.

The internal strain ϵ can be calculated from the internal stress σ, where C is the stiffness tensor:[113]

$$\epsilon = C\sigma + \alpha\Delta T \tag{6.4}$$

To model a three-dimensional problem without symmetry, calculating the rank 12 strain tensor ϵ is computationally expensive and takes considerably more computing time than calculating the temperature distribution.

Reciprocity calculates the surface distortion from the temperature distribution in a different way, resulting in a reduction in computation time.

6.2.3 Elasto-dynamic Reciprocity

The theory of elasto-dynamic reciprocity is summarized in the book "Reciprocity in Elastodynamics" by Achenbach [114]. It was used by Levin et al to determine creep in fibers[115]. It has not been used to model optics before.

The general equation for elasto-dynamic reciprocity is expressed in Equation 6.5, where t is the traction, u is the displacement and f is the internal body force, S is a surface of the optic and V is the volume of the optic, superscripts 1 and 2 represent two different states, and the Einstein convention is used.[116]

$$\int_S (t_i^2(\vec{r})u_i^1(\vec{r}) - t_i^1(\vec{r})u_i^2(\vec{r}))dS = \int_V (f_i^2(\vec{r})u_i^1(\vec{r}) - f_i^1(\vec{r})u_i^2(\vec{r}))dV \tag{6.5}$$

We demonstrate that these equations can be used to calculate the surface distortion of an optic due to heating in a way which is more time efficient than conventional FEA modeling, as will be further explained in Section 6.4 Part II.

6.3 Modeling Thermal Deformations using Reciprocity

This section covers some of the factors that needed to be considered in order to successfully implement the method described in Section 6.4. The most important considerations were the appropriate choice of boundary conditions on the optic and mathematical basis set for describing the surface distortion.

6.3.1 Boundary Conditions

The LIGO optics are suspended on pendulum suspensions, and when modeling them using FEA we assume they are unconstrained in all directions. All attempts to constrain an edge, face or point of the optic (eg Figure 6.1 parts a and b), led to nonphysical deformations along the edge of the constraint.

This posed a difficulty when applying the pseudo-forces required to calculate the

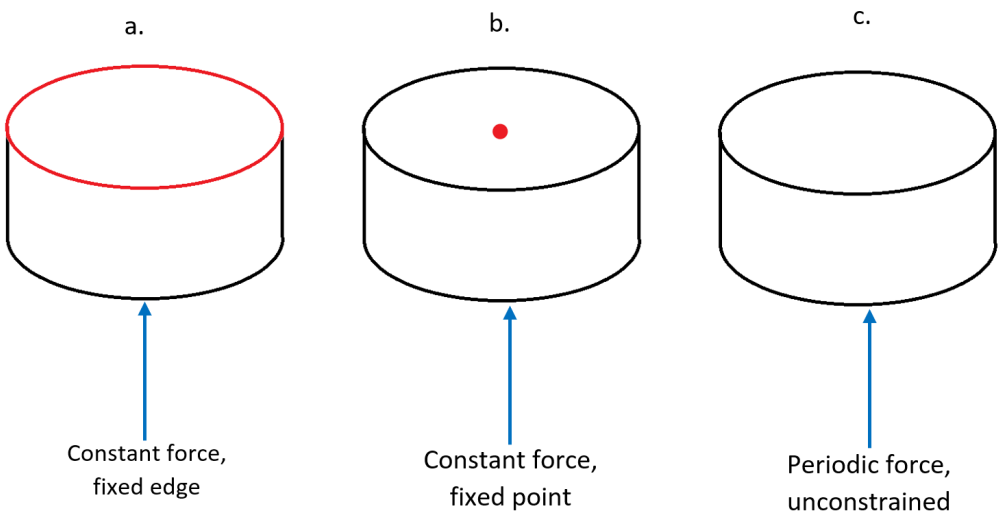

Fig. 6.1: The various boundary conditions that were applied to the optic: (a) a fixed boundary condition around one edge of one face and a constant force applied across the other face; (b) a fixed boundary condition applied to the center point of one face and a constant force applied across the other face; (c) no boundary constraints, and a periodic force applied to one face which averages over time to zero.

basis set of strains using reciprocity, because applying a constant force to one face of the optic will cause the optic to accelerate in one direction, and the solution will never converge.

To overcome this issue, we moved away from a steady force to a time-varying, periodic force (Equation 6.6). As long as the period of oscillation is less than the mechanical harmonic modes of the material, the deformation of the optic at maximum force will be approximately equal to the deformation of the unconstrained optic with the same force applied.

$$t_i(\vec{r}, t) = t_i(\vec{r})e^{i\omega t} \tag{6.6}$$

6.3.2 Choice of Basis Set

The choice of an appropriate basis set to describe the surface displacement was key to calculating the surface distortion to sufficient accuracy. We tried using Zernike

functions, Seidel functions, Hermite-Gauss (HG) functions and Laguerre-Gauss (LG) functions as potential basis sets[117]. Zernike functions have the desirable property that they are orthonormal over a unit disc, so that they can be scaled to be orthonormal over the front surface of an optic. Seidel functions express the deformation in terms of 3rd order aberrations. However, HG and LG functions are desirable because their shape is close to actual thermal profiles commonly seen in optics absorbing laser power, but using them in reciprocity relations proved problematic because they are not orthonormal over a circular disc. However, it is possible to normalize them over this surface using the Gram-Schmidt procedure of symmetric orthogonalization. (This method is explained in more detail in Section 6.4 Part IV.) Once normalized over a circular disc, the LG modes look similar to HG modes, but are orthonormalized (Figure 6.2). This orthonormalization step proved crucial for accurately generating the correct surface shape using reciprocity.

6.4 Publication

The results of this investigation are summarized in the following paper; "Modelling Thermal Distortion of Optics using Elastodynamic Reciprocity". My contribution to this paper was to take the equations for elasto-dynamic reciprocity and use them in finite element analysis modeling to develop a proof of concept model of a mirror. I applied the theory to the optical system under investigation, created all of the models, lead the investigations into boundary conditions and choice of basis sets, and performed all calculations and computational analyses. David Ottaway and Yuri Levin formulated the original approach. Yuri consulted on choice of basis set. David suggested the application of the method to scattering coefficients. Peter Veitch assisted with the choice of boundary conditions, suggested moving from static to periodic time-dependent forces, and using symmetric othogonalization of the HG LG bases.

Statement of Authorship

Title of Paper	Modelling Thermoelastic Distortion of Optics Using Elastodynamic Reciprocity
Publication Status	☒ Published ☐ Accepted for Publication ☐ Submitted for Publication ☐ Unpublished and Unsubmitted work written in manuscript style
Publication Details	Published in Physical Review D 92, 022005 - on 20 July 2015

Principal Author

Name of Principal Author (Candidate)	Eleanor King
Contribution to the Paper	Created proof of concept model, performed all calculations and computational analyses, lead investigation into boundary conditions and basis sets
Overall percentage (%)	60%
Certification:	This paper reports on original research I conducted during the period of my Higher Degree by Research candidature and is not subject to any obligations or contractual agreements with a third party that would constrain its inclusion in this thesis. I am the primary author of this paper.
Signature	Date: 20/1/21

Co-Author Contributions

By signing the Statement of Authorship, each author certifies that:

i. the candidate's stated contribution to the publication is accurate (as detailed above);

ii. permission is granted for the candidate in include the publication in the thesis; and

iii. the sum of all co-author contributions is equal to 100% less the candidate's stated contribution.

Name of Co-Author	David Ottaway
Contribution to the Paper	Formulated original approach with Yuri and suggested application of method to scattering coefficients
Signature	Date: 20/1/2021 ~~31/6/2021~~

Name of Co-Author	Peter Veitch
Contribution to the Paper	Assisted with choice of boundary conditions and suggested moving to time dependent forces and using symmetric orthogonalization of basis sets
Signature	Date: 20/1/21

Please cut and paste additional co-author panels here as required.

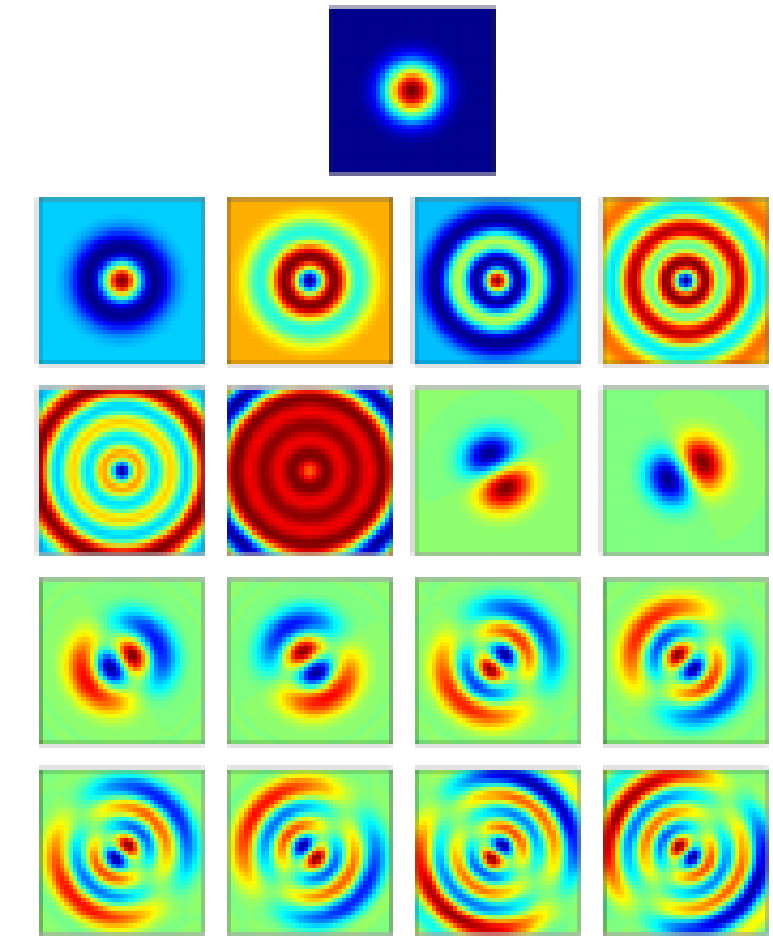

Fig. 6.2: The 17 lowest order Laguerre Gauss modes, after they have been orthonormalized to a unit disk using Gram-Schmidt orthonormalization.

Statement of Authorship

Title of Paper	Modelling Thermoelastic Distrotion of Optics Using Elastodynamic Reciprocity
Publication Status	☒ Published ☐ Accepted for Publication ☐ Submitted for Publication ☐ Unpublished and Unsubmitted w ork w ritten in manuscript style
Publication Details	Published in Physical Review D 92, 022005 - on 20 July 2015

Principal Author

Name of Principal Author (Candidate)	See page 1		
Contribution to the Paper			
Overall percentage (%)			
Certification:	This paper reports on original research I conducted during the period of my Higher Degree by Research candidature and is not subject to any obligations or contractual agreements with a third party that would constrain its inclusion in this thesis. I am the primary author of this paper.		
Signature		Date	

Co-Author Contributions

By signing the Statement of Authorship, each author certifies that:

i. the candidate's stated contribution to the publication is accurate (as detailed above);

ii. permission is granted for the candidate in include the publication in the thesis; and

iii. the sum of all co-author contributions is equal to 100% less the candidate's stated contribution.

Name of Co-Author	Yuri Levin		
Contribution to the Paper	Formulated original approach with David and consulted on choice of basis set		
Signature		Date	25/1/2021

Name of Co-Author			
Contribution to the Paper			
Signature		Date	

Please cut and paste additional co-author panels here as required.

Modelling Thermoelastic Distortion of Optics Using Elastodynamic Reciprocity

Eleanor King,[1,*] Yuri Levin,[2] David Ottaway,[1] and Peter Veitch[1]

[1] *Department of Physics, The University of Adelaide, Adelaide SA 5005, Australia*
[2] *School of Physics, Monash University, Clayton VIC 2800, Australia*

Thermoelastic distortion resulting from optical absorption by transmissive and reflective optics can cause unacceptable changes in optical systems that employ high power beams. In advanced-generation laser-interferometric gravitational wave detectors, for example, optical absorption is expected to result in wavefront distortions that would compromise the sensitivity of the detector; thus necessitating the use of adaptive thermal compensation. Unfortunately, these systems have long thermal time constants and so predictive feed-forward control systems could be required - but the finite-element analysis is computationally expensive. We describe here the use of the Betti-Maxwell elastodynamic reciprocity theorem to calculate the response of linear elastic bodies (optics) to heating that has arbitrary spatial distribution. We demonstrate using a simple example, that it can yield accurate results in computational times that are significantly less than those required for finite-element analyses.

I. INTRODUCTION

Advanced-generation interferometric gravitational wave detectors, such as Advanced LIGO [1], Advanced Virgo [2] and KAGRA [3] are currently being commissioned. Their sensitivity is expected to surpass that achieved by first generation instruments by almost an order of magnitude in the high frequency region. To achieve this, very high circulating power levels (0.5-1 MW) will be stored within the Fabry-Perot arm cavities. At these power levels, even low levels of optical absorption can lead to significant thermoelastic distortion of optical surfaces and unacceptable levels of wavefront distortion [4], resulting in reduced circulating power and a reduction in the efficiency of the detector signal readout. Thermally actuated compensation systems will be thus used to ameliorate the wavefront distortion. However, the thermal time constants for the absorption-induced distortion and the compensation are long, typically 12 hours, and thus incorporating predictive modeling in the control systems may prove essential.

The response of a linear elastic system to heating is described by the theory of thermo-elasticity and its applications to highly symmetric, idealized systems are described in many books (see [5] for example). It has also been used to develop analytic expressions for less idealized optical systems [4, 6]. The expressions developed by Hello and Vinet [6] are relevant to the work described here, but apply only to cylindrical isotropic mirrors heated by coaxial laser beams.

More complicated systems, which incorporate asymmetric heating or anisotropic elasticity, can be investigated using finite-element numerical models that apply the equations of thermo-elasticity on a three-dimensional spatial mesh. For dynamic systems, the thermoelastic equations must be solved at each epoch, requiring computational times that can run to many days. This approach would be untenable for use in predictive feed-forward actuation to control systems. In such cases, the solution of the scalar problem to determine the temperature profile throughout the optic can be solved rapidly; the time consuming part is solving the tensor-based elasticity problem to convert the thermal profile into an elastic distortion.

The Betti-Maxwell theorem of elastodynamic reciprocity [7] provides an alternative approach to using finite-element methods (FEM) to solve the tensor part of the thermoelastic distortion. It has previously been used to investigate the excitation of Rayleigh-Lamb elastic waves in a metal plate due to heating produced by a line-focused pulsed laser beam assuming that the heating is confined to the surface of the plate and it has infinite lateral extent [8, 9]. In the context of gravitational wave detection, it has been used to compute the interferometer's response to creep events in the fibers that suspend the optics [10]. We extend its use to predict thermoelastic distortion of an optic of finite size with asymmetric heating.

We describe here how elastodynamic reciprocity and FEM can be combined to provide accurate predictions of thermoelastic surface distortion more quickly than using FEM alone. In summary, FEM is used to determine the response of the optic to a set of orthonormal tractions, or pressures —a computationally expensive calculation that is performed once for an optic. Then, using reciprocity, the distortion due to the instantaneous temperature profile in the optic is calculated using a sum of scalar volume integrals that incorporate these responses. The computational cost of this step is much less than that of a full elastostatic FEM evaluation. Additionally, it is amenable to parallelization, which would further reduce the computational time.

The layout of the rest of the paper is as follows: in Section II we introduce the Betti-Maxwell theorem of elastodynamics and show how it can be used to determine the surface distortion by careful choice of a suitable auxiliary elastic system. We demonstrate its application by calculating the distortion of the end face of a cylindrical optic that is heated by a Gaussian heat flux that

* Corresponding author: eleanor.king@adelaide.edu.au

is (a) coaxial with and (b) laterally displaced from the axis. The approach and model are described in Sections III and IV. Finally, the resulting surface distortions are presented in Section V and compared with the results of elastostatic FEM calculations. Computation times for these two approaches are compared in Section VI

II. ELASTODYNAMIC RECIPROCITY AND THERMAL DISTORTION

The Betti-Maxwell reciprocity theorem for elastodynamics [7, 9] specifies the relationship between the displacement $\vec{u}(\vec{r},t)$ that results from an applied surface traction $\vec{t}(\vec{r},t)$ and internal body force $\vec{f}(\vec{r},t)$ for two elastic states of a linear elastic body:

$$\int_S (t_i^2 u_i^1 - t_i^1 u_i^2) dS = \int_V \Big[(f_i^1 - \rho \ddot{u}_i^1) u_i^2 - (f_i^2 - \rho \ddot{u}_i^2) u_i^1 \Big] dV \quad (1)$$

where ρ is the density, $\ddot{u}$ is acceleration, the superscripts 1 and 2 represent the two states, and the Einstein summation convention is used. If $t_i(\vec{r},t) = t_i(\vec{r})e^{i\omega t}$ and $f_i(\vec{r},t) = f_i(\vec{r})e^{i\omega t}$ then $u_i(\vec{r},t) = u_i(\vec{r})e^{i\omega t}$, and thus Eq. (1) becomes

$$\int_S \Big(t_i^2(\vec{r}) u_i^1(\vec{r}) - t_i^1(\vec{r}) u_i^2(\vec{r}) \Big) dS = \int_V \Big(f_i^1(\vec{r}) u_i^2(\vec{r}) - f_i^2(\vec{r}) u_i^1(\vec{r}) \Big) dV \quad (2)$$

We shall use this theorem to determine the surface displacement (distortion) due to heating of an optic by, for example, partial absorption of an incident laser beam. For the first state, which we shall refer to as the thermal state and label T, we assume that the optic is free and thus $t_i^T = 0$, and there is a non-zero body force due to the heating. Since we are interested in the distortion of the end face of the optic, we choose the second state, which is often referred to as the auxiliary state and we shall label A , to have a traction t_z^A applied to the end face of the optic and assume $f_i^A = 0$. Thus, Eq. (2) becomes

$$\int_S t_z^A(\vec{r}) u_z^T(\vec{r}) dS = \int_V f_i^T(\vec{r}) u_i^A(\vec{r}) dV = \int_S \sigma_{ij}^T(\vec{r}) \varepsilon_{ij}^A(\vec{r}) dV \quad (3)$$

where $\varepsilon_{ij}^A(\vec{r})$ is the internal strain produced by the traction $t_z^A(\vec{r})$, and $\sigma_{ij}^T(\vec{r})$ is the internal stress associated with the body force: $f_i^T = -\frac{\partial \sigma_{ij}^T}{\partial x_j}$.

Consider now applying time-harmonic tractions with amplitude $t_z^A(\vec{r}_s) = \chi_n(\vec{r}_s)$ $n = 1, 2, ...$ It is convenient to choose $\chi_n(\vec{r}_s)$ to be orthonormal, so that $\int \chi_n(\vec{r}_s)\chi_m(\vec{r}_s) dS = \delta_{nm}$. Then, expressing the surface displacement amplitude as:

$$u_z^T(\vec{r}) = \sum_m a_m \chi_m(\vec{r}) \quad (4)$$

transforms the left-hand term of Eq. (3) to

$$\int_S t_z^A(\vec{r}) u_z^T(\vec{r}) dS = \int_S \chi_n(\vec{r}) \sum_m a_m \chi_m(\vec{r}) dS = a_n. \quad (5)$$

Therefore

$$a_n = \int_V \sigma_{ij}^T(\vec{r}) \varepsilon_{ij}^A(\vec{r}) dV \quad (6)$$

That is, if the amplitude of the elastic response of the optic, $\epsilon_{ij}^A(\vec{r})$, to each of the tractions $\chi_n(\vec{r})$ is known then the amplitude of the distortion of the end face of the optic, $u_z^T(\vec{r})$, due to any thermal stress distribution can be calculated using Eqs. (4) and (6).

We shall use this approach to calculate the surface distortion due to non-uniform heating of a homogeneous isotropic body for which

$$\sigma_{ij}^T(\vec{r}) = \frac{-E\alpha}{1-2\nu} \Delta T(\vec{r}) \delta_{ij} \quad (7)$$

where E is Young's modulus, α is the coefficient of thermal expansion, ν is Poisson's ratio, $\Delta T = T(\vec{r}) - T_0$, and T_0 is the ambient temperature. Eq. 6 thus becomes

$$a_n = \frac{-E\alpha}{1-2\nu} \int_V (T(\vec{r}) - T_0) \mathrm{Tr}\big\{ \varepsilon^A(\vec{r}) \big\} dV \quad (8)$$

III. IMPLEMENTATION

To determine the distortion of the end-face using reciprocity, one must first characterize the response of the elastic system, $\varepsilon_{ij}^A(\vec{r})$, to a set of orthonormal basis tractions $t_z^A(\vec{r},t) = \chi_n(\vec{r}) \exp[i\omega t] : n = 1, ..., N$ using an elastostatic FEM [11].

Zernike functions would be a tempting choice given our cylindrical geometry, particularly as they are orthogonal to a uniform traction and thus applying the auxiliary tractions should not apply net forces to the system. However, as shown in Section IV, they are not well suited to describing the surface distortion.

The orthonormal basis tractions we shall use apply a non-zero (instantaneous) force to the optic, leading to ill-conditioning of the FEM at very low frequencies. We thus used a traction frequency of $\omega = 1$ Hz as the response is

independent of frequency for frequencies well below the first resonance - see [12] for example.

In all of our numerical tests, we assume a cylindrical fused silica optic with height $h = 200$ mm , radius $R = 170$ mm , $E = 731$ MPa, $\nu = 0.17$ and $\alpha = 0.55 \times 10^{-6}$ K^{-1} . A radial cross section of the optic and the meshing used for the FEM is shown in Fig. 1.

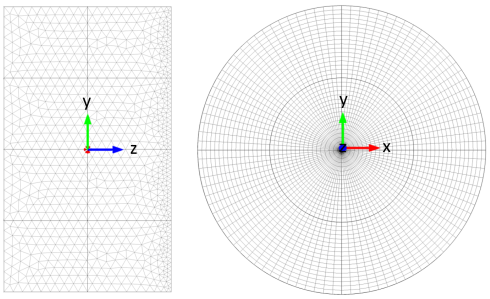

Figure 1. A radial cross-section of the cylindrical optic, showing the mesh used for the FEM. The mesh consisted of 32000 nodes, and is finest on the heated top surface of the test mass.

We assume heating of the top face by 1 W of power absorbed with a Gaussian-distributed flux:

$$Q(x,y) = \frac{2}{\pi w^2} \exp\left[-2\big((x-x_0)^2 + (y-y_0)^2\big)/w^2\right]$$

where the beam radius $w = 53$ mm, and radiative cooling of all surfaces of the optic to surroundings at 293 K. A thermal FEM [11] is used to calculate the temperature distribution, $T(\vec{r})$, resulting from the heating. The displacement amplitude for each basis function, a_n , and the total displacement, $u_z^T(\vec{r},t)$, are then calculated using Eq. 4 and Eq. 8.

IV. CHOICE OF ORTHONORMAL BASIS FUNCTIONS

Choosing a set of orthonormal functions $\chi_n(\vec{r})$ that can describe the surface distortion without requiring a large number of functions, which would necessarily include high spatial frequencies, is crucial as it reduces both the number of auxiliary tractions that must be evaluated and the requirement for using a fine mesh in the FEM. Thus, we describe the choice of basis functions for on-axis and off-axis heating of the optic.

A. Orthonormal basis for on-axis heating ($x_0 = 0, y_0 = 0$)

Zernike polynomials (see Appendix A) are often used to describe cylindrically symmetric optical aberrations, as they are orthogonal over a circular disc and can be normalized. However, as shown in Figure 2, these polynomials are not well suited to describing the distortion.

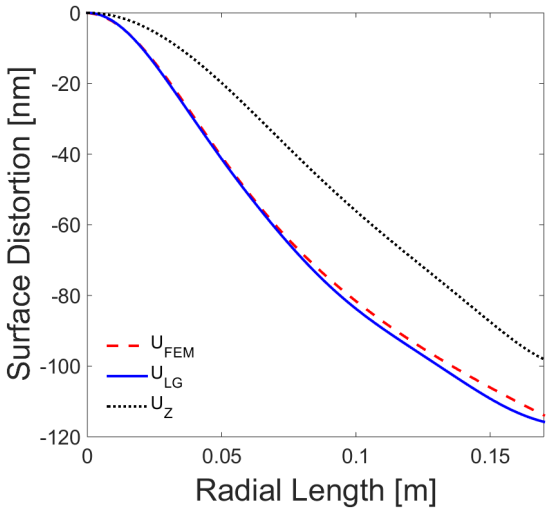

Figure 2. Comparison of the surface distortion calculated using the elastodynamic FEM, $u_{\rm FEM}$, the sum of the first six Zernike components $u_{\rm Z}$, and the sum of the first six orthonormalized LG components $u_{\rm LG}$

On-axis surface distortion due to the heating can also be described using Laguerre-Gauss (LG) functions:

$$LG_p(r) = L_p\Big(\frac{2r^2}{r_0^2}\Big) \exp\Big[\frac{-r^2}{r_0^2}\Big]$$

where L_p are Laguerre polynomials of order p : $\{0, 1, 2...\}$ (see Appendix A), r is the radial coordinate and r_0 is a free parameter. These functions are orthogonal only over the infinite plane however.

Symmetric orthogonalization [12] is therefore used, as outlined in Appendix B, to construct linear combinations, χ_n , of LG functions that are orthonormal over the end face for a given r_0 . In this type of orthogonalization, the difference between the new and original functions is minimized in the least-squares sense [12].

The optimum value of r_0 was chosen as described in Appendix C, giving $r_0 = 1.5w$. The six lowest-order orthonomalized-LG functions are defined in Appendix D. A comparison of $u_{\rm FEM}$ and the sum of these components in Fig. 2 shows that the LG basis is much superior to the Zernike basis.

B. Orthonormal basis for off-axis heating

The distortion due to off-axis heating can be described using the sets of functions listed below:

(a) Hermite-Gauss (HG) functions:

$$HG_{mn}(x,y) = H_m\Big(\frac{\sqrt{2}x}{r_{0x}}\Big) \exp\Big[\frac{-x^2}{r_{0x}^2}\Big] H_n\Big(\frac{\sqrt{2}y}{r_{0y}}\Big) \exp\Big[\frac{-y^2}{r_{0y}^2}\Big]$$

where H_i are the (physicists) Hermite polynomials of order $i : \{0, 1, 2, ...\}$ (see Appendix A). These functions are orthogonal over the interval $x, y : (-\infty, \infty)$. We choose $r_{0x} = r_{0y} \equiv r_0$ as the heat flux has a circular cross section and we shall use $x_0, y_0 << R$, and thus

$$HG_{mn}(x, y) = H_m\Big(\frac{\sqrt{2}x}{r_0}\Big)H_n\Big(\frac{\sqrt{2}y}{r_0}\Big)\exp\Big(\frac{-(x^2+y^2)}{r_0^2}\Big)$$

(b) Generalized LG functions:

$$LG_p^l(r) = L_p\Big(\frac{2r^2}{r_0^2}\Big)\exp\Big[\frac{-r^2}{r_0^2}\Big]\begin{cases}1\\ \sin l\phi\\ \cos l\phi\end{cases}$$

where ϕ is the azimuthal angle, and $l : \{1, 2, 3, ...\}$ for $p > 0$. We restricted the azimuthal dependence to $l = 1$ due to the symmetry of the expected distortion.

Orthonormalized HG and generalized-LG functions were constructed, and an optimized value of $r_0 = 1.4w$ was selected as discussed above.

HG functions up to $m+n = 15$ (136 functions in total) were initially used to describe the distortion due to a heating beam that was displaced from the center of the optic according to (x_0, y_0) =(0,10 mm), (10 mm, 0) and (8.7 mm, 5 mm).

In each case, the distortion was dominated by the same 17 components, the functions for which are plotted in Appendix E. A comparison of u_{FEM} and the sum of the dominant 19 components is shown in Fig. 3 .

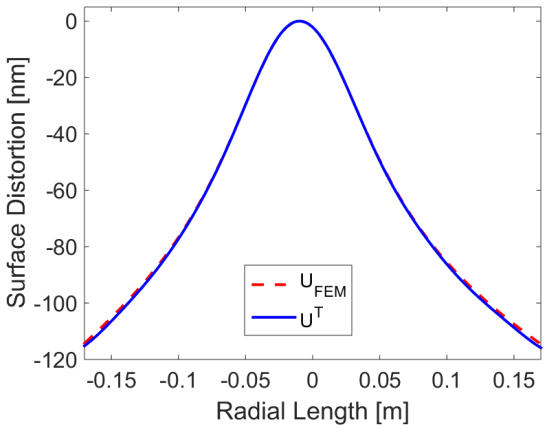

Figure 3. Comparison of u_{FEM} and the sum of the 17 dominant orthonormalized-HG components u^T for a heat flux offset of 10 mm

Orthonormalized generalized-LG functions up to $p = 5$ (16 functions in total) were also generated and used to describe the distortion due to a heat flux displaced from the center of the optic by 10 mm, but they yielded slightly poorer agreement with u_{FEM} . In addition, since the lower order orthonormalized-HG functions appear similar to the TEM_{01} and TEM_{10} eigenmodes observed in optical cavities, we chose to use that basis.

Zernike polynomial	a_n(nm)	$a_{n,\text{FEM}}$(nm)
Z02	42.6	42.9
Z04	-15.2	-15.0
Z06	6.3	5.9
Z08	-2.8	-3.6

Table I. Zernike amplitudes calculated using reciprocity, a_n , and thermoelastostatic FEM, $a_{n,FEM}$, for the axisymmetric Gaussian heat flux.

V. SURFACE DISTORTION CALCULATED USING RECIPROCITY

We now show how to use the orthonormal bases described above with reciprocity to determine the surface distortion. In each case, the equilibrium $\varepsilon_{ij}^A(\vec{r})$ values were calculated for the basis tractions and then combined with the temperature distribution $T(\vec{r})$ from the thermal FEM to yield the amplitudes a_n.

A. On-axis heating: Zernike basis

While Zernike polynomials are not appropriate for describing the surface distortion in the example presented here, they can be used for a reciprocity-based calculation. Table I shows a comparison of the reciprocity Zernike amplitudes with those calculated by decomposing the distortion predicted by the thermoelastostatic FEM.

B. On-axis heating: orthonormalized-LG basis

The u_{FEM} and $u^T = \sum_{n=0}^{5} a_n\chi_n$, and the difference between the two curves are plotted in Fig. 4. Since we are not interested in the average displacement of the optics, we have set $u^T = u_{\text{FEM}}$ at $r = 0$. The asymmetry of the difference is due to non-ideal cylindrical symmetry in the FEM meshing.

C. Off-axis heating: orthonormalized-HG basis

The u_{FEM} and $u^T = \sum_{n=1}^{19} a_n\chi_n$ and the difference between the two curves are plotted in Fig. 5

Figures 4 and 5 show that even though < 20 auxiliary tractions were used to characterize the optic and the FEM was restricted to only 30,000 nodes,

- Elastodynamic reciprocity predicts u^T within $<$ 1.5% of u_{FEM} over the majority of the incident laser beam
- Displacing the beam by 20% of its radius does not degrade the agreement.

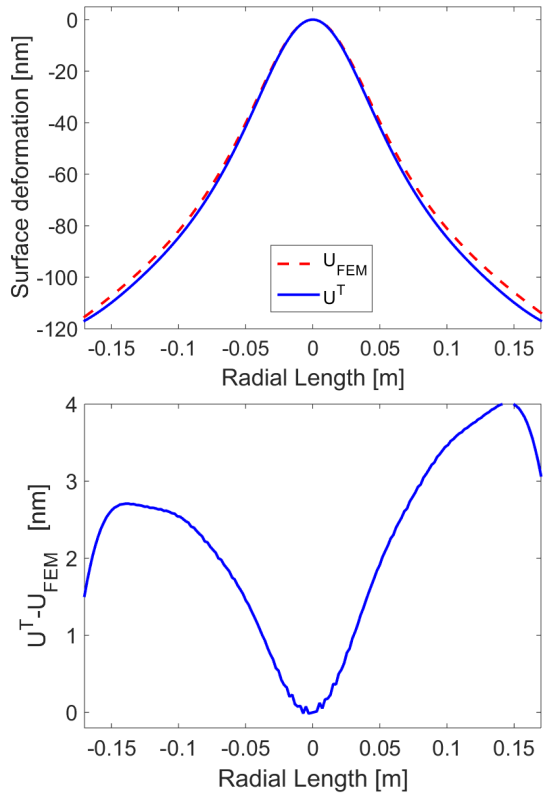

Figure 4. a) A plot of u_{FEM} and u^T calculated for the on-axis heating using the 6 lowest-order orthonormalized-LG functions. b) A plot of $u_{\text{FEM}} - u^T$.

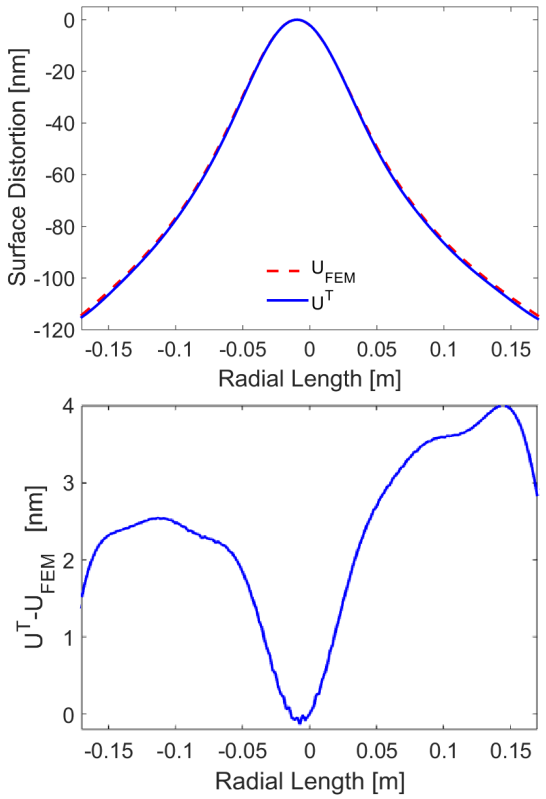

Figure 5. a) A plot of u_{FEM} and u^T calculated for the off-axis heating using the 17 dominant orthonormalized-HG functions. b) A plot of $u_{\text{FEM}} - u^T$.

Additionally, increasing the number of auxiliary tractions further improves the agreement, particularly at large radius.

VI. COMPARISON OF COMPUTATIONAL TIMES

We compare here the times required to calculate the surface distortion using our hybrid FEM-reciprocity approach and using a conventional thermo-elastic FEM analysis. The times are specific to the example of partial absorption of a Gaussian-intensity-profile light beam by the surface of an isotropic cylindrical optic.

In both cases we use 32,000 nodes in the FEM calculations. We have not yet investigated how many nodes or auxiliary tractions are required to achieve a particular accuracy for each approach, or how this might affect the computational times.

As discussed earlier, our hybrid FEM-reciprocity approach consists of two parts, the first of which is done only once for an optic:

1. (a) Calculate the elastic response of the optic to each of the orthonormal tractions, and store these arrays in memory. Here, this consisted of a 32,000 long 6-element array in which the 3D coordinates and strains at each node were recorded for each traction. This part required approximately 1 hour per traction.

   (b) Upload 20 responses into memory in preparation for part 2 required 20 minutes.

2. At each epoch of interest

   (a) Calculate the thermal induced stress at each node using FEM: 90 seconds

   (b) Evaluate the volume integral for each traction component using Eq. (6): 3 seconds per traction. Thus for a serial calculation with 20 tractions, this step required 60 seconds.

A conventional thermo-elastic FEM calculation for this simple problem required about 13 minutes.

Thus, once the response of the optic has been determined and uploaded, the hybrid FEM-reciprocity calculation is at 5.2 times faster is using a serial calculation, and 8.7 times faster if using a parallelized calculation of the distortion using reciprocity.

VII. CONCLUSION

We have shown how Betti-Maxwell reciprocity can be used in combination with thermal finite-element modeling to calculate the thermoelastic distortion of a linear elastic system. As an example, we described in detail its application to calculating the distortion of the end face of an isotropic cylindrical glass optic heated by an off-axis Gaussian laser beam. Despite using less than 20 auxiliary eigenfunction tractions to characterize the optic, the distortion calculated using reciprocity agrees to < 1.5 % with that calculated using a full thermoelastic FEM over the majority of the incident beam.

The computational time required for the reciprocity approach was a factor of 5-8 less than that for the full FEM once the optic had been characterized. The advantage of this approach will thus be most evident in cases where the elastic distortion must be calculated frequently, such as in feed-forward control of systems with long thermal time constants for example. Parallelization of the reciprocity calculation would also allow further improvements to the accuracy by employing additional tractions but with negligible additional computational cost.

Our reciprocity approach can be applied to systems with arbitrarily distributed heat fluxes and asymmetric anisotropic elastic bodies. Furthermore, while our example assumed a free optic, other boundary conditions could easily be incorporated into the analysis with an appropriate set of auxiliary eigenfunctions.

VIII. ACKNOWLEDGEMENTS

This research was supported by the Australian Research Council (ARC). Yuri Levin is supported by an ARC Future Fellowship

[1] Aasi, J., *et al.* (LIGO Scientific Collaboration) Class. Quant. Grav. **32**, 074001 (2015).
[2] Virgo Collaboration *et al.* , "Advanced virgo baseline design," (2009) VIR-027A-09 The Virgo Collaboration.
[3] K. Somiya, Class. Quant. Grav. **29**, 124007 (2012).
[4] R. C. Lawrence, Ph.D. thesis, Massachusetts Institute of Technology (2003).
[5] B. A. Boley and J. H. Weiner, *Theory of thermal stresses*, Courier Dover Publications, (2012).
[6] P. Hello and J.-Y. Vinet, J. Phys. **51**, 1267(1990).
[7] J. D. Achenbach, "Reciprocity and related topics in elastodynamics," Appl. Mech. Rev. **59**, 13 (2006).
[8] J. D. Achenbach, J. Therm. Stress. **28**, 713 (2005).
[9] J. D. Achenbach, J. Therm. Stress. **30**, 841 (2007).
[10] Y. Levin, Phys. Rev. D **86**, 122004 (2012).
[11] "Comsol multiphysics".
[12] H. Schweinler and E. Wigner, J. Math. Phys. **11**, 1693(1970).
[13] J. Vinet *et al.*, "The Virgo physics book", available online at: http://wwwcascina.virgo.infn.it/vpb .

Appendix A: Polynomials used in this paper

Zernike Polynomial	orthogonal form with $\rho = r/R$)
Z02	$\sqrt{\frac{3}{\pi}}(2\rho^2 - 1)$
Z04	$\sqrt{\frac{5}{\pi}}(6\rho^4 - 6\rho^2 + 1)$
Z06	$\sqrt{\frac{7}{\pi}}(20\rho^6 - 30\rho^4 + 12\rho^2 - 1)$
Z08	$\sqrt{\frac{9}{\pi}}(70\rho^8 - 140\rho^6 + 90\rho^4 - 20\rho^2 + 1)$

Table II. Zernike amplitudes calculated using reciprocity,a_n , and thermoelastostatic FEM, $a_{n,FEM}$, for the axisymmetric Gaussian heat flux.

n	$L_n(x)$	$H_n(x)$
0	1	1
1	$-X + 1$	$2x$
2	$(x^2 - 4x + 2)/2$	$4x^2 - 2$
3	$(-x^3 + 9x^2 - 18x + 6)/6$	$8x^3 - 12x$
4	$(x^4 - 16x^3 + 72x^2 - 96x + 24)/24$	$16x^4 - 48x^2 + 12$

Table III. Laguerre and Hermite polynomials used.

Appendix B: Summary of symmetric orthogonalization

The linearly independent LG and HG functions, denoted here by $f_k(\vec{r})$, were orthonormalized over the end face of the mirror using the following process [12]:

1. Calculate the matrix of inner products of the functions: $M_{kl} = \iint\limits_{end\ face} f_k(\vec{r}) f_l(\vec{r}) dS$ where the integration was evaluated for the mesh used to export the data from the FEM. In this work, the data was exported on a 1mm-pitch mesh and cropped to fit within the circular endface of the optic.

2. Determine the eigenvalues p_k and eigenvectors $\vec{u}_\lambda$ of the inner product matrix such that $\sum_l M_{kl} u_{l\lambda} = p_\lambda u_{k\lambda}$

3. The orthonormalized functions $\chi(\vec{r})$ are then given by $\chi_n = \frac{1}{\sqrt{p_n}} \sum_k u_{kn} f_k$

Appendix C: Optimization of r_0

The optimum r_0 was chosen to minimize the mean squared difference, weighted by the amplitude of the incident laser beam, between u_{FEM} and the sum of the selected orthonormalised components using:

$$\frac{\iint_{end\ face}\left(u_{FEM}-\sum_{n=0}^{5}a_n\chi_n\right)^2\exp\left[\frac{(x-x_0)^2+(y-y_0)^2}{w^2}\right]dS}{\iint_{end\ face}\exp\left[\frac{(x-x_0)^2+(y-y_0)^2}{w^2}\right]dS}$$

where

$$a_n=\iint_{end\ face}u_{\mathrm{FEM}}\chi_n dS$$

and a new orthonormal set of functions χ_n was generated for each value of r_0 . The integrations were evaluated using a square array of pitch 1 mm within the end face.

The variation of this mean-weighted-squared difference with r_0 for the axisymmetric heating ($y_0 = 0$) is plotted in Figure 6.

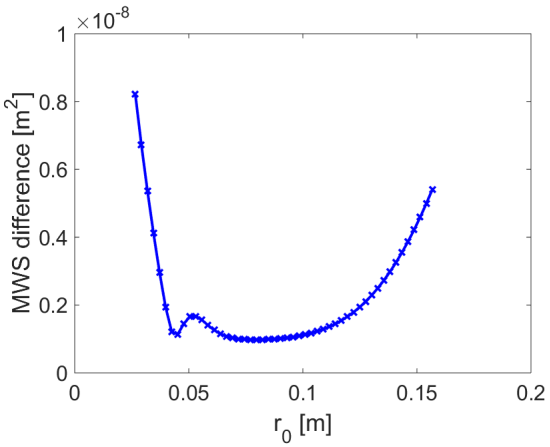

Figure 6. Plot of the mean-weighted-squared difference between u_{FEM} and the sum of the first six orthonormalized-LG components as a function of r_0 .

The variation of this mean-weighted-squared difference with r_0 for orthonormalized-HG functions and off-axis heating $y_0 = 10$ mm is plotted in Fig. 7.

Appendix D: Orthonormalized-LG functions used in this paper

$$\chi_n = c_{0n}LG_0 + c_{1n}LG_1 + c_{2n}LG_2 + c_{3n}LG_3 + c_{4n}LG_4 + c_{5n}LG_5$$

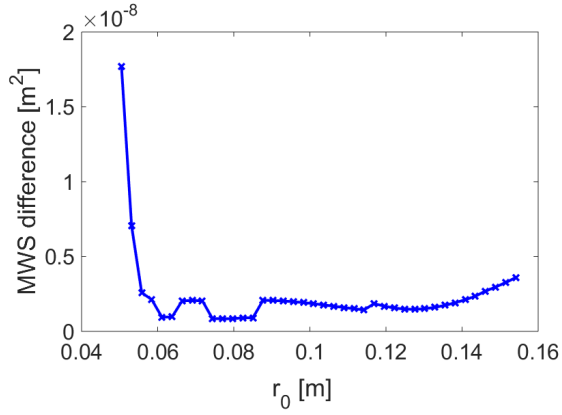

Figure 7. Plot of the mean-weighted-squared difference between u_{FEM} and the sum of the first six orthonormalized-HG components as a function of r_0 .

n	c_{0n}	c_{1n}	c_{2n}	c_{3n}	c_{4n}	c_{5n}
0	-0.97	-0.25	-0.06	-0.01	-0.001	-0.0001
1	0.24	-0.86	-0.43	-0.13	-0.028	-0.003
2	0.062	-0.42	0.69	0.55	0.20	0.039
3	0.016	-0.15	0.52	-0.53	-0.62	-0.24
4	0.005	-0.055	0.26	-0.58	0.40	0.79
5	-0.005	0.07	-0.4	1.23	-2.24	2.17

Appendix E: The 17 dominant orthonormalized-HG functions

The Hermite Gauss functions up to order $n + m = 15$ are orthogonalized using symmetric orthogonaliazation. Of these 136 modes, the 17 modes that make the largest contribution to describing the deformed surface were selected. These modes are shown in Fig. 8

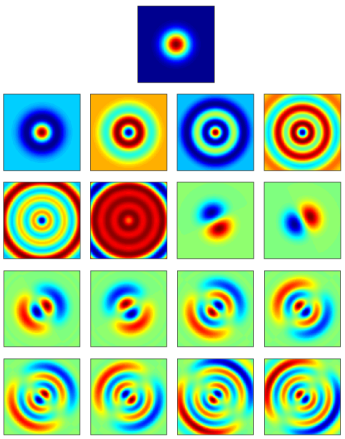

Figure 8. The 17 dominant orthonormalized-HG functions

6.5 Future work

The next step in using this method for modeling of GW interferometers would be to incorporate the reciprocity technique into interferometer modeling software such as FINESSE[77] in order to investigate the interaction between the thermal compensation system, which acts over long timescales, and the length and alignment control systems, which act over shorter time scales. This would involve calculating the change in phase distortion at each mirror for different heat inputs; a process which could be sped up using reciprocity.

Reciprocity can be used in FINESSE to calculate the change in shape of each mirror due to various TCS inputs. This could be calculated using the current reciprocity method, but would be faster to go directly from temperature profile to scattering coefficients. Coupling coefficients calculate the proportion of light scattered from one mode to another. FINESSE uses phase deformations to calculate scattering coefficients using the equation:

$$k_{n,m,n',m'} = exp(i2kz') \iint dx'dy' u_{n'm'} exp(ikx') u*_{n,m} \tag{6.7}$$

[118]

The proportion scattered light from the n, m^{th} to the n', m'^{th} mode for a beam entering a cavity parallel to the cavity axis . The exponential term can be simplified using linear expansion:

$$k_{n,m,n',m'} = exp(i2kz') \iint dx'dy' u_{n'm'} (1 + ikx' - k^2 x'^2 + ...) u*_{n,m} \tag{6.8}$$

[118]

Note the second term can be calculated directly from reciprocity integrals (and the calculation of the first term is trivial), but we also need to calculate the third x^2 term to reach a useful accuracy for k. Expanding the reciprocity technique to

calculate the x^2 term for k is would be an interesting area for future work.

6.6 Conclusion

The work in this chapter demonstrates that elasto-dynamic reciprocity can be used to speed up calculations of thermal deformations of optics, compared to using finite element analysis and the conventional stress-strain relations. A potential area for further study is to apply this technique to calculating scattering coefficients. This would allow the technique to be incorporated into interferometer modeling software such as FINESSE.

7. CONCLUSION

The aim of this thesis was to improve the understanding of the as-built alIGO detectors by performing characterization measurements of the these detectors. I used combination of measurements and modeling to improve the understanding of the as-built parameters of the LIGO interferometers, in order to advance commissioning efforts. The results are used in models for control design and additional system designs.

The measurements included:

1. Characterizing aLIGO cavities by measurements of cavity length, gouy phase, and mode matching.
2. Measuring scattering and absorption properties of the test masses in situ.
3. Developing techniques for faster modeling of thermal deformations of optics.

Chapter two presented a mathematical description of a Fabry-Perot and compound cavities, which is needed to perform the measurements in Chapters 3 and 4.

In chapter three, we used cavity scanning techniques to measure length gouy phase of following cavities. This was done to check that the as-built parameters agreed with the design values. Measurements were performed on the PRC length, the Michelson Schnupp asymmetry, and the SRC length. All agree with the as-built parameters except for the SRC length. For in-vacuum cavities, this is an accurate method for probing high-Finesse cavities cavities. It falls down for lower Finesse cavities, such as the SRC.

In chapter 4, looked at alternative way of probing the SRC gouy phase. I presented a mathematical description of the measurement technique and a model of the

range of expected results. I performed the measurement, however I was unable to obtain a meaningful result due to the too-large uncertainties on the spot positions on the cameras. This uncertainty cannot be reduced as the suspensions movement is uncontrolled in the unlocked cavity and because the SRC mirrors are too small to move the beam over a larger distance.

In chapter 5 we looked at the ITM and ETM optics, characterizing scatter and absorption. These measurements were performed using cameras and HWS cameras. The Scatter in the IMC stayed at a relatively constant over time. In the ETM was used to determine there was contamination on the ETM, and that it significantly decreased after cleaning. The investigation of scatter in the interferometers shows that the current contamination control procedures are working well. The absorption measurements on the ETMs show that the absorption is within expected design levels. The absorption measurements have been used to update models of the thermal compensation system.

In chapter 6, I developed a faster method for calculating surface deformations. This technique may be used to speed up modeling of thermal effects on cavity fields in programs such as Finesse.

An instrument that is largely in-vacuum, requires a special range of techniques probe and characterize the cavities. These measurements verify that the detector components are behaving as expected, and improve the understanding of the as-built detector, because as-built cavities and optics can vary from the design.

Appendix A

LIST OF SELECTED PUBLICATIONS

King, E., Levin, Y., Ottaway, D., Veitch, P. (2015). **Modeling thermoelastic distortion of optics using elastodynamic reciprocity.** Physical Review D - Particles, Fields, Gravitation, and Cosmology, 92(2), 022005-1-022005-8. doi:10.1103/PhysRevD.92.022005

Staley A, Hoak D, Effler A, Izumi K, Dwyer S, Kawabe K, King EJ, Rakhmanov M, Savage RL, Sigg D (2015). **High precision optical cavity length and width measurements using double modulation.** Optics Express, 23(15), 19417-19431. doi:10.1364/OE.23.019417

Mueller CL, Fulda P, Adhikari RX, Arai K, Brooks AF, Chakraborty R, Frolov VV, Fritschel P, King EJ, Tanner DB, Yamamoto H, Mueller G (2015). **In situ characterization of the thermal state of resonant optical interferometers via tracking of their higher-order mode resonances.** Classical and Quantum Gravity, 32(13), 135018-1-135018-13. doi:10.1088/0264-9381/32/13/135018

Brooks AF, Abbott B, Arain MA, Ciani G, Cole A, Grabeel G, Gustafson E, Guido C, Heintze M, Heptonstall A, Jacobson M, Kim W, King E, Lynch A, O'Connor S, Ottaway D, Mailand K, Mueller G, Munch J, Sannibale V, Shao Z, Smith M, Veitch

P, Vo T, Vorvick C, Willems P (2016). **Overview of Advanced LIGO adaptive optics.** Applied Optics, 55(29), 8256-8265.
doi:10.1364/AO.55.008256

Evans M, Gras S, Fritschel P, Miller J, Barsotti L, Martynov D, Brooks A, Coyne D, Abbott R, Adhikari RX, Arai K, Bork R, Kells B, Rollins J, Smith-Lefebvre N, Vajente G, Yamamoto H, Adams C, Aston S, Betzweiser J, Frolov V, Mullavey A, Pele A, Romie J, Thomas M, Thorne K, Dwyer S, Izumi K, Kawabe K, Sigg D, Derosa R, Effler A, Kokeyama K, Ballmer S, Massinger TJ, Staley A, Heinze M, Mueller C, Grote H, Ward R, King E, Blair D, Ju L, Zhao C (2015). **Observation of parametric instability in advanced LIGO.** Physical Review Letters, 114(16), 6 pages.
doi:10.1103/PhysRevLett.114.161102

Staley A, Martynov D, Abbott R, Adhikari RX, Arai K, Ballmer S, Barsotti L, Brooks AF, Derosa RT, Dwyer S, Effler A, Evans M, Fritschel P, Frolov VV, Gray C, Guido CJ, Gustafson R, Heintze M, Hoak D, Izumi K, Kawabe K, King EJ, Kissel JS, Kokeyama K, Landry M, McClelland DE, Miller J, Mullavey A, Oreilly B, Rollins JG, Sanders JR, Schofield RMS, Sigg D, Slagmolen BJJ, Smith-Lefebvre ND, Vajente G, Ward RL, Wipf C (2014). **Achieving resonance in the Advanced LIGO gravitational-wave interferometer.** Classical and Quantum Gravity, 31(24), 245010-1-245010-14.
doi:10.1088/0264- 9381/31/24/245010

BIBLIOGRAPHY

[1] LIGO Scientific Collaboration, Virgo Collaboration, et al. **Observation of Gravitational Waves from a Binary Black Hole Merger**. *Physical Review Letters*, 116(6):061102, 2016.

[2] LIGO Scientific Collaboration, Virgo Collaboration, et al. **Properties of the Binary Black Hole Merger GW150914**. *Physical Review Letters*, 116(24):241102, 2016.

[3] LIGO Scientific Collaboration, Virgo Collaboration, et al. **GW151226: Observation of Gravitational Waves from a 22-Solar-Mass Binary Black Hole Coalescence**. *Physical Review Letters*, 116(24):241103, 2016.

[4] LIGO Scientific Collaboration, Virgo Collaboration, et al. **GW170104: Observation of a 50-Solar-Mass Binary Black Hole Coalescence at Redshift 0.2**. *Physical Review Letters*, 118(22):221101, 2017.

[5] LIGO Scientific Collaboration, Virgo Collaboration, et al. **GW170817: Observation of Gravitational Waves From a Binary Neutron Star Inspiral**. *Physical Review Letters*, 119(16):161101, 2017.

[6] Albert Einstein. **Approximative Integration of the Field Equations of Gravitation**. *Sitzungsber. Preuss. Akad. Wiss. Berlin (Math. Phys.)*, 688:1916, 1916.

[7] Eric D Black and Ryan N Gutenkunst. **An Introduction to Signal Ex-**

traction in Interferometric Gravitational Wave Detectors. *American Journal of Physics*, 71(4):365–378, 2003.

[8] Kip S Thorne. **Gravitational Radiation-a new window onto the Universe.** In *Reviews in Modern Astronomy*, volume 10, pages 1–28, 1997.

[9] LIGO Scientific Collaboration, Virgo Collaboration, et al. **LIGO: the Laser Interferometer Gravitational-Wave Observatory**. *Reports on Progress in Physics*, 72(7):076901, 2009.

[10] Brett Bochner. ***Modelling the Performance of Interferometric Gravitational-Wave Detectors with Realistically Imperfect Optics***. PhD thesis, Massachusetts Institute of Technology, 1998.

[11] Krzysztof Belczynski, Vassiliki Kalogera, and Tomasz Bulik. **A comprehensive study of Binary Compact Objects as Gravitational Wave Sources: Evolutionary channels, rates, and physical properties**. *The Astrophysical Journal*, 572(1):407, 2002.

[12] LIGO lab. **Frequently Asked Questions**. `http://www.ligo.org/science/faq.php`, [Accessed: 4/1/2017].

[13] E Sterl Phinney. **The rate of Neutron Star Binary mergers in the universe-Minimal predictions for Gravity Wave Detectors**. *The Astrophysical Journal*, 380:L17–L21, 1991.

[14] Kent Yagi and Leo C Stein. **Black Hole Based Tests of General Relativity**. *Classical and Quantum Gravity*, 33(5):054001, 2016.

[15] LIGO Scientific Collaboration, Fermi GBM Virgo Collaboration, et al. **Multi-Messenger Observations of a Binary Neutron Star Merger**. *Astrophysical Journal Letters*, 848(2):L12, 2017.

[16] Francesco Maione, Roberto De Pietri, Alessandra Feo, and Frank Löffler. **Binary neutron star merger simulations with different initial orbital frequency and equation of state**. *Classical and Quantum Gravity*, 33(17):175009, 2016.

[17] Patrick R Brady, Teviet Creighton, Curt Cutler, and Bernard F Schutz. **Searching for periodic sources with LIGO**. *Physical Review D*, 57(4):2101, 1998.

[18] LIGO Scientific Collaboration et al. **Application of a Hough search for continuous gravitational waves on data from the fifth LIGO science run**. *Classical and Quantum Gravity*, 31(8):085014, 2014.

[19] Bruce Allen. **The stochastic gravity-wave background: sources and detection**. In *Relativistic Gravitation and Gravitational Radiation, Proceedings of the Les Houches School of Physics, held in Les Houches, Haute Savoie*, volume 26, pages 373–418, 1997.

[20] The NANOGrav Collaboration, Zaven Arzoumanian, Adam Brazier, Sarah Burke-Spolaor, Sydney Chamberlin, Shami Chatterjee, Brian Christy, James M Cordes, Neil Cornish, Kathryn Crowter, Paul B Demorest, Timothy Dolch, Justin A. Ellis, Robert D. Ferdman, Emmanuel Fonseca, Nathan Garver-Daniels, Marjorie E. Gonzalez, Fredrick A. Jenet, Glenn Jones, Megan L. Jones, Victoria M. Kaspi, Michael Koop, Michael T. Lam, Joseph W. Lazio, Lina Levin, Andrea N. Lommen, Duncan R. Lorimer, Jing Luo, Ryan S. Lynch, Dustin Madison, Maura A. McLaughlin, Sean T. McWilliams, David J. Nice, Nipuni Palliyaguru, Timothy T. Pennucci, Scott M. Ransom, Xavier Siemens, Ingrid H. Stairs, Daniel R. Stinebring, Kevin Stovall, Joseph K. Swiggum, Michele Vallisneri, and Rutger van Haasteren. **The NANOGrav nine-year**

data set: Observations, arrival time measurements, and analysis of 37 millisecond pulsars. *The Astrophysical Journal*, 813(1):65, 2015.

[21] JM Cordes and RM Shannon. **Minimum Requirements for Detecting a Stochastic Gravitational Wave Background Using Pulsars**. *The Astrophysical Journal*, 750(2):89, 2012.

[22] George Hobbs, William Coles, RN Manchester, MJ Keith, Ryan M Shannon, D Chen, M Bailes, NDR Bhat, Sarah Burke-Spolaor, D Champion, et al. **Development of a pulsar-based time-scale**. *Monthly Notices of the Royal Astronomical Society*, 427(4):2780–2787, 2012.

[23] Joseph H Taylor and Joel M Weisberg. **A new test of general relativity-Gravitational radiation and the binary pulsar PSR 1913+ 16**. *The Astrophysical Journal*, 253:908–920, 1982.

[24] Joel M Weisberg, David J Nice, and Joseph H Taylor. **Timing measurements of the relativistic binary pulsar PSR B1913+ 16**. *The Astrophysical Journal*, 722(2):1030, 2010.

[25] Joseph Weber. **Gravitational-wave-detector events**. *Physical Review Letters*, 20(23):1307, 1968.

[26] Odylio Denys Aguiar. **Past, present and future of the Resonant-Mass gravitational wave detectors**. *Research in Astronomy and Astrophysics*, 11(1):1, 2011.

[27] P Astone, R Ballantini, D Babusci, M Bassan, P Bonifazi, G Cavallari, A Chincarini, E Coccia, S D'Antonio, M Di Paolo Emilio, et al. **EXPLORER and NAUTILUS gravitational wave detectors: a status report**. *Classical and Quantum Gravity*, 25(11):114048, 2008.

[28] Antonio Branca, Michele Bonaldi, Massimo Cerdonio, Livia Conti, Paolo Falferi, Francesco Marin, Renato Mezzena, Antonello Ortolan, Giovanni A Prodi, Luca Taffarello, et al. **Search for an ultralight scalar Dark Matter candidate with the AURIGA detector**. *Physical Review Letters*, 118(2):021302, 2017.

[29] University of Maryland. **Photograph of Weber**. `http://www.physics.umd.edu/GRE/GWdetect.htm`, [Accessed: 4/1/2017].

[30] Karsten Danzmann, LISA Pathfinder, eLISA Consortium, et al. **LISA and its Pathfinder**. *Nature Physics*, 11:613–615, 2015.

[31] Eanna E Flanagan and Scott A Hughes. **Measuring gravitational waves from binary black hole coalescences. Signal to noise for inspiral, merger, and ringdown**. *Physical Review D*, 57(8):4535, 1998.

[32] SJ Waldman. **The advanced LIGO gravitational wave detector**. *arXiv preprint arXiv:1103.2728*, 2011.

[33] T Accadia et al. **Virgo: a laser interferometer to detect gravitational waves**. *Journal of Instrumentation*, 7(03):P03012, 2012.

[34] KL Dooley, JR Leong, T Adams, C Affeldt, A Bisht, C Bogan, J Degallaix, C Gräf, S Hild, J Hough, A Khalaidovski, N Lastzka, J Lough, H Lück, D Macleod, L Nuttall, M Prijatelj, R Schnabel, E Schreiber, J Slutsky, B Sorazu, K A Strain, H Vahlbruch, M Ws, B Willke1, H Wittel, K Danzmann, and Grote H. **GEO 600 and the GEO-HF upgrade program: successes and challenges**. *Classical and Quantum Gravity*, 33(7):075009, 2016.

[35] Raffaele Flaminio, KAGRA collaboration, et al. **The cryogenic challenge: status of the KAGRA project**. In *Journal of Physics: Conference Series*, volume 716, page 012034. IOP Publishing, 2016.

[36] Tarun Souradeep. **LIGO-India**. *Resonance*, 21(3):225–231, 2016.

[37] LIGO Scientific Collaboration, Virgo Collaboration, KAGRA Collaboration, et al. **Prospects for Observing and Localizing Gravitational-Wave Transients with Advanced LIGO and Advanced Virgo and KAGRA**. *Living Rev. Relativity*, 19(1), 2016.

[38] Guido Mueller, Hiro Yamamoto, Bill Kells, David Ottaway, Muzammil Arain, Yi Pan, and Peter Fritschel. ***Stable recycling cavities for Advanced LIGO***, 2007. LIGO DCC Document G050423-00. `http://www.ligo.caltech.edu/docs/G/G050423-00/G050423-00.pdf`.

[39] Jun Mizuno, Kenneth A Strain, PG Nelson, JM Chen, Roland Schilling, Albrecht Rüdiger, Walter Winkler, and Karsten Danzmann. **Resonant sideband extraction: a new configuration for interferometric gravitational wave detectors**. *Physics Letters A*, 175(5):273–276, 1993.

[40] Eric D Black. **An Introduction to Pound–Drever–Hall Laser Frequency Stabilization**. *American journal of physics*, 69(1):79–87, 2001.

[41] Peter Fritschel, Nergis Mavalvala, David Shoemaker, Daniel Sigg, Michael Zucker, and Gabriela González. **Alignment of an interferometric gravitational wave detector**. *Applied Optics*, 37(28):6734–6747, 1998.

[42] Muzammil A Arain and Guido Mueller. ***Optical layout and parameters for the Advanced LIGO cavities***. LIGO DCC Document T0900043-v5.

[43] SM Aston, MA Barton, AS Bell, N Beveridge, B Bland, AJ Brummitt, G Cagnoli, CA Cantley, L Carbone, AV Cumming, L L Cunningham, R M R M Cutler, R J S Greenhalgh, G D Hammon, K Haughian, T Hayler, A Heptonstall, J Heefner, D Hoyland, J Hough, R Jones, J S Kissel, R Kumar, N A

Lockerbie, D Lodhia, I W Martin, P G P G Murray, J O'Dell, M V Plissi, S Reid, J Romie, N A Robertson, S Rowan, B Shapiro, C C Speake, K A Strain, K V Tokmakov, C Torrie, A A van Veggel, A Vecchio, and I Wilmut. **Update on quadruple suspension design for Advanced LIGO**. *Classical and Quantum Gravity*, 29(23):235004, 2012.

[44] aLIGO. **aLIGO** About Website. `https://www.ligo.caltech.edu/page/about-aligo`.

[45] Aidan F Brooks, Benjamin Abbott, Muzammil A Arain, Giacomo Ciani, Ayodele Cole, Greg Grabeel, Eric Gustafson, Chris Guido, Matthew Heintze, Alastair Heptonstall, Mindy Jacobson, Won Kim, Eleanor King, Alexander Lynch, Stephen OConnor, David Ottaway, Ken Mailand, Guido Mueller, Jesper Munch, Virginio Sannibale, Zhenhua Shao, Michael Smith, Peter Veitch, Thomas Vo, Cheryl Vorvick, and Phil Willems. **Overview of Advanced LIGO adaptive optics**. *Applied optics*, 55(29):8256–8265, 2016.

[46] Denis V Martynov, ED Hall, LIGO Scientific Collaboration, et al. **Sensitivity of the Advanced LIGO detectors at the beginning of gravitational wave astronomy**. *Physical Review D*, 93(11):112004, 2016.

[47] Daniel Sigg. **Commissioning of LIGO detectors**. *Classical and Quantum Gravity*, 21(5):S409, 2004.

[48] Sheila Dwyer. ***H1 Duty Cycle durring ER7***. LIGO DCC Document T1500368-v1. `https://dcc.ligo.org/LIGO-T1500368`.

[49] Matthew Evans, Slawek Gras, Peter Fritschel, John Miller, Lisa Barsotti, Denis Martynov, Aidan Brooks, Dennis Coyne, Rich Abbott, Rana X Adhikari, et al. Observation of parametric instability in Advanced LIGO. *Physical review letters*, 114(16):161102, 2015.

[50] Eric Oelker, Tomoki Isogai, John Miller, Maggie Tse, Lisa Barsotti, Nergis Mavalvala, and Matthew Evans. **Audio-band frequency-dependent squeezing for gravitational-wave detectors**. *Physical Review Letters*, 116(4):041102, 2016.

[51] LIGO Scientific Collaboration et al. **A gravitational wave observatory operating beyond the quantum shot-noise limit**. *Nature Physics*, 7(12):962–965, 2011.

[52] L. Barsotti. ***Low loss squeezed light injection and signal readout for Advanced LIGO+***. LIGO DCC Document T1400715-v3. `https://dcc.ligo.org/DocDB/0116/T1400715/003/T1400715-v3.pdf`.

[53] S. Ballmer L. Barsotti P. Fulda A. Perreca D. Ottaway A. F. Brooks, R. X. Adhikari. ***Active wavefront control in and beyond Advanced LIGO***. LIGO DCC Document T1500188. `https://dcc.ligo.org/DocDB/0118/T1500188/005/mainAWC.pdf`.

[54] Anthony E Siegman. ***Lasers***, volume 37. 1986.

[55] Hiro Yamamoto. **Mirror quality and interferometer performance**. LIGO DCC Document G1300120. `https://dcc.ligo.org/LIGO-G1300120`.

[56] Hiro Yamamoto. **Optics, Cavity and Loss : What we learned in aLIGO**. LIGO DCC Document G1100857. `https://dcc.ligo.org/LIGO-G1100857`.

[57] Muzammil A Arain and Guido Mueller. **Design of the Advanced LIGO recycling cavities**. *Optics express*, 16(14):10018–10032, 2008.

[58] Herwig Kogelnik and Tingye Li. **Laser beams and resonators**. *Applied optics*, 5(10):1550–1567, 1966.

[59] David Shoemaker. **Advanced LIGO reference design**, 2009. LIGO DCC Document M060056. https://dcc.ligo.org/public/0001/M060056/002/AdL-reference-design-v2.pdf.

[60] Orazio Svelto and David C Hanna. ***Principles of Lasers***, volume 4. Springer, 1998.

[61] RP Photonics. **RP Photonics Encyclopedia**. https://www.rp-photonics.com/encyclopedia.html.

[62] Optique pour l'ingnieur. **Optical Resonators and Gaussian Beams**. http://www.optique-ingenieur.org/en/courses/OPI_ang_M01_C03/co/Contenu_13.html.

[63] Dana Z Anderson. **Alignment of resonant optical cavities**. *Applied Optics*, 23(17):2944–2949, 1984.

[64] Koji Arai. **On the accumulated round-trip Gouy phase shift for a general optical cavity**. LIGO DCC Document T1300189.

[65] Gregory M Harry, LIGO Scientific Collaboration, et al. **Advanced LIGO: the next generation of gravitational wave detectors**. *Classical and Quantum Gravity*, 27(8):084006, 2010.

[66] A Staley, D Hoak, A Effler, K Izumi, S Dwyer, K Kawabe, EJ King, M Rakhmanov, RL Savage, and D Sigg. **High precision optical cavity length and width measurements using double modulation**. *Optics express*, 23(15):19417–19431, 2015.

[67] Aidan Brooks. **Results from Thermal Compensation System testing in the One Arm Test**. LIGO DCC Document T1200465. https://dcc.ligo.org/DocDB/0096/T1200465/002/T1200465-v2.pdf.

[68] Chris L Mueller, Paul Fulda, Rana X Adhikari, Koji Arai, Aidan F Brooks, Rijuparna Chakraborty, Valery V Frolov, Peter Fritschel, Eleanor J King, David B Tanner, et al. **In-situ characterization of the thermal state of resonant optical interferometers via tracking of their higher-order mode resonances**. *arXiv preprint arXiv:1502.02284*, 2015.

[69] Chris L Mueller, Muzammil A Arain, Giacomo Ciani, Ryan T DeRosa, Anamaria Effler, David Feldbaum, Valery V Frolov, Paul Fulda, Joseph Gleason, Matthew Heintze, et al. **The advanced LIGO input optics**. *Review of Scientific Instruments*, 87(1):014502, 2016.

[70] Zujie Fang, Haiwen Cai, Gaoting Chen, and Ronghui Qu. **Optical Phase Locked Loop and Frequency Transfer**. In *Single Frequency Semiconductor Lasers*, pages 235–266. Springer, 2017.

[71] Jaclyn Sanders. **Cavity scan methodology**. LIGO Hanford alog 4033. `https://alog.ligo-wa.caltech.edu/aLOG/index.php?callRep=4033`.

[72] Daniel Sigg. **Executive Summary of the One Arm Test**. LIGO DCC Document L100261. `https://dcc.ligo.org/public/0096/L1200261/002/L1200261-v2.pdf`.

[73] D Sigg, K Kawabe, P Fritschel, and LIGO Scientific Collaboration. **Commissioning advanced ligos HIFO-y**, 2013. LIGO DCC Document T1300174-v1.

[74] Comsol. ***COMSOL Multiphysics: Version 3.3***. Comsol, 2006.

[75] Aidan Brooks. **Update on TCS testing for OAT**. LIGO DCC Document G1200844.

[76] A. Rudiger W. Winkler, K. Danzmann and R. Schilling. **Heating by Optical**

Absorption and the Performance of Interferometric Gravitational-Wave Detectors. *Physical Review A*, 44(11):7022–7036, 1991.

[77] A Freise. ***FINESSE 0.99. 8 User manual***. 2008.

[78] Evan Hall. **PRC Length Measurement**. LIGO Hanford alog 10642. `https://alog.ligo-wa.caltech.edu/aLOG/index.php?callRep=10642`.

[79] Paul Fulda. **PRC aux laser measurement: preliminary results from HOM sweeps**. Hanford alog 15761. `https://alog.ligo-wa.caltech.edu/aLOG/index.php?callRep=15761`.

[80] Kiwamu Izumi and Daniel Sigg. **Advanced LIGO: length sensing and control in a dual recycled interferometric gravitational wave antenna**. *Classical and Quantum Gravity*, 34(1):015001, 2016.

[81] Matt Evans. **Non-Resonant Sidebands and the 4k Schnupp Asymmetry**.

[82] Lisa Barsotti and Matt Evans. **Modeling of alignment sensing and control for advanced LIGO**, 2009. LIGO DCC Document T0900511.

[83] Kiwamu Izumi. **Arm cavities increases SRC mode hops**. LIGO Hanford alog 14694. `https://alog.ligo-wa.caltech.edu/aLOG/index.php?callRep=14694`.

[84] Nicholas Metropolis and Stanislaw Ulam. **The Monte Carlo Method**. *Journal of the American statistical association*, 44(247):335–341, 1949.

[85] Nicolas Smith. **A La Mode: Mode matching and beam propagation solutions for MATLAB**. `https://github.com/nicolassmith/alm`.

[86] Manuel Ruiz. **ACB 1 HOLE RIGHT QPD SKIN (w PD)**. LIGO DCC Document D1200296. `https://dcc.ligo.org/LIGO-D1200296/public`.

[87] David J Ottaway, Peter Fritschel, and Samuel J. Waldman. **Impact of upconverted scattered light on advanced interferometric gravitational wave detectors**. *Opt. Express*, 20(8):8329–8336, Apr 2012.

[88] Hiro Yamamoto. **LIGO I mirror scattering loss by non smooth surface structure**. LIGO DCC Document T070170.

[89] LIGO Scientific Collaboration et al. **Advanced LIGO**. *Classical and Quantum Gravity*, 32(7):074001, 2015.

[90] Margot H Phelps, Kaitlin E Gushwa, and Calum I Torrie. **Optical contamination control in the Advanced LIGO ultra-high vacuum system**. In *SPIE Laser Damage*, pages 88852E–88852E. International Society for Optics and Photonics, 2013.

[91] Kaitlin E Gushwa and Calum I Torrie. **Coming clean: understanding and mitigating optical contamination and laser induced damage in advanced LIGO**. In *Laser-Induced Damage in Optical Materials: 2014*, volume 9237, page 923702. International Society for Optics and Photonics, 2014.

[92] Eric S Bailey, Nicholas R Confer, Vanessa Lutzke, Dana Drochner, Kyle Vircks, and James P Hamilton. **Increased laser damage threshold by protecting and cleaning optics using first contact polymer stripcoatings: preliminary data**. In *Laser-Induced Damage in Optical Materials: 2008*, volume 7132, page 71321M. International Society for Optics and Photonics, 2008.

[93] Adrian Avila-Alvarez, Garilynn Billingsley, Joshua Hacker, Joshua Smith, Daniel Vander-Hyde, and Liyaun Zhang. **Imaging Scatterometer Characterization of Advanced LIGO Optic ITM06**. LIGO DCC Document T1400252.

[94] Hiro Yamamoto. **LCGT test mass surface specification**. LIGO DCC Document T1100351. http://gwdoc.icrr.u-tokyo.ac.jp/DocDB/0003/T1100351/001/JGW-T1100351.pdf.

[95] Fabian Magaña-Sandoval, Rana X Adhikari, Valera Frolov, Jan Harms, Jacqueline Lee, Shannon Sankar, Peter R Saulson, and Joshua R Smith. **Large-angle scattered light measurements for quantum-noise filter cavity design studies**. *JOSA A*, 29(8):1722–1727, 2012.

[96] Stephen E. Nauyoks and Michael A. Marciniak. **Effects of a measurement floor on Mueller matrix measurements in a dual rotating retarder polarimeter bidirectional scatter distribution function system**. *Appl. Opt.*, 54(18):5668–5674, Jun 2015.

[97] Alexa Staley. **CARM at 0pm, controlled by digital REFL9 I**. LIGO Hanford alog 15424. https://alog.ligo-wa.caltech.edu/aLOG/index.php?callRep=15424.

[98] Evan Hall. **Y arm lossy?** LIGO Hanford alog 15432. https://alog.ligo-wa.caltech.edu/aLOG/index.php?callRep=15432.

[99] Kiwamu Izumi. **Y arm intracavity loss can explain the low recycling gain**. LIGO Hanford alog 15450. https://alog.ligo-wa.caltech.edu/aLOG/index.php?callRep=15450.

[100] T Isogai, J Miller, P Kwee, L Barsotti, and M Evans. **Loss in long-storage-time optical cavities**. *Optics express*, 21(24):30114–30125, 2013.

[101] Michael Smith. **Viewports Subsystem Preliminary Design Document** , 2010. LIGO DCC Document T0900511.

[102] Valery Frolov. **IMC mirror large angle scattering**. LIGO Livingston alog 4944. https://alog.ligo-la.caltech.edu/aLOG/index.php?callRep=4944.

[103] Valery Frolov. **IMC scattered light**. LIGO Livingston alog 5740. https://alog.ligo-la.caltech.edu/aLOG/index.php?callRep=5740.

[104] Ryan Christopher Lawrence. ***Active wavefront correction in laser interferometric gravitational wave detectors***. PhD thesis, Massachusetts Institute of Technology, 2003.

[105] Aidan Brooks, Peter Veitch, and Jesper Munch. **Hartmann Sensor for advanced gravitational wave interferometers**, 2006. LIGO DCC Document G060103.

[106] Aidan Brooks. **L1 ITMY thermal lens measurement and analysis**. LIGO Livingston alog 14634. https://alog.ligo-la.caltech.edu/aLOG/index.php?callRep=14634.

[107] Aidan Brooks. **aLIGO TCS actuator calibrations**. LIGO DCC Document T1400685. https://dcc.ligo.org/T1400685-x0.

[108] Aidan Francis Brooks. ***Hartmann wavefront sensors for advanced gravitational wave interferometers.*** PhD thesis, 2007.

[109] David V Hutton. ***Fundamentals of finite element analysis***. McGraw-hill, 2004.

[110] Patrice Hello and Jean-Yves Vinet. **Analytical models of thermal aberrations in massive mirrors heated by high power laser beams**. *Journal de Physique*, 51(12):1267–1282, 1990.

[111] Patrice Hello and Jean-Yves Vinet. **Analytical models of transient thermoelastic deformations of mirrors heated by high power cw laser beams**. *Journal de Physique*, 51(20):2243–2261, 1990.

[112] Bruno A Boley and Jerome H Weiner. ***Theory of thermal stresses***. Courier corporation, 2012.

[113] Roland deWit. **Elastic constants and thermal expansion averages of a nontextured polycrystal**. *Journal of mechanics of materials and structures*, 3(2):195–212, 2008.

[114] Jan Drewes Achenbach. ***Reciprocity in elastodynamics***. Cambridge University Press, 2003.

[115] Yuri Levin. **Creep events and creep noise in gravitational-wave interferometers: Basic formalism and stationary limit**. *Physical Review D*, 86(12):122004, 2012.

[116] Jan D. Achenbach. **Reciprocity and Related Topics in Elastodynamics**. *Applied Mechanics Reviews*, 59(1):13–32, 01 2006.

[117] Eleanor King, Yuri Levin, David Ottaway, and Peter Veitch. **Modeling thermoelastic distortion of optics using elastodynamic reciprocity**. *Physical Review D*, 92(2):022005, 2015.

[118] Charlotte Bond, Daniel Brown, Andreas Freise, and Kenneth A Strain. **Interferometer techniques for gravitational-wave detection**. *Living reviews in relativity*, 19(1):1, 2016.